Development of a time projection chamber prototype with micromegas technology for the search of the double beta decay of 136XE

Francisco José Iguaz Gutiérrez

Tesis Doctoral
Universidad de Zaragoza

Development of a Time Projection Chamber prototype with Micromegas technology for the search of the Double Beta Decay of ^{136}Xe

Memoria presentada por
Francisco José Iguaz Gutiérrez
para optar al grado de Doctor en Física

Laboratorio de Física Nuclear y Astropartículas
Área de Física Atómica, Nuclear y Molecular
Departamento de Física Teórica
Universidad de Zaragoza

Contents

Agradecimientos

Durante cuatro largos años he estado pensando en el día que escribiría esta página. Tras muchas horas en el laboratorio, delante de un ordenador o en alguno de los viajes que he disfrutado durante el doctorado, creo que todo este trabajo ha valido la pena. Sin embargo, los resultados que expongo no son fruto solamente de mi trabajo sino que han sido muchas personas los que en mayor o menor medida han puesto su granito de arena en esta tesis.

Querría en primer lugar dedicar esta tesis a Julio Morales Villasevil, mi tutor durante todos estos años. Julio me abrió las puertas de la Física de Astropartículas y supo no solo infundirme el entusiasmo por este campo sino mantener el buen humor con ese tono socarrón que siempre le caracterizaba. Debido a la enfermedad de Julio, fue Igor G. Irastorza quien asumió el peso de mi tutela y me introdujo en el fascinante campo de los detectores Micromegas. Siempre le agradeceré la libertad que me concedió en mis iniciativas, su cercanía en el trabajo de cada día, sus discusiones animadas y su apoyo constante.

Sin Alfredo Tomás Alquézar no existirían muchos de los resultados. Hace cuatro años empezamos juntos el doctorado y fruto de nuestro trabajo y de largas discusiones, son los programas de simulación y análisis que actualmente usamos. Tampoco hubieran sido las mismas las medidas de caracterización de las micromegas que hicimos en París, ya que antes incluso de empezar medir hubo una labor larga y gris tarea de revisión del sistema de gas y vacío del experimento HELLAZ. Aún recuerdo a Theopisti Dafní, a Alfredo, a Igor y a mí midiendo el outgassing de cada trozo de tubería que añadíamos al sistema. A ella, también le agradezco su apoyo, sus discusiones y entusiasmo.

A Esther Ferrer-Ribas, mi tutora en el IRFU/CEA-Saclay, le debo el haberme enseñado a manejar los detectores micromegas tanto a hacer "bricolage" para reducir el ruido como como recuperarlos si habíamos tenido "problemillas" con ellos. Gracias por tus ánimos cuando no parecía haber mejoras y por tu entusiasmo cuando surgía algo nuevo. Y sobre todo el haberme sentido como en casa durante las diferentes estancias en el centro.

No me puedo olvidar de todas las personas que nos ayudaron en nuestro trabajo: Jean Phillipe Mols, Arnaud Giganon, Stephan Aune, Pierre Salin, Philippe Gordetszky, David Attié, Thomas Papaevangelou, Marc, Julien Palacin, Fabien Jeanneau, Caroline, Begoña, Ilias, Samuel y muchos otros. Y, sobre todo, de Ioannis Giomataris, inventor del detector Micromegas, y que transmite su entusiasmo y apoyo en todas las posibles aplicaciones de este detector.

Quiero agradecer a Alfredo Gimeno, Fredi, por su esfuerzo en la construcción del laboratorio de micromegas y en el diseño, construcción y manejo de la TPC de alta presión de Zaragoza. También contribuyeron Alfonso, David, Juan y Silvia. A Javi Galán le agradezco el haberme enseñado a programar en linux y sus numerosas ideas. Las simulaciones no hubieran llegado a buen puerto sin las revisiones detalladas de Gloria. Tampoco puedo olvidarme de Susana, Asun, Laura y Héctor por su discusiones siempre provechosas y su apoyo siempre constante. Gracias a ti, Ysrael, por tu interés en mi trabajo. Muy largas hubieran sido las tardes delante del

ordenador sin esas largas discusiones sobre ROSEBUD y las Micromegas en el café de la tarde. Al resto de los compañeros del departamento, les agradezco su constante apoyo y disposición.

También le estoy agradecido a José Antonio, Ayalid y Estela, con los que tomamos el café de media mañana. Gracias por sacarnos "a la fuerza" de nuestro despacho, hacernos olvidar durante un rato nuestros problemas y volver con más ganas a nuestro trabajo. Tampoco puedo olvidarme de mis amigos: los físicos, los matemáticos y los que conocí en mi estancia en el Colegio de España de París y en Ginebra, en el experimento CAST.

Dedico esta tesis a mis padres Domingo y Paquita, a mi hermana Belén y a ti, Aurora. Toda la tesis os la debo a vosotros. Vosotros me habéis apoyado en todo momento y me habéis hecho sentirme como en casa cuando estaba lejos.

A ti lector, una sencillas palabras: dicen que todo buen libro de aventuras empieza con una fiesta o en una taberna. Éste comienza hablando del neutrino. Avisado quedas.[1]

Francisco José Iguaz Gutiérrez
24 de noviembre de 2009

[1] Una opinión de Aurora Terés Blanco.

Resumen de la memoria

Desde hace varios años, el Grupo del Investigación de Física Nuclear y Astropartículas (GIFNA) de la Universidad de Zaragoza colabora con el centro de investigación IRFU-CEA/Saclay en el desarrollo y caracterización de detectores micromegas. Fruto de este trabajo son los nuevos detectores micromegas que han remplazado la TPC (siglas en inglés de cámara de proyección temporal) del experimento CAST.

Esta colaboración se ha extendido a más proyectos. Uno de ellos es la medida de la resolución en energía de estos detectores usando fuentes gamma y alfa en gases a alta presión. En un trabajo continuo que ha supuesto varias estancias en Saclay, se han obtenido varios resultados, publicados en una revista de referencia [1] y en varias comunicaciones a congresos [2, 3, 4, 5].

Como aplicación de estos resultados, en esta memoria se ha estudiado la viabilidad de una TPC equipada con un detector micropattern tipo micromegas y llena con 100 kg de xenon enriquecido en ^{136}Xe para un experimento de doble beta. Este trabajo se ha centrado en tres parámetros fundamentales: la resolución en energía, la eficiencia y el nivel de fondo.

La masa del neutrino y la desintegración doble beta

Desde su descubrimiento en 1956 [6], el neutrino ha tenido gran importancia en la Física de Partículas. A lo largo de los años, se han detectado varias fuentes de neutrinos como son el sol, la atmósfera o las centrales nucleares. También se ha comprendido su interacción con la materia, se ha demostrado la existencia de tres familias de neutrinos (electrónico, muónico y tauónico) y se han observado transformaciones u oscilaciones entre neutrinos de diferentes tipos.

Las oscilaciones de neutrinos tienen una conclusión sorprendente: los neutrinos tienen masa. Por tanto, las familias de neutrinos (ν_e, ν_μ, ν_τ) son en realidad una combinación lineal de estados con una masa definida (ν_1, ν_2, ν_3). La observación de las oscilaciones permite delimitar las diferencias cuadráticas entre las masas de los estados. Así, son posibles tres tipos de jerarquías: la estándar, en la que hay dos neutrinos ligeros y un pesado; la inversa, con dos pesados y uno ligero; y la degenerada, en la que las tres masas son mucho mayores que la raíz cuadrada de la mayor diferencia cuadrática. Estas jerarquías se muestran en la figura 1 (izquierda). Sin embargo, las observaciones no permiten estimar la masa absoluta del neutrino.

Este hecho ha impulsado los experimentos de medida absoluta de la masa del neutrino como los que buscan la desintegración doble beta. Éste es un proceso de segundo orden en el que un núcleo se transforma en un isóbaro y se emiten simultáneamente dos electrones. En el modelo estándar de partículas, existe la llamada desintegración con dos antineutrinos

$$(A, Z) \rightarrow (A, Z+2) + 2\ e^- + 2\ \bar{\nu_e} \tag{1}$$

que produce un espectro continuo, como el que se muestra en la figura 1 (derecha). Esta desintegración solamente se puede observar en los núcleos cuyos números atómico y másico sean ambos pares y la diferencia de energía entre los núcleos padre e hijo sea mayor de 2 MeV.

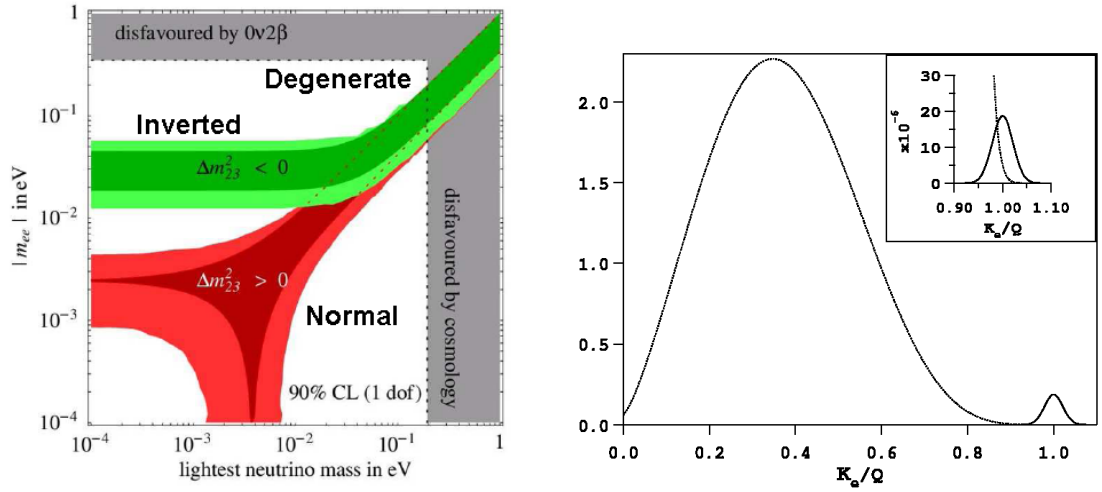

Figure 1: Izquierda: La masa efectiva del neutrino frente a la masa del neutrino más ligero. Las zonas grises están descartadas por los experimentos $\beta\beta0\nu$ y la cosmología [7]. Derecha: El espectro de energía de la desintegración $\beta\beta2\nu$ normalizado en el eje x a la energía $Q_{\beta\beta}$. A la derecha de la imagen, se muestra la señal esperada de la desintegración $\beta\beta0\nu$ y en la esquina superior derecha, el fondo generado por la primera señal en la segunda [8].

Sin embargo, es el decaimiento sin neutrinos el que daría información de nueva física más allá del modelo estándar.

$$(A, Z) \rightarrow (A, Z + 2) + 2\ e^- \tag{2}$$

Este proceso puede suceder si el neutrino dextrógiro virtual emitido por el primer neutrón coincide con su antineutrino y su helicidad coincide con la del neutrino levógiro absorbido por el segundo neutrón. Este cambio en la helicidad solamente puede ocurrir si el neutrino es una partícula de Mayorana (el neutrino y el antineutrino son la misma partícula) y tiene masa. Otra expliciación se basa en la existencia de bosones dextrógiros W_R. Si el neutrino fuera una partícula de Mayorana, un neutrino dextrógiro puede interaccionar con el otro vértice sin necesidad de un cambio de helicidad.

La observación de la desintegración doble beta sin neutrinos permitiría calcular la masa efectiva del neutrino mediante

$$\langle m_\nu \rangle = \frac{m_e}{\sqrt{F_N\ T^{0\nu}_{1/2}}} \tag{3}$$

donde $T^{0\nu}_{1/2}$ es el periodo de semidesintegración del proceso y F_N es un factor de mérito nuclear, diferente para cada isótopo y que depende de un factor de fase y de los elementos matrices nucleares. El cálculo de estos últimos es motivo de controversia ya que existen dos modelos (QRPA [9] y NSM [10]) con resultados muy diferentes para ciertos núcleos. Esta incertidumbre se traslada a la masa del neutrino, en caso de una detección positiva.

Hasta la fecha, los experimentos doble beta han observado el modo estándar en diferentes isótopos midiendo el espectro de energía de los dos electrones. Excepto una discutida observación hecha por H. Klapdor en 2001 [11], no se ha detectado la desintegración sin neutrinos. La mayor sensibilidad se ha conseguido con los experimentos IGEX y HM, basados en detectores de germanio y con una masa de alrededor 10 kg. Éstos han fijado los mejores límites de $T^{0\nu}_{1/2} \geq 1,57 \times 10^{25}$ años y de $\langle m_\nu \rangle \leq 0,35$ eV [12], con un nivel de confianza del 90 %.

Las nuevos experimentos proponen una masa de detección de alrededor de 100 kg para explorar la jerarquía degenerada, que corresponde a masas efectivas del nuetrino mayores de 100 meV, y para confirmar o refutar la observación de Klapdor. En caso de no detectar la señal, el detector debería ser fácilmente escalable a uno de una tonelada, para explorar masas entre 20 y 50 meV, correspondiente a la jerarquía inversa.

Los detectores gaseosos del tipo TPC ya se han usado en experimentos doble beta como el detector Gothard [13]. Su principal ventaja es la observación de la topología de cada evento, que permite discriminar los eventos de señal y de los generados por contaminaciones internas o externas. Sin embargo, su sensibilidad ha estado siempre limitada por su modesta resolución en energía, que en el caso de Gothard era de 6.6 % FWHM en $Q_{\beta\beta}$ (equivalente a 70 keV σ) frente a los 4 keV σ de un detector de germanio.

Los detectores micropattern tipo micromegas

En los años 80, surgieron los detectores *micropattern* que utilizan los avances en microelectrónica y fotolitografía. Uno de éstos detectores es el detector MICROMEGAS (siglas en inglés de MICRO MEsh GAseous Structure), inventados por I. Giomataris en 1995 [14]. Consiste en una final red metálica (o mesh) y un plano de ánodos separados una pequeña distancia (entre 20 y 100 μm) por pilares aislantes, tal como se muestra en la figura 2. La mesh y el plano de cátodos definen el volumen de conversión (o región de deriva), que puede medir desde unos pocos milímetros hasta varios metros. La rejilla y el plano de ánodos definen el volumen de amplificación o gap.

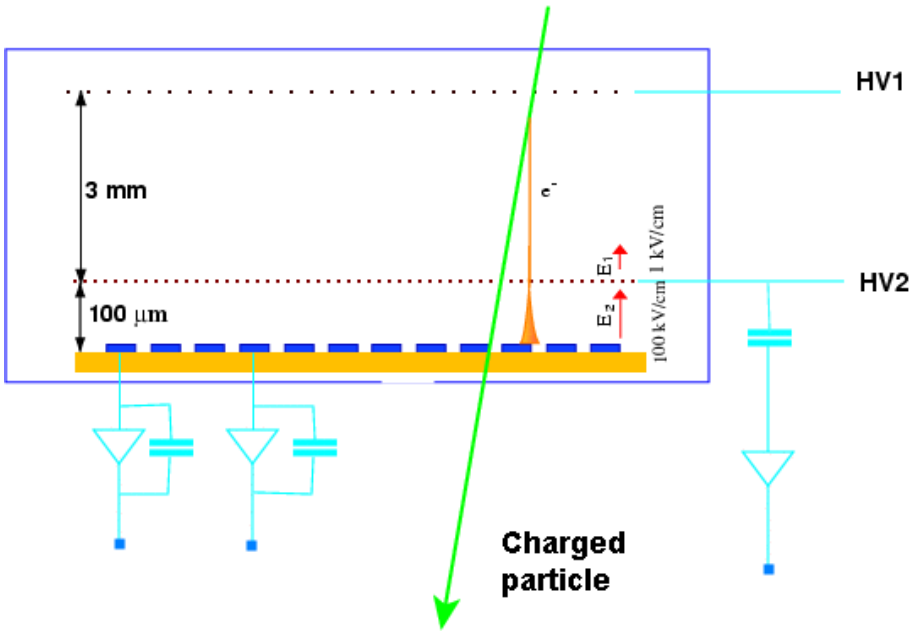

Figure 2: Esquema de un detector micromegas [15]. En el volumen de conversión, delimitado por el cátodo y la rejilla, interaccionan las partículas. En el gap de amplificación, definido por la rejilla y los ánodos, se produce la amplificación de la carga.

El principio de funcionamiento es simple, tal como se muestra en la figura 2. Con unos voltajes moderados, se puede conseguir un elevado campo eléctrico en la región de amplificación (de alrededor 100 kV/cm) y un campo de deriva bajo (hasta 1 kV/cm). Los electrones liberados

en el volumen de conversión derivan hasta el detector. Allí atraviesan la mesh por sus agujeros y cada electrón produce una avalancha debido al intenso campo de amplificación, induciéndose una señal en la mesh y en los ánodos. Los iones son rápidamente recogidos en la mesh y los electrones en los ánodos.

Los detectores micromegas tienen la mejor resolución en energía de los detectores micropattern. Por ejemplo, con los últimos detectores se ha conseguido un valor de 11 % FWHM a 5,9 keV en una mezcla de Ar + 5 % iC_4H_{10} a una atmosfera [1]. Si suponemos que este valor es también válido en xenón puro y que la resolución en energía es proporcional a la inversa de la raíz cuadrada de la energía, se obtendría un valor de 0,54 % FWHM en 2480 keV (5,7 keV σ). Esta estimación sugiere la posibilidad de usar un detector micromegas en un experimento de doble beta.

La caracterización de un detector microbulk en alta energía

En las medidas de resolución en energía, se han utilizado los detectores micromegas de última generación (tipo microbulk [16]) y se han caracterizado con una fuente radioactiva de ^{241}Am, que emite partículas alfas de 5.486 MeV. Para ello, se han empleado dos montajes diferentes: uno previamente utilizado por el experimento HELLAZ [17] y otro totalmente nuevo, en el que se han aplicado los conocimientos adquiridos en el uso del primero.

Las medidas en el primer montaje han mostrado una resolución en energía de hasta 1,8 % y 2 % FWHM para mezclas de argón e isobutano a 4 atmósferas y porcentajes de isobutano de 2 % y 5 % respectivamente. En la mayoría de los casos, el pico es asimétrico, lo que parece indiciar que hay efectos externos que limitan la resolución en energía y que pueden ser intepretados con una función de Landau. Ajustando cada espectro a la convolución de esta función con una gaussiana, se obtiene un valor de 0,7 % y 0,9 % FWHM para 2 % y 5 % respectivamente, tal como se muestra en la figura 3 para la mezcla del 2 %.

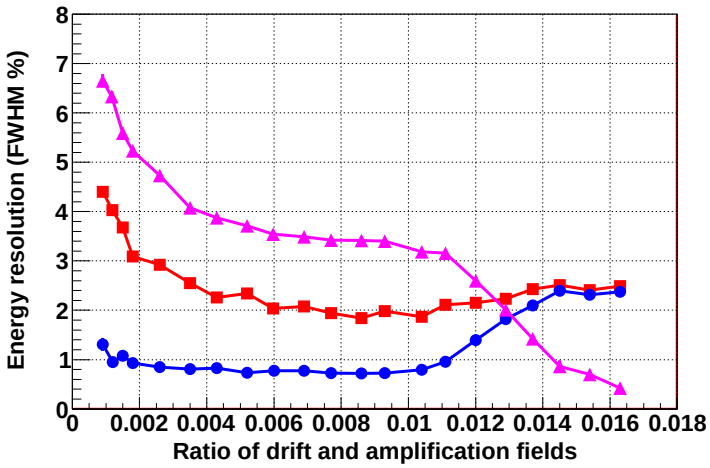

Figure 3: La resolución en energía (% FWHM) frente al cociente de campos de deriva y amplificación para una mezcla de argón e isobutano al 2 % y 4 atmósferas. La línea roja a cuadros indica el valor tras el ajuste a una gaussiana. La línea azul con círculos muestra los valores tras ajustar cada espectro a la convolución de una gaussiana y una función de Landau. La línea magenta con triángulos describe la evolución del parámetro de Landau del segundo ajuste.

En la mezcla del 5 %, se ha medido además el quenching factor o la energía electrón equivalente

correspondiente a una partícula alfa de 5,5 MeV. Para ello, se ha comparado el pico alfa con uno de los rayos x, obteniéndose un valor de aproximadamente la unidad.

Las medidas en xenón puro para presiones entre 2 y 4 atmósferas muestran claramente efectos de *attachment* o absorción de los electrones por impurezas. El efecto más claro es la correlación entre el tiempo de subida y la amplitud de los pulsos a la salida del preamplificador, como muestra la figura 4 (izquierda) y que no aparece en el argón (derecha).

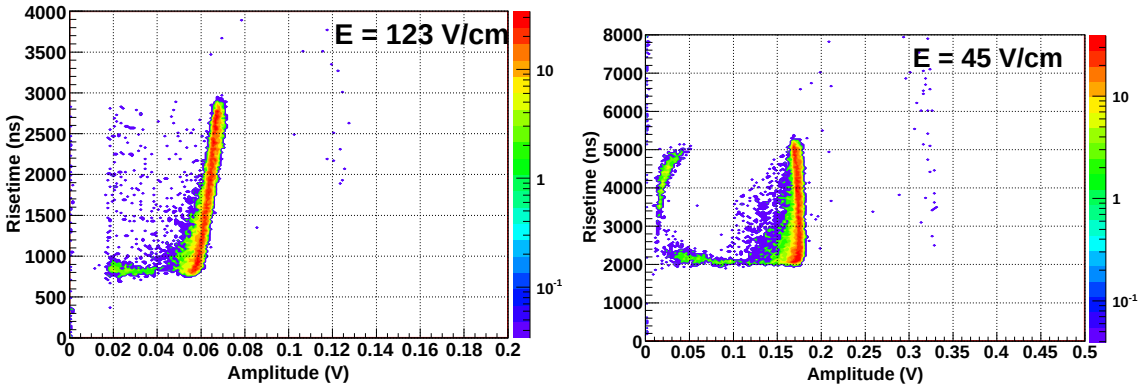

Figure 4: Dos distribuciones del tiempo de subida frente a la amplitud de los pulsos a la salida del preamplificador para xenón puro en 2 atmósferas (izquierda) y argón puro en 4 atmósferas (derecha). La gradación de color indica el número de eventos en escala logarítmica.

Los pulsos de tiempo de subida más largo corresponden a aquellos con una traza perpendicular a la fuente, mientras aquellos con un tiempo de subida menor forman un cierto ángulo con la vertical. El hecho de que estos últimos tengan una amplitud menor es una evidencia de *attachment* porque los electrones de esta traza derivan en promedio más tiempo y, por tanto, tienen una mayor probabilidad de ser absorbidos por impurezas.

Un modelo sencillo permite explicar la dependencia lineal y calcular valores máximos en la vida media de los electrones: 47 ± 5 y 4.0 ± 0.2 μs respectivamente para 3 y 4 atmósferas. Si se supone que el *attachment* está causado principalmente por oxígeno, se puede calcular su concentración en el gas. El mejor valor que se obtuvo fue de ≈ 1000 ppm, tras la instalación de un fitro oxisorb en el sistema de gas.

Si se seleccionan pulsos con un tiempo de subida parecido, se puede minimizar la dispersión debido al *attachment* y hacer un estimación conservadora de la resolución en energía en ausencia de éste. Los valores obtenidos son 2,8 % y 4,5 % FWHM para 2 y 4 atmósferas respectivamente.

El nuevo montaje situado en Zaragoza ha sido diseñado y construido para testear detectores micromegas para diferentes gases y presiones hasta 10 atmósferas. Su diseño optimizado y el sistema de calentamiento (o *bake-out*) de la TPC ha reducido la emisión de gas por parte de las paredes internas (también llamado degasificación u *outgassing* [18]) a menos de 10^{-5} mbar l/seg. Con las medidas en xenón puro, los efectos del *attachment* son claramente menores ya que la amplitud de los pulsos es prácticamente independiente del tiempo de subida para presiones entre 2 y 4 atmósferas. Esto deja de suceder a 5 atmósfera.

Esta observación se ha cuantificado en términos del tiempo de vida medida del electrón. Se ha fijado un valor mínimo de 0.6 ms para 3 y 4 atmósferas, limitado por la precisión del método. Este valor está cerca de los 6 ms necesarios para una reducción de carga menor del 1 % en

mezclas de xenón y distancias de deriva de alrededor de 1 metro. Por lo tanto, la pureza del gas en estas presiones es casi la ideal. En 5 atmósferas, se ha hallado un valor máximo de 38 ± 1 μs.

Si suponemos que el *attachment* está causado principalmente por oxígeno, se obtienen concentraciones alrededor de 80 ppm para los primeros días de medida y de hasta 60 ppm tras recircular el gas por el filtro oxisorb durante una noche. Aunque estos valores son claramente mejores que los obtenidos en Saclay, el *attachment* se puede reducir todavía más con un menor número de componentes plásticos en la TPC, un mejor sistema de calentamiento y periodos más largos de recirculación del gas por filtros de purificación.

El ritmo elevado de la fuente alfa usada en Zaragoza (alrededor de 13 kBq) ha afectado las medidas, como parecen apuntar claramente las curvas de ganancia (ganancias menores de 1) y de transparencia (rangos más estrechos de transparencia máxima). A pesar de esto, se ha medido la velocidad de deriva en argón y xenón puro con valores cercanos a la teoría. Además, la resolución en energía en mezclas de argón e isobutano es parecida a la medida en Saclay y los valores en argón y xenón puro son claramente mejores. También se ha podido medir su dependencia con el campo de deriva.

El mejor valor obtenido en xenón puro ha sido 2,5 % FWHM a 4 atmósferas. En la misma presión y haciendo cortes en el tiempo de subida, se ha estimado la resolución en energía en 1,8 % FWHM en ausencia de *attachment*, tal como muestra la figura 5. Si suponemos que este valor es también válido a 10 atmósferas y que el valor del quenching factor es aproximadamente la unidad como en el caso de mezclas de argon-isobutano, deducimos un valor de 2,7 % FWHM en 2480 keV (σ = 28,3 keV). Si consideramos el factor de quenching de 6,5 medido por la colaboración de Gothard a 5 atmósferas [13], deducimos una resolución en energía de 1,05 % FWHM (σ = 11,1 keV). En ambos casos, se mejora el valor de Gothard (6,6 % FWHM).

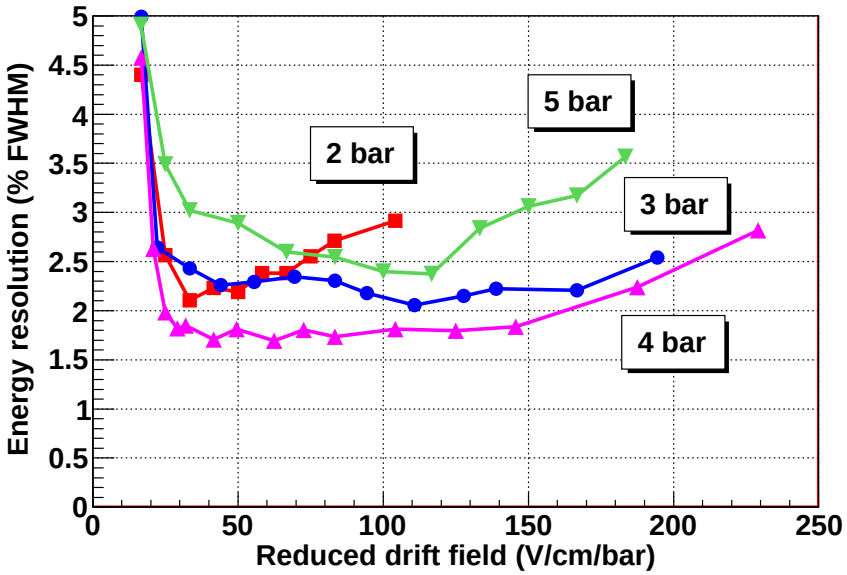

Figure 5: La resolución en energía (% FWHM) estimada con una selección de tiempos de subida frente al campo de deriva en xenón puro en 2 (cuadrados rojos), 3 (círculos azules), 4 (triángulos magenta) y 5 atmósferas (triángulos verdes invertidos).

Eficiencia y nivel de fondo

Se han desarrollado dos programas para simular las señales esperadas de $\beta\beta$ y el fondo en una TPC con un dispositivo de lectura micromegas pixelizado. El primero, basado en Geant4, simula las interacciones físicas en la TPC y da como resultado una serie de depósitos de energía. El segundo, llamado RESTSoft, convierte estos depósitos en píxeles tridimensionales, simulando las características propias de una TPC: la creación de carga, la difusión y la pixelización. Además, permite analizar los eventos generados.

Antes de la simulación, se han estudiado las mayores contribuciones al fondo de una TPC. Para ello, se han definido dos rangos de interés para cada una de las señales esperadas ($\beta\beta2\nu$ y $\beta\beta0\nu$). Para el modo sin neutrinos, se ha concluido que las contaminaciones de ^{208}Tl, ^{214}Bi and ^{60}Co son las más importantes. Para el modo con neutrinos, hay que incluir además los isótopos ^{40}K, ^{212}Bi, ^{228}Ac and ^{234m}Pa. Ésta selección es válida para energías mayores de 1200 keV.

Se han simulado tres geometrías compuestas de una vasija de acero de 1 cm de grosor, un blindaje de plomo de 5 cm y un blindaje de cobre interno de diferentes grosores: 0, 1 y 6 cm. No se ha simulado una vasija de 1 cm de cobre porque no está clara su viabilidad mecánica pero se ha estimado su fondo a partir de los resultados de las tres geometrías. Se han usado los valores medidos por diferentes colaboraciones para fijar la contaminación esperada de cada material. Exceptuando el ^{60}Co y el ^{40}K, se han asignado valores de 1, 0,1 y 0,01 mBq/kg al acero, cobre y plomo respectivamente.

La eficiencia geométrica del detector se ha estimado en un 99,4 % para $\beta\beta2\nu$ y un 72,4 % para $\beta\beta0\nu$. El nivel de fondo más bajo de los simulados con vasija de acero y blindaje interno de cobre se ha obtenido para un blindaje de 6 cm de cobre. En el modo con neutrinos, el valor obtenido (6.75 ± 0.01 cuentas keV^{-1} kg^{-1} año^{-1}) es 30 veces mayor que la señal esperada (0.206 ± 0.001) en un detector enriquecido completamente en ^{136}Xe y una vida media de 10^{22} años, el valor más bajo esperado. En el caso sin neutrinos, el nivel de fondo (0.856 ± 0.001 cuentas keV^{-1} kg^{-1} año^{-1}) es 8 veces mayor que el valor publicado por IGEX (0.1) y dos órdenes de magnitud respecto a Gothard (0.01). Estas diferencias motivan el uso de métodos de discriminación.

Comparando la topología de los eventos en la región de interés generados por la señal $\beta\beta0\nu$ con aquellos producidos por contaminaciones de fondo, se han creado tres métodos de discriminación basados en tres características propias de las señales $\beta\beta0\nu$: la distancia a las paredes, la existencia de una sola conexión y la carga en los dos extremos del eventos. Estos métodos también se han aplicado al rango de interés de $\beta\beta2\nu$.

La aplicación de los tres métodos reduce el nivel de fondo en la región de interés del $\beta\beta2\nu$, como se observa en la figura 6. Cuantitativamente, se alcanzan unos valores de $0,277 \pm 0,003$ y $0,077 \pm 0,001$ cuentas keV^{-1} kg^{-1} año^{-1} respectivamente para la mejor configuración con una vasija de acero y la estimación para el cobre. Estos niveles son mejores que el esperado por Gothard ($2,42 \pm 0,01$)) y comparable a DAMA ($0,0543 \pm 0,0002$) para una vasija de cobre.

En el modo sin neutrinos, el nivel de fondo más bajo con vasija de acero se consigue en la geometría con 6 cm de cobre. El valor obtenido es $(1,27 \pm 0,04) \times 10^{-3}$ cuentas keV^{-1} kg^{-1} año^{-1}, dos órdenes de magnitud mejor que IGEX y uno en comparación con Gothard, tal como muestra la figura 7. Este nivel se reduce a $(3,3 \pm 0,2) \times 10^{-4}$ cuentas keV^{-1} kg^{-1} año^{-1} en el caso de una vasija de cobre de 1 cm. Sin embargo, la acceptancia de las señales es baja: solamente el $37,6 \pm 0,2$ %, que supone una eficiencia total del detector de sólo $28,4 \pm 0,1$ %.

El 80 % de los eventos en la región de interés del $\beta\beta2\nu$ han sido generados por contaminaciones de ^{208}Tl y ^{214}Bi. En el caso del $\beta\beta0\nu$, más del 90 % de los eventos son producidos solamente por impurezas de ^{208}Tl. Notar que estas proporciones dependen de las contaminaciones iniciales.

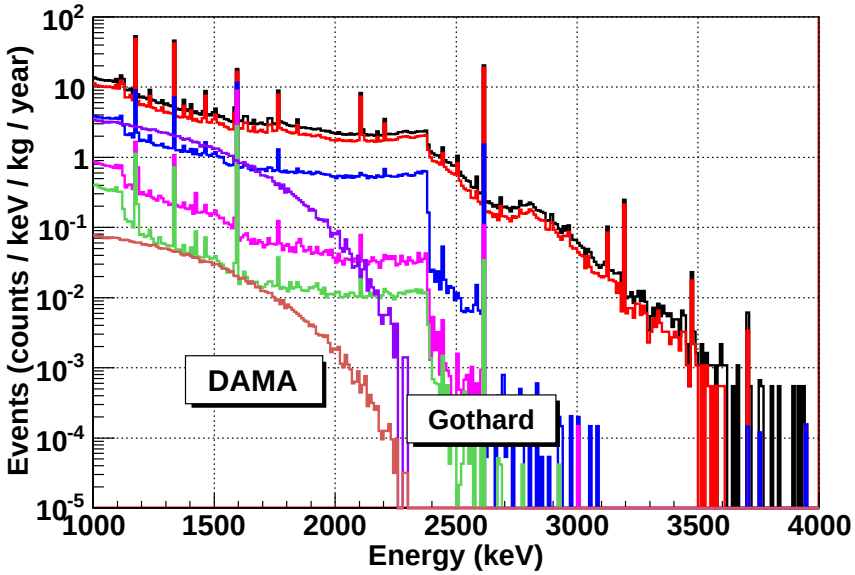

Figure 6: Espectro de energía entre 1 y 4 MeV tras la aplicación de los sucesivos cortes topológicos para la geometría de una vasija de 1 cm de acero con un blindaje interno de cobre de 6 cm. De arriba a abajo: nivel antes de los cortes (línea negra) y tras el corte de las paredes (línea roja), el de una sola conexión (línea azul) y el de los blobs (línea magenta). También se han dibujado el espectro final de la geometría para una vasija de cobre de 1 cm de grosor con un blindaje de 5 cm de plomo (línea verde) y la señal esperada en el NEXT (enriquecido un 80 % en ^{136}Xe) para los límites fijados por Gothard (línea violeta) y DAMA (línea marrón).

El proyecto NEXT: descripción y sensibilidad

Los resultados presentados en este trabajo han motivado el proyecto NEXT [19], que propone la construcción de una TPC de 100 kg de xenon enriquecida en ^{136}Xe para la búsqueda de los dos modos de decaimiento del ^{136}Xe en 5 años.

Como novedad, se medirán por separado la energía, la topología y el tiempo inicial del evento para optimizar la tecnología de cada tarea. La luz primaria producida por una partícula será detectada inmediatamente en el cátodo, determinándose la posición temporal del evento. A continuación, la carga derivará al ánodo, donde será amplificada y la topología reconstruida. La energía se medirá en uno o en ambos extremos. En la figura 8 se muestra un posible diseño del experimento NEXT.

Como primer opción para medir la energía, no necesariamente la tecnología elegida, se propone usar la electroluminiscencia (EL). Consiste en la generación de luz por un campo eléctrico intenso entre dos finas redes y detectada por una matriz de fotosensores, como fotomultiplicadores (PMT), fotomultiplicadores de Silicio (SiPMT) o fotodetectores de avalancha (APD). En teoría, la resolución en energía solo está limitada por las fluctuaciones de la ionización primaria, que en xenón puro es de 0.27 % FWHM en $Q_{\beta\beta}$. Sin embargo, esta hipótesis debe ser confirmada experimentalmente para energías mayores de 1 MeV en xenón a alta presión.

El principal inconveniente de la EL es la necesidad de obtener distancias uniformes entre las dos redes donde se genera la luz. Esto requiere que las redes queden tensadas fuertemente en sus marcos, lo cual es mecánicamente complicada para detectores grandes. Los detectores micromegas no tienen ese problema ya que se construyen mediante técnicas litográficas, obteniéndose *gaps*

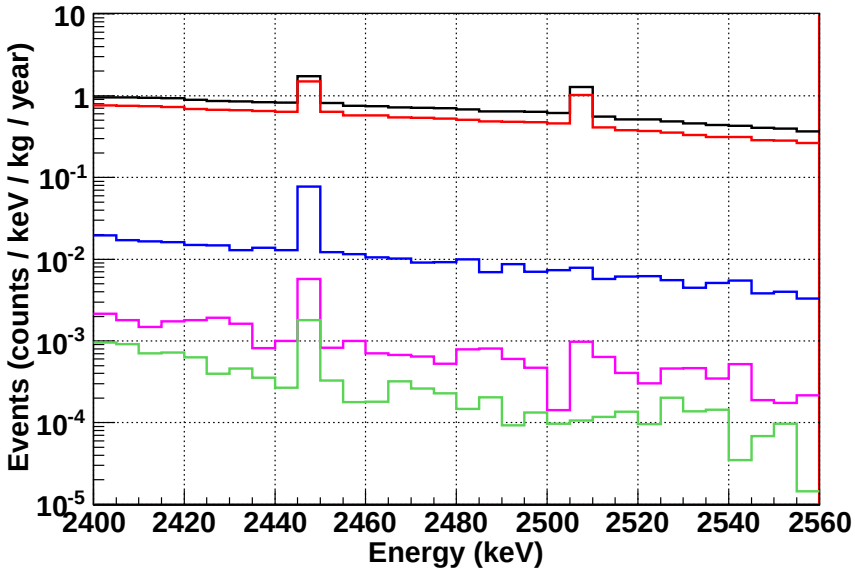

Figure 7: Espectro de energía en la región de interés de $\beta\beta0\nu$ tras la aplicación de los sucesivos cortes topológicos para la geometría con una vasija de acero blindada internamente con 6 cm de cobre. De arriba a abajo: nivel antes de los cortes (línea negra) y tras el corte de las paredes (línea roja), el de una sola conexión (línea azul) y el de los blobs (línea magenta). También se ha dibujado el espectro final de una vasija de cobre de 1 cm y un blindaje de 5 cm de plomo (línea verde).

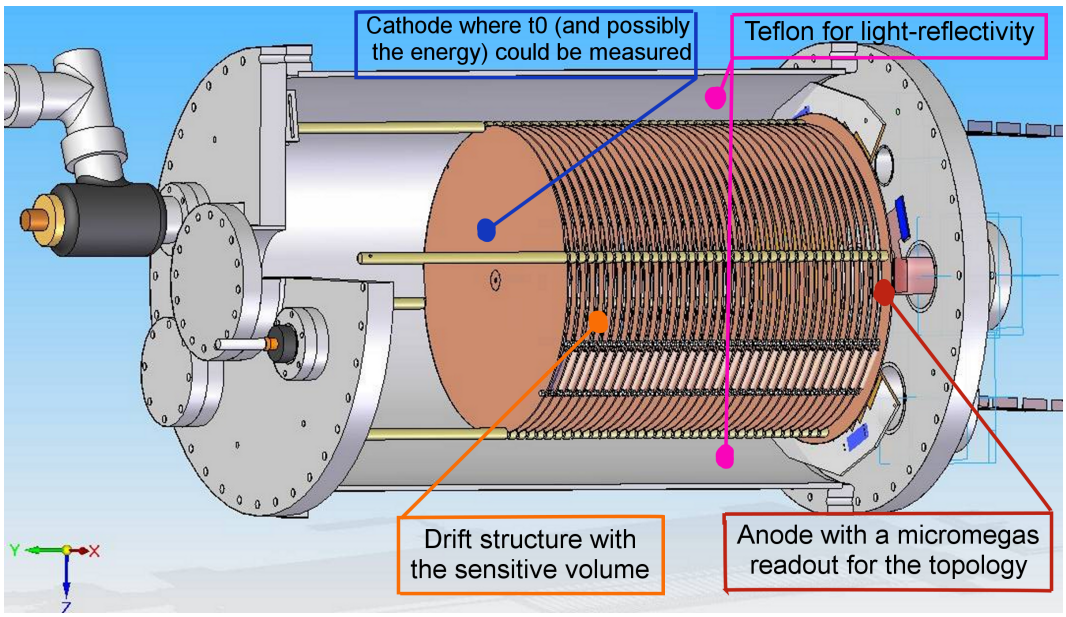

Figure 8: Un diseño de NEXT1-MM [20], que sirve para describir el posible detector de NEXT. La TPC de alta presión tendrá dos dispositivos de lectura (o *readouts*): uno situado en el cátodo para medir t_0; y otro en el ánodo, que registrará la topología del evento. La energía se medirá en uno u otro extremo. Las posibles tecnologías de estos *readouts* son las Micromegas y la Electroluminiscencia (EL), esta última medida por PMTs, SiPMTs o APDs.

de gran precisión. Además, se puede elegir el *gap* de forma que se compensen las fluctuaciones debidas a defectos en la mesh.

Los resultados obtenidos para la resolución en energía, la eficiencia y el nivel de fondo se han combinado para estimar la sensibilidad del experimento NEXT. Se ha considerado un dispositivo Micromegas y una TPC llena de xenón puro a 10 atmósferas enriquecido un 80 % en ^{136}Xe. Se han supuesto tres escenarios: conservador (con una vasija de acero inoxidable y una resolución en energía del 2,8 % FWHM), optimista (con una vasija de cobre y una resolución del 1.1 % FWHM) y agresivo (un vasija de cobre con los niveles medidos por EXO y una resolución del 0.54 % FWHM). La sensibilidad se ha estudiado con tiempos de exposición entre 100 y 5000 kg año, equivalente a masas de detección de 100 kg y 1 tonelada y tiempos de medida entre 1 y 5 años.

Para la señal $\beta\beta2\nu$, NEXT fijará un límite mayor que el de DAMA ($T^{2\nu}_{1/2} > 1,6 \times 10^{22}$ años) en todos los casos. Solamente con una masa de 1 tonelada, 5 años de datos y en el escenario más agresivo se pueden dar cotas por encima de 10^{24} años.

Para el caso $\beta\beta0\nu$ y el escenario conservador, NEXT puede fijar un límite de $1,1 \times 10^{25}$ años en el periodo de semidesintegración del proceso, mejorando un orden de magnitud el límite anterior fijado por DAMA. Valores mayores de 10^{26} años se pueden alcanzar con una masa de exposición mayor de 1000 kg yr en el escenario optimista. El siguiente orden de magnitud (10^{27} años) solamente se puede alcanzar con una masa de detección de 1 tonelada y 5 años de datos.

Con los valores de la vida media y los factores de mérito nuclear, se puede calcular el rango de masas efectivas a los que sería sensible NEXT. Si tomamos los elementos de matriz del modelo QRPA, los rangos de masas son demasiado anchos para estudiar todos los escenarios. En el escenario conservador, se necesitaría un tiempo de exposición de 5000 kg año para confirmar o descartar la evidencia de Klapdor. En el resto de los casos, se necesitarían masas menores. La jerarquía quasidegenerada solamente se podría explorar de forma completa en el escenario agresivo con un detector de 1 tonelada y 5 años de datos. La exploración de la jerarquía inversa requiere una reducción adiccional del nivel de fondo.

Los elementos matriciales del modelo NSM dan rangos más estrechos que el modelo QRPA. La evidencia de Klapdor podría ser confirmada o descartada con una TPC de 100 kg en 1 año de datos en los dos escenarios más optimistas. Sin embargo, los modelos cuasidegenerados solamente se podrían explorar de forma completa con una masa de 100 kg y 5 años de datos en el escenario más agresivo. Masas efectivas del neutrino menores de 20 meV solamente se pueden alcanzar con una reducción adicional del fondo o una mejora de la eficiencia del detector.

Introduction

The neutrino has focused a big interest of the Particle Physics community since its detection in 1956. Many of its properties have been observed: the number of families, the interaction with matter and their sources. However, little light has been shed on two aspects: the mass and the possible autoconjugate nature. Only in the last years with the discovery of the oscillations between families, has it been possible to conclude that its mass was not zero.

The last two properties can be studied by a double beta ($\beta\beta$) decay experiment. The latest collaborations plan to use about 100 kg of detection mass in order to explore the so-called degenerate hierarchy, which corresponds to effective neutrino masses greater than 50 meV. If it were not detected, the detector should be easily scalable to one more ambitious with a mass of few tonnes, capable to study a range of masses between 20 and 50 meV.

Gaseous detectors of type TPC (Time Projection Chamber) have been also used in $\beta\beta$ decay experiments like in the Gothard collaboration. However, their performance has been limited by their modest energy resolution. The introduction of Micro Pattern Gas Detectors in the 80ies has improved this feature to competitive values. Moreover, a TPC with a granular readout can register the topology of each event, which is a key future to discriminate the expected signal from events that fake it, normally called backgrounds.

Since many years ago, the Laboratory of Nuclear Astroparticle Physics (LFNAE) of the University of Zaragoza collaborates with the research center IRFU-CEA/Saclay in the development and characterization of micromegas readouts. For example, it has resulted in the new micromegas detectors that have replaced the TPC in the CAST experiment.

This collaboration has been extended to more projects. One of them is the measurement of the energy resolution of micromegas detectors using gamma and alpha particles and gases at high pressure. For this purpose, we have made several internships in the center and this work has given several interesting results, published in a refereed international journal [1] and several presentations to conferences [2, 3, 4, 5]. Besides, we have gained a lot of experience in different aspects of TPC and micromegas readouts: gain, drift velocity, attachment, gas installations, filters, ...

As an application of these results, the viability of a TPC equiped with a micromegas readout and filled at high pressure with 100 kg of enriched xenon in ^{136}Xe for an experiment of double beta decay is being studied. This is the main objective of this work, which can be considered as a first approach to the question.

The thesis is set out as follows. The properties of the neutrino and the double beta decay are described in chapter 1. In chapter 2, double beta experiments are reviewed, including a description of the desired properties of future experiments and a preliminary study of the sensitivity of a xenon TPC equipped with the micromegas technology. In chapter 3, the basic phenomena of gaseous detectors are studied, which serve as a motivation of the TPC concept and the micromegas technology in particular, described in chapter 4.

Chapter 5 contains the tests with the latest micromegas detectors in the former HELLAZ setup at the IRFU-CEA/Saclay. They include their characterization with a gamma source and different argon-isobutane mixtures and the measurement of the energy resolution with an alpha source and gases at high pressure. The experience acquired in the TPC and the gas system has served in the design and building of a complete new setup in Zaragoza especifically designed and built for this work. In this upgraded setup, the same tests with alphas have been carried out. This is the topic of the chapter 6.

Chapters 7 and 8 treat the efficiency and background level of a future TPC with xenon at high pressure and equipped with a pixelized micromegas. Chapter 7 covers the simulation of the signals and backgrounds, including the description of the simulation codes, the possible contributions to background and a first approach to the design of the experiment. In chapter 8, the topology of signal and background events motivates three discrimination methods, which are used for reducing the expected level of background.

The results of the four former chapters are used in chapter 9 to make a more detailed study of the sensitivity of a xenon TPC equipped with a micromegas readout. In this chapter, the NEXT project, which has been motivated by the results of this work, is also described. Finally, the chapter 10 summarizes the work and gives a conclusion.

Chapter 1

The neutrino mass and the Double Beta Decay

Since the apperance of the neutrino, a great effort has been focused on the study of this particle. Several facts have been learnt: the theory of its interaction with matter, the existence of three families (electron, muon and tau) and the oscillations between these flavours. This last fact has an important consequence: neutrinos have mass.

The first two sections of this chapter are devoted to the history of the neutrino and the the study of its properties. The oscillation of neutrinos, the possible mass hierarchies and the possible Majorana nature of the particle serve as motivation of the double beta decay [8, 23, 24, 25], discussed in the last section.

1.1 A little history of neutrino

The history of neutrino starts in 1930, as a solution proposed by W. Pauli to solve the problem of the continous spectrum of electrons in beta desintegrations, previously observed by J. Chadwik in 1914. In 1933 E. Fermi published the first theory for beta decay, incorporating and naming the neutrino [26]. Two years later, M. Goeppert-Mayer was the first to consider double beta decay [27] and in 1937 the young E. Majorana published his theory on neutrinos, stating that neutrinos and antineutrinos are the same particle and suggesting an experiment to prove this fact [28]. A succession of papers by Racah, Furry and Primakoff formulated what is called now the $\beta\beta0\nu$ theory.

The experimental proof of neutrino's existence needed more time. It happened in 1956 when F. Reines and C. Cowan passed a beam of neutrinos from the River Nuclear Plant through a target of heavy water and cadmium chloride [6]. Since then, neutrinos have been detected in several natural sources like the sun, the atmosphere (produced by cosmic rays) or a supernova explosion.

Atmospheric neutrinos were the first to be observed in 1965. F. Reines used a large area liquid scintillator detector situated in the East Rand gold mine in South Africa [29]. Three years later R. Davis obtained the first radiochemical results for solar neutrinos at the Homestake mine in South Dakota [30]. On February 23rd 1987 the blue supergiant Sanduleak-69d 202a exploded in the Large Magellanic Cloud, about 50 kpc away from the Earth. Three experiments (KamiokaNDE, IMB and Baksan) observed the neutrino burst from the type II supernova. The 24 events detected have provided valuable information on neutrino's properties.

The existence of more families of neutrinos only required six years. It was in 1962 when L. Lederman, M. Schwartz and J. Steinberger identified the muon neutrino at th Brookhaven National Laboratory [31]. However, the number of families remained an open question until 1989. The SLC (SLAC Linear Collider) [32] and LEP (Large Electron Positron collider) [33] produced almost simultaneous results from studying the Z boson, constraining the number of types in the Standard Model of Particles to only three. The last family of neutrinos needed more time and efforts to be detected. The DONUT (Direct Observation of NU Tau) was set up to search for the tau neutrino utilising the Tevatron beam at Fermilab. The detector took data six months in 1997 but it took three years of hard analyis to announce the discovery of the tau neutrino in July 2000 [34].

The detection of solar neutrinos created a mystery that remained unexplained until 2002: the "solar neutrino problem". When R. Davis detected solar neutrinos, he observed a third of the expected number, estimated the Solar theory. This deficit was confirmed twenty years later by the experiment Kamiokande II (in Mozumi mine in Japan) [35]. The solution was provided by the SNO experiment (Sudbury Neutrino Observatory), located in the Creighton Mine in Sudbury (Canada), in 2001 giving the first convincing evidence of the solar neutrinos oscillations [36]. This concept had been previously proposed by B. Pontecorvo in 1957 [37]. Four years later, Z. Maki, M. Nakagawa and S. Sakata developed this idea in the theory of neutrino flavour mixing and flavour oscillations [38].

Not only solar neutrino oscillations have been observed. This phaenomena also happens in neutrinos produced in the atmosphere or in reactors. As in the solar case, it causes a deficit in the number of detected neutrinos. This was the conclusion of the Irvine Michigan Brookhave (IMB) [39] and the Kamioka Nucleon Decay (KamiokaNDE) [40] experiments in 1985 for atmosphere neutrinos. And as in the solar case, it required ten years to be explained by oscillations.

This happened in 1998, by another experiment based in Kamioka, the Super-Kamiokande [41]. It consisted of a large water Cerenkov detector located 1000 m undergound at the Mozumi Mine. The first detection of a deficit of reactor neutrinos was observed by KamLAND (Kamioka Liquid scintillator AntiNeutrino Detector) in 2002 [42]. This experiment was built inside the old KamiokaNDE cavity and designed to detect electron antineutrinos from nuclear reactors surrounding it.

1.2 The nature of neutrino

Neutrinos are weakly interacting, spin 1/2 particles, with no charge and a very small mass. In the Particle Standard Model, this mass is exactly zero. As mentioned in the previous section, the LEP and SLC experiments have shown that there are three flavours (ν_e, ν_μ, ν_τ) which are linear combinations of states with a well defined mass. The existence of more massive neutrino states is possible but they must be sterile (a neutrino that only interacts with matter through gravity) or have a mass less than 0.5 M_Z (M_Z is the mass of the Z-Boson), so as not to disagree with LEP and SLC results [32, 33].

Oscillation experiments (solar, atmospheric, reactor and accelerator) have shown that neutrinos have mass. The absolute mass determination is pursued by two types of experiments: those that measure the end point energy of the beta spectrum (typically tritium beta decay experiments) and neutrinoless double beta decay experiments. If successful, they will shed light on the possible mass hierarchies, not to mention the new physics beyond the Standard Model of particles.

Another property that must be elucidated is the Dirac of Majorana nature of neutrino. In Particle Physics, the distinction between particle and antiparticle is related to the presence of a conserved quantity like charge. This happens not only for charged particles, whose antiparticles have opposite electric charge, but also for other particles like neutron or the K^0, whose antiparticles have opposite baryon number. These particles are normally called Dirac particles. If a particle and its antiparticle are the same, it is called Majorana particle.

In the next subsections, the flavour mixing theory of neutrinos and its application to oscillation is reviewed. In the final one, a short description of the direct mass measurements is described.

1.2.1 Flavour mixing

Late experimental observations have lead to the conclusion that neutrinos of a definite flavour (ν_e, ν_μ, ν_τ) are not necessary states of a definite mass (ν_1, ν_2, ν_3). On the contrary, they are generally coherent superpositions of such states

$$|\nu_l\rangle = \sum_i U_{li} \, |\nu_i\rangle \tag{1.1}$$

where U is an unitary matrix that describes the mixture. It is generally called the PNMS matrix, in honour to the developpers of neutrinos mixing theory: Pontecorvo, Maki, Nakagawa and Sakata. Using the Chau-Keung parametrization [43], U is expressed by

$$\begin{pmatrix} \nu_e \\ \nu_\mu \\ \nu_\tau \end{pmatrix} = \begin{pmatrix} c_{12}c_{13} & s_{12}c_{13} & s_{13}e^{-i\delta} \\ -s_{12}c_{23} - c_{12}s_{23}s_{13}e^{i\delta} & c_{12}c_{23} - s_{12}s_{23}s_{13}e^{i\delta} & s_{23}c_{13} \\ s_{12}c_{23} - c_{12}c_{23}s_{13}e^{i\delta} & -c_{12}s_{23} - s_{12}c_{23}e^{i\delta} & c_{23}c_{13} \end{pmatrix} \times \\ \times \begin{pmatrix} 1 & 0 & 0 \\ 0 & e^{i\phi_2/2} & 0 \\ 0 & 0 & e^{i(\phi_3/(2+\delta))} \end{pmatrix} \begin{pmatrix} \nu_1 \\ \nu_2 \\ \nu_3 \end{pmatrix} \tag{1.2}$$

where $c_{ij} = cos(\theta_{ij})$ and $s_{ij} = \sin(\theta_{ij})$ are the mixing angles measured in neutrino oscillations and δ is the Dirac CP phase. The second matrix contains the Majorana CP phases (ϕ_2 and ϕ_3) that do not exits in the case of Dirac neutrinos.

1.2.2 Neutrino oscillations

Neutrino oscillation is a process whereby a neutrino of one flavour evolves in time, changing into a neutrino of a different flavour. In vacuum the probability of this process between types α and β is

$$P(\nu_\alpha \to \nu_\beta) = \left| \sum_i U^*_{\alpha i} \, U_{\beta i} \exp\left(-\frac{i m_i^2 L}{2E} \right) \right|^2 \tag{1.3}$$

where m_i are the neutrino mass eigenstates, $U_{\alpha\beta}$ are the elements of the PMNS matrix, L is the propagation length and E is the neutrino energy. In the simplified two families case, the oscillation probability becomes

$$P(\nu_\alpha \to \nu_\beta) = \sin^2(2\theta) \sin^2\left[1.27 \frac{\Delta m^2 \; L}{E} \right] \tag{1.4}$$

where $\Delta m^2 = \left| m_i^2 - m_j^2 \right|$ in eV, L is in km and E in GeV.

Parameter	Value	C.L.	Reference
$\sin^2 2\theta_{12}$	$0.86^{+0.03}_{-0.04}$	68%	[44]
$\sin^2 2\theta_{23}$	> 0.92	90%	[45]
$\sin^2 2\theta_{13}$	< 0.19	90%	[46]
Δm^2_{21}	$8.0^{+0.4}_{-0.3} \times 10^{-5}\ eV^2$	68%	[44]
$\lvert\Delta m^2_{32}\rvert$	$2.4^{+0.6}_{-0.5} \times 10^{-3}\ eV^2$	68%	[45]
$\langle m_\nu \rangle\ (\beta)$	$< 2eV$	95%	[47, 48]
$\langle m_\nu \rangle\ (\beta\beta)$	$< 0.7eV$	90%	[12, 49]
$\sum_i m_i$	$< 2\ eV$	95%	[50]

Table 1.1: The most recent values for the neutrino mixing angles, the quadratic mass differences and the mass limits, extracted from [51].

From the PNMS matrix we note that the oscillation probability is independent of the two Majorana phases. The angles θ_{ij} correspond to neutrinos of different origins: θ_{23} appears in the oscillations of atmospheric neutrinos (atm), θ_{12} in those coming from the sun (sol) and θ_{13} is governed by the short baseline reactor neutrinos (rtr). With this nomenclature, we rewrite the mass squared differences as

$$\Delta m^2_{atm} = \left|m_3^2 - m_2^2\right|,\ \Delta m^2_{rtr} = \left|m_3^3 - m_1^2\right|,\ \Delta m^2_{sol} = m_2^2 - m_1^2 \tag{1.5}$$

Parameters formerly described (mainly the mixing angles θ_{ij} and the quadratic mass differences Δm^2_{ij}) have been determinated or limited by the four neutrinos sources mentioned in last section. In table 1.1, a summary of these values is given.

1.2.3 Mass hierarchies

From the table 1.1, we know that $\Delta m^2_{sol} = m_2^2 - m_1^2$ is positive. This means that ν_2 is heavier than ν_1. We don't know if ν_3 is heavier or lighter. In the first case, the arrangement of masses is called **normal hierarchy** (two light neutrinos and a third significantly heavier one). In the second case, the arrangement is called the **inverted hierarchy**. When all three masses are significantly larger than $\sqrt{\Delta m^2_{32}}$, the hierarchy is referred to as **quasidegenerate**, no matter which eigenstate is the lightest.

All these three mass schemes are still possible and the distinction between them is an important open question, like the absolute neutrino mass value. The two non-degenerate hierarchies are schematically shown in figure 1.1 (left) and the upper mass limits (from direct mass determination and double beta decay experiments) are shown in table 1.1.

From equation 1.5, one may express two of the neutrinos in function of the lightest one and the quadratic square masses:

- Normal hierarchy: $m_2 = \sqrt{m_1^2 + \Delta m^2_{sum}}$ and $m_3 = \sqrt{m_2^2 + |\Delta m^2_{atm}|}$.
- Inverted hierarchy: $m_1 = \sqrt{m_1^3 + |\Delta m^2_{atm}|}$ and $m_2 = \sqrt{m_1^2 + \Delta m^2_{sum}}$.

The measurement of the effective electronic neutrino mass can shed light on this question. By using equation 1.2, this observable is defined by

$$|\langle m_\nu \rangle| = |c_{12}^2 c_{13}^2 m_1 + s_{12}^2 c_{13}^2 e^{i\phi_2} m_2 + s_{13}^2 e^{i\phi_3} m_3| \tag{1.6}$$

The relation between the effective mass and the lightest neutrino mass is shown in figure 1.1 (right). At high values of the minimum neutrino mass, the mass spectrum is quasi-degenerate. For masses lower than 50 meV, the degenerate band splits into two levels, representing the normal and inverted hierarchies. In this case, it would be possible the identification of the appropiate band.

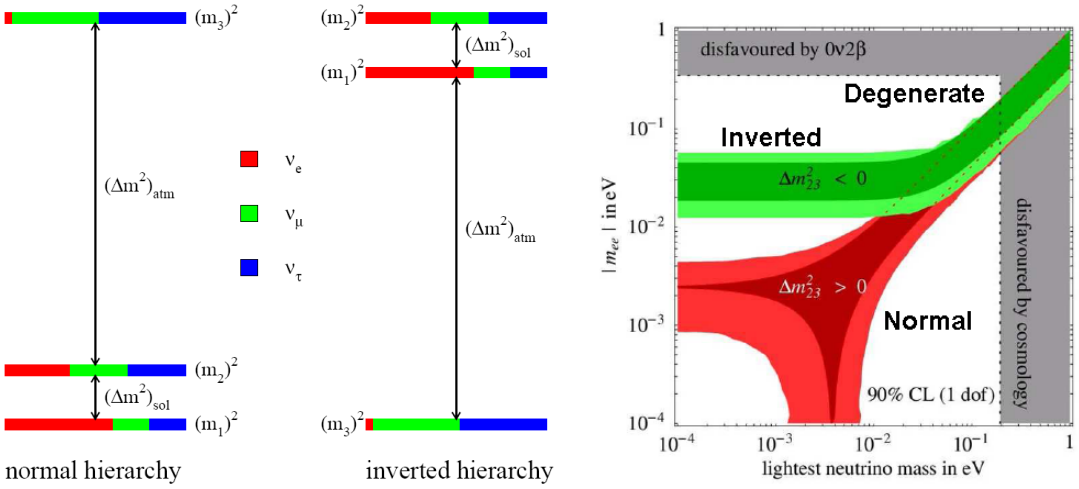

Figure 1.1: Left: A scheme of the hierarchy models (normal and inverted) consistent with data from oscillation experiments [52]. Right: Dependence of the effective neutrino mass with the lightest neutrino mass. The grey bands are disfavoured by cosmology and $\beta\beta0\nu$ decay observations[7].

1.2.4 Direct mass determination

The measurement of the neutrino oscillations has fixed the quadratic mass differences but the absolute mass must be determined by the observation of the neutrinoless double beta decay (explained in next section) or the study of the endpoint of the tritium β decay spectrum. This element decays into ^{3}He via the reaction

$$^3H \rightarrow ^3 He^+ + e^- + \nu_e \tag{1.7}$$

with a half-life of 12.3 yr. The mass of the neutrino creates a distorsion at the spectrum, which is expressed as

$$\frac{dN}{dE} = C\ F\ p_e\ E\ (E_0 - E)^2\ \sqrt{1 - \frac{m^2_{\nu_e} c^4}{(E_0 - E)^2}} \tag{1.8}$$

where C is a constant, F is the Fermi function, p_e and E are the momentum and energy of the electron and $E - E_0$ is the energy of the neutrino.

Tritium β decay experiments have several difficulties such as the low counting rate at the end point, the energy resolution of the spectrometer, the luminosity and the background. The first measurements were made in 1948 by Curran, Angus and Cockcroft, which fixed a conservative upper limit of $\approx$ 1 keV [53]. The best result to date come from Mainz [47] and Troitsk [54], which combined give a limit of $m_{\nu_e} < 2.2$ eV. The Karlsruhe TRItium Neutrino experiment (KATRIN) is a next generation experiment designed to reach neutrinos values near 0.3 eV. KATRIN is currently being built [55].

1.3 The double beta decay

The double beta decay is a second-order, weak semileptonic process in which a nucleus transforms into an isobar and two electrons are simultaneusly emitted. This means that the proton number Z is changed by two units, leaving the mass number A unchanged. In the Standard Model, electrons are emitted with two antineutrinos:

$$(A, Z) \rightarrow (A, Z + 2) + 2\ e^- + 2\ \bar{\nu}_e \tag{1.9}$$

This is called the two-neutrinos double beta decay mode ($2\nu\beta\beta$). As a first approximation, this process is 10^{21} times slower that the single beta decay, resulting in half-lives of the order of 10^{18}-10^{22} years. The energy spectrum of the two electrons is continuous as shown in figure 1.2.

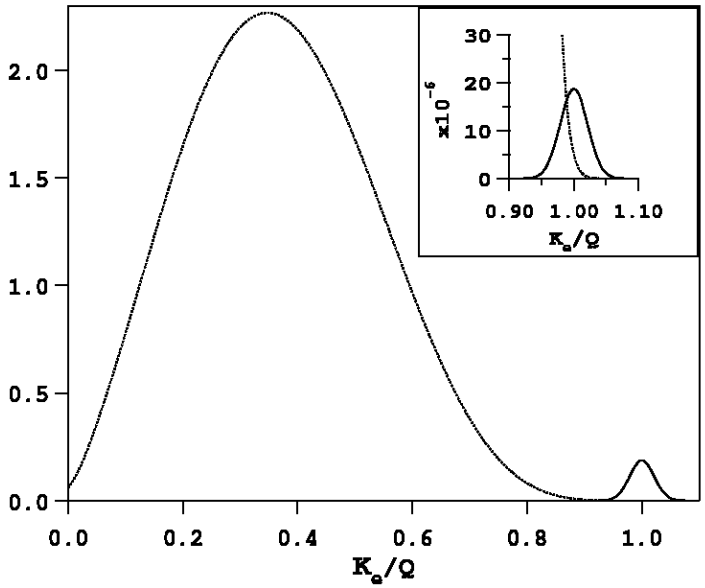

Figure 1.2: The $\beta\beta2\nu$ energy spectrum normalized in the x-axis to the endpoint $Q_{\beta\beta}$. On the right it is also shown the expected spectrum for $\beta\beta0\nu$ and at the upper right corner, the background generated by the first signal in the range of interest of second one. The plot has been extracted from [8].

Its experimental observation is only possible if the single beta decay is forbidden by energy conservation or, at least, strongly hindered by a small transition energy and/or large change of angular momentum. These two facts only happen if the intermediate nucleus has more energy than both nuclei and Z and A are both even. If $Q_{\beta\beta}$ is the difference of energy between the parent and the daughter nuclei, the probability of the double beta decay is proportional to $Q^5_{\beta\beta}$. This is why only nuclei with $Q_{\beta\beta}$ greater than 2 MeV are normally considered. There are 11 nuclei which fulfill these conditions, shown in table 1.2.

The general equation for the ground to ground state ($0^+ \rightarrow 0^+$) decay rate for the 2ν mode is expressed by

$$\left[T^{2\nu}_{1/2}(0^+ \rightarrow 0^+)\right]^{-1} = G_{2\nu}\ \left|M^{2\nu}_{GT}\right|^2\ , \tag{1.10}$$

where $G_{2\nu}$ is an integrated kinematical factor and $M^{2\nu}$ is the nuclear (double Gamow-Teller) matrix element. This decay rate does not depend on the neutrino mass and there is no distinction

Isotope	%	Q(keV)	$T^{2\nu}_{1/2}$(yr)
^{48}Ca	0.19	4271	$4.2^{+2.1}_{-1.0}\ 10^{19}$
^{76}Ge	7.4	2039	$(1.5 \pm 0.1)\ 10^{21}$
^{82}Se	8.73	2995	$(0.92 \pm 0.07)\ 10^{20}$
^{96}Zr	2.8	3350	$(2.0 \pm 0.3)\ 10^{19}$
^{100}Mo	9.6	3034	$(7.1 \pm 0.4)\ 10^{18}$
^{116}Cd	7.49	2802	$(3.0 \pm 0.2)\ 10^{19}$
^{128}Te	31.69	868	$(2.5 \pm 0.3)\ 10^{24}$
^{130}Te	33.8	2533	$(0.9 \pm 0.1)\ 10^{21}$
^{136}Xe	8.9	2480	$\geq 1.6\ 10^{22}$
^{150}Nd	5.6	3367	$(7.8 \pm 0.7)\ 10^{18}$
^{238}U	99.3	1145	$(2.0 \pm 0.6)\ 10^{21}$

Table 1.2: List of $\beta\beta 2\nu$ decay measurements showing for each isotope, its natural abundance (%), the available energy $Q_{\beta\beta}$ and the half-time of the process [25].

made between Majorana and Dirac neutrinos. From the above equations one can thus calculate the matrix elements using experimentally measurements of the $2\nu\beta\beta$ decay half-lives.

In the transition $0^+ \rightarrow 0^+$ electrons are emitted in the states S- and P-wave states and with an angular momentum $j = 1/2$. The angular correlation between the electrons is described by the distribution 1.11. In this expression, an aproximation in the plane wave limit for electrons is made (see [56] for details).

$$\begin{aligned} \frac{d^3\Gamma}{dT_1 dT_2 d\cos\theta} &= A\ (m_e + T_1)^2\ (m_e + T_2)^2\ (Q_{\beta\beta} - T_1 - T_2)^5\ h_{2\nu}(T_1, T_2) \\ & \quad d_0(T_1)\ d_0(T_2)\ \left[1 - \frac{\sqrt{T_1\ T_2\ (T_1 + 2\ m_e)\ (T_2 + 2\ m_e)}}{(T_1 + m_e)\ (T_2 + m_e)} \cos(\theta)\right]\ , \end{aligned} \tag{1.11}$$

where T_1 and T_2 are the kinetic energies of the electrons, θ is the angle between their initial directions and m_e is the electron mass. The rest of the terms consists of the normalization factor $h_{2\nu}(T_1, T_2)$, the constant A described by

$$A = \left|\frac{M_{GT}}{\mu_0}\right|^2\ g_0\ (2\pi\alpha Z)^2\ , \tag{1.12}$$

and the Fermi functions $d_0(T_i)$ expressed by

$$d_0(T_i) = 1 - \exp\left(\frac{2\pi\alpha(T_i + m_e)}{\sqrt{T_i\ (T_i + 2\ m_e)}}\right)\ , \tag{1.13}$$

1.3.1 The neutrinoless mode

The neutrinoless double beta decay ($0\nu\beta\beta$) is a lepton violating process not allowed by the Standard Model. During the transition, only two electrons are emitted.

$$(A, Z) \rightarrow (A, Z + 2) + 2\ e^-\ . \tag{1.14}$$

For this non-standard transition to happen, the virtual right-handed neutrino emitted by the first neutron decay must be equal to its antineutrino and match the helicity of the virtual

left-handed neutrino absorbed by the second neutron. This helicity flip can only occur if the neutrino is a Majorana particle and is massive. It would be impossible if the neutrino were massless, as there would be no reference frame where the direction of momentum is reserved. This mechanism, that involves the helicity flip of the neutrino mass due to its mass, is know as the **mass mechanism**. The half-life of this process is described by

$$\left(T_{1/2}^{0\nu}\right)^{-1} = G_{0\nu} \left|M^{0\nu}\right|^2 \left(\frac{\langle m_\nu \rangle}{m_e}\right)^2 , \tag{1.15}$$

where $G_{0\nu}$ is a phase space factor and $M^{0\nu}$ are the (neutrinoless) Nuclear Matrix Elements (NME). The first parameter can be easily calculated with high precission for all isotopes with $Q_{\beta\beta} > 2$ MeV. Some of them are shown in the table 1.3. However, the determination of the NMEs is still a controversial topic, described in section 1.3.2.

^{76}Ge	7.93	^{100}Mo	57.3	^{130}Te	55.4
^{82}Se	35.2	^{116}Cd	62.3	^{136}Xe	59.1
^{96}Zr	73.6	^{128}Te	2.21	^{150}Nd	269

Table 1.3: The phase space factors $G_{0\nu}$ (10^{-15} yr) calculated in [58].

In some references like [23, 25], a nuclear figure-of-merit F_N is defined by the multiplication of the two first terms to keep the nuclear dependence in just one term. The effective neutrino mass can be then calculated from the neutrinoless half-life by the formula

$$\langle m_\nu \rangle = \frac{m_e}{\sqrt{F_N \; T_{1/2}^{0\nu}}} . \tag{1.16}$$

Apart fromt the helicity flip, there are other possibilities that lead to the emission of two electrons without neutrinos. There are theories beyond the Standard Model which predict the existence of pure right-handed W bosons (W_R) or W bosons with mixtures of left-handed and right-handed W bosons ($W = W_R + W_L$) [57]. If W_R exists and the neutrino is a Majorana particle, a righthanded neutrino can interact at the other vertex without need for a helicity flip. This mechanism is known as the **right-handed current mechanism** of the neutrinoless double beta decay. The half-life of this process is inversely related to the phase-space-factor of the process, the NME and the coupling constant λ of the right-handed neutrino with W_R by the expression

$$\left(T_{1/2}^{0\nu}\right)^{-1} = G_{0\nu} \left|M^{0\nu}\right|^2 \left\langle \lambda^2 \right\rangle \tag{1.17}$$

The neutrinoless mode has not yet been observed, excepted for a claim described in section 2.3.2. Its observation would allow to measure the effective mass and would give information on the mass hierarchy. Moreover, it would have big implications in Particle Physics, due to the Majorana nature of the neutrino. In table 1.4, the best limits for each isotope and the detection technique used are shown.

As in the two-neutrinos mode, electrons in the transition $0^+ \rightarrow 0^+$ are emitted in the S-wave and P-wave states and with an angular momentum $j = 1/2$. The angular correlation between

Isotope	Tecnique	$T^{0\nu}_{1/2}$ (yr)	$\langle m_{\beta\beta}\rangle$ (eV)	Ref.
^{48}Ca	CaF_2 scintillating crystals	$> 1.4 \times 10^{22}$	$< 7.2 - 44.7$	[59]
^{76}Ge	Germanium detector	$> 1.57 \times 10^{25}$	$< 0.33 - 1.35$	[12]
^{82}Se	Foils and tracking	$> 2.1 \times 10^{23}$	$< 1.2 - 3.2$	[60]
^{100}Mo	Foils and tracking	$> 5.8 \times 10^{23}$	$< 0.6 - 2.7$	[60]
^{116}Cd	$CdWO_4$ scintillating crystals	$> 1.7 \times 10^{23}$	< 1.7	[61]
^{128}Te	Geochemical	$> 7.7 \times 10^{24}$	$< 1.1 - 1.5$	[62]
^{130}Te	TeO_2 bolometers	$> 1.8 \times 10^{24}$	$< 0.2 - 1.1$	[63]
^{136}Xe	Liquid Xe scintillator	$> 1.2 \times 10^{24}$	$< 1.1 - 2.9$	[21]
^{150}Nd	Foils and tracking	$> 3.6 \times 10^{21}$		[64]

Table 1.4: List of the best limits for the half-time of $\beta\beta0\nu$ decay reached in different isotopes, with the technique used, the equivalent effective neutrino mass and the reference. The table has been extracted from [51].

emitted electrons can be described by

$$\begin{aligned} \frac{d^2\Gamma_{0\nu}}{dT_1 d\cos\theta} &= |M_{GT}|^2 \; N_{0\nu}\left[A_{0\nu}(0) + B_{0\nu}(0)\cos\theta\right] \\ \begin{pmatrix} A_{0\nu}(0) \\ B_{0\nu}(0) \end{pmatrix} &= (T_1+1)^{2\gamma_1}(T_2+1)^{2\gamma_1} d_{00} \begin{pmatrix} A_0 \\ B_0 \end{pmatrix} . \end{aligned} \tag{1.18}$$

As described in [65], coefficients A_0 and B_0 can be expressed in terms of products of the NMEs and the phase-space integrals coming from the effective neutrino mass and from the effective right-handed current parameters. In addition, equation 1.18 can be written in a similar way as the two-neutrinos case if all parameters are included in two constants a_0 and b_0. In that case, it reduces to

$$\begin{aligned} \frac{d^3\Gamma}{dT_1\; dT_2\; d\cos\theta} = A \;\; & (m_e + T_1)^2 \;\; (m_e + T_2)^2 \;\; h_{2\nu}(T_1, T_2) \;\; d_0(T_1) \;\; d_0(T_2) \\ & \left[(1+a_0) - (1+b_0) \; \frac{\sqrt{T_1 \; T_2 \; (T_1{+}2 \; m_e) \; (T_2{+}2 \; m_e)}}{(T_1{+}m_e) \; (T_2{+}m_e)} \cos(\theta)\right] . \end{aligned} \tag{1.19}$$

Under the purely phenomenological condition that only one of the mechanisms (the helicity flip or the right-handed currents) contributes, we find that a_0 and b_0 are 1. In [65] distributions with other possible parameters values can be found.

Another form of neutrinoless decay consists in the emission of a Majoron

$$(A, Z) \rightarrow (A, Z+2) + 2\; e^- + \chi \tag{1.20}$$

This mode will reveal the existence of the Majoron (χ), the Goldstone boson emerging from the spontaneous symmetry breaking of B-L and with far-reaching implications in Astrophysics and Cosmology. Although it is an interesting process, it will not be further discussed.

1.3.2 The Nuclear Matrix Elements

If $0\nu\beta\beta$ decay is observed, the Majorana nature of neutrinos will be confirmed. However, the knowledge of the Nuclear Matrix Elements (NME) with little uncertainties is necesary to determine the effective neutrino mass. The calculation of the NME has been described in many

references like [9, 66]. In this section, we introduce the formalism and describe the most common methods used. The calculation starts with the expression

$$M^{0\nu} = -\left(\frac{g_V}{g_A}\right)^2 \; M_F^{0\nu} + M_{GT}^{0\nu} - M_T^{0\nu} \; , \tag{1.21}$$

where $M_K^{0\nu}$ (K = F, GT, T) are the corresponding Fermi (F), Gamow-Teller (GT) and Tensorial (T) contributions and g_A and g_V are respectively the axial-vector and vector relative weak coupling constants. The three terms can be calculated by

$$M_K = \left\langle 0_i^+ | \sum_{n,m} \tau_n^- \; \tau_m^- \; H_K(r) \; \Omega_K | 0_f^+ \right\rangle \; . \tag{1.22}$$

In this formula, τ_m^- are transitions operators in the momentum space, Ω_K is the operator of each contribution and $H_K(r)$ is the neutrino potential. These neutrino potentials have the following form

$$H_K(r) = \frac{2}{\pi} \frac{R}{g_A^2(0)} \int_0^\infty f_K(qr) \frac{h_K(q)}{\left(q + E_a^m - \frac{1}{2}\left(E_i - E_f\right)\right)} \; q \; dq \; , \tag{1.23}$$

where $f_K(qr)$ are the spherical Bessel functions, $h_K(q)$ are related to the weak Hamiltonian of the $\beta\beta0\nu$ decay and E_m are the energies of the virtual intermediate states.

The calculation of the neutrino potentials has changed along time. In the past, the nucleide chart was divided into regions according to different types of nuclei, i.e., whether the nucleus was spherical, deformed or exhibits a more complex behaviour. Each region was then treated by a different model. Now with the huge increase in computing resources these models have been deserted and new approaches have been adopted. The most popular ones are the Nuclear Shell Model (NSM) and the Quasiparticle Random Phase Approximation (QRPA).

The Nuclear Shell Model (NSM)

The first attempts to calculate NMEs were made using this model. However, as most emitters were heavy nuclei, it was necessary to use a truncation of the model space to cope with the calculation. The first efforts were restricted to ^{48}Ca, ^{76}Ge, ^{82}Se and ^{136}Xe.

In the last years, new progresses have extended the number of nuclei studied to almost all double beta emitters and truncations have been eliminated [67, 66]. This method has the following characteristics:

1. The intermediate states of the equation 1.23 are replaced by an average value $\langle E_a^m \rangle$. This approximation (called BCS) has an error below the 10 % and is justificed by the large momentum of the virtual neutrino in comparison with the energy of the intermediate states.

2. The interaction is treated with monopole corrected G-matrices.

3. The valence space has a limited number of orbits, but all the possible ways of distributing the valence particles among the valence orbits are taken into account.

4. The pairing correlation is treated exactly in the valence space. Proton and neutron numbers are exactly conserved and all possible correlations (proton-proton, neutron-neutron, and proton-neutron) are included.

5. The multipole correlations and deformations are described properly in the laboratory frame. The angular momentum conservation is preserved.

In general, the kinematic factor $G_{0\nu}$ depends on the value of g_A. Therefore the NMEs obtained with different g_A cannot be directly compared. If we redefine the NME as

$$M^{,0\nu} = \left(\frac{g_A}{1.25}\right)^2 M^{0\nu}, \tag{1.24}$$

the values of NMEs are directly comparable, no matter which was the value of g_A employed in their calculation, since they share a common $G_{0\nu}$, that of $g_A = 1.25$. In table 1.5, the most recent NME values calculated by the standard approach (first column) and including the SRCs (Short Range Corrections, later described) are shown.

	No SRC	Jastrow	UCOM
^{48}Ca	0.92	0.85	0.61
^{76}Ge	2.96	2.81	2.30
^{82}Se	2.79	2.64	2.18
^{124}Sn	2.77	2.62	2.10
^{128}Te	3.05	2.88	2.34
^{130}Te	2.81	2.65	2.12
^{136}Xe	2.32	2.19	1.76

Table 1.5: The NME calculated by different approaches of the Shell Model: without and with Short-Range-Correlations (via a Jastrow function or a Unitary Correlation Operator Method (UCOM)). Values have been extracted from [66].

The Quasiparticle Random Phase Approximation (QRPA)

The QRPA method is simple from a computing point of view and was first applied to compute the $2\nu\beta\beta$ matrix elements by the Caltech ground. Values in agreement with experimental results were obtained for various $\beta\beta$ measured decays, when the value of the parameter g_{pp}, which describes the particle-particle interaction, was the one fitting the β^+ decay on nuclei with magic number of neutrinos.

This method has the following characteristics:

1. It calculates the matrix elements connecting the initial and final 0^+ states with the intermediate 1^+ states, where the initial and final states are based on BCS states. These states are an approximation of the quantum mechanical state of the nuclear system.

2. The interaction is treated with realistic or schematic interactions tuned with the g_{ph} and g_{pp} strengths.

3. The valence space has a larger number of orbits, but only 1p-1h and 2p-2h excitations from the normal filling are considered.

4. Only proton-proton and neutron-neutron pairing are considered and are treated in the BCS approximation. Proton and neutron numbers are not exactly conserved.

5. The multipole correlations and deformations are treated at the Random Phase Approximation (RPA) level, which does not incorporate permanent deformations.

In table 1.6, the most recent QRPA values calculated by the standard approach (first column) and including the SRC corrections (other columns) are shown.

	CCM SRC	Jastrow	UCOM
^{76}Ge	$4.07 - 4.64$	$3.33 - 4.68$	$3.92 - 5.73$
^{82}Se	$3.53 - 5.92$	$2.82 - 4.17$	$3.35 - 5.09$
^{96}Zr	$1.43 - 2.12$	$1.01 - 1.34$	$1.31 - 1.79$
^{100}Mo	$2.91 - 5.56$	$2.22 - 3.53$	$2.77 - 4.58$
^{116}Cd	$2.30 - 4.14$	$1.83 - 2.93$	$2.18 - 3.54$
^{128}Te	$3.21 - 5.65$	$2.46 - 3.77$	$3.06 - 4.76$
^{130}Te	$2.92 - 5.04$	$2.27 - 3.38$	$2.84 - 4.26$
^{136}Xe	$1.57 - 3.24$	$1.17 - 2.22$	$1.49 - 2.76$

Table 1.6: The NME calculated by different approaches of the QRPA Model: without and with Short-Range-Correlations (via a Jastrow function or a Unitary Correlation Operator Method (UCOM)). Values have been extracted from [9, 68].

The situation today

In the last years, the results of both methods have started to converge due to the elimination of approximations and the introduction of new corrections. One of them is the problem of the Short-Range-Correlations (SRC) in the valence space, which have recently inspired new studies [9, 10, 68]. SRC has been treated in a conventional way via a Jastrow-type correlation function or with a unitary correlation operator method (UCOM). In the NSM model, these methods have respectively reduced the NME values by a 5 % and 20-30 %.

Apart from that, new experimental information has appeared for the neutron [69] and proton [70] occupancies of nuclei involved in the A = 76 transition. The occupancies generated by the NSM show a reasonable agreement with this data. However, the original QRPA occupations, notably for neutrons, deviate significantly from experimental data, leaving too empty the $g_{9/2}$ orbit. A modification of the Wood-Saxon single particle energies has been performed to solve this problem and reproduce experimental data [9, 71].

This correction in the interactions has brought new values for the NMEs, reducing the gap between the NSM and the QRPA results in almost a 50 %. Nevertheless, there are still big differences. The NME values fo the NSM are systematically smaller (up to a factor 2 for lighter nuclei like ^{76}Ge) than the corresponding QRPA ones, as respectively shown for the Jastrow and UCOM treatments in figures 1.3 and 1.4. There is now an active discussion in literature on what could be the reason of such a discrepancy: a too small single-particle model space of the NSM or a neglect of complex nuclear configurations witin the QRPA.

As a comparison of the actual situation, the lower and upper values of the NMEs for each model and isotope are shown in table 1.7, whenever there are results for both models In these cases, the range of possible nuclear figure-of-merits F_N has been calculated using the phase space factors of table 1.3.

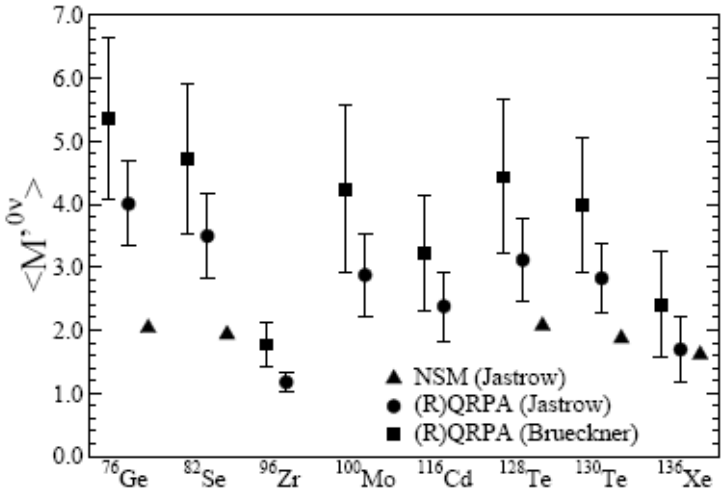

Figure 1.3: The NMEs calculated by the CCM and Miller-Spencer Jastrow treatments of the SRC. For comparison, the results of the NSM using the same treatment are also shown. The plot has been extracted from [9].

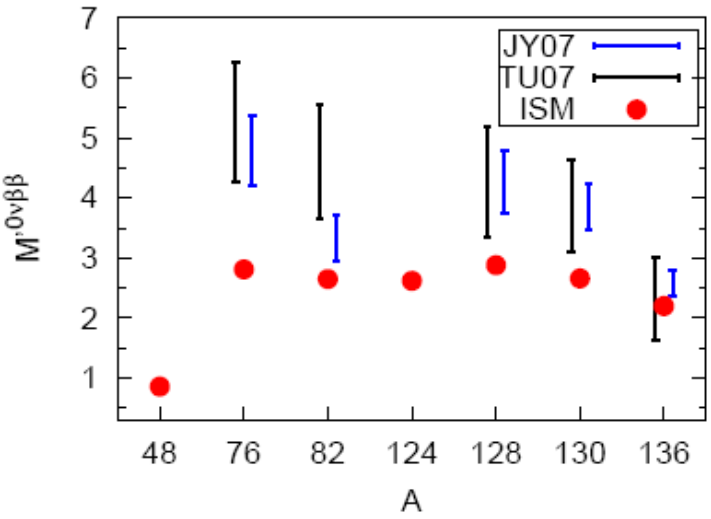

Figure 1.4: The NMEs calculated by the NSM and the QRPA using the SRC with the UCOM approach [10].

	NSM		QRPA	
Isotope	$M^{0\nu}$	$F_N(\mathrm{yr}^{-1})$	$M^{0\nu}$	$F_N(\mathrm{yr}^{-1})$
^{76}Ge	$2.30 - 2.96$	$(4.19 - 6.94) \times 10^{-14}$	$3.33 - 5.73$	$(0.88 - 2.60) \times 10^{-13}$
^{82}Se	$2.18 - 2.79$	$(1.67 - 2.74) \times 10^{-13}$	$2.82 - 5.92$	$(0.34 - 1.23) \times 10^{-12}$
^{128}Te	$2.34 - 3.05$	$(1.21 - 2.06) \times 10^{-14}$	$2.46 - 5.65$	$(1.34 - 7.05) \times 10^{-13}$
^{130}Te	$2.12 - 2.81$	$(2.49 - 4.37) \times 10^{-13}$	$2.27 - 5.04$	$(0.29 - 1.41) \times 10^{-12}$
^{136}Xe	$1.76 - 2.32$	$(1.83 - 3.18) \times 10^{-13}$	$1.17 - 3.24$	$(0.81 - 6.20) \times 10^{-13}$

Table 1.7: Lower and upper values of the NMEs and the nuclear figure-of-merit F_N for different isotopes and for the NSM and QRPA, whenever there are results for both models.

Chapter 2

Past and future of Double Beta Decay experiments

In double beta decay experiments, three general aproaches have been followed: geochemical, radiochemical and direct counting measurements. The first one consists in the observation of the isotopic anomalies in the noble gases daughter of the $\beta\beta$ decaying nucleus over geological time scales. Some examples are ^{82}Se, ^{96}Zr and ^{128}Te. The second approach is based on the fact that daughter nuclei are themselves radioactive and therefore, they can be extracted and counted. If the daughter has a half-life smaller than 10^9 years and has no other long-lived parent, its presence can be only due to a double beta decay. An example is $^{238}U \rightarrow^{239} Pu$ (88 yr, α decay).

Recent activity refers to direct counting experiments, which measure the energy spectrum of the emitted electrons. Some of them also track the electrons, measuring the energy, angular distribution and topology of the events. All of them can be classified in three types according to their approach to the experimental problem:

1. Calorimeters where the detector is also the $\beta\beta$ source.

2. Tracking detectors differenciated from the source.

3. Tracking calorimeters, where the tracking volume is also the $\beta\beta$ source, as a TPC detector.

Calorimeters have a good energy resolution and almost 100% efficiency (like Ge detectors and bolometers). However, they have a limited tracking capability and, in consequence, a limitation on the identification of backgrounds on an event-by-event analysis. They compensate this fact by the little leakage of ordinary double beta decay into the neutrinoless region, which means no intrinsic sensitivity limitation. In contrast, tracking detectors are able to discriminate background from signal events. However, their efficiency is little and the energy resolution is modest, which makes their background be ultimately limited by $\beta\beta2\nu$ events. Another possible classification is based on the type of the detector like semiconductors, scintillators, cryogencis or TPCs.

In the first two sections, the desiderable features of a double beta experiment are qualitative and quantitative discussed. This discussion is followed by an overview of the most important past and future direct counting experiments. Finally, we motivate the NEXT project, which uses the results of this thesis, and we make a preliminary study of its sensitivity, which will be further developped in chapter 9.

2.1 Design criteria for a double beta decay experiment

Before the design and construction of a double beta decay experiment, several parameters must be evaluated to assess its viability. These criteria have been discussed most recently in [25, 72, 73]. As the ultimate goal of any experiment is the detection of the neutrinoless decay mode, some of these parameters are focused on an energy windows around the $Q_{\beta\beta}$.

From this point of view, these criteria are succesively discussed in a qualitative way. In the next section, the quantitative influence of these parameters in the sensitivity of an experiment is rigorously defined.

The type of isotope

The isotope source is the first important issue as it defines the available energy $Q_{\beta\beta}$ in the decay. A high $Q_{\beta\beta}$ makes more probable the observation of the $\beta\beta0\nu$ as the rate of this process is proportional to $Q^5_{\beta\beta}$. Apart from that, it places the energy region of interest over many potential backgrounds, as it is later explained. As a comparison, values for $Q_{\beta\beta}$ for isotopes with $Q_{\beta\beta}$ greater than 2 MeV are shown in table 1.2.

The type of isotope also determines its natural abundance. In most of the cases, an enrichment of the material is necessary, which can be very complicated depending on the isotope. In some cases, it is unnecessary because the natural abundance is high. For instance, the abundance of the ^{130}Te is 30 %.

Finally, the nuclear theory is better understood in some isotopes than others. In those cases, the interpretation of results in terms of the effective neutrino mass seems easier. As a comparison, the ranges of the nuclear figure of merit according to the NSM and the QRPA models for different isotopes are respectively shown in tables 1.5 and 1.6.

The detector mass

The mass of the isotope determines the range of neutrino effective masses to which an experiment is sensible. Past experiments contained between 5 and 10 kg. of mass and ran for several years. The most sensitive limits are those fixed by the Heidelberg-Moscow, IGEX and CUORICINO experiments, with half-lives between 10^{24} and 10^{25} yr. As the values of F_N are typically between 10^{-14} and 10^{-13} yr^{-1}, these experiments were sensible to masses around 1 eV.

In order to cover the degenerate mass region ($\langle m_\nu \rangle \approx 0.1$ eV), an experiment must be able to observe a half-life of 10^{26}-10^{27} yr. These values are expected to be reached with detection masses around 100 kg. Apart from that, the detector should be easily scalable to reach the inverted-hierarchy scale region, which is expected to be reached for masses around 1 tonne.

The efficiency

The efficiency is the ratio between the number of events which are fully contained in the detector and have not been rejected by a selection criterium; and the total number emitted by the isotope. Experiments where the source and the detector are the same have in general a higher efficiency. The greatest values are reached for germanium detectors and bolometers (higher than 90 %). TPCs have a slightly lower efficiency (around 70 %, depending on the geometry) and tracking detectors much less (about 10 %).

The energy resolution

The energy resolution is the variation in the determination of the energy. This value depends on the detector and the range of energy. Normally the detectors of germanium have the best resolution due to the low energy necessary to generate a pair electron-hole in this material. Values down to 4 keV (FWHM) have been reached. This value is around 8 keV for bolometers of TeO_2, used in the double beta experiments of ^{130}Te. The worse energy resolutions are obtained for TPCs and scintillators.

A good energy resolution increases the signal-to-noise ratio, reducing the background in the region of interest. It also prevents the tail of the $2\nu\beta\beta$ decay spectrum from becoming a background itself. As pointed out in [8], the fraction F of two-neutrino events that are contained in a ΔE energy window centered in $Q_{\beta\beta}$ can be expressed as

$$F \approx \frac{C_\delta \; Q_{\beta\beta} \; \delta^6}{m_e} \tag{2.1}$$

where $\delta = \frac{\Delta E}{Q_{\beta\beta}}$ is the FWHM energy resolution, m_e is the electron mass and C_δ is a coefficient which depends on the energy resolution. It is 5 at 10 %, 7 at 5 % and 8.5 at 1 %. The background level of the two-neutrino mode (B) in the neutrinoless mode (S) can be calculated by

$$\frac{S}{B} \approx \frac{m_e}{C_\delta \; Q_{\beta\beta} \; \delta^6} \; \frac{T^{2\nu}_{1/2}}{T^{0\nu}_{1/2}} \tag{2.2}$$

From this equation, we deduce that the contribution of the $\beta\beta2\nu$ signal to the neutrinoless mode is low if the rate of the two-neutrino mode is low or the energy resolution is good enough.

The background level

The background consists in those events which cannot be initially distinguished from $\beta\beta0\nu$. These events can fake the expected signal if their rate is similar or greater than the signal. The components of background are several but only those that deposit energy in the region of interest (RoI) of the specific isotope considered. The selection of this region is determinated by the expected signal and the energy resolution. Detectors with good energy resolution will have a narrower RoIs but it is better to consider a wider range for including all possible background sources.

As a first approach, the main components of background can be classified as:

- **Cosmic radiation**: It is composed of protons which enter in the Earth's atmosphere and produce the so-called secondary cosmic radiation, formed by muons, neutrons, photons, electrons and positrons. At the surface, it is a very important contribution to the background and they can also produce radioactive isotopes by cosmogenesis in materials near the detector or in the detector itself. Apart from that, the interaction of muons with materials near the detector can produce neutrons.

- **Natural radiation**: It is composed of the radioactive chains of ^{232}Th, ^{235}U and ^{238}U and some contaminations like ^{40}K, ^{60}Co or ^{137}Cs. They exist in all materials but with different activities. Radon, present in air, is also very important and can reach a big concentration in places with a bad ventilation.

  From the possible particles, alphas and electrons contribute to the background only if they originate very close to the detector. From gamma emissions, as the $Q_{\beta\beta}$ values are greater

than 2 MeV, the most important emission is the 2614.5 keV line of ^{208}Tl, from the ^{232}Th chain. Other gammas that have to be considered are those from ^{60}Co and ^{214}Bi.

Almost all particles generated by cosmic radiation can be eliminated if the experiment is installed in a laboratory at significant depth. Only muons remain but with a clear reduction [74]. In a recent work [75], the background level produced by muons in a Germanium detector at the Gran Sasso underground laboratory has been estimated. It has been concluded that a value as low as 10^{-4} counts keV^{-1} kg^{-1} yr^{-1} can be achieved with a dedicated and efficient muon veto.

The techniques applied for reducing the natural radiation are diverse. The most common is the use of a shielding with materials capable to stop the incident radiation. This capacity depends on the type and energy of the incident particle and the atomic number of the material. The shielding of an experiment is normally composed of several layers so that each material stops a specific component. The most common materials are copper, cadmium, lead and polyethylene.

It also exists the so-called active shielding, which implies the use of background detectors. The muons veto is a common example. It consists of scintillator plastics placed all around a detector. If a muon crosses one of these plastics, a signal is generated in this background detector. Therefore, the possible event generated by the muon in the detector is rejected due to the temporal coincidence of both signals.

The selection of materials is one of the most important ways for reducing background. Over the years, progress has been made identifying the level of contamination in materials that compose detectors and their shieldings. The high contaminated ones have been replaced by cleaner ones and purification techniques have been developped, too. As a result, detectors are now fabricated from very pure components, some of them with activites as low as 1 μBq/kg.

Finally, there are other techniques which are based on the event topology or the timing information of the signal. In this work, three discrimination criteria have been developped to reject background based on the first aspect. More details are given in chapter 8.

2.2 The sensitivity of an experiment

In order to evaluate the sensitivity of a double beta experiment (for both $\beta\beta2\nu$ and $\beta\beta0\nu$ signals), the half-time of the process is used as figure of merit, defined by

$$T_{1/2} = \frac{\ln 2 \; N}{A} \tag{2.3}$$

where A is the activity of the signal and N is the number of nuclei. This last value can be calculated by

$$N = A_0 \; a \; \frac{10^3 \; M}{W} \tag{2.4}$$

In this expression, A_0 is the Avogadro number, M is the detector mass in kg, a is the abundance of the isotope and W is the atomic weight. The activity is instead expressed as

$$A = \frac{s}{\epsilon \; t} \tag{2.5}$$

where s is the measured signal in a time t supposing an efficiency of ϵ for the detector. In the absence of a positive signal, an upper limit to the signal can be given depending on the

statistical fluctuation of the background b (expressed in counts keV^{-1} kg^{-1} yr^{-1}) and the level of confidence (CL). With a CL of n_σ σ, it is described by

$$s < n_\sigma \sqrt{b\ \Delta E\ M\ t} \tag{2.6}$$

where ΔE is the energy resolution of the detector in keV. Grouping all the last equations, a lower limit is fixed in the half-time, expressed as

$$T_{1/2} > \frac{10^3\ \ln 2\ A_0\ a\ \epsilon}{n_\sigma\ W} \sqrt{\frac{m\ t}{b\ \Delta E}} \tag{2.7}$$

For comparing different experiments, the value of n_σ is normally fixed and the former lower limit corresponding to the neutrinoless mode is used as a figure of merit, normally noted as F_D [76]. In our case, we will use $n_\sigma = 2$, which corresponds to a CL of 90 %. We can check in this equation all the features described for an ideal $\beta\beta$ decay experiment: a fantastic energy resolution, a very low level of background, a big amount of source, a high isotopic abundance and a high detector efficiency. A similar figure of merit has been defined in [25].

2.3 A summary of past experiments

The purpose of this section is not to make an exhaustive review of all double beta decay experiments, like in [23, 24, 25], but to describe the most representative ones. The most relevant experiments have been those using germanium detectors, like IGEX and HM, because they have fixed the best limits to the neutrino mass. Another experiment, CUORICINO, has presented similar results using bolometers. Finally, two tracking detectors are described: NEMO, which has studied several isotopes, and the Gothard Xenon TPC, which is the first use of a TPC in this field.

2.3.1 IGEX

The experiment IGEX (International Germanium EXperiment) [77] had the aim to detect the neutrinoless mode of ^{76}Ge with three cristals of about 2 kg of high purity germanium and enriched to 86 %. They were mounted in the Canfranc Underground Laboratory, as shown in figure 2.1. The detector had a high efficiency (more than 90 %), an excellent energy resolution (4 keV at $Q_{\beta\beta}$) and a background level of ≈ 0.1 counts keV^{-1} kg^{-1} yr^{-1} in the region of interest.

From the analysis of 116.75 yr mol of data and applying pulse discrimination techniques, 60 % of the background was rejected [78] and no positive signal was observed. With a 90 % of confidence, a limit at the half-life of $0\nu\beta\beta$ was fixed: $T^{0\nu}_{1/2} \geq 1.57 \times 10^{25}$ yr; and an upper bound to the neutrino mass was given: $\langle m_\nu \rangle \leq 0.33 - 1.35$ eV [12]. The authors also concluded that the main count rate in the $\beta\beta0\nu$ window was generated by radon but even if it were reduced, Germanium activation isotopes would be the limiting background source.

2.3.2 Heidelberg-Moscow

Based on the same type of detectors as the IGEX collaboration, the Heidelberg-Moscow experiment (HM) [79] operated in the Underground Laboratory of Gran Sasso five detectors, enriched 86 % and with a total mass of 10.96 kg. This collaboration presented a first result based on 47.7 kg yr for the two-neutrinos mode and 35.5 kg yr for the neutrinoless one, where no positive signal was observed. It established the bounds of $T_{1/2} \geq 1.55 \times 10^{25}$ yr and $\langle m_\nu \rangle \leq 0.35$ eV [49].

Figure 2.1: A detail of the IGEX shielding in preparation. There are two detectors of 0.7 kg each and one of 2 kg inside the Marinellis lead.

Apart from these results, the collaboration identified the contaminations that contributed to the background by their associated peaks within the spectrum. With these identification, the response of the detectors was simulated with a Monte Carlo code and the fit with data provided an indication of the location of the activity. The conclusion was that the copper parts of the cryostat were the main source of background events.

Despite strong discrepancies inside the collaboration, a part of it announced the observation of the neutrinoless double beta decay with a half-life of 1.2×10^{25} yr, $\langle m_\nu \rangle = 0.24$-$0.58$ eV and a confidence level of 4.2 σ. These results were strongly discussed by the scientific community due to the faint signal and the existence of unidentified peaks in the surroundings of the suppossed signal. The reader is referred to some general reviews on this claim [24, 25], its presentation and reanalysis [11, 80, 81, 82, 83] and the main critisism arised [84, 85, 86].

2.3.3 CUORICINO

The CUORICINO experiment [88] looks for the $\beta\beta0\nu$ of ^{130}Te. It has a total mass of 40.7 kg and has been taking data since 2003 at the Underground Laboratory of Grand Sasso. It can be considered the evolution of a previous experiment called MIBETA (MIlano doble BETA) [87], which used a mass of 6.8 kg. The most recent published results give a limit for the half-life of ^{130}Te of 3.0×10^{24} yr.

The setup is an array of 62 crystals of TeO_2, which corresponds to a mass of ^{130}Te of $\approx$ 11 kg. The crystals are arranged in a tower made by 13 planes, shown in figure 2.2 (left), 11 of them are filled with 4 cubes of 5 cm side while the other two are filled with 9 cubes of $3 \times 3 \times 6$ cm^3. Four of these last crystals are enriched, two of which in ^{128}Te, 82.3 % isotopic abundance, and the other two in ^{130}Te, isotopic abundance of 75 %.

The crystals are operated at a temperature of 10 mK, where they have tiny specific heats. When an event leaves energy in the crystal, the temperature rises and this increase is measured by a sensitive thermistor, which produces an electric signal proportional to the energy deposited. These bolometers have a very good efficiency (up to 85 %) and energy resolution (FWHM = 8 keV at $Q_{\beta\beta}$). Their main drawback is their cryogenic nature, which difficults the operation during long time periods.

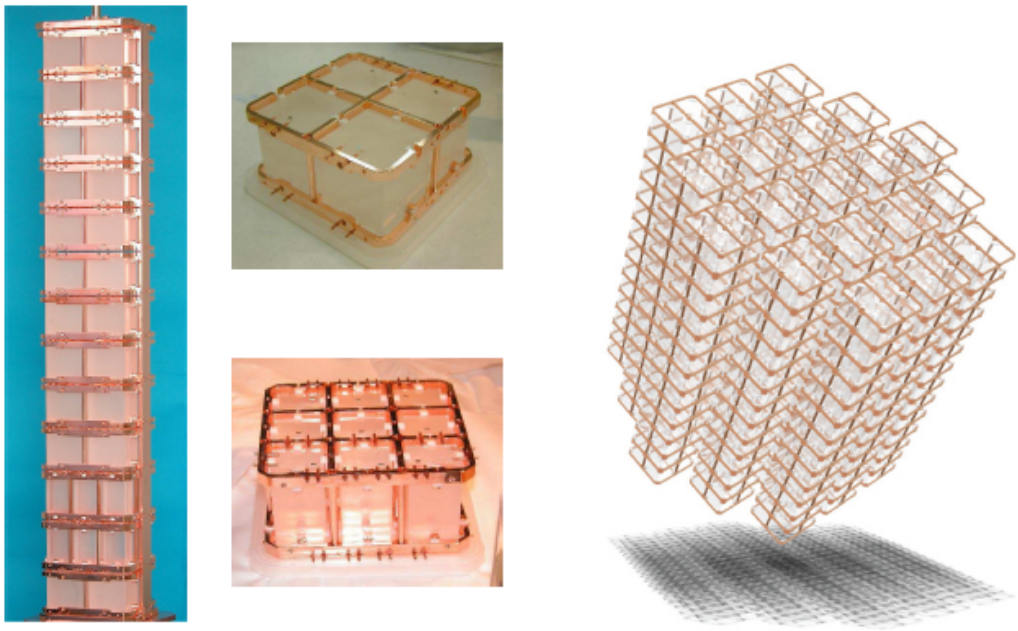

Figure 2.2: Left: Photographs of the CUORICINO setup. The two small photographs are respectively the planes of four 5 cm cubes and the $3 \times 3 \times 6$ cm^3 bolometers. The main one is the tower with the 13 planes. Right: An artistic view of the future CUORE experiment. Both figures have been extracted from [73].

2.3.4 NEMO3

The NEMO3 experiment (Neutrino Ettore Majorana Observatory) [89] is a double beta experiment looking for signals of different isotopes and is operational since 2003 in the Undergound Laboratory of Modane. As shown in figure 2.3 (right), it consists of a cylindrical electron tracking detector filled with helium gas. The volume is divided in 20 segments of thin source planes, with a total area of 20 m^2. In the actual configuration, there is a total mass of 10 kg, distributed in 7 kg of ^{100}Mo, 1 kg of ^{82}Se and low quantities of ^{150}Nd, ^{130}Te, ^{116}Cd, ^{96}Zr and ^{48}Ca.

The electron tracking is a three-dimensional readout wire drift chamber, with 6180 cells operating in the Geiger mode. In the center of the setup, there is a magnetic solenoide that creates a vertical induction field of about 25 G. The tracking in the magnetic field allows the differentiation between electron and positron tracks. The volume is surrounded by 1940 plastic scintillator-block calorimeters that measure the electron energies and the time of flight.

Its main advantage is its capacity to reconstruct the emission track. However, it has a very low efficiency (less than 10 %) and a bad energy resolution (FWHM = 240 keV at 3 MeV). Nevertheless, it has measured $\beta\beta2\nu$ spectra for many isotopes with a quantity of data never seen [91]. It has fixed bounds on $\beta\beta0\nu$ of 5.8×10^{23} yr for ^{100}Mo and 2.1×10^{23} yr for ^{85}Se [92].

2.3.5 Gothard Xenon TPC

The Gothard Xenon experiment [13] used a 5-atm gas TPC with 3.3 kg of xenon enriched a 62.5 % in ^{136}Xe. The tracking feature of the detector permitted the identification of the two-electron tracks indicative of $\beta\beta$ decay. Even if the energy resolution at $Q_{\beta\beta}$ was not very competitive (164 keV, 6.6 % FWHM), the discrimination techniques applied reduced the level of background to 0.01 counts keV^{-1} kg^{-1} yr^{-1} [93], one order of magnitude lower than the IGEX experiment.

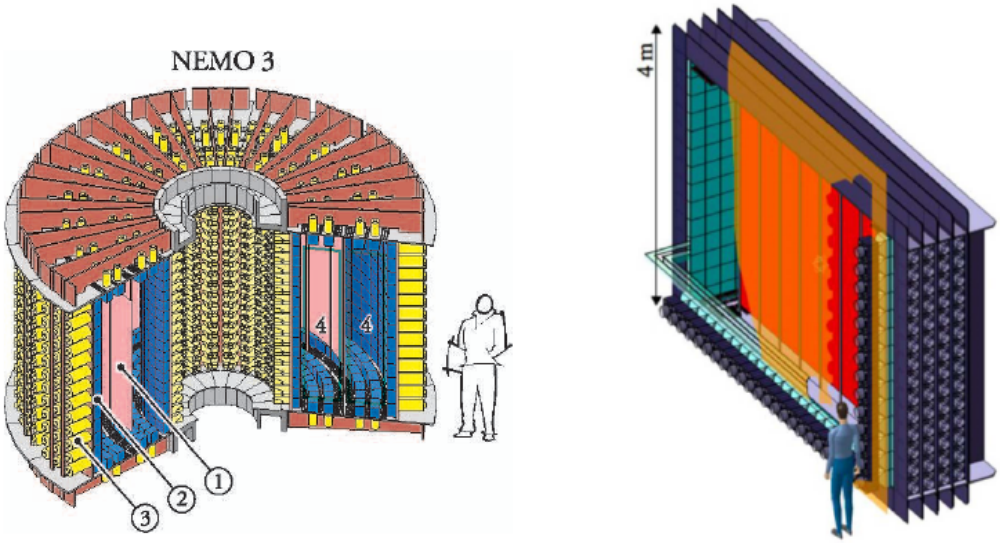

Figure 2.3: Left: A schematic view of NEMO3 without the shielding [90]. The different parts of the detector are the source foil (1), the plastic scintillators (2), the photomultipliers (3) and the tracking volume (4). Right: A schema of a SuperNEMO module where the isotope layers can be seen [73].

The dominant background for the neutrinoless mode was concluded to be generated by the Compton-scattered electrons from gamma activities. These electrons were some times misidentified as two-electron events. For this experiment, cosmogenic activities were not a serious issue because there are no long lived xenon isotopes and gaseous xenon was continuously purified.

The limits established in the half-lives of both modes by this experiment were $T^{0\nu}_{1/2} > 4.4 \times 10^{23}$ yr (90 % CL) and $T^{2\nu}_{1/2} > 3.6 \times 10^{20}$ yr (90 % CL), which took into account 12843 hours of data-taking [13].

More strict limits were fixed by the experiment DAMA-Xe in [21], with a mass of xenon of 6.5 kg, 8824 of data-taking and a similar enrichment in ^{136}Xe. The setup consisted in a copper vessel containing 2 liters of liquid xenon (6.5 kg). The scintillation light was collected by three PMTs working in coincidicence. The energy resolution was quite worse that the Gothard experiment, approximately 20 % FWHM for the 2614.5 keV-γ peak of ^{208}Tl was .

2.4 A view of the new generation of experiments

As in the previous section, a small number of experiments are described. They include the future germanium experiments (GERDA and MAJORANA), the evolutions of CUORICINO and NEMO3 (respectively named CUORE and SuperNEMO) and the xenon calorimeter EXO. We note that future experiments have in general three main goals, according to the right plot of figure 1.1:

- For mass values of 200 meV or less, the claim described in section 2.3.2 will be confirmed or totally discarded.
- If the upper limit of the range is 50 meV or less, the quasi-degenerate mass hierarchies will be confirmed or totally discarded.

- For mass values of 20 meV or less, the inverted mass hierarchies will be confirmed or totally discarded.

2.4.1 MAJORANA

The idea of the MAJORANA collaboration is to build eight modules with 57 1.1-kg segmented Ge detectors each, for a total of 500 kg of Ge enriched to 86 % in ^{76}Ge. The detectors will be arranged in an hexagonal configuration of 19 towers, each three detectors high, inside a copper cryostat. A sketch of a future MAJORANA module is shown in figure 2.4 (left). These cryostats will be electroformed as in the case of the IGEX detectors, trying to reduce the internal contamination due to cosmogenic activation.

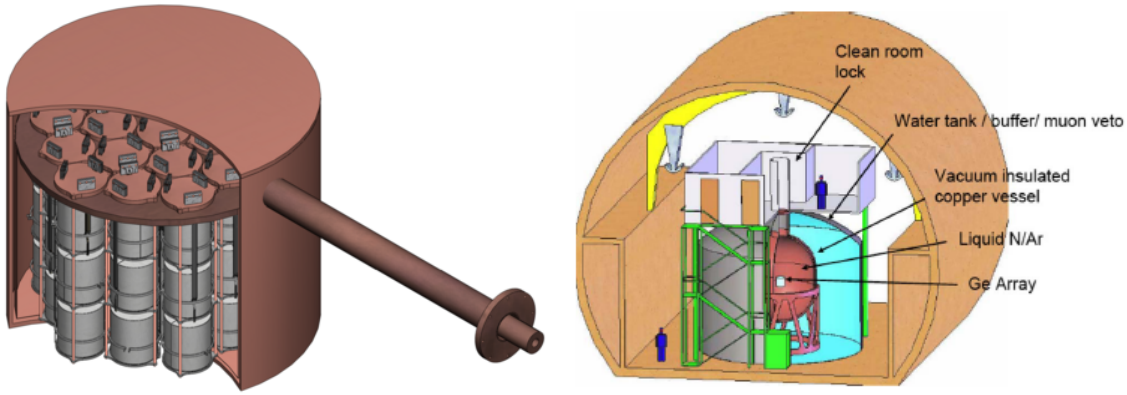

Figure 2.4: Left: A sketch of a MAJORANA module containing 19 strings of Ge detectors. Right: An artist's conception of the GERDA experiment. Figures have been extracted from [73].

There is an intense R&D project underway to reach a radiopurity for copper of around 0.1 μBq/kg for ^{214}Bi and ^{232}Th. Apart from that, the experiment will use discrimination techniques based on pulse analysis and crystals will be segmented. The main objective is to reduce the level of background two orders of magnitude in comparison with IGEX and HM and to be sensitive to neutrino masses down to 20 meV. More details are given in [94, 95].

2.4.2 GERDA

GERDA (GERmanium Detector Array) [96, 97] is a planned array of Ge detectors fabricated from germanium enriched a 86 % in ^{76}Ge, cooled and shielded by direct immersion in liquid argon or nitrogen. In this way, the presence of any material near the detectors is reduced and, in some sense, the conclusions of the HM collaboration are followed.

The project is divided in three phases. In the first one, data taking with crystals already used in IGEX and HM collaboration will be made, with a total mass of 18 kg. In a second phase, the mass will be increased up to 40 kg, using segmented crystals. The final goal of the experiment is to reach a mass of 1 tonne, which will explore neutrino masses lower than 20 meV.

The goal of GERDA is to reduce the background in the first phases to levels between 0.01 and 0.001 counts keV^{-1} kg^{-1} yr^{-1} with the use of ultraclean materials, pulse-shape analysis, segmentation and the shielding in liquid argon. An artistical view of the experiment is shown in figure 2.4 (right). The facility is presently under construction in the Underground Laboratory of Grand Sasso.

2.4.3 CUORE

The CUORE detector is the evolution of the CUORICINO experiment and has been approved and funded by the Instituto Nazionale de Fisica Nuclear in Italy. It will be an array of 19 towers, similar to the CUORICINO except that all crystals will be $5 \times 5 \times 5$ cm^3. It will have 988 bolometers with a mass 760 g each. This makes a total mass of 750 kg of TeO_2, i.e., 200 kg of ^{130}Te. An artistic view of the experiment is shown in figure 2.2 (right).

In the future design, efforts are focused on the crystal polish, as it will reduce the surface background, and the structure where they will be contained, minimizing the mass and the radiopurity of materials. Apart from that, it will be a challenge the operation of all crystals at the same temperature of operation (10 mK). It is expected to be sensitive to effective neutrino masses near 50 meV [98].

2.4.4 SuperNEMO

It can be considered as an extension of the actual NEMO3, as it will be based on the same technology but with a total mass of 100 kg [92]. It will be composed of 20 modules, like the one shown in figure 2.3 (right). Each module will have 12 m^2 of tracking volume with 3000 channels of readout and 1000 photomultiplier tubes and a plate with 5 kg. of enriched isotope. Two possible isotopes are considered now: ^{82}Se and ^{150}Nd.

Some features of the new experiment are expected to be a significant breakthrough like the energy resolution (passing from 240 keV to 120 keV at 3 MeV) or the efficiency (rising it to 30 %). Apart from that, a complete R&D programme called BiPo is being carried out to measure possible materials of the modules and the future foils with a sensitivity of ^{208}Tl < 2 μBq/kg and ^{214}Bi < 10 μBq/kg. These improvements will make the detector sensitive to neutrino masses near 50 meV.

2.4.5 EXO

EXO (Enriched Xenon Observatory) [22] is a proposed large next generation experiment that will search the $\beta\beta0\nu$ of ^{136}Xe. The goal is to use between one and ten tonnes of xenon enriched to 80 % in ^{136}Xe. One of its key futures will be the identification of the daughter ^{136}Ba ion by laser spectroscopy, described in [99]. If this feauture works, EXO is expected to explore neutrino effective masses down to 30 meV.

The EXO Collaboration has the approval and funding to construct a 200-kg liquid TPC with xenon enriched up to 80 % in ^{136}Xe. This project is called EXO-200 and will be installed in the WIPP site in Carlsbad, New Mexico. It will not have the barium-ion tagging feature but it will developpe the TPC itself. Its sensitivity has been estimated in neutrino masses about 0.3 eV. The TPC will measure the charge by 114 x wires and 114 y wires at one end and the light by 258 large area photodiodes at the other side. In a small chamber, both signals have been used to improve the energy resolution and it has estimated a value of 1.5 % σ for EXO-200.

2.5 A Micromegas Xenon TPC for the $\beta\beta$ decay: the NEXT project

As described in the last sections, the use of a Xenon TPCs in this field of search is not new. In principle, a TPC has an excellent background discrimination due to the topological signature but it has always been limited by a modest energy resolution and a low efficiency. Are the actual

features of a TPC good enough to be a competitive detector in double beta decay? We will have a first look at this question calculating the figures of merit F_D defined in equation 2.7 and estimating the range of neutrino masses with the equation 1.16. A more detailed study of this question is made in chapter 9.

The new micropattern detectors have improved the energy resolution in gaseous TPCs, as described in section 4.4. For instance, a value of 4.68 % σ (11 % FWHM) for photons of 5.9 keV has been reached with a micromegas detector in a mixture of argon-isobutane. If this value were also valid in pure xenon at high pressure, a value of 0.54 % FWHM, i.e, 13.3 keV at 2480 keV would be measured (using the expresion 4.6 explained later). In terms of background level, the Gothard collaboration reached a value of 0.01 counts keV^{-1} kg^{-1} yr^{-1} with an efficiency about 30 %.

The potential of these two features (good energy resolution and discrimination techniques for background reduction) to improve the sensitivity of a TPC in a $\beta\beta$ decay experiment has motivated the birth of the NEXT project [19]. It consists in the design and construction in 5 years of a TPC filled with 100 kg of high pressure xenon enriched in ^{136}Xe. The project will be described in detail in chapter 9.

As a preliminary study, we will consider NEXT-100 equiped with a micromegas readout. We can suppose the very optimistic estimation of the energy resolution at $Q_{\beta\beta}$ (0.23 % σ), a background level an order of magnitude better than Gothard (10^{-3} counts keV^{-1} kg^{-1} yr^{-1}) and a similar efficiency (30 %). We will compare its sensitivity with three future double beta experiments (GERDA, EXO and CUORE). Their parameters and sensitivity for a detector mass of 100 kg are summarized in table 2.1 with its corresponding reference.

	GERDA [96]	EXO [22]	CUORE [98]	NEXT
a (%)	75	80	34	80
ϵ (%)	86	58	84	30
b (10^{-3}c/keV/kg/yr)	3.0	2.5	10	1
ΔE(keV σ)	4	40	5	5.7
$F_D(10^{26}$yr & 90 % CL)	1.62	0.23	0.21	0.41
$\langle m_\nu \rangle_{NSM}$ (meV)	$152 - 196$	$188 - 249$	$168 - 223$	$141 - 186$
$\langle m_\nu \rangle_{QRPA}$ (meV)	$79 - 136$	$135 - 374$	$94 - 207$	$101 - 280$

Table 2.1: Prospects of the experiments GERDA, EXO and CUORE, compared with NEXT, equiped with a Micromegas readout. The parameter Mt has been fixed in 100 kg yr. The enrichment (a), the efficiency (ϵ) and the background level (b) values have been taken from the references quoted.

From this table, we note that the highest value for F_D is reached for a germanium detector, due to its high efficiency, low background level and excellent energy resolution. The figure of merit of a NEXT is not very good due its low efficiency. However, as the nuclear figure of merit is higher for ^{136}Xe than for ^{76}Ge, their sensitivities to neutrino mass are comparable. Only for the QRPA model the GERDA experiment will have more sensitivy than a MMTPC of similar mass.

In the case of 1 tonne detection mass, actual collaborations plan to reduce the background level to 10^{-4} counts keV^{-1} kg^{-1} yr^{-1}. In that case, a detector with 1 tonne of xenon enriched a

68 % in ^{136}Xe taking data during 5 year will be sensible (with a CL of 90 %) to neutrino masses of only 30-39 meV (for the NSM) and 21-59 meV (for the QRPA).

Chapter 3

Phenomena of gaseous detectors

The detection of radiation and particles is the main goal of experiments in Particle Physics and has motivated the invention of new detectors since its birth. Gas is an obvious medium for this purpose. Particles and radiation interact with the gas molecules, ionizing them and creating charges. These charges drift to an electrode following the electric field lines. Near the electrode, they are amplified by a high field and an electrical signal is created. These phenomena (interaction, ionization, transport, amplification and signal generation) are the basic pillars of gaseous detectors and are treated in this chapter.

Two main sources have been used for this description. The first one is a general book on particle detection [100]. The second one studies in deepness drift chambers [101]. Readers who want to learn more about these topics are referred to them.

3.1 Interaction of photons and charged particles in a gas

A gaseous detector can detect photons, electrons and heavy charged particles like muons or alphas. Each kind of particle goes through different physical processes, making necessary a different study for each one.

3.1.1 Photons

A photon travelling through a material can undergo three different interactions depending on its energy:

- The **photoelectric effect**, where the photon is absorbed by an atomic electron which is then ejected with a part of the photon energy.
- **Compton scattering**, where part of the photon energy is transferred to an atomic electron. In this process, the photon is deflected and its wavelength increases.
- **Pair production**, where the photon traversing the electromagnetic field of a nucleus materializes into an electron-positron pair.

Less common but also possible are nuclear dissociation reactions but they are neglected in this study. The former interactions explain two main qualities of photons: they are more penetrating in matter than charged particles (due to their lower cross-sections) and a beam of photons is not degraded in energy as it passes through matter (because interactions are governed by probabilities).

The cross-sections of these interactions depend on the photon energy and on the atomic number and the density of the material. In gases with an atomic number larger than 4, the cross-section for the photoelectric effect dominates up to energies of several tens of keV. Above this value, the Compton scattering takes over. The pair production occurs for a photon energy higher than 1 MeV and quickly surpasses the other processes. As an example, the cross-sections for xenon are shown in figure 3.1).

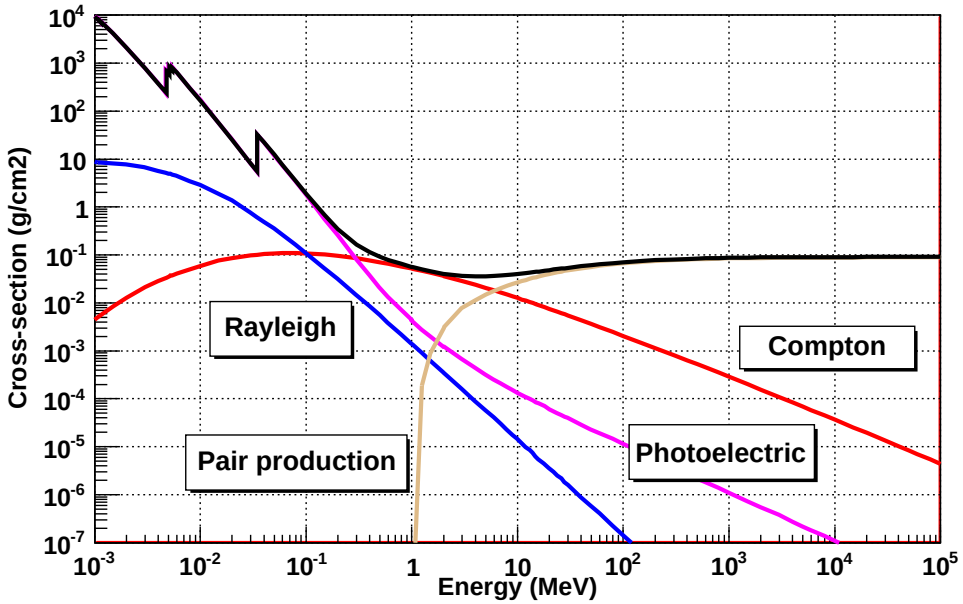

Figure 3.1: The cross-section of each process (the Rayleigh scattering, the photoelectric effect, the Compton scattering and the pair production) for photons passing through xenon. Plots have been generated by the application [102].

The photoelectric effect

The photoelectric effect consists on the absorption of a photon of energy E_0 by an atomic electron (called photoelectron) followed by its emission with a kinetic energy equal to:

$$E = E_0 - E_{shell} \tag{3.1}$$

with E_{shell} the energy of the shell the electron belongs to. As the photon energy is completely absorbed, the photoelectric effect must involve a third collision partner to take the recoil momentum: the nucleus.

When the photon energy increases above the energy of a shell, the electrons of this shell become available for the photoelectric effect and the cross-section sharply rises (the so-called shell edge). This sharp increase is clearly seen at energies lower than 1 MeV, as shown in figure 3.1. The total cross-section for the photoelectric effect is the sum of the cross-sections for the photoelectric effect on the various shells energetically allowed. At energies higher than the K-shell energy, the cross-section for absorption in the K-shell is about 80 % of the total cross-section because of the proximity of the third collision partner.

In the non-relativistic limit ($E_0 << m_e c^2$) and at photon energies higher than the energy of

the K-shell, the cross-section for the photoelectric effect is

$$\sigma_{pe} = 4\alpha^4\sqrt{2}Z^5\frac{8\pi r_e^3}{3}\left(\frac{m_e c^2}{E_0}\right)^{7/2} \tag{3.2}$$

where α is the fine structure constant, r_e is the classical radius of the electron, m_e is the electron mass, Z is the atomic number of the material and E_0 is the photon energy. This formula is valid up to energies of 500 keV and shows a very strong dependence of the cross-section on the number of electrons in the medium (Z). This fact explains the low cross-section for the photoelectric effect in helium compared to xenon.

The emission of a photoelectron leaves a vacancy in the shell to which it belongs. This vacancy can be filled by two mechanisms

- **Fluorescence**: The vacancy is filled by an electron from an outer shell and the energy difference is liberated in the form of an x-ray.
- **Auger transition**: the vacancy is also filled by an electron from an outer shell but the energy difference is transferred to an electron of the same atom. If the energy is larger than its binding energy, the latter is ejected from the atom. This electron is called Auger electron.

In both processes, a vacancy is replaced by another vacancy and the complete atomic relaxation can involve more than one transition. The fraction of the deexcitation through fluorescence is called the fluorescence yield. It is negligible in helium where a photoelectron is always accomplished by an Auger electron. In argon, the K-shell fluorescence yield is equal to 13.5 % while the one of the L-shell is negligible.

The Compton scattering

It consists in the scattering of photons on free electrons. Even if electrons are bound in atoms, if the photon energy is high enough with respect to the binding energy, this latter energy can be ignored and the electrons considered free. A Compton scattered photon transfers energy to an atomic electron (so-called Compton electron) and its wavelength shifts by

$$\Delta\lambda = \frac{h}{m_e c}(1 - \cos(\theta)) \tag{3.3}$$

where h is the Planck constant. m_e is the electron mass, c is the light speed in vacuum and θ is the angle between the initial and final wave vector of the photon. If the transferred energy is larger than the electron binding energy, the electron is ejected from the atom. The maximum transferred energy is given by

$$\Delta E_{max} = E\ \frac{2E/(m_e c^2)}{1 + 2E/(m_e c^2)} \tag{3.4}$$

where E is the initial energy.

The cross-section for Compton scattering was one of the first ones to be calculated by quantum electrondynamics and can be found in [100]. For photons less energetic than x-rays, the cross-section is independent of the photon energy and the transferred energy becomes negligible (the so-called Thomson scattering). Another Compton process is the coherent scattering of the atom as a whole, the so-called Rayleigh scattering. It has no direct interest for particle detection as no energy is transferred to the medium. Atoms are neither excited nor ionized and only the direction of the photon is changed.

The pair production

This process involves the transformation of a photon into an electron-positron pair. It only occurs in the presence of a third body like a nucleus to conserve momentum and the photon must have at least an energy of 1.022 MeV. The cross-section of this process is throughly discussed in [100].

3.1.2 Charged particles

Charged particles suffer a continuous energy loss and a deflection from its incident direction when passing through a gas detector. These two facts are mainly due to three processes:

1. Inelastic collisions (also called Coulomb interactions) with atomic electrons of the gas.
2. Elastic scattering from nuclei.
3. Bremstrahlung.

Other reactions can occur but are rare at the energies of interest here. They include the emission of Cherenkov radiation and nuclear reactions. They are neglected in this study. From the former processes, the inelastic collisions are almost the only responsible for the energy loss. In each collision, energy is transferred from the particle to the atom, normally a very small fraction of particle's kinetic energy. The transferred energy can cause an excitation or ionization of the atom and, in some cases, the ionizated electron can cause substantial secondary ionization. These high-energy electrons are called **δ-rays** or knock-on electrons. Elastic scattering from nuclei also occurs but very little energy is transferred due to the large difference between incident and gas masses.

Coulomb interactions: the Bethe-Bloch formula

The first calculation of the energy loss due to Coulomb interactions was performed by Bethe, Bloch and other authors. The formula obtained is

$$-\frac{dE}{dx} = 2\pi N_a r_e^2 m_e c^2 \rho \frac{Z}{A}\frac{z^2}{\beta^2}\left[ln\left(\frac{2m_e\gamma^2 v^2 W_{max}}{I^2}\right) - 2\beta^2 - \delta - 2\frac{C}{Z}\right] \tag{3.5}$$

where

r_e	classical electron radius	z	charge of incident particle
m_e	electron mass	β	v/c of incident particle
N_a	Avogadro's number	γ	$1/\sqrt{1-\beta^2}$
I	Mean excitation potential	δ	density correction
Z	atomic number of gas	C	shell correction
A	atomic weight of gas	W_{max}	maximum energy transferred in single emission
ρ	gas density		

The meaning of each parameter and the validity of this expression is discussed in [100].

At non relativistic energies, dE/dx is dominated by the overall $1/\beta^2$ factor and decreases with increasing velocity until about $v = 0.96c$ where a minimum is reached (see figure of 3.2). Particles at this point are known as minimum ionizing. In the very low energy region, the Bethe-Bloch formula reaches a maximum and then drops sharply again. This means that more energy per length unit is deposited towards the end of a particle path rather than its beginning. In figure 3.3 the energy loss as function of the penetration depth in matter is shown. This curve is also called the Bragg curve.

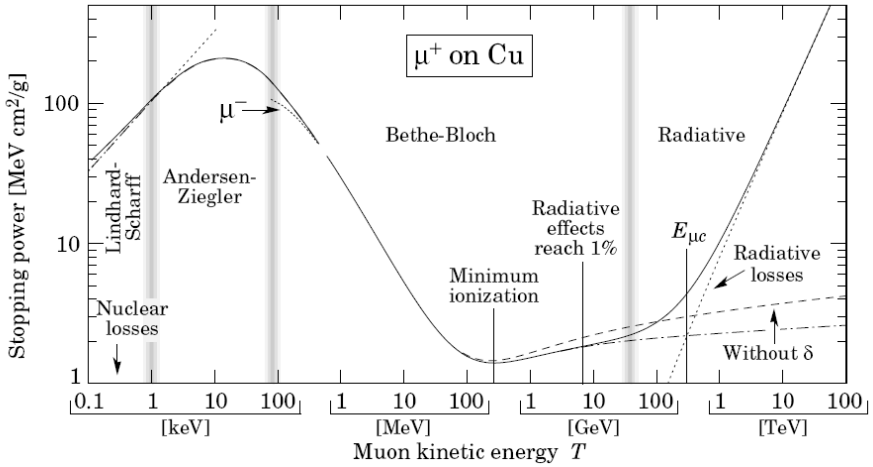

Figure 3.2: Energy loss as function of kinetic energy for muons in copper, extracted from [103].

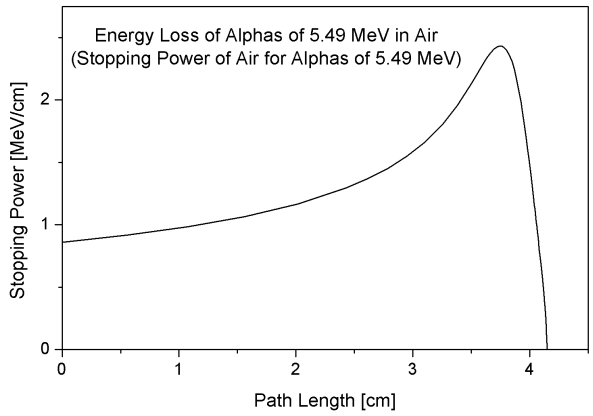

Figure 3.3: The Bragg curve for alphas of 5.49 MeV in air, extracted from [104].

3.1.3 Electrons

Electrons also lose energy by collisions when passing through matter. However, an additional energy loss mechanism comes into play due to its small mass: the emission of electromagnetic radiation arising from scattering in the electric field of a nucleus (bremsstrahlung). Classically, this may be understood as radiation arising from the acceleration of the electron as it is deviated from its straight-line course by the electrical attraction of the nucleus. At energies of less than 10 MeV, this process has little importance and can be neglected in this study.

The mechanism of collision for electrons described for heavy charged particles is also valid for electrons. However, the Bethe-Bloch formula must be modified due to two facts: the incident and the atom electrons are identical and the first one can be deflected during the collision. The new formula becomes

$$-\frac{dE}{dx} = 2\pi N_a r_e^2 m_e c^2 \rho \frac{Z}{A}\frac{1}{\beta^2}\left[ln\left(\frac{\tau^2(\tau+2)}{2(I/m_e c^2)}\right) + 1 - \beta^2 + \frac{\frac{1}{8}\tau^2 - (2r+1)ln2}{(\tau+1)^2} - \delta - 2\frac{C}{Z}\right] \quad (3.6)$$

where τ is the kinetic energy of partice in units of $m_e c^2$.

3.2 Ionization of the media

In section 3.1 we concluded that a photon transfers its energy to electrons freed from gas atoms. Meanwhile, heavy charged particle and electrons lose their energy in discrete amounts through inelastic collisions with the gas molecules. These collisions mainly result in electronic excitations and ionizations, while for more complex molecules (e.g. CO_2, CH_4 and heavier organic gases), excitations of vibrational and rotational levels are also possible. Therefore, the electron energy E_0 is not all invested in ionization and the number of primary electrons N_e depends on the gas mixture.

3.2.1 Mean energy per electron-ion pair

The outcome of each collision between an electron and a gas molecule is governed by probabilities. This means that two identical particles with the same kinetic energy will not, in general, produce the same number of ion-electron pairs. Experimentally, the mean obeys the following equation

$$N_e = E_0/W \tag{3.7}$$

where W is the mean energy per electron-ion pair. The value of W is governed by the cross-sections for the various inelastic collisions and the corresponding energy losses. It thus depends on the gas composition and on the nature and energy of the charged particle. Values of W measured with α sources are similar to those measured with β ones but the ratio W_α/W_β can reach 1.15 for some organic vapours [105]. It was also found that W is independent of the initial energy above a few keV for electrons and a few MeV for alpha particles.

In general, W is not the same as the ionization potential (I_{ion}) because some energy is also lost to excitation. The ratio W/I_{ion} indicates the fraction of the primary energy invested into ionization. It is approximately 69 % in noble gases and about 40 % in molecular gases. Values of W and I_{ion} for some gases are found in table 3.1.

Gas	$I_{exc}(eV)$	$I_{ion}(eV)$	$W_e(eV)$
H_2	10.8	15.4	37
He	19.8	24.6	41
N_2	8.1	15.5	35
O_2	7.9	12.2	31
Ne	16.6	21.6	36
Ar	11.6	15.8	26
Kr	10.0	14.0	24
Xe	8.4	12.1	22
CO_2	10.0	13.7	33
CH_4		13.1	28
iC_4H_{10}		10.8	23

Table 3.1: Excitation (I_{exc}) and ionization (I_{ion}) potentials and mean energy for ion-electron pair creation (W) for various gases extracted from [100].

In a gas mixture, the number of primary electrons N_e can be calculated as a weighted average of N_e in the pure gases. The weights are determined by the relative concentrations C and ionization cross-sections σ. For a mixture of two gases A and B, the value W_{AB} should thus

obey:

$$\frac{1}{W_{AB}} = \frac{C_A \sigma_A}{W_A} + \frac{C_B \sigma_B}{W_B} \tag{3.8}$$

where $\sigma_A + \sigma_B = 1$.

3.2.2 The Fano factor

As the ionization process is governed by statistics, the number of primary electrons generated by identical particles fluctuates. In the case of independent ionizing collisions, the number of primary electrons N_e follows Poisson statistics with a variance equal to N_e. However, the number of ionizing collisions is constrained by the initial energy of the charged particle: $N_E \leq E_0/I_i$. The process is therefore not Poissonian and N_e exhibits a reduced variance. The Fano factor F accounts for this reduction, described by

$$\sigma^2_{N_e} = F\ N_e \tag{3.9}$$

The Fano factor indicates the magnitude of the fluctuations of the number of electrons. Like W, F depends on the gas mixture and the electron energy. Values lie between 0.15-0.2 for noble gases and 0.2-0.4 for molecular gases. A compilation of measurements suggest that it decreases with the ratio I_i/W. Table 3.2 gives some measured values for various gases.

Gas	F	Energy (keV)	Particle
He	0.17		β
Ne	0.17		
Ar	0.17		
Ar	0.22		α
	0.23 ± 0.05	5.9	γ
	0.23 ± 0.05	5305	α
Xe	≤ 0.15	1.49	γ
	0.170 ± 0.007	1.49	γ
	0.13 ± 0.01	5.9	γ
C_4H_10	0.26	1.49	γ
CO_2	0.33	1.49	γ

Table 3.2: Measured Fano factors for various gas mixtures and particles extracted from [106].

The variation in the initial number of ion-electron pairs is the first contribution to the energy resolution of any gas detector. In consequence, it gives a lower limit to the energy resolution of a particle with energy E, generally called the **Fano limit**, and expressed by

$$R(\%\ \text{FWHM}) = 2.35\ \sqrt{\frac{F\ W}{E}} \tag{3.10}$$

According to this formula, the intrinsic energy resolution of a TPC in pure xenon at 2480 keV, the $Q_{\beta\beta}$ of the double beta decay, is 0.27 % FWHM. This is equivalent to 2.9 keV σ.

3.3 Transport of electrons

The classical kinetic theory of gases can be used to estimate drift properties of electrons [107]. It also provides instructive relationships between the macroscopic quantities of drift velociy u and isotropic diffusion coefficient D on the one hand, and the microscopic quantities of electron velocity c, mean time τ between collisions and the fractional energy loss λ on the other. These last parameters are randomly distributed and we deal with suitable averages [101]. Relations are expected to be corrected within factors of the order of unity.

3.3.1 Drift velocity

In the absence of external forces, electrons in a gas at temperature T move around with a Maxwellian energy distribution with a most probable value kT (0.04 eV at room temperature). In the presence of an electric field, electrons are accelerated along the field lines towards the anode. This acceleration is interrupted by collisions with a gas molecule, which randomize its direction of motion. On average, a constant drift velocity u is assumed along the direction of the electric field E. This velocity is much smaller than the instantaneous velocity c between collisions.

Let us consider an electron between two collisions. Immediately after the first collision, it has no preferential direction. Some short time later, it has picked up an extra velocity u equal to its acceleration along the field, multiplied by the average time elapsed since the last collision,

$$u = \frac{eE}{m}\tau \tag{3.11}$$

This extra velocity appears macroscopically as the drift velocity. In the next encounter, the extra energy is on the average lost in the collision through recoil or excitation. Therefore there is a balance between the energy picked up and the collision losses. On a drift distance x, the number of encountes is $n = (x/u)(1/\tau)$, the time of the drift divided by the average time τ between collisions. If λ denotes the average fraction energy loss per collision, the energy balance is the following

$$\frac{x}{u\tau}\lambda\epsilon_E = eEx. \tag{3.12}$$

Here the equilibrium energy ϵ_E carries an index E because it does not contain the part due to the thermal motion of the gas molecules, but only the part taken out of the electric field.

For drifting particles with instantaneous velocity c, the mean time τ between collisions can be expressed in terms of the cross-section σ and the number density N by

$$\frac{1}{\tau} = N\sigma c. \tag{3.13}$$

Here c is related to the total energy of the drifting electron by

$$\frac{1}{2}mc^2 = \epsilon = \epsilon_E + \frac{3}{2}kT \tag{3.14}$$

because the total energy is made up of two parts: the energy received from the electric field and the thermal energy that is appropiated for 3 degrees of freedom (k = Boltzmann's constant and T gas temperature). For electron drift in particle detectors, we usually have $\epsilon_E >> 3/2kT$. We can neglect the thermal motion and equations 3.11, 3.12 and 3.14 combine to give the two equilibrium velocities as follows

$$u^2 = \frac{eE}{mN\sigma}\sqrt{\frac{\lambda}{2}} \tag{3.15}$$

$$c^2 = \frac{eE}{mN\sigma}\sqrt{\frac{2}{\lambda}} \tag{3.16}$$

where $\epsilon = (1/2)mc^2 \approx \epsilon_E >> (3/2)kT$.

Both σ and λ are functions of ϵ. We notice that if the energy loss λ in the collisions vanishes, the drift velocity will become zero. If ϵ is below the excitation level of the gas molecules, the scattering is elastic [108] and λ is approximately the ratio of the masses of the partners. For helium gas, this ratio is roughly 2.7×10^{-4}.

In the plot 3.4 of the cross-section for xenon and isobutante with energy, we observe a clear dip near $\epsilon \approx 0.7$ eV. This is the called Ramsauer minimum [109], which is due to quantum mechanical processes as the electron wavelength approaches those of the electron shells of the gas molecule. Other noble gases like krypton and argon show the same behaviour but helium and neon do not [110].

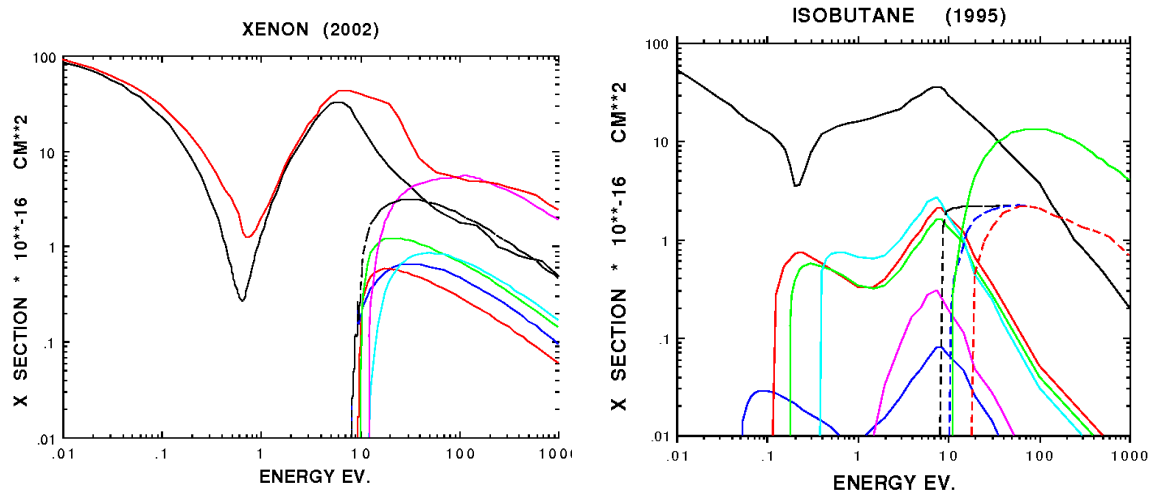

Figure 3.4: Effective cross-sections $\sigma(\epsilon)$ (black upper line) for xenon (left) and isobutane (right) extracted from [111]. The other lower lines are contributions to the energy loss per excitation $\lambda(\epsilon)$.

In the same figure 3.4, the lower lines are contributions to $\lambda(\epsilon)$ for xenon and isobutane. The threshold for excitation of the xenon atom is about 10 eV, that for the isobutane molecule is two order of magnitude lower. Under these circunstances it is not surprising that the drift velocity for electrons depends critically on the exact gas composition. Even small additions (10^{-2}) of molecular gases to a noble gas dramatically increase the fractional energy loss λ, by absorbing the collision energy in the rotational states. This change of λ results in an increase of the electron drift velocity by large factors, as points out the equation 3.15.

We note that the dependence of the drift velocity and the electron energy on E and P is always by the ratio E/P, called the **reduced drift field**. This fact implies that in two gases operated with different gas pressures and identical temperature, the E field must be adjusted in proportion to the gas pressures in order to obtain identical drift velocity.

As it was mentioned in the beginning, the deduced relations are just instructive. Exact values are obtained by a rigorous statistical calculation called the **transport theory**. This theory is based on the solution of transport and energy conservation equations for electrons under the influence of external fields. The main approximation made before was to take a single

velocity c to represent the motion between collisions of the drifting electrons. In reality, these velocities are distributed around a mean value according to a distribution function $f_0(c)dc$. A more detailed review can be found in [101, 112].

During the last decades, the drift properties have been studied in a large variety of gas mixtures used for various reasons in gaseous detectors. These include a very large amount of data on drift for argon [112, 113, 114] and xenon [110, 114, 115] based mixtures. There is also a computer programme called Magboltz [111] for simulation of electrons in gases that gives drift and diffusion values with an accuracy better than 2 %.

Drift curves for argon- and xenon-mixtures have been generated by this programme for a later comparison with experimental data. They are respectively shown in figures 3.5 and 3.6. We note the very low values of drift velocity for pure noble gases (0.1-0.2 cm/s in pure xenon for fields 10^2-10^3 V/cm/bar) and the increase of an order of magnitude with the addition of a little quantity of a complex molecule.

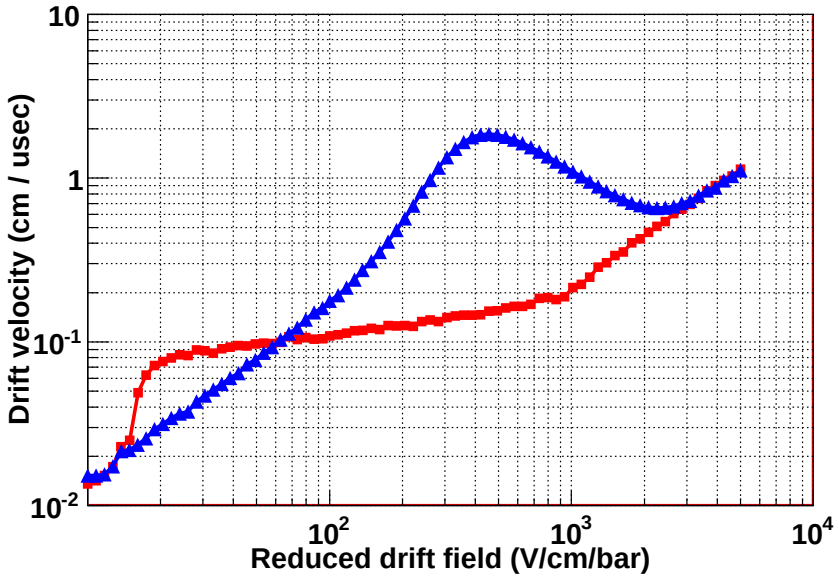

Figure 3.5: Dependence of the drift velocity with the reduced drift field for pure xenon (red squares) and Xe + 1 % CH_4 (blue triangles). It is clear the velocity increase of an order of magnitude due to the quencher at fields between 10^2 and 10^3 V/cm/bar.

3.3.2 Diffusion

In the absence of an electric field, electrons and ions liberated by passing radiation diffuse uniformly outward from their point of creation. In this process they suffer multiple collisions with the gas molecules and lose their energy. They thus come quickly into thermal equilibrium with the gas and eventually recombine. At thermal energies, the velocities of the charges are described by the Maxwell distribution which gives a mean speed of

$$v = \sqrt{\frac{8kT}{\pi m}} \tag{3.17}$$

where k is the Boltzmann's constant, T is the temperature and m is the mass of the particle. The average speed of the electrons is much greater than that of the ions due to their small mass.

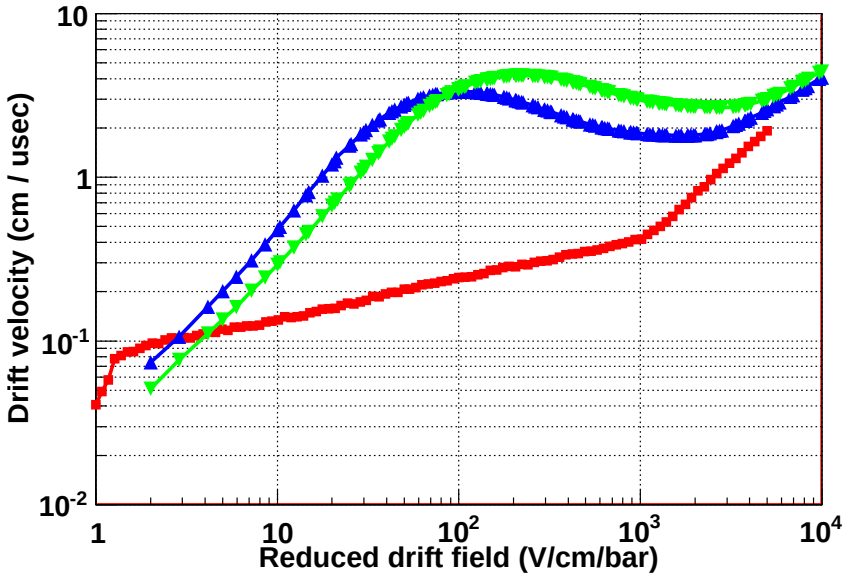

Figure 3.6: Dependence of the drift velocity with the reduced drift field for pure argon (red squares), Ar + 2 % iC_4H_{10} (blue triangles) and Ar + 5 % iC_4H_{10} (green inverted triangles). As in the case of xenon, a little quantity of quencher increase the velocity an order of magnitude.

At room temperature, the electron speed is a few times cm/μs while the positive ion speeds are of the order of 10^{-2} cm/μs.

In the presence of a drift field, the drifting electrons are scattered on the gas molecules. This causes a deviation from the average on their drift velocity due to the random nature of collisions. In principle, the deviation is the same in all directions. A point-like cloud of electrons which begins to drift at time $t = 0$ from the origin in the z direction will, after some time t, assume the following Gaussian density distribution:

$$n = \left(\frac{1}{\sqrt{4\pi Dt}}\right)^3 \exp\left(\frac{-r^2}{4Dt}\right) \tag{3.18}$$

where $r^2 = x^2 + y^2 + (z - ut)^2$ and D is the diffusion constant. n satisfies the continuity equation for the conserved electron current Γ:

$$\mathbf{\Gamma} = n\mathbf{u} - \nabla Dn \tag{3.19}$$

$$\frac{\delta n}{\delta t} + D\Gamma = 0 \tag{3.20}$$

$$\frac{\delta n}{\delta t} + n\mathbf{u} - \nabla Dn = 0 \tag{3.21}$$

The diffusion constant D, defined by 3.19, makes the mean squared deviation of the electrons equal to $2Dt$ in any direction from their centre. In order to express the diffusion constant in terms of the microscopic picture, we suppose that one electron starts to drift at time $t = 0$ with a velocity c. If τ is the average time between collisions, the differential probability $f(t)dt$ that the next encounter happens between t and $t + dt$ away from any point $t = 0$ in time is

$$f(t)dt = \frac{1}{\tau} e^{-t/\tau} dt. \tag{3.22}$$

From equation 3.22, we deduce that the probability distribution of the free path l is equal to

$$g(l)dl = \frac{1}{l_0}\exp(-t/t_0)dl \tag{3.23}$$

where $l_0 = c\tau$ is the mean free path.

We suppose that scattering is isotropic with respect to the drift equation, which is a good approximation for electrons. We take a time t where a large number of collisions n has happened. It is clear that $n = t/\tau$. The mean square displacement in one direction, say x, is

$$2Dt = \int \left(\sum_{i=1}^{n} l_i \cos(\theta_i)\right) \prod_{k=1}^{n} g(l_k)dl_k \frac{d\cos(\theta_k)}{2} = n\frac{2}{3}\, l_0^2 = \frac{2}{3}\frac{l_0^2}{\tau}t \tag{3.24}$$

Here $l_i \cos(\theta_i)$ is the displacement along x between the (i-1)th and the ith collision; the $\cos(\theta_i)$ are uniformly distributed between -1 and +1 according to our assumption. The l_i are distributed by the probability density of equation 3.23. Note that the mixed terms in the sum vanish. The part proportional to $2t$ is the diffusion constant D,

$$D = \frac{l_0^2}{3\tau} = \frac{cl_0}{3} = \frac{c^2\tau}{3} = \frac{2}{3}\frac{\epsilon}{m}\tau \tag{3.25}$$

Using the expression for the electron mobility

$$\mu = \frac{e}{m}\tau, \tag{3.26}$$

we notice that the electron energy can be determined by a measurement of the ratio D/μ:

$$\epsilon = \frac{3}{2}\frac{De}{\mu} \tag{3.27}$$

When the diffusing body has thermal energy, $\epsilon = (3/2)kT$, equation 3.27 takes the form

$$\frac{D}{\mu} = \frac{kT}{e} \tag{3.28}$$

which is known as the Nernst-Townsend formula or Einstein formula.

The energy determines the diffusion width σ_X of an electron cloud which after starting a point-like, has travelled over a distance L:

$$\sigma_X^2 = 2Dt = \frac{2DL}{\mu E} = \frac{4\epsilon L}{3eE} \tag{3.29}$$

In drift chambers we therefore require small electron energies at high drift fields in order to have σ_X^2 as small as possible. In literature it is also expressed in terms of the characteristic energy ϵ_k, which is related to ϵ by $\epsilon_k = (2/3)\ \epsilon$. Another common variable is the diffusion coefficient σ_d, which is defined in terms of the drift length as

$$\sigma_X^2 = \sigma_d^2 L = \frac{4\epsilon}{3eE}\ L \tag{3.30}$$

In figure 3.7 the variation of ϵ_k with the electric field strength, measured with electrons drifting in two gases, argon and carbon dioxide, is shown. They represent extreme cases concerning the change-over from thermal to field-dominated behaviour. In argon a field strength as low as 1 V/cm produces electron energies distinctly larger than the thermal (hot gas). In carbon

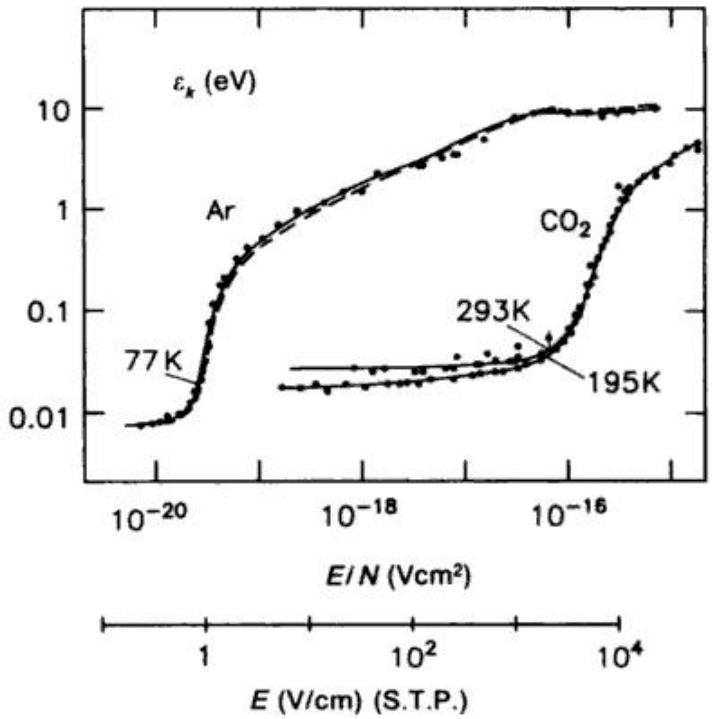

Figure 3.7: The characteristic energy of electrons in Ar and CO_2 as a function of the reduced electric field, extracted from [101].

dioxide the same behaviour occurs only at field strengths above 2 kV/cm (cold gas). The reason is the large relative energy loss λ in CO_2, due to the internal degrees of freedom of the CO_2 molecule, which are accesible at low collision energies.

Until 1967 it was assumed that the electron diffusion was isotropic. But then Wagner et al. discovered experimentally that the value of electron diffusion along the electric field can be quite different from that in the perpendicular direction. Equation 3.18 is thus expressed by

$$n = \left(\frac{1}{\sqrt{4\pi D_L t}}\right)\left(\frac{1}{\sqrt{4\pi D_T t}}\right)^2 \exp\left(-\frac{x^2+y^2}{4Dt} - \frac{(z-ut)^2}{4D_L t}\right) \tag{3.31}$$

As in section 3.3.1, the Magboltz programme has been used to generate longitudinal and transversal diffusion coefficients for argon- and xenon-based mixtures. They are shown in figures 3.8 and 3.9. Note that x-axis is the reduced drift field (E/P) and y-axis is the diffusion coefficient multiplied by the squared root of pressure ($P^{1/2}$).

3.3.3 Attachment

Electrons may be absorbed during their drift in the gas by the formation of negative ions. Noble gases and most organic molecules can only form stable negative ions at collision energies of several electronvolts, which are higher than energies reached during any electron drift. However, there are some molecules that are capable of attaching electrons at much lower collision energies. Such molecules are sometimes present as impurities. Among them, the largest electron affinities are found with the halogenides (3.1-3.7 eV) and oxygen (0.43 ± 0.2 eV). This means that attachment is mainly generated by contamination of air, water and halogen-containing chemicals.

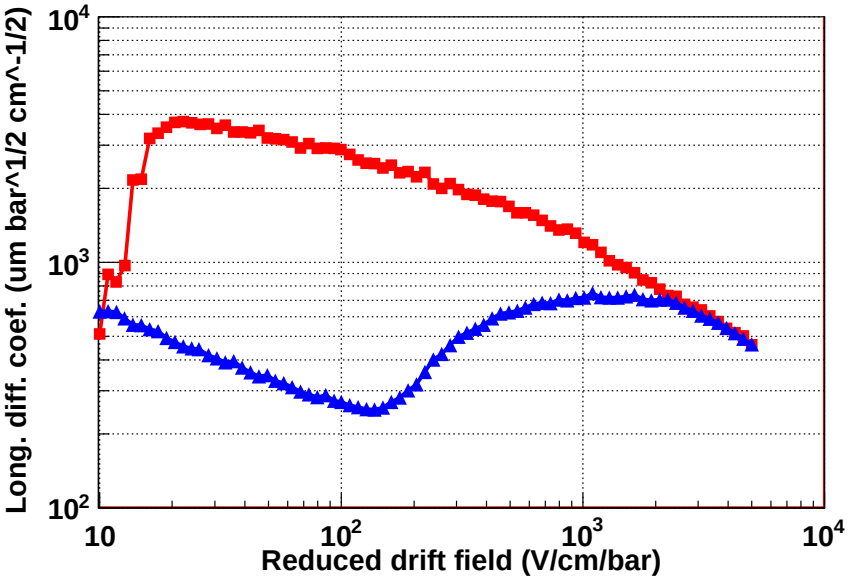

Figure 3.8: Dependence of the longitudinal diffusion coefficient with the reduced drift field for pure xenon (red squares) and Xe + 1 % CH_4 (blue triangles). The addition of a little quantity of quencher reduces the diffusion coefficients an order of magnitude for drift fields between 10^2 and 10^3 V/cm/bar

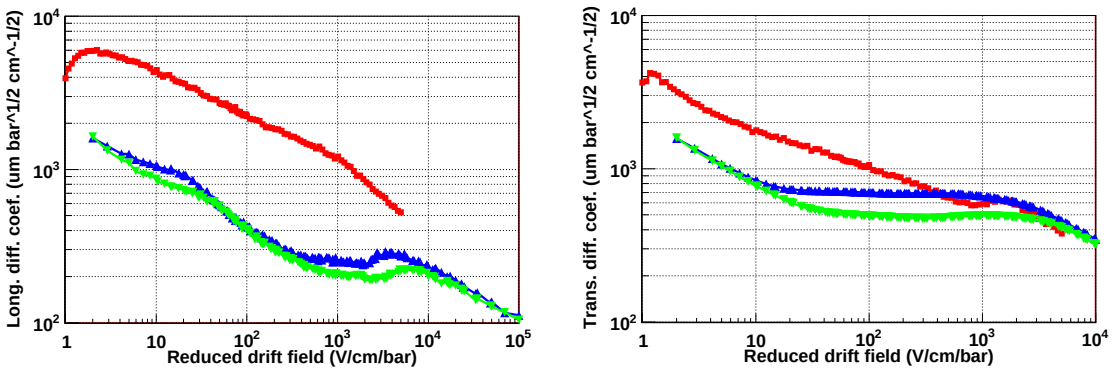

Figure 3.9: Dependence of the longitudinal and transversal diffusion coefficients with the reduced drift field for pure argon (red squares), Ar + 2 % iC_4H_{10} (blue triangles) and Ar + 5 % iC_4H_{10} (green inverted triangles). In pure argon, the longitudinal coefficient has bigger values than the transversal one. This behaviour changes if a quencher is added.

In attachment theory there are two-body and three-body processes. We will study them separately.

Dissociative attachment

It consists of the break-up of a molecule M into several constituents A, B, ..., one of which forms a negative ion

$$e^- + M \rightarrow M^- \text{ or } e^- + M \rightarrow A^- + B + \ldots$$

The probability of the molecule staying intact is generally higher at lower electron energies.

The rate R of the attachment is given by the cross-section σ, the electron velocity v and the density N of the attaching molecule

$$R = c\sigma N = k\sigma \tag{3.32}$$

where k is called the two-body attachment rate constant. This process is very important for freons like CCl_4, CCl_2F_2, CF_3I and BCl_3. Several values for these gases can be found in [116].

The BBH mechanish

The most important mechanism for energies below the dissociation energy is a three-body process proposed in 1935 by Bloch and Bradbury (BBH). According to this model, attachment occurs as a two-step process. First, the electron encounters an electronegative molecule like O_2 and forms a negative ion in an excited state

$$O_2 + e^- \rightarrow O_2^{-*} \tag{3.33}$$

O_2^{-*} is one of the lowest vibrational states of the O_2^- ion, with a lifetime of the order of 10^{-10} s. This process is followed either by its spontaneous decay

$$O_2^{-*} \rightarrow O_2 + e^- \tag{3.34}$$

where the electron is released and the excitation energy is liberated in the form of kinetic energy, or by stabilization of the excited ion in a collision with a molecule of the buffer gas

$$O_2^{-*} + M \rightarrow O_2 + M^+ \tag{3.35}$$

by resonant energy transfer to the buffer gas molecule. Reactions 3.34 and 3.35 are competing processes and electron attachment occurs only if reaction 3.33 is followed by 3.35. The probability of reactions 3.34 and 3.35 depend on the nature of the buffer gas. A complex molecule like isobutane has a dense vibrational energy-level structure and may therefore more likely absorb the excitation energy of O_2^{-*} by reaction 3.35 than a simple molecule. Noble gases like argon have no vibrational energy level structure at all and hence favour reaction 3.34. This means that in principle attachment in noble gases is very small.

The vdW-M mechanish

The Van der Waals mechanism (vdW-M) is a three-body process where the electron attach to a molecular dimer or polymer due to Van der Waals forces. The process follows the chain

$$O_2 + M \rightarrow (O_2M) \tag{3.36}$$

$$(O_2M) + e^- \rightarrow (O_2M)^{-*} \tag{3.37}$$

$$(O_2M)^{-*} + M \rightarrow O_2^- + M + M \tag{3.38}$$

The mean electron lifetime

If a number of electrons ($N(0)$) is deposited in a gas with the tendency to attach electrons, the time evolution of the number of free electrons will follow the law

$$N(t) = N(0) \exp\left(-\frac{t}{\tau}\right) \tag{3.39}$$

where τ is the **mean lifetime** of an electron in the gas. Some authors also use $A = 1/\tau$, called the **attachment rate**.

Some simple behaviours can be deduced from a simple reasoning. The cross section for processes 3.33 and 3.37 is proportional to $1/\epsilon$, where ϵ is the mean energy of electrons in the gas. In a drift chamber, ϵ grows with the drift field. This means that the attachment rate should decrease when increasing the drift field. Secondly, the rate of processes 3.35 and 3.38 grows linearly with the pressure of gas ($P(M)$). Finally, at relatively low oxygen concentrations of a few hundred ppm, O_2-O_2 collisions can be neglected and the rate of reactions would grow linearly with the pressure of O_2 ($P(O_2)$).

In conclusion, the attachment rate follows the expression

$$A = k(\mathrm{O_2}, \mathrm{M})\ P(\mathrm{M})\ P(\mathrm{O_2}) \tag{3.40}$$

where $k(O_2, M)$ is the **attachment cofficient**. This parameter is independent of the gas pressure. In table 3.3, attachment coefficients for different buffer gases for thermal drift velocities ($E/P = 0$) are shown. The BBH mechanism is the predominant attachment process for gases at the lower part of the table. Meanwhile, vdW-M is the most important for gases at the upper part.

Gas	He	Ne	Ar	Kr	Xe	N_2
$k(\mu s^{-1} bar^{-2})$	24 ± 2	17 ± 2	7 ± 7	36	61 ± 4	61 ± 4

Gas	H_2	CO_2	CH_4	C_2H_6	C_3H_8	iC_4H_{10}
$k(10^2 \mu s^{-1} bar^{-2})$	3.5 ± 0.2	23.1 ± 1.4	2.5 ± 0.1	9.4 ± 1.4	21.7 ± 3.6	30.3 ± 1.4

Table 3.3: Attachment coefficients for different buffer gases given in [117].

As explained before, attachment coefficients depend on the electrical field. In figure 3.10, it is shown this dependency for a Xenon mixture. Other examples for Argon-Methane mixtures and SF_6 mixtures are respectively given in [118] and [119]

Attachment to other molecules

Concerning the attachment of electrons to H_2O molecules, the situation is not clear. It is known since longtime [121] that it can occur via molecular dissociation but it is not established whether or not attachment to H_2O occurs at all for energies below dissociation threshold. BBH mechanism is considered an explanation for this effect (formation of an excited H_2O^{-*} ion and subsequent stabilization) but other authors attribute it to residual impurities in the gas, as exposed in [118].

In this same reference, the effect of water impurities in Argon mixtures was studied. In absence of oxygen, no effect in argon-methane and argon-methanol mixtures of water was observed. In contrast, the addition of 950 ppm of H_2O to Ar + 10% CH_4 with an oxygen contamination of 200 ppm increased $k(O_2, M)$ a factor 2 in a range of drift fields between 110 and 270 V/cm/bar. This effect was described by the approximate formula

$$k(\mathrm{O_2}, \mathrm{M} + \mathrm{H_2O}) = k(\mathrm{O_2}, \mathrm{M}) \left(1 + \frac{[\mathrm{H_2O}]}{1000}\right) \tag{3.41}$$

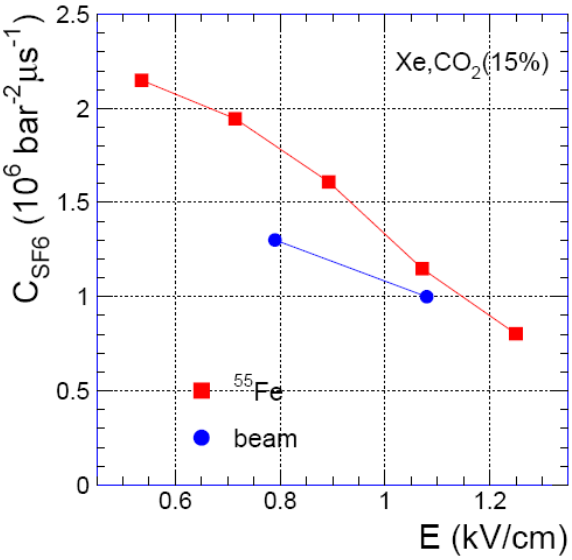

Figure 3.10: Dependence of the attachment coefficient for SF_6 with the drift field in Xe + 15% CO_2 [120].

where $[H_2O]$ is the concentration of water expressed in ppm. This increase was attributed to the participation of water molecules to attachment via the reaction

$$O_2^{-*} + H_2O \rightarrow O_2^- + H_2O^* \tag{3.42}$$

Another impurity responsible of attachment in gases is the sulphur hexafluoride (SF_6). Concentrations at the ppm level in xenon clearly affected the signal, as it is shown in figure 3.11. Apart from that, this impurity has a more intense effect in xenon than in argon for fields between 2.7 and 27 V/cm/bar as shown in figure 3.12.

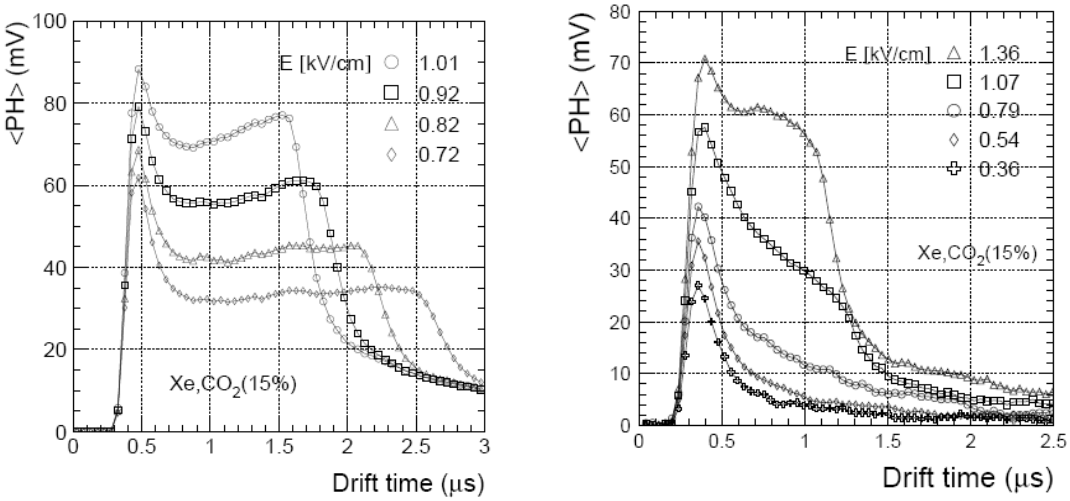

Figure 3.11: Pulse height for electrons drifting different distances for Xe + 10% CO_2 with 100 ppm of water and no SF_6 (left) and 1.1 ppm of SF_6 (right). More details are given in [120].

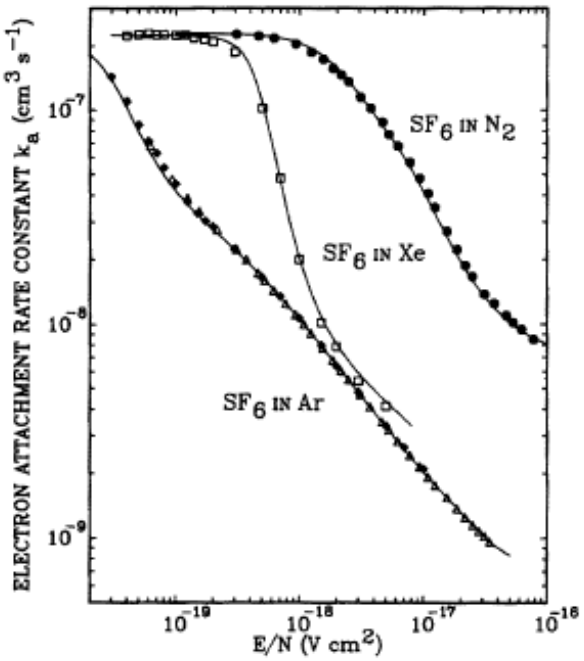

Figure 3.12: Attachment coefficient for SF_6 in pure N_2, Ar and Xe, extracted from [119].

Attachment origins: Outgassing

The inner walls of a TPC release gas molecules, like oxygen and water, causing attachment. This emission, generally referred to as outgassing, is actually a result of several processes:

- **Real leaks**: They are produced by manufacture deffects.
- **Internal leaks**: Volumes of air separated from the chamber by little tubes (like screw holes) are difficult to be extracted by pumping or a clean gas flow.
- **Vaporization**: The molecules of a gas are absorbed and released from a surface according to its pressure of vapor. This exchange can be favoured by a little increase of temperature.
- **Permeation**: It is the transport of the gas to the interior wall of the chamber followed by the desorption into the volume. It is important if the TPC has many plastic O-rings.

If we exclude real leaks and diffusion, the other processes can be reduced by a continuous flow of clean gas during many hours or by pumping, normally combined with a bake-out of the vessel. As shown in the figure 3.13, the outgassing rate reduces logarithmically by this second method, being in the end limited by the plastic components inside the chamber.

3.4 Avalanche multiplication

The multiplication in a gas detector occurs when the electrons generated by radiation or a particle gain sufficient energy from an accelating electric field to also ionize gas molecules. The resulting secondary electrons can ionize also the medium, generating more electrons and this process can repeat several times. In the end, an avalanche is generated. As the mobility of the electrons is much greater than that of the ions, electrons move fastly at the front of the cloud of

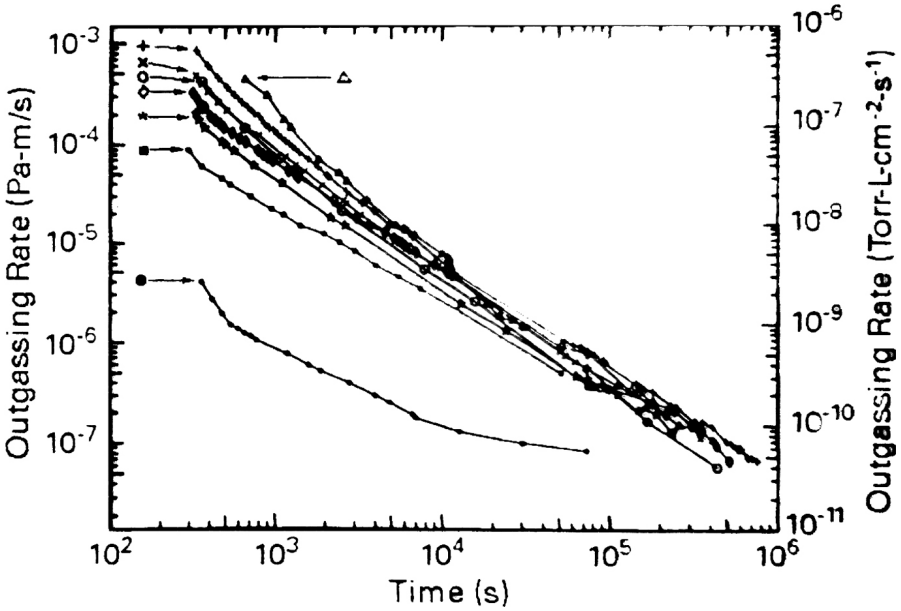

Figure 3.13: Dependence of the outgassing rate with the pumping time for stain steel extracted from [18].

charges, while the new ions move slowly to the back of this cloud. The result of this movement is a drop-like distribution.

The distance that an electron will travel until ionization defines the mean free path for ionization. The inverse of this quantity is the **first Townsend coefficient** α, which represents the number of ion pairs generated per unit length. If at some point there are n electrons, after they drift for a path dx,

$$dn = n\ \alpha\ dx \tag{3.43}$$

new electrons will have been produced. The total number of electrons created in a path from x_1 to x_2 is

$$n = n_0 \exp\left(\int_{x_1}^{x_2} \alpha(x)dx\right) \tag{3.44}$$

The multiplication factor or gas gain (G) is then given by

$$G = \frac{n}{n_0} = \exp\left(\int_{x_1}^{x_2} \alpha(x)dx\right) \tag{3.45}$$

The multiplication factor cannot be increased without limit as a spark breakdown will occur. This limit is about $G < 10^8$ and is known as the **Raether limit**. In practice, the gain achieved is less than two orders of magnitude less than this value.

The gas gain is of fundamental importance for gas detectors. The highest gain obtained in a gaseous detector is a key issue for the large number of applications. In particular, a detection of minimum ionzing particles requires a large dynamic range because of the Landau fluctuation of the deposited energy and the emission of heavy ionizing particles. The goal of a good detector is to achieve stable operation before the breakdown.

For this reason, various theoretical models have been developped te calculate α for different gases. A very early one by Rose and Korff [122] neglects the secondary ionization and gives the

following formula

$$\alpha = \frac{1}{\lambda} \exp\left(\frac{-I_e}{E_{amp}\ \lambda}\right) \tag{3.46}$$

where λ is the electron mean free path, E_{amp} is the amplification field and I_e is the threshold energy for ionization.

3.5 Signal generation

The moving charges between electrodes of a chamber are the source of the electric signals induced in the electrodes, which are then amplified by the electronic chain and recorded by the acquisition system. The determination of their amplitudes can be calculated by the Ramo's theorem. This theorem states that the current $i(t)$ induced by a moving charge Q in a particular electrode is expressed by

$$i(t) = Q\ \mathbf{E_{W_i}}\ \mathbf{v}(t) \tag{3.47}$$

where $\mathbf{E_{W_i}}$ is the weighted field, defined as the electric field calculated with the electrode i biased to 1 volt and the rest of the electrodes connected to ground. The units of $\mathbf{E_{W_i}}$ are 1/m.

If we consider an ion-electron pair created in the avalanche near an electrode, the contribution of the electrode to the signal will be a very fast pulse as it drifts very fast compared to the ion. Even if the pulse generated by the ion will be slow, its area will be the same as the one created by the electron, because their charge is the same.

Chapter 4

From the MWPC to the Micromegas technology

Gaseous detectors [123, 124] were born at the beginning of the twentieth century with the invention of the single wire proportional counter [125] and the Geiger-Müller counter [126]. They can be considered the ancestors of all modern gas detectors and were for decades a major tool for the study of ionzing radiation. However, they were not capable to determine particle trajectories. Until 1968, all tracking devices were optical in nature: photographic emulsions, the cloud chamber, the bubble chamber, the spark chamber, etc. All these detectors required the recording of the track information of film which was then analyzed frame by frame. Therefore, a full-electronic device was greatly desired as it would allow more events to be treated accurately.

The breakthrough occurred in 1968 with the invention of the Multi Wire Proportional Chamber (MWPC) by G. Charpak [127]. He showed that an array of many closely spaced anode wires in the same chamber could each act as independent proportional counters. Moreover, with transitorized electronics, each wire could have its own amplifier integrated onto the chamber frame to make a practical detector for position sensing. Due to its excellent position accuracy and rate capability, the MWPC was quickly adopted in particle and high energy physics and stimulated a new generation of detectors: drift and time chambers and the Time Projection Chamber [128].

However, a MWPC has two fundamental limitations on space resolution and rate capability. Wires cannot be placed closer due to mechanichal problems and ions cannot be evacuated fast enough. In order to deal with this problem, A. Oed invented in 1986 the Micro-Strip Gas Chamber (MSGC) [129], which was the first of a new kind of detectors known as micropattern detectors. All of them take advantage of the improvement of microelectronics and the development of photolithography. These techniques allow the imprinting of very thin strips on an isolating board, in a succession of anodes and cathodes, closer than the wires of a MWPC. Moreover, due to the shape of the electric field, the ions produced by the avalanche are rapidly evacuated, which increases the counting capacity.

Another micropattern detector, the micromegas [14] was introduced by this time and since then, has been used in several experiments. This chapter serves as an introduction to this technology, studying first its predecesors and motivating its main features.

4.1 The Multiwire Proportional Chamber

A basic Multi Wire Proportional Chamber (MWPC) consists of a plane of equally spaced anode-wires centered between two cathode planes, as shown in figure 4.1 (left). The typical wire spacing

is 2 mm and the anode-cathode gap width is about 7 or 8 mm. If a negative voltage is applied to the planes, an electric field configuration as shown in figure 4.1 (right) arises. The field lines are essentially parallel except for the region very close the anode wires.

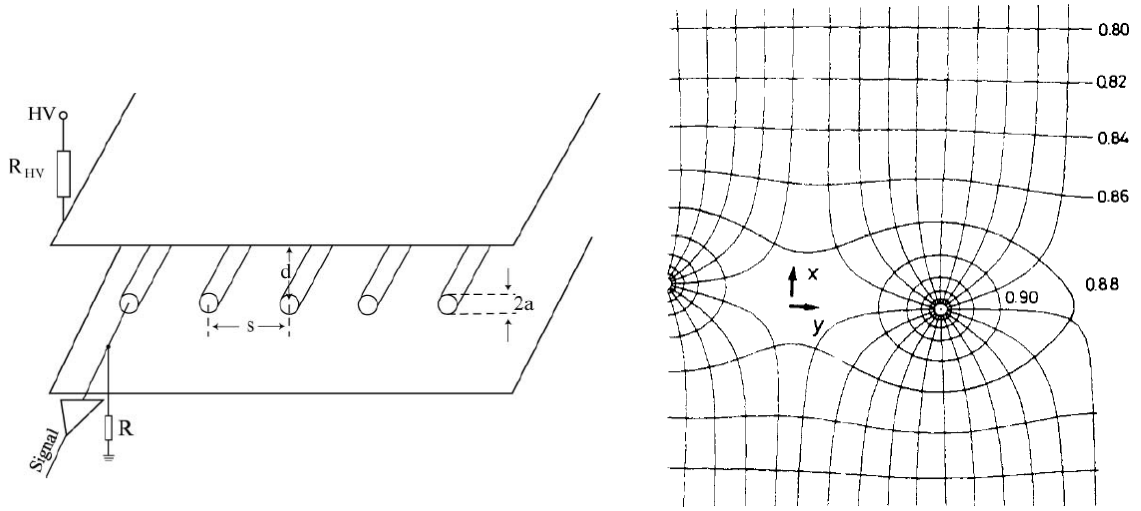

Figure 4.1: Basic sketch and field configuration of a MWPC extracted from [130].

If we assume an infinite mode plane with zero diameter wires and a voltage V_0 on the wires, the electric field is given by

$$E(x,y) = \frac{CV_0}{2\epsilon_0 p}\left(1+\tan^2\left(\frac{\pi x}{p}\right)\tan^2\left(\frac{\pi y}{p}\right)\right)^{1/2}\left(\tan^2\left(\frac{\pi x}{p}\right)+\tan^2\left(\frac{\pi y}{p}\right)\right)^{-1/2} \tag{4.1}$$

where the capacity per unit length C is equal to

$$C = \frac{2\pi\epsilon}{\pi h/p - ln(2\pi a/p)} \tag{4.2}$$

When a particle creates an ion-pair in the drift region, the electron and the ion respectively drift to the nearest anode and cathode. Near the anode wires the field takes on a $1/r$ dependence, which quickly accelerates electrons and produces an avalanche. The positive ions liberated in the multiplication process also induce a negative signal on the anode wire. Meanwhile, the neighbouring wires are also affected but signals induced are positive and of small amplitude. This fact allows the determination of the wire closest to the ionizing event. The spatial resolution of a MWPC is $p/\sqrt{12}$ where p is the wire pitch [100].

The signal from one anode plane only gives information on one coordinate of the ionizing event. The second coordinate can be obtained by using a second detector whose anode wires are oriented perpendicularly to the first. Usually both detectors are integrated in the same chamber to form an X-Y MWPC.

4.2 The Drift Chamber

The drift chamber has a design similar to that of a MWPC. Its main goal is to measure the distance drifted by primary electrons produced by a particle traversing the detector volume perpendicular to the wire planes. This measurement requires the time of passage of the particle

(t_1), the arrival time to the anode (t_2) and a relation between the distance d and the drift time, which is just $\Delta t = t_2 - t_1$. This relation is fulfilled if the drift velocity is constant over the drift volume. Note that this is not the case of MWPCs where the electric field around the wires varies. Technically, the field homogeneity can be improved if field shaping wires are placed in between anode wires. The gas mixture can also be chosen for a minimum dependence of the drift velocity on field variations.

The spatial resolution of drift chambers depends mainly on the arrival time measurement precision, the electron longitudinal and transversal diffusion in the gas and the homogeneity of the field. An overview of these detectors can be found in [131].

4.3 The Time Projection Chamber

The Time Projection Chamber (or TPC) [128] combines the two-dimensional information of a MWPC and the third dimension measurement of a drift chamber. The original design was a cylindrical chamber with a cylindrical field cage and a thin electrode in the middle. In this way a uniform electric field along the axis is created with opposite directions in the two regions. The cylinder is closed with two endcaps, segmented into sectors of proportional anodes in between cathode pads. A sketch of this TPC is shown in figure 4.2. The actual designs are various but keep the phylosophy of creating a uniform field.

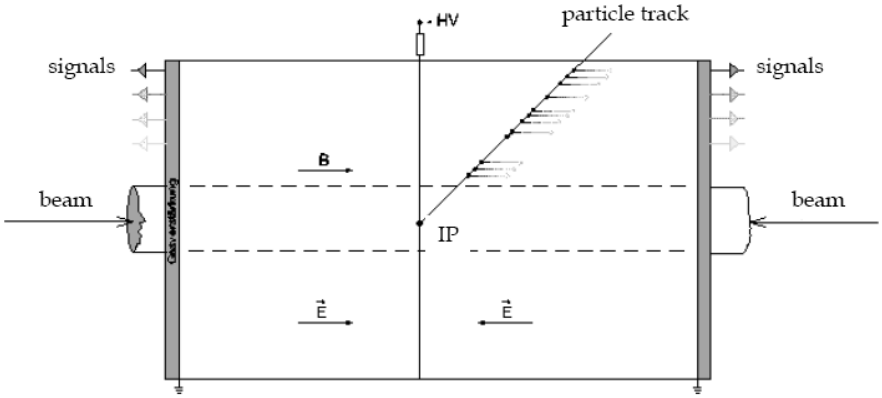

Figure 4.2: Layout of a Time Projection Chamber (TPC).

The operating principle is simple. Electrons freed by a particle drift along the field towards a pad plane. When approaching the anode wire plane, the electrons enter a high field region where they are multiplied. Some of the ions produced in the avalanche drift in the direction of the pads on which signals are picked up. Hence, a pattern of hits is recorded and a two-dimensional projection of the track onto the pad plane is obtained. Due to the uniform field in the drift region, the electron drift velocity is constant and the third coordinate of the hits is determined from the arrival time of the signals at the pads.

If the drift distance is of the order of several tens of centimeters or event meters, diffusion can be a problem, particularly in the lateral direction. This is remedied by a parallel magnetic field, which confines electrons to helical trajectories about the drift direction. In this way, the diffusion is reduced as much as a factor of 10. This solution requires a perfect alignment of electric and magnetic fields.

Some ions produced in the avalanches can drift back towards the central cathode and enter the drift region. This effect is called the **ion backflow** and if it is large enough, the drift field

can be disturbed. This is prevented by placing a grid at ground potential just before the anode wires, to capture there positive ions. The grid also serves to separate the drift region from the avalanche zone and allows an independent control of each.

4.4 Micro Pattern Gas Detectors

The first attempt to replace wires by micro-pattern structures was conducted by Oed in 1986 [129] with the Micro Strip Gas Counter (MSGC). It consists in printing metal strips onto a flat glass plate above which is placed a drift plane. The strip configuration consists in alternate anode and cathode strips separated about 50-100 μm, as shown in figure 4.3. With an appropiate voltage on the anodes, a uniform drift field of a few hundred V/cm is generated in the region from the drift plane down to a short distance from the strip plane. The resulting field gradient focuses the primary electrons towards the anode strips, where the avalanche takes place due to the increase of the electric field up to several tens of kV/cm.

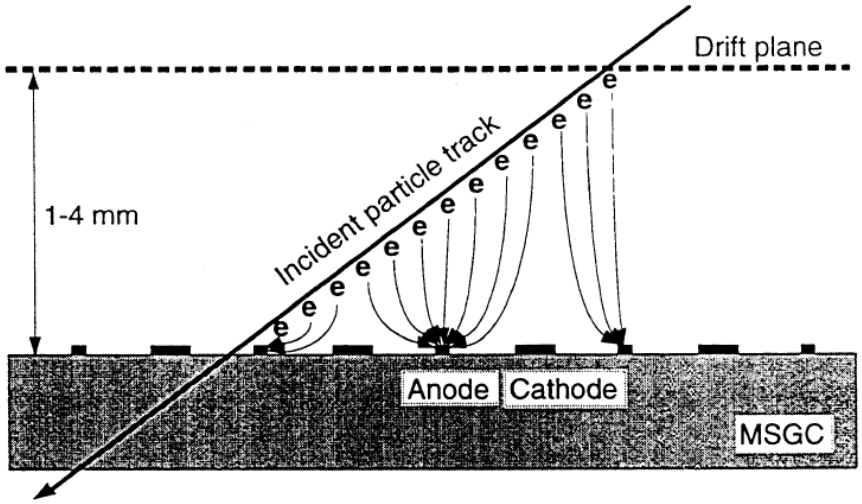

Figure 4.3: Sketch of a Micro-Strip Gas Chamber (MSGC).

Gains as high as 10^4 are obtained with this detector in argon-based mixtures. Moreover, due to the electric field configuration, ions are rapidly evacuated (50-100 ns) which allows the operation of the chamber at counting rates as high as 10^6 counts mm^{-2} s^{-1} [132]. This is a factor 100 greater than for the MWPC. Moreover, the traversing particle position is determined with a spatial resolution as good as 30 μm [133]. Finally, the precise control of the electrode dimensions provides a good gain uniformity across the strip plate and better energy resolution.

The MSGC was planned to be used in major experiments for the new high-luminosity colliders [134]. However, it appeared to be affected by aging and discharge damages. The first problem was solved with a proper choice of construction material and operating gases [135] but the second was an unavoidable consequence of high gains. During the amplification, some electrons can reach the insulating substrate, which will progressively get charged. As a consequence, very high fields can be generated at the substrate surface, increasing the discharge probability. In one of these discharges (also called **sparks**), the thin electrodes could melt, precluding the operation of the detector [136]. For more details on the performance and limitations of MSGCs, the reader is referred to [124, 134].

4.4.1 The Gas Electron Multiplier

The Gas Electron Multiplier (GEM) was introduced in 1996 by Sauli [137]. It consists of a conversion and a transfer gas volumes, separated by a composite layer acting as amplifier. This one is a polymer foil, metal-clad on both sides and etched with a regular matrix of holes, as shown in figure 4.4 (left). A typical detector has hole pitches of 100 μm, metal and insulator layer thickness of 5-10 μm and 50 μm respectively.

A suitable difference of potential applied across the thin layer generates the field structure shown in figure 4.4 (right). When approaching the hole along its axis, the field lines compress due to the increase of field and de-focus at the exit of the hole. Electrons released in the upper conversion volume drift into the holes. There they are multiplied due to the high field inside the holes but only 50 % of the avalanche electrons can exit into the transfer region.

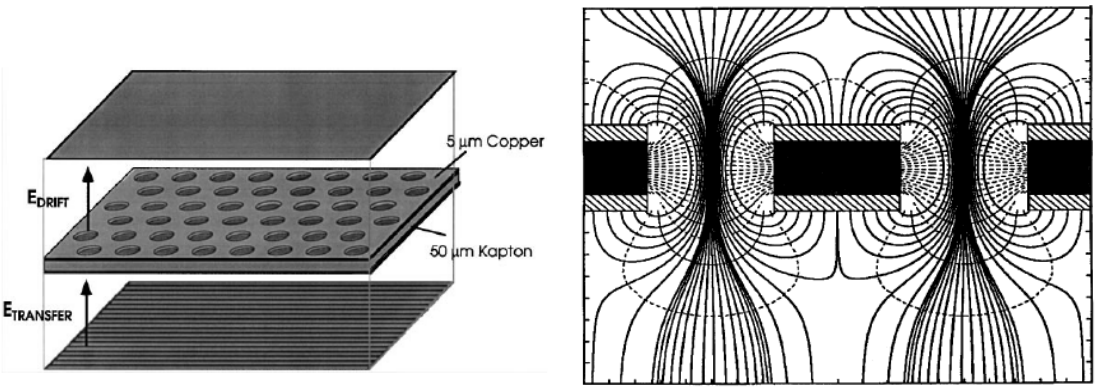

Figure 4.4: Sketch of a GEM detector (left) and its electric field structure (right), extracted from [123].

As the multiplication and the readout functions are separated, spark problems are eliminated. However, GEM detectors have a not very high gain (about several hundreds), which makes necessary the use of a second element of amplification. For example, values higher than 10^4 can be obtained with a double or a triple GEM. In these composed detectors, due to the electron transverse diffusion in between the GEMs and between the bottom GEM and the readout plane, the electron charge distribution is broad. With a readout plane segmented in pads of a few milimeters width, an electron avalanche induces signals on several pads. This effect is used to accurately measure the track cluster position by the centre-of-gravity method in GEM-based TPCs.

GEM detectors have been used in the inner tracker of HERA-B in combination with MSGCs [138] and more recently in COMPASS [139]. At the Large Hadron Collider (LHC), they are part of the LHCb muon system [140] and used for triggering and tracking purposes in the TOTEM experiment [141]. They are also foreseen as UV-photon detectors for an upgrade of the PHENIX detector at the Relativistic Heavy Ion Collider in Brookhaven [142].

4.5 Micromegas: A Micro-Pattern Gas Chamber detector

The micromegas (for MICRO MEsh GAseous Structure) is a parallel-plate detector invented by I. Giomataris in 1995 [14]. It consists of a thin metallic grid and an anode plane, separated by a very little gap (between 20 and 100 μm) by insullated pillars. Inside a TPC, the mesh and the cathode plane define the conversion space (or drift region). It stretches from some mm up

to several meters. The mesh and the anode plane define the amplification gap. A sketch with the operating principle is shown in figure 4.5.

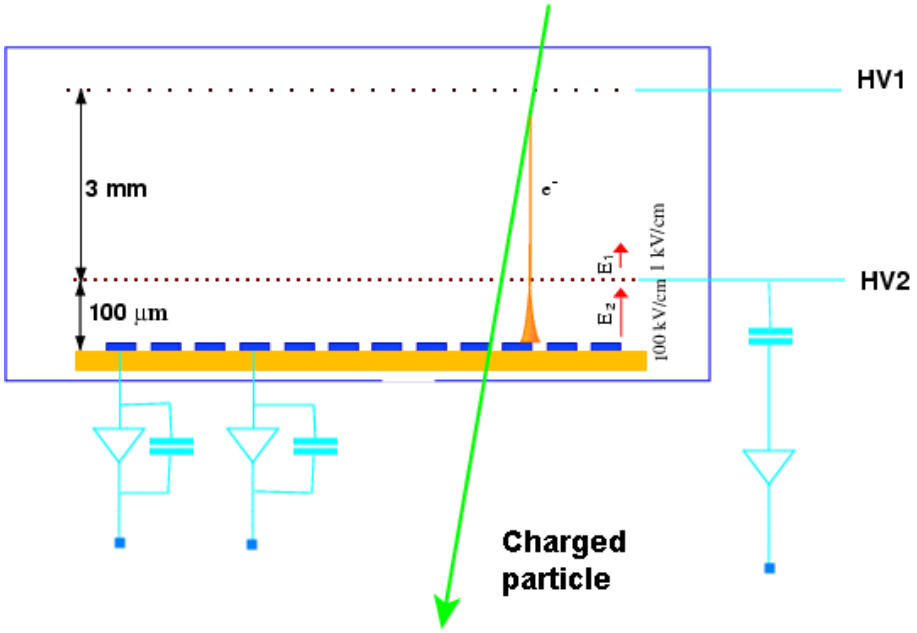

Figure 4.5: A schematic view of a micromegas detector. In the conversion gap, delimited by the cathode and the mesh, the particles ionize the gas. In the conversion gap, defined by the mesh and the anodes, the amplification of the charge is produced [15].

The operation principle is just like the one of a TPC. By applying voltages in the three electrodes, this configuration allows the user to obtain a very high electric field in the amplification region (of about 100 kV/cm) and a quite low one in the drift region (up to 1 kV/cm), as shown in figure 4.6. The electrons freed in the conversion volume drift to the detector. There they cross the mesh by its holes and each electron produces an avalanche due to the high field in the amplification region. The generated ions are collected on the grid and the electrons on the anodes.

The high ratio and the shape of the fields (shown in figure 4.6) have two advantages in the operation:

- A good electron transmission from the conversion space to the amplification gap; the bigger the ratio the higher the electron transmission is.
- A quick collection at the grid of the ion cloud generated in the amplification gap. In this way, local modifications of the amplification field, which may cause a drop of the gain, are avoided.

The micromegas technology is being applied in several physics experiments. For instance, as a kaon beam spectrometer in KABES [143] and as an x-ray detector in CAST for axion search [144, 145]. In the COMPASS fixed target experiment at CERN, twelve 40×40 cm^2 Micromegas chambers are part of the tracking system [146]. The application in the three TPCs of the near neutrino detector for the T2K experiment is reported in [147].

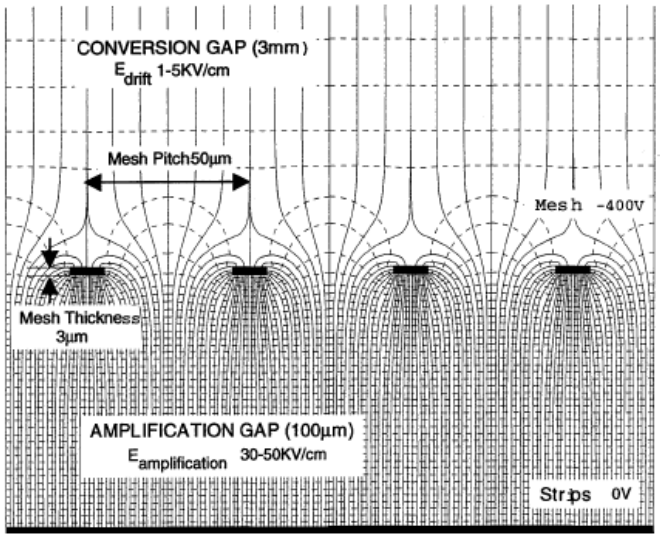

Figure 4.6: A sketch of the field lines in a micromegas detector.

4.5.1 Micromegas properties

In this subsection, the main characteristics of Micromegas detectors are described. We focus on the gain, transparency and energy resolution because they will be studied in chapters 5 and 6.

Gain

The micromegas gain is a simple application of the theory described in section 3.4. If the amplification field is supposed constant in the gap and the Rose and Korff model is used, the substitution of equation 3.46 in 3.45 leads to

$$ln(G) = \frac{d}{\lambda} \exp\left(\frac{-I_e\ d}{\lambda\ V_{amp}}\right) \tag{4.3}$$

where V_{amp} is the applied voltage. Under constant pressure, when d increases, the gain increases up to a maximum and then decreases for higher values of d. The maximum is obtained by differentiation of the equation, resulting in

$$\frac{\delta G}{G} = \alpha\ d\left(1 - \frac{d\ I_e}{V_{amp}}\right)\frac{\delta d}{d} \tag{4.4}$$

The maximum value is reached for $d_{max} = V/I_e$. If the amplification gap is chosen in this way, the multiplication factor is maximized. In consequence, fluctuations due to defects of flatness between the mesh and the anode plane are compensated, leading to a steady gain [15, 148].

Micromegas detectors have been tested with a large variety of gas mixtures. Some examples of gain curves are shown in figure 4.7 (right), for argon-isobutane mixtures of 2 % and 5 %; and pure xenon. Mixtures of high Z-gases, such as krypton or xenon, are relevant for many applications in x-ray digital radiography, crystallography and synchrotron radiation studies. Although the gain is low in noble gases, it can be increased with the addition of little quantities of heavy hydrocarbon quenchers with lower ionization potentials [149]. The maximum safe gain

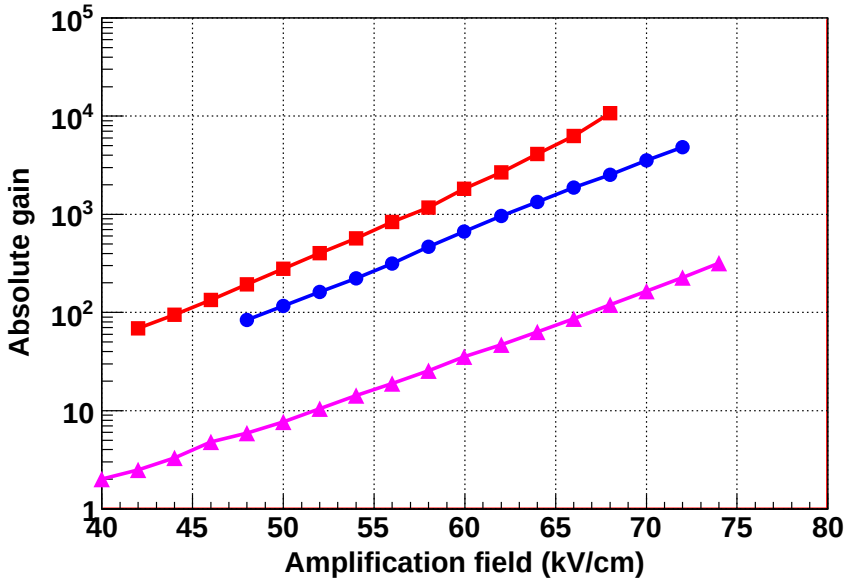

Figure 4.7: Gain curves measured in this work with a micromegas detector for argon-isobutane mixtures of 2 % (red squares) and 5 % (blue circles); and pure xenon (magenta triangles).

is close to 10^5 in argon-isobutane mixtures of 5-10 %, and three times higher with a small amount of cyclohexane.

Adding CF_4 to the previous mixtures improves the time resolution and the total deposited energy [150]. Neon or helium mixtures with hydrocarbons increase the total charge per single avalanche and approaches the Rather values. In a mixture of He + 6 % iC_4H_{10}, a maximum gain about 1.8×10^7 was reached [151]. Such high gain gives the required margin factor when a detector has to cope with very high x-ray environments or at high-pressure operations.

Electron transmission or transparency

As explained in section 3.4, the gain is the ratio between the total number of electrons after the amplification and the number of primary electrons. For a precise measurement, it is thus important that the largest fraction of primary electrons participate in the signal. The proportion of primary electrons produced in the drift region that reaches the amplification region is called **electron transmission** or **transparency** of the mesh and is defined by

$$T = \frac{n_A}{n_D} \tag{4.5}$$

where n_D is the initial number of electrons and n_A the number of those reaching the amplification gap. For practical reasons, this quantity cannot be absolutely measured and as an approximation, signals are normalized to the maximum. This parameter depends mainly on the geometrical dimensions of the detector and the ratio of fields.

For a given amplification field, the transparency at high drift field is lower than 1 because many drift lines end at the mesh. As the drift field decreases, more lines pass through the holes and for a certain value, transparency reaches the unity. For very low field values, the transparency sharply decreases because the drift velocity in gas is very low and attachement effects become more evident.

As an example of this behaviour, two transparency curves for two different grids are shown in figure 4.8. The red squared and the blue circled lines correspond to the left and right photographs of figure 4.9 respectively. Note that the holes in the left figure are bigger than those of the right one. In consequence, field lines have a higher probability to end in the mesh in the second case than in the first. This means that a lower drift field is required for collecting all the charge.

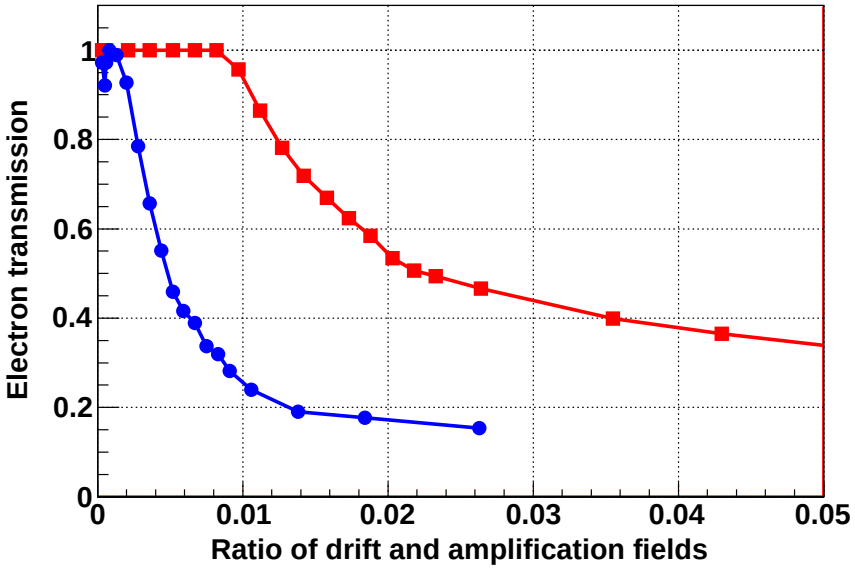

Figure 4.8: Transparency curves of two different micromegas grids, type microbulk (explained in section 4.5.2). The red squared and the blue circled lines correspond respectively to the left and right meshes shown in figure 4.9. The plateau of the first mesh is wider due to its bigger holes (40 μm) than the first one (30 μm).

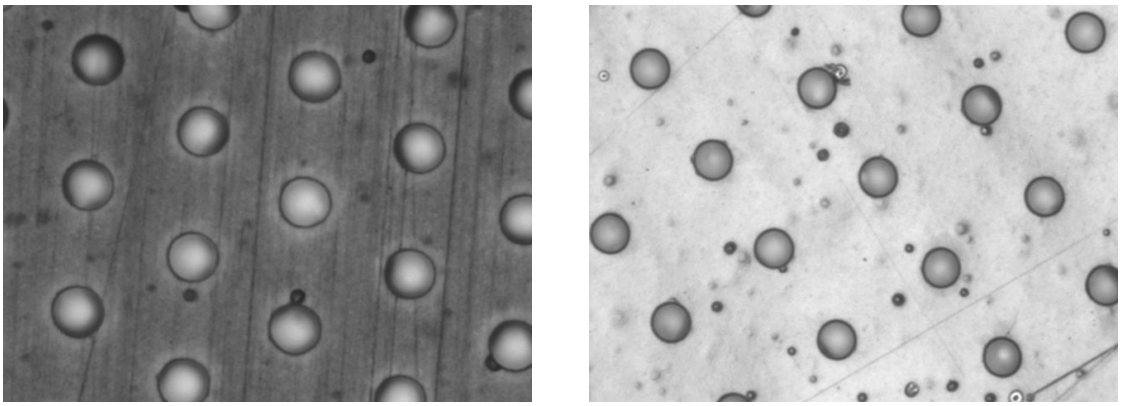

Figure 4.9: Microbulk meshes at the microscope [152]. The hole diameters is respectively 40 μm and 30 μm and the distance between holes is 100 μm. Note the different hole pattern of each grid: hexagonal and squared respectively.

In principle, the ratio of drift/amplification fields at which the mesh stops being transparent is defined by the geometry. However, a dependence of this ratio with the type of gas was observed for the micromegas detector InGrid F11 in [106]. The ratio of fields increased to higher values of the fields ratio when the quencher concentration was increased. This fact is explained by a

reduction of the electron diffusion coefficients with the quantity of quencher.

Energy resolution

The energy resolution is the variation of the signal generated in a detector by particles of the same nature and energy. Ideally, signals should be the same but in practice, the energy measurement involves several processes like gas ionization, electron drift and multiplication, signal readout, etc. They all contribute to the pulse height distribution. Some sources can be optimized, like those due to attachment and the mesh transparency.

Assuming primary and avalanche fluctuations only, it can be expressed directly from the distribution of the number of electrons N_e by

$$R(\%\ \text{FWHM}) = \frac{2.35\ \sigma_{N_e}}{N_e} = 2.35\sqrt{\frac{F+b}{N_b}} = 2.35\sqrt{\frac{W}{E_0}(F+b)} \tag{4.6}$$

where E_0 is the energy of the particle, W is the mean energy per electron-ion pair of the gas, F is the Fano factor and b is the readout contribution.

The energy resolution of a specific micromegas detector is usually measured using an iron source ^{55}Fe. This isotope emits two gammas of respectively 5.9 and 6.5 keV in a proportion 9:1. This ratio can be slightly different due to the energy dependence of the absoption coefficients in the materials that photons cross [106]. The best value obtained in the fit at 5.9 keV is the one normally mentioned in the literature.

The energy resolution has two clear dependences with the amplification field and the ratio of drift and amplication fields, respectively shown at left and right plots of figure 4.10. It remains stable at the maximum electron transmission and it degrades as the electron transmission reduces. Regarding its dependence with the gain, the energy resolution worsens at the extremities: at low gain because the signal amplitude is comparable to the noise level; at high gain due to the proximity to the spark limit.

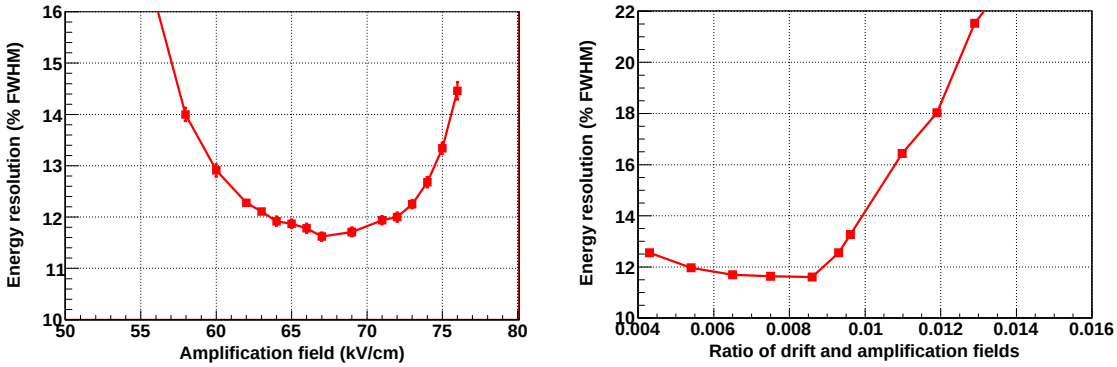

Figure 4.10: Dependence of the energy resolution (% FWHM) with the amplification field (left) and the drift/amplification fields ratio (right) for a micromegas detector type microbulk measured in this work Ar + 5 % iC_4H_{10} at 1 bar. The energy resolution worsens at low gains because the signal amplitude is comparable to the noise level; and at high gain due to the proximity to the spark limit. Regarding the dependence with the transparecy, it remains stable at the maximum electron transmission.

For an argon-isobutane mixture 90/10, a value of 11.7 % FWHM at 5.9 keV and another one of 5.4 % at 22 keV (generated by a ^{109}Cd source and shown in figure 4.11 (left)) were published in [153]. The first value has been improved to 11.0 % FWHM for the most modern detectors [1].

Measurements with other particles, energies, mixtures and pressures are rare. In fact, this is one of the objectives of this work, described in chapters 5 and 6. Other studies along this time are described in [154, 155]. In the first study, a degradation of the energy resolution with pressure was observed in CF_4, as shown in figure 4.11 (right).

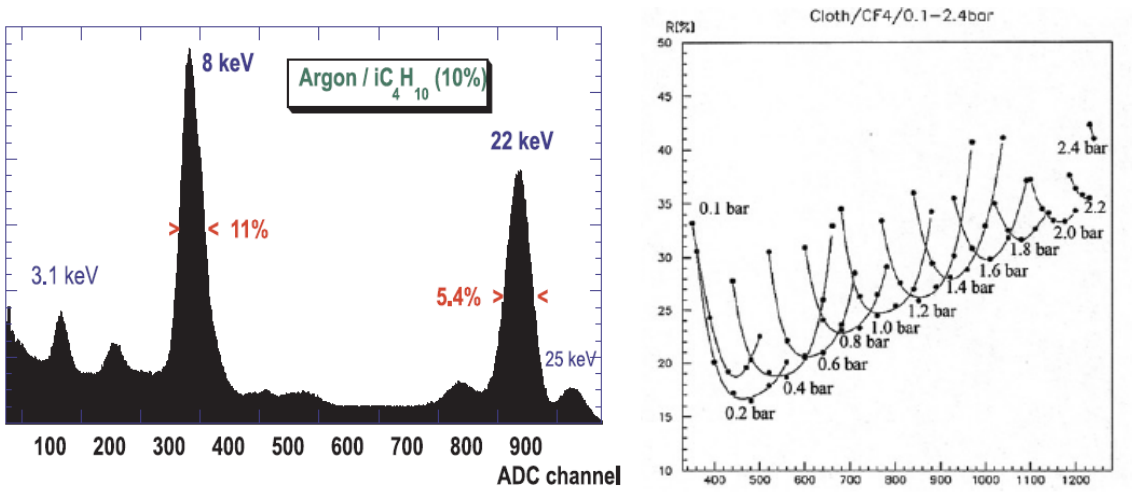

Figure 4.11: Left: Energy spectrum of a micromegas detector obtained with a ^{109}Cd source [153]. Right: Dependence of the energy resolution of a micromegas detector (type bulk, explained in section 4.5.2) at 5.9 keV with the mesh voltage in CF_4 for gas pressures between 0.1 and 2.4 bar [154]. It is clear the degradation of the energy resolution with the increase of pressure.

Other features

The micromegas detectors show other characteristics, which are important in many applications:

1. They are stable during long periods of operation [2].
2. The time resolution of these detectors can be less than 0.60 ns. This value has been measured by the KABES experiment [143].
3. The space resolution of micromegas detectors is in most cases only limited by diffusion. Detectors with a strip pitch of 100 μm showed a spatial resolution of 11 μm, obtained in CF_4 + 20 % iC_4H_{10} [156].
4. Because of the small size of the amplification gap, electrons and ions produced in the gap are collected in 1 ns and 30-100 ns respectively. This allows the operation of the detector up to very high rates. As an example, no drop of the gain was observed at proton fluxes of 2×10^9 counts mm^{-2} s^{-1} [157].
5. In a high-intensity hadron beam, the sparking probability has been measured in 5×10^{-9} per incident proton at gains around 10^4 in a mixture of Ne + 5 % iC_4H_{10} [158].

4.5.2 Fabrication

The construction of micromegas detectors has changed since their birth. The first prototypes [14] were composed of two frames, to which the mesh and the anode plane were glued. The first meshes were made of nickel using electroforming techniques and the anode plane contained anode strips of gold-coated copper, fabricated by metal deposition techniques. Insulating pillars

were printed on top of the anode plane by conventional lithography of a photoresistive film. The two frames were then screwed together. By applying a voltage on the two sides, the intense electric field pulled down the mesh, and the flatness was thus defined by the height of the pillars, which had an accuracy of better than 10 μm. The good flatness and parallelism between the anode and the mesh was obtained only if the delicate operation of screwing was successful.

The specific dimensions of each detector changed depending on the application. As a reference, the first detector had a grid of 3 μm thickness with 17 μm openings every 25 μm. The anode strips had a thickness of 5 μm and a pitch of 200 μm.

Another type of mesh, based on etching techniques, was later developed for micromegas detectors [153]. The raw material was a double-sided kapton foil, 50 μm thick streched on a frame. A solid photoresist of 15 μm thickness was then applied on both sides. In the third step, two lithograpic masks were applied at both kapton sides: one mask for the holes pattern and the other one for the pillar pattern. Copper and kapton were finally removed providing the final mesh and pillars. The accuracy of the photolithography technique allowed to make opening holes of 25 μm diameter and a pitch of 50 μm.

In order to avoid the delicate operation of screwing the anode and mesh frames, two different technologies (called bulk and microbulk) have been developed so that the readout plane and the mesh formed a single piece.

The bulk technology

In the bulk technology [159] the usual electroformed micromesh is replaced by a woven wire mesh. This kind of grids is inexpensive, robust to stretching and handling and is available commercially in large surfaces (2×40 m^2) and different materials (Fe, Cu, Ti, Ni and Au). Its thickness varies from 30 μm to 80 μm.

This mesh, the anode plane carrying the copper strips and a photoresistive film having the right thickness of the gap are then laminated together at a high temperature forming a single object. The photoresistive material is subsequently etched by a photolithographic method, producing the pillars. The pillars have a cylindrical shape of 300 μm diameter and are printed with a distance of 2 mm. The fabrication process is sketched in figure 4.12.

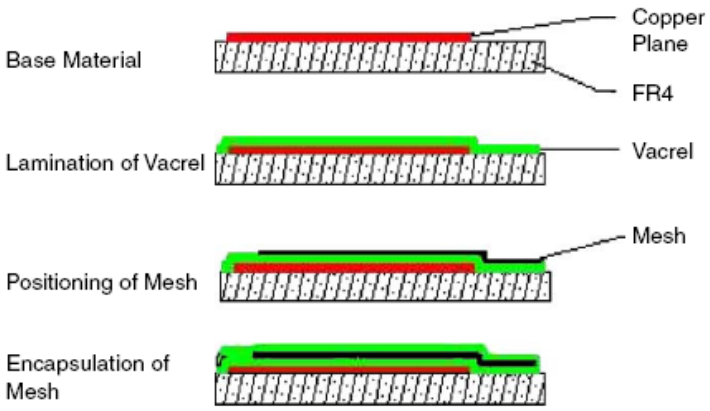

Figure 4.12: Fabrication process of the bulk micromegas detector [159], described in the text.

The bulk detectors have several advantages. They are robust, easy to construct and their mesh is quite uniform. They have also an acceptable energy resolution (18 % FWHM at 5.9 keV

limited by the mesh thickness), a good maximal gain before break down (2×10^4 in Ar + 5 % iC_4H_{10}) and a low noise due to lower capacity. However, low energy signals have a higher risetime (60 ns for a 75 μm gap and 150 ns for a 150 μm one) and detectors may be more sensitive to pressure variations [159].

The microbulk technology

A novel fabrication technique using kapton thin-foil etching technology has been recently applied to the fabrication of micromegas detectors, called **microbulk** [16, 160]. The manufacturing process uses a thin flexible polyimide foil with double side thin copper layer. The foil is glued on top of a rigid substrate that provides the support of the micro-structure and most of the time carries anode strips or pixels. In some applications demanding low detector material the foil is stretched and glued on a suitable frame.

The photoresistive film is laminated on top of the kapton foil and is insulated by UV light to produce the required mask. The copper is then removed by a standard lithographic process, producing a pattern of a thin mesh. The first prototypes have holes of 30 μm in diameter and a pitch of 80 μm. The polyimide is then etched and partially removed in order to create tiny pillars in the shadow part of the mesh below the copper mesh.

These detectors have the highest precision in the gap homogenity, which have led to the best energy resolutions among micropattern detectors ever reached. In [1], an energy resolution of 11 % FWHM at 5.9 keV has been obtained in Ar + 5 % iC_4H_{10}. They are also stable at long term runs and are less sensitive to pressure variations. However, they have higher electronic noise due to their higher capacity and are more fragile [2]. Low capacity versions are now being developed.

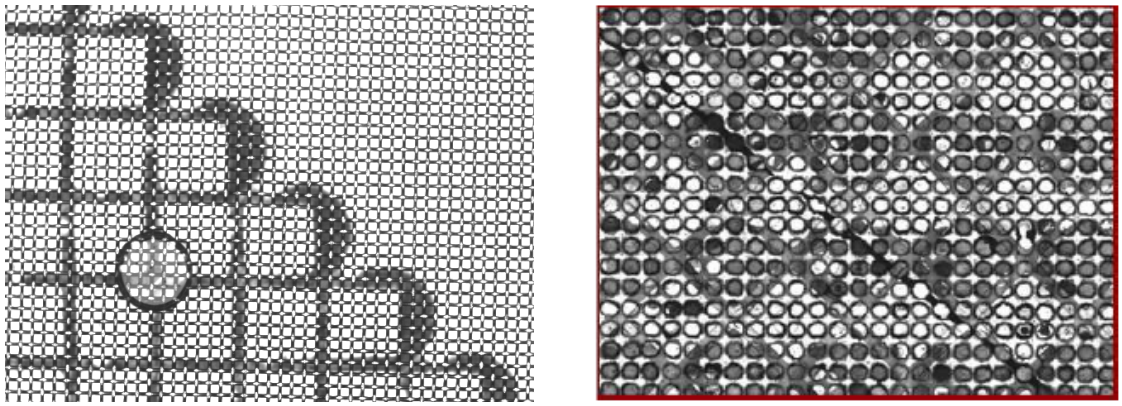

Figure 4.13: Two microscope pictures of a bulk (left) and a microbulk (right) detector extracted from [2]. In both arrangements one can distinguish the 400 μm readout pads. On the left side of the bulk configuration is visible one of the pillars, which maintains the gap between the micromesh and the readout plane, absent in the picture of the microbulk.

Chapter 5

Tests with a Microbulk detector in the Hellaz high pressure TPC

As described in section 4.5.1, the latest generation of microbulk detectors have an energy resolution of 11 % FWHM for the 5.9 keV ^{55}Fe line and in a mixture of Argon + 5 % iC_4H_{10} at 1 bar. Supposing a square root energy dependency of the energy resolution (equation 4.6), this implies a value of 0.54 % FWHM for electrons of 2.480 MeV. If this value were also valid in xenon, the use of micromegas as a calorimeter in a $\beta\beta$ experiment would be possible.

In order to desmonstrate experimentally this estimation, measurements with a high pressure TPC equiped with an alpha source and a Micromegas detector were made during summer 2007 and the whole year 2008. This work has been developped in collaboration with the SEDI departement of the French research center IRFU-CEA/Saclay, in Gif-sur-Yvette (near Paris).

In the first section, the micromegas readout used in the alpha test and its characterization in argon-isobutane mixtures is presented. In the next section, the setup used in alpha measurements is described and in the next two sections, the main results in argon-isobutane mixtures and pure xenon are discussed. A short discussion on the absolute determination of the z-axis position is then carried out. The chapter ends with the conclussions of these tests.

5.1 The microbulk readout

The readout used in alpha measurements is a 3.5 cm diameter circular micromegas detector of 50 microns gap, named **N15**. It has been fabricated by the microbulk manufacturing technique described in section 4.5.2. A view of its mesh at the microscope can be seen in figure 4.9 (left). The particular readout used was tested before and after the measurements with a ^{55}Fe source in Ar + 5 % iC_4H_{10} at 1 bar. It shows an energy resolution of 12.8 % FWHM at 5.9 keV and an absolute gain of 3×10^4 was reached before the spark limit, as shown in figure 6.2. Its transparency curve is similar to the red-squared line of figure 4.8. No appreciable deterioration has been observed during the measurements over more than one year.

Before the alpha measurements, this type of detectors was characterized in argon-isobutane mixtures (isobutane percentage varies between 2 % and 20 %) with a ^{55}Fe source. In these tests, we confirmed that the best energy resolution is reached in a mixture of 5 % in the same gain conditions, as it is shown in figure 5.1 for the particular readout N18.

Finally, a linear dependence between the isobutane percentage and the amplification field necessary to get the same gain was observed. For a gain of ≈ 7950, the fit obtained is

$$E_{amp}(\mathrm{kV/cm}) = 1.17\ iC_4H_{10}(\%) + 62.23 \tag{5.1}$$

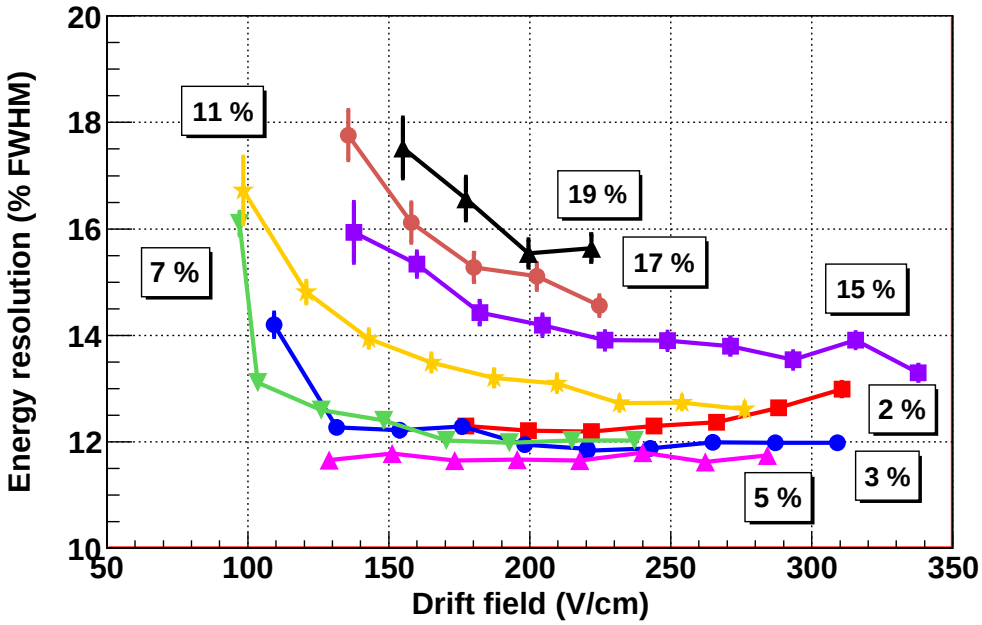

Figure 5.1: Dependence of the energy resolution (% FWHM) at 5.9 keV with the drift field for different argon-isobutane mixtures at the same gain conditions (absolute gain about 1500). Quencher percentages are 2 % (red squares), 3 % (blue circles), 5 % (green triangles), 7 % (inverted magenta triangles), 11 % (orange stars), 15 % (purple squares), 17 % (pink circles) and 19 % (black triangles).

5.2 Setup description

The experimental setup used in these measurements was adapted from the former HELLAZ setup at the IRFU-CEA/Saclay, described in [17]. It consisted of a high pressure TPC, a gas and a vacuum system. All of them have been designed to make research with gas mixtures at high pressures. In the following subsection, each part is described in detail.

5.2.1 The High Pressure TPC

The main element of the setup is the high pressure vessel. It is composed by two 5 cm thick aluminium caps sketched (left) and photographed (right) in figure 5.2, which close with a viton o-ring and leave a 1-liter inner space able to hold gas up to 20 bar. The dimensions of the inner space are 16 cm in diameter and 5 cm of height. The vessel is provided with two high voltage (SHV) and two signal (BNC) feed-throughs for the internal readout setup. There is also a CF40 outlet for pumping, equipped with an all-metal pressure valve. This one is able to keep tight the high pressure vessel even with high vacuum at the other side.

The upper cap consists of a copper cathode used as a drift plate. Attached to it there is an aluminium sourceholder with an americium radioactive source (^{241}Am). The source consists of a metallic circular substrate of 25 mm diameter where the radioactive material has been deposited on its center, in an approximate circular region of about 8 mm diameter. The source is unsealed, i.e., no material is present on top of the americium that could stop the alphas. Its activity induces a counting rate in the detector of 200 Hz. The main alpha emissions of ^{241}Am are 5388.2 keV (2.6 %), 5485.6 keV (84.5 %) and 5442.8 keV (13.0 %). It also emits x-rays and gammas of low energy (less than 60 keV).

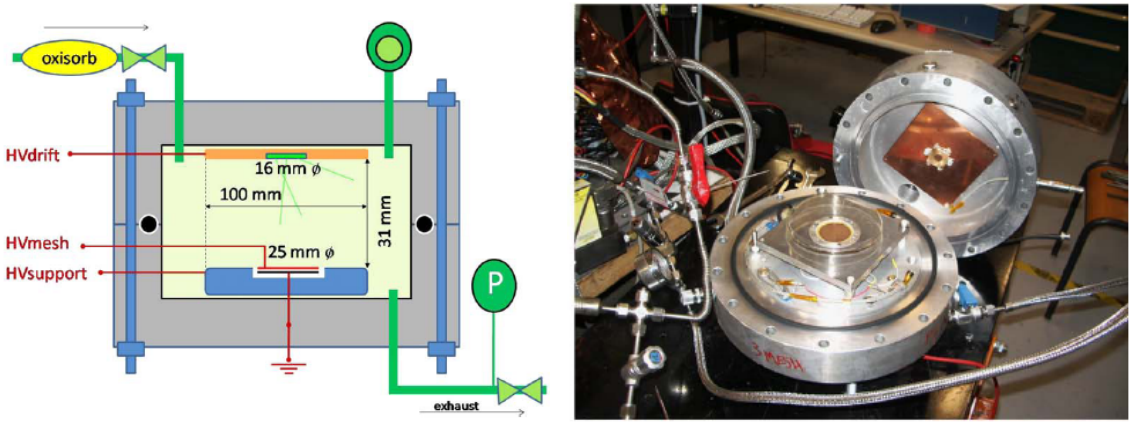

Figure 5.2: On the left, sketch of the setup inside the high pressure vessel, showing the position of the Micromegas readout, the drift cathode and the source. On the right, photograph of the same setup, showing the two vessel end-caps when the TPC is open.

The lower cap consists of a 10×10 cm^2 aluminium plate fixed but electrically isolated from the cap by plastic screws. The micromegas readout is attached to the center of this piece by a metallic ring with a plastic o-ring. This last piece keeps the aluminium plate and the detector electrically isolated. When the TPC is closed, the distance between the source and the readout is 31 mm.

The drift cathode, the Micromegas mesh and the supporting piece are independently powered by a CAEN power supply. The voltages of the last two elements have been usually put to the same value in order to keep straight drift field lines. The signal has been read out from the Micromegas mesh using a CANBERRA 2004 preamplifier, whose output is fed into an ORTEC VT120 amplifier/shaper and subsequently into a multichannel analyzer AMPTEK MCA-8000A for spectra building. Alternatively, the output of the preamplifier was digitized directly by a LeCroy WR6050 oscilloscope and saved into disk for further offline inspection.

5.2.2 The gas and vacuum system

The gas system is composed of a gas mixer, a MESSER oxysorb filter [161] for gas purification, a pressure controller at the vessel's gas output, a recirculation loop and an exhaust line with a bubbler. The vacuum system consists of a vacuum pump (turbomolecular during summer 2007 and just primary during 2008) and a pressure gauge. In figure 5.3 an overall sketch of both systems is shown.

The gas mixer consists of three independent gas lines with Bronkhorst mass flow controllers able to work at pressures up to 20 bar. However, the rest of the gas elements limit the maximum work to pressures up to 5 bar. A recirculation line has been built with the intention to clean the gas by passing continuously by the oxysorb filter. However, the available pump (a KNF PMF 1210-86 one) is not leak-tight enough for this purpouse. Its leak rate has been measured to be greater than 10^{-3} mbar l / sec.

5.2.3 Working procedure

The system is cleaned before every measurement either by pumping it (down to pressures below 10^{-5} mbar for the turbomolecular pump and 10^{-3} mbar for the primary one) or by purging it with argon several times. The gas used has been provided by MESSER and has a purity 4.6 or

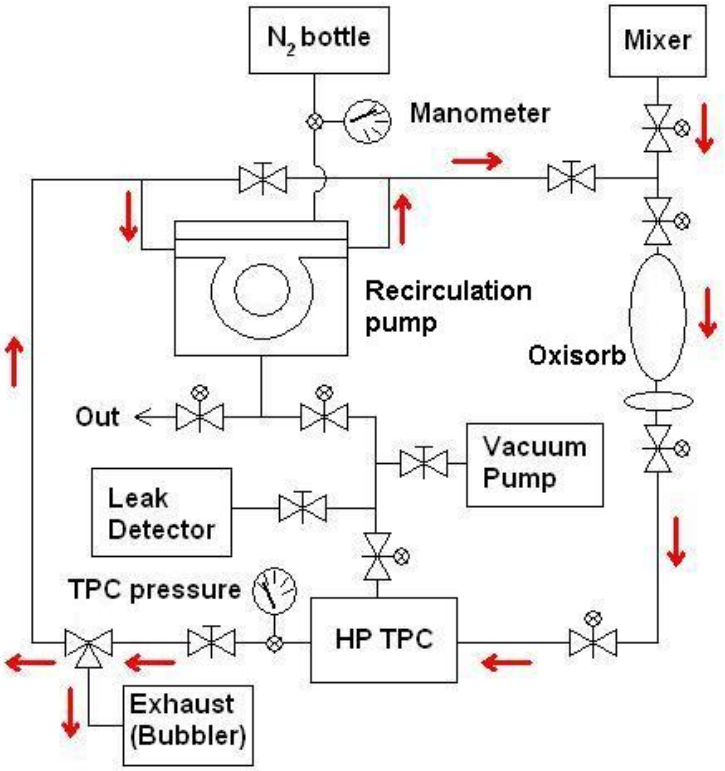

Figure 5.3: Sketch of the vacuum and gas system used in Saclay's measurements.

superior. The final purity is also determined by the leak-tightness of the system, the outgassing of the materials and the effect of the oxysorb filter. It has been proven to be adequate for short-term runs with argon-based mixtures and the drift distance of 3.1 cm. However, evidence of attachment has been found for pure xenon, as explained in section 5.4.

The desired gas is introduced into the vessel using the gas mixer with the appropiate relative flows. During summer 2007, only argon-isobutane mixtures (2 % and 5 % isobutane) were used. During 2008, available gases also included pure argon and xenon. The desired gas pressure has been set via the back-pressure controller. Two operation modes have been used, with no clear difference in result between them:

1. **Open-loop**: the gas flow is directed towards the exhaust line and then to the atmosphere, keeping an input flow of some l/h.

2. **Sealed moded**: the vessel is filled up to the desired pressure and the input and output valves are closed.

For each gas mixture and pressure, the drift and mesh voltages have been systematically changed, registering each position of the 5.5 MeV alpha peak, as well as its width. In argon-isobutane mixtures, the mesh voltage has been typically varied between 200 and 500 V, corresponding to amplification fields between 40 and 100 kV/cm. In pure xenon, the values are a bit higher: voltages between 250 and 650 V and fields between 50 and 130 kV/cm. The specific values for each pressure can be seen in figures 5.5 and 5.10. The drift voltage has been normally changed between 300 V and 4000 V (the limit of the power supply used), corresponding to drift fields between 100 to 1333 V/cm.

5.3 Argon-isobutane mixtures

In these measurements, a turbomolecular pump has been used, reaching vacuum pressures of 10^{-5} mbar. However, no analysis of pulses after the preamplifier has been made as in pure xenon. In the following subsections, the main results are presented.

5.3.1 Electron transparency

The evolution of the peak position with the drift field (for a fixed mesh voltage) gives the electron transparency of the readout. Two examples for 2 % and 5 % isobutane mixtures are shown in figure 5.4. There is a rather flat dependence over a wide range of drift/amplification field ratios (0.002-0.012). Both curves are compatible with the usual ones taken with the ^{55}Fe source at atmospheric pressure (the red squared line of figure 4.8) and shows that no significant attachment is present in the system.

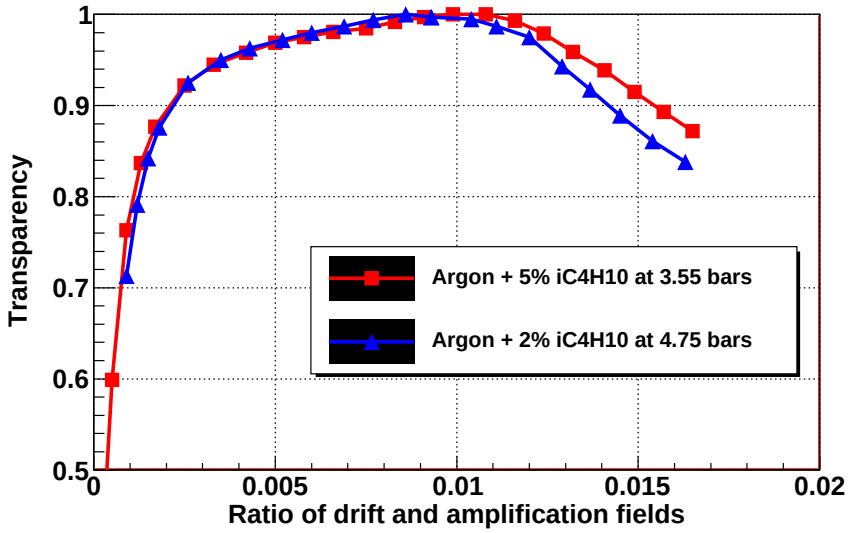

Figure 5.4: Dependence of the alpha peak position with the ratio of drift and amplification fields for two argon-isobutane mixtures. The values are normalized to the maximum of each series.

5.3.2 Absolute gain

The evolution of the peak position with the mesh voltage gives the gain curve. In some cases, the drift voltage has been changed to keep the ratio of fields in the full transmission region. In order to calculate the absolute gain from the position at the MCA spectrum, it is necessary to take into account several factors of the electronic chain.

The first one is the conversion factor of the preamplifier (normally expressed in mV/e$^-$), which depends on the specific model. In this measurements, we have used an ORTEC 142C, with a value of 2.1×10^{-5} mV/e$^-$. The second one is the amplification factor of the amplifier. This parameter depends strongly on both the amplifier and the preamplifier and is normally calibrated measuring alternitavelly the preamplifier pulses and the peak at the MCA spectrum for different gains. Its units are mV/channel.

With these considerations, the absolute gain is expressed by

$$\text{Gain} = \frac{\text{MCA}}{R_{MCA-Amp}\ R_{Pre}} \times \frac{1.0}{E/W} \tag{5.2}$$

where MCA is the peak's channel in the MCA spectrum, $R_{MCA-Amp}$ is the amplifier factor, R_{Pre} is the preamplifier conversion factor and E_α/W is the mean number of charges created by a particle in a specific gas. In an argon-based mixture, an alpha of 5486 keV creates in average 2.086×10^5 electrons.

Gain curves for pressures between 2 and 4 bar in Ar + 5 % iC_4H_{10} are shown in figure 5.5. Note that the higher the pressure is the higher amplification field is needed to get the same gain. Gains greater than approximately 10^3 were reached before the spark limit for all cases.

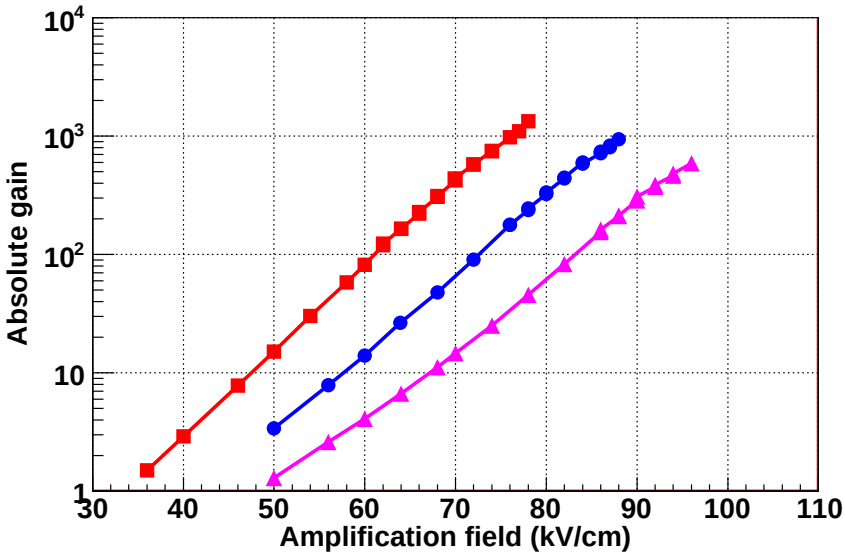

Figure 5.5: Dependence of the absolute gain with the amplification field for Ar + 5 % iC_4H_{10} at 2 bar (red squares), 3 bar (blue circles) and 4 bar (magenta triangles). The highest values are reached just before the spark limit.

5.3.3 Energy resolution

The spectra obtained with the MCA have been fitted to a gaussian function in an offline analysis. A typical example of this fit is shown in figure 5.6. The low energy events present in the spectrum have been attributed to incomplete alpha charge recollection because the noise level is very low (typically 5 channels over 1024).

The energy resolution obtained for the alpha peak shows a characteristic dependency with the drift field, as shown in figure 5.7 (red squared line), clearly correlated with the transparency plot of figure 5.5. The best values have been obtained for larger drift fields inside the transparency plateau, although resolutions around 2 % and 2.3 % (respectively for 2 % and 5 % isobutane mixtures) have been measured for a relatively wide range of values. The best values are respectively 1.8 % and 2 %. No dependence on the integration time of the amplifier has been observed.

Except for very high drift fields, the peak shows a clearly asymmetric shape, as shown in figure 5.8. This shape is not expected from just fundamental fluctuations in the primary

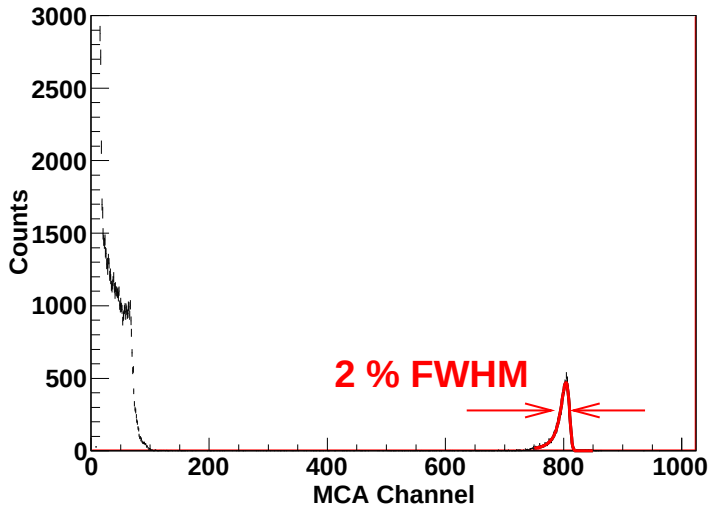

Figure 5.6: A typical spectrum of ^{241}Am measured in Ar + 2 % iC_4H_{10} at 4 bar. The peak on the right has been generated by alphas of the source. The fit of the peak to a gaussian function shows an energy resolution of 2 % FWHM.

or secondary charge and it could be indicative of small external effects related to incomplete charge collection for some events. Examples of this incompletness can be alphas coming from the bulk of the Americium and leaving some energy before exiting, or cases where alpha tracks are in small angle with the cathode plane and part of its ionization is lost back to the cathode. The asymmetry cannot be attributed to attachment, as the voltage configuration for which it is observed is always in the electron transmission plateau.

In the last cases, the amount of charge loss probably follows a Landau distribution. In order to asess this afirmation, each spectrum has been fitted to a negative Landau function convoluted with a Gaussian function. If the external effects are attributed to the Landau function, the Gaussian will have the intrinsic energy resolution of the micromegas readout. The results of this analysis is shown in figure 5.7, and for a specific case in figure 5.8.

This deconvolution analysis points out an intrinsic energy resolution of 0.7 % and 0.9 % FWHM respectively for argon-isobutane mixtures of 2 % and 5 %. "Deconvoluted" resolutions are constant along the electron transmission plateau and get worse for high drift fields because the peak becomes symmetric. It is reasonable to assume that whatever the origins of this asymmetry, they become less important compared with other effects of gain fluctuation at higher field ratios (electron loss in the mesh, larger statistical fluctuations in the avalanche, etc).

Finally, we note that the Landau parameter (shown in figure 5.7) is also constant along the transmission plateau and becomes zero at high drift fields, due to the loss of the peak asymmetry.

5.3.4 Quenching factor

Although the average energy required to ionize is similar for alphas and electrons [162], the effective ionization of an alpha particle of a given energy may be less than that of an electron of the same energy in the same conditions. This can be due to recombination of electron-ion pairs, which is stronger in denser alpha tracks. This effect is dependent on the density of the media and on the applied electric drift field (strong electric fields prevents the recombination). The presence of quenchers could also have some effect.

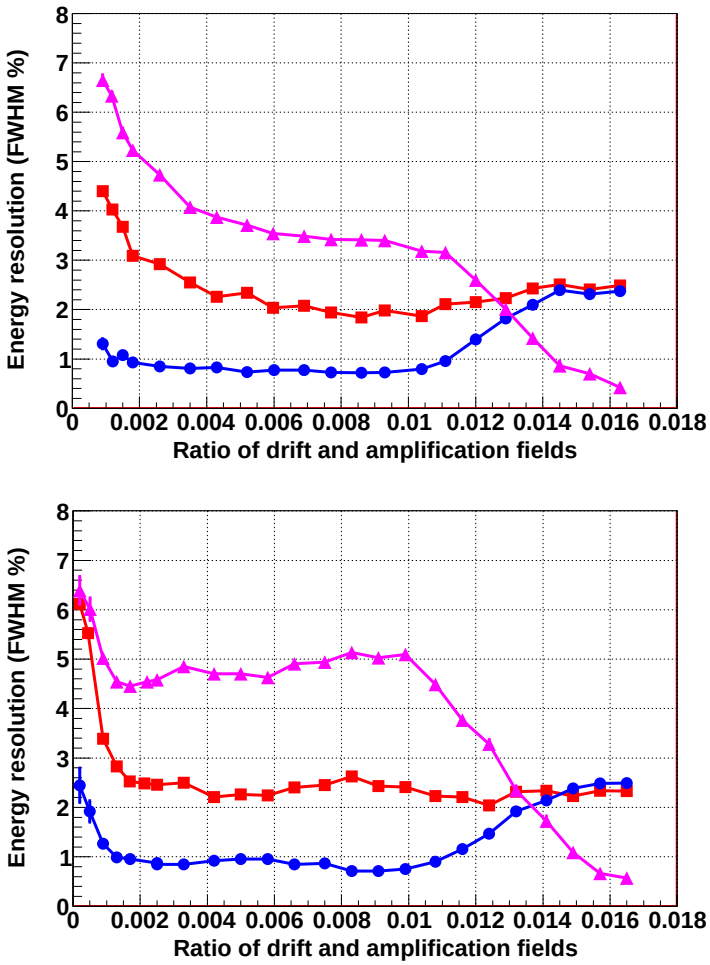

Figure 5.7: Dependence of the energy resolution (% FWHM) with the ratio of drift and amplification fields at 4 bar for 2 % (top figure) and 5 % isobutane (bottom). Red squared lines correspond to the FWHM of the peak obtained by a simple fit to gaussian. Blue circled line correspond to deconvoluted energy resolution obtained by fitting to Gaussian + Landau. Magenta triangled line describes the evolution of Landau parameter obtained in the second fit.

If alphas suffer an appreciable recombination, a correction or **quenching factor** should be applied in order to know which electron-equivalent energy corresponds to the 5.5 MeV alpha peak. This value is difficult to find in literature for gases. One of the reference is the Gothard collaboration, which estimated a value of 6.5 for alphas in pure xenon at 5 bar [13].

In these measurements, it has been tried to observe the alpha peak with the gamma lines of the americium in the same conditions. The source has been collimated in such a way that the intensity of the alpha peak is reduced without contaminating excessively the low energy region and, in this way, observing the x-ray and gamma peaks. For each gas mixture and pressure, the gain of the alpha and the x-ray of 13.9 keV has been determinated. Their comparison is used for determining the quenching factor.

The quenching factor has been measured in Ar + 5 % iC_4H_{10} for 2-4 bar, as shown in table 5.1. We can conclude that the recombination effects are very small in this case. Similar measurements have been performed in argon-metane mixtures (with different amounts of CH_4) with similar reults. More details are given in [5, 1].

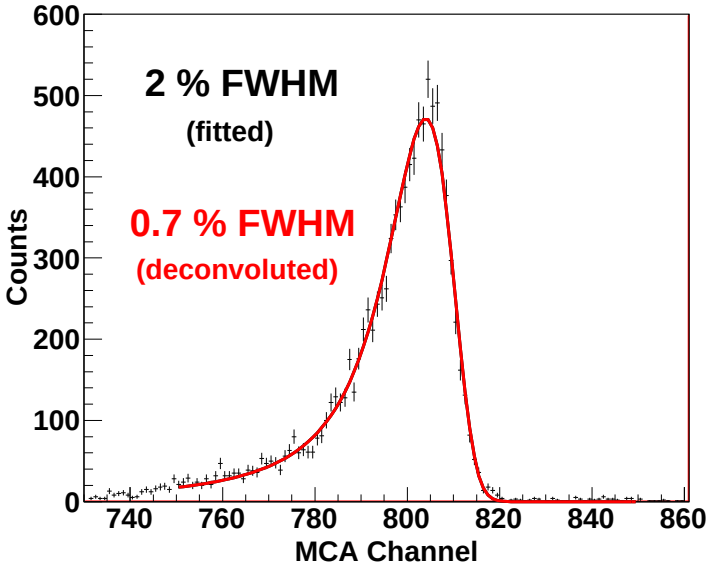

Figure 5.8: Example of an alpha peak measured illustrating the asymmetry observed. The red line and the value for the energy resolution are the results of the fit to a Gaussian + Landau functions, explained in the text.

Pressure (bar)	2.0	3.0	4.0
Quenching factor	0.987 ± 0.006	0.984 ± 0.007	0.966 ± 0.010

Table 5.1: Alpha-electron quenching factors measured for Ar + 5 % iC_4H_{10} at 2, 3 and 4 bar. The error shown represents only one sigma statistical error from the dispersion of the points of the averaged series and is therefore underestimated.

5.4 Pure xenon

In pure xenon measurements, a primary pump has been used due to the non-availibity of the tubomolecular pump. This change has limited the reduction of the outgassing as the minimum pressure reached has been 7×10^{-4} mbar. Nevertheless, this limitation was compensated with the installation of a MESSER oxysorb filter, obtaining the same results in argon-isobutane mixtures as before. Only the gas-sealed mode has been used and gases considered are pure xenon for pressures between 2 and 4 bar and pure argon at 4.5 bar.

As it will be later discussed, the status of this system was not suitable to achieve the required levels of gas purity to work with xenon, and therefore the results achieved were to be considered as preliminary and certainly a conservative upper limit to the energy resolution.

5.4.1 Transparency

In contrast to argon-isobutane mixtures, no plateau in the electron transmission curve has been observed for pure xenon, as shown in figure 5.9. This fact is an evidence of attachment.

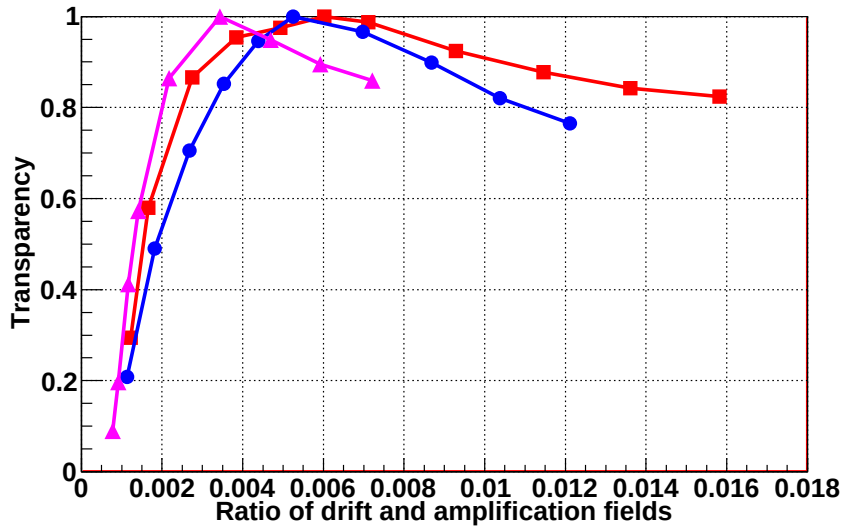

Figure 5.9: Dependence of the electron transmission with the ratio of drift and amplification fields for pure xenon and pressures of 2 (red squares), 3 (blue circles) and 4 bar (magenta triangles). The values are normalized to the maximum of each series.

5.4.2 Gain

As in the argon case, gain curves have been measured at the maximum of the electron transmission, as shown in figure 5.10. It is remarkable that the maximum gain is at least 200 independently of the pressure. This value seems limited by the amount of charge locally generated in the micromegas gap, i.e., by the rate of our alpha source (200 Hz), and not by the intrinsic readout limit. Single runs with the source collimated have shown indeed higher gains.

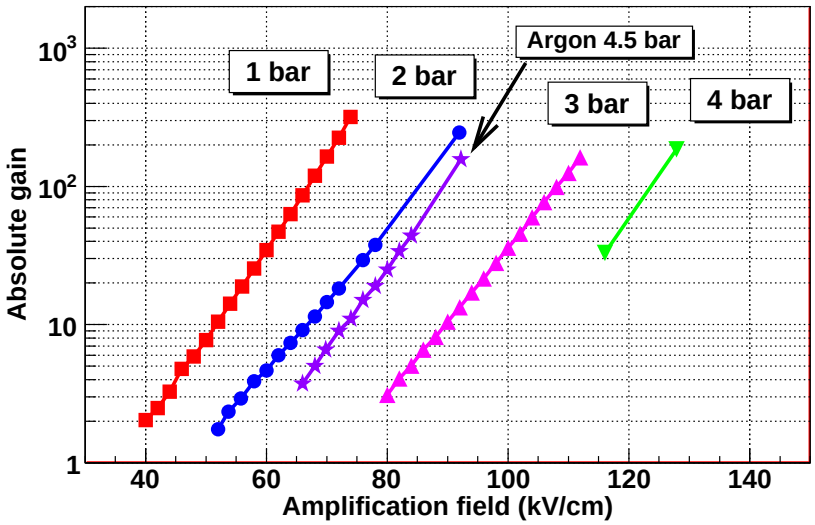

Figure 5.10: Dependence of the absolute gain with the amplification field for pure xenon at 1 (red squares), 2 (blue circles), 3 (magenta triangles) and 4 bar (inverted green triangles; and pure argon at 4.5 bar (violet stars). The highest values are reached just before the spark limit.

We cannot exclude that the same impurities that produce attachment (see later) allow us to obtain larger gains. It is also possible that this particular microbulk geometry is able to reach relatively high gains in pure xenon compared to other amplification geometries. This question needs further study.

5.4.3 Pulse analysis

The output pulses of the preamplifier, which were digitized by an oscilloscope, have been analyzed. In a first step, pulses are smoothed generating for each point the mean value of the nearer 9 points, including itself. The result of this process is shown in figure 5.11. In a second step, the highest and the lowest values are found to determine the amplitude. Finally, the risetime is calculated as the temporal distance between points whose amplitudes are 10 % and 90 % of the amplitude. The calculation of these two variables is graphically shown in the same figure.

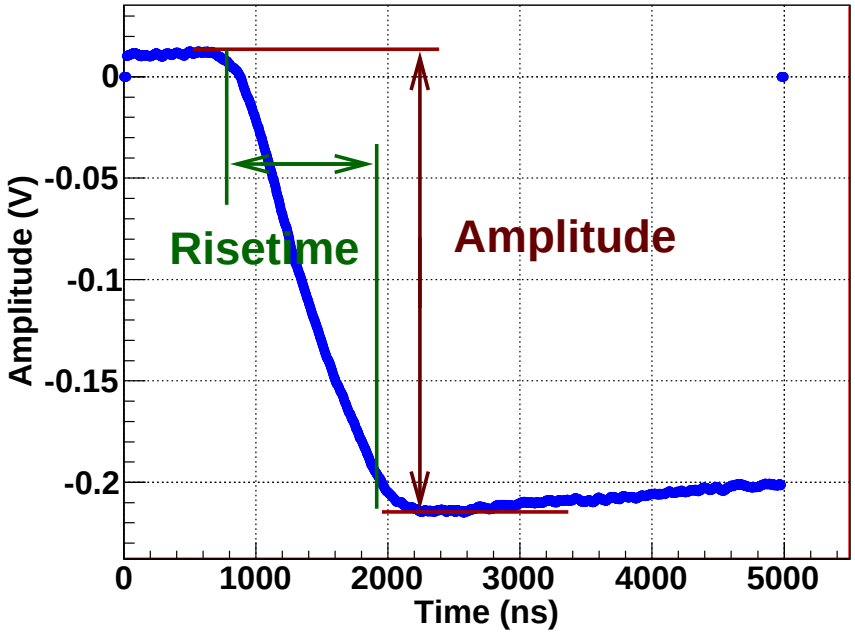

Figure 5.11: An example of a smoothed preamplifier pulse. The determination of the risetime and the amplitude, explained in the text, is graphically shown.

The results of this analysis show a clear correlation between the risetime and the amplitude of the pulse for pure xenon, illustrated in figure 5.12 for different drift fields. Pulses of long risetimes correspond to alpha track orientations close to perpendicular to the readout plane, while pulses of shorter risetimes correspond to tracks closer to parallel to the plane. The fact that the latter have lower amplitudes is an evidence of attachment because their electrons have more probability to be absorbed by impurities.

The linear dependence can be justified by a quantitative argument. We consider an alpha emitted from the source whose initial direction leans an angle θ with the vertical axis, as the one shown in figure 5.13. This particle produces a straight track of electrons with length d, determinated by the initial energy (5.5 MeV) and the gas pressure.

The generated electrons drift to the micromegas readout but they do not arrive all because some of them are absorbed by attachment. If we suppose that attachment has an exponential

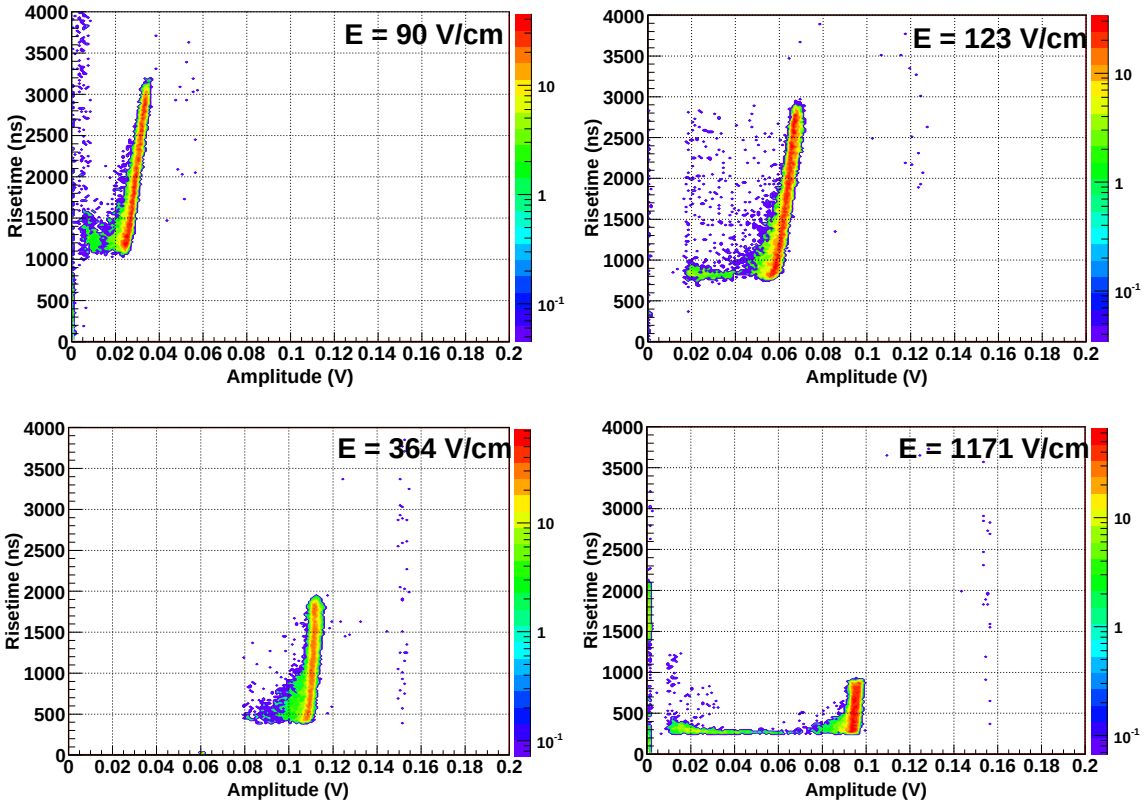

Figure 5.12: Risetime-amplitude distributions for for pure xenon at 2 bar and different drift fields. Left upper corner: E = 90 V/cm; right upper corner: E = 123 V/cm; left down corner: E = 364 V/cm; right down corner: E = 1171 V/cm. The color scale indicates the number of events in logarithmic scale.

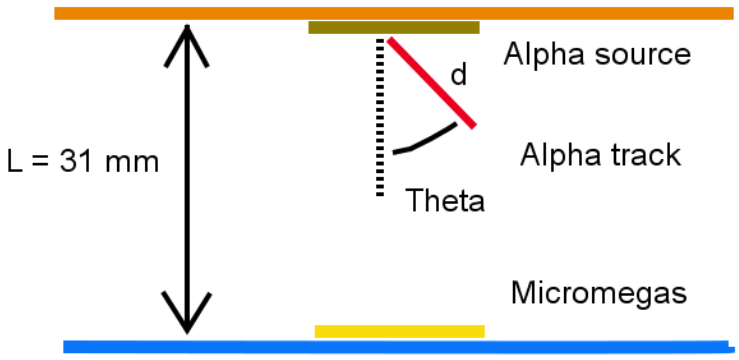

Figure 5.13: Sketch of the inside of the TPC. An alpha is emitted from the source with an initial an angle θ with the vertical axis.

decay dependence with drift time, like equation 3.39, we can calculate the total charge arriving to the detector by

$$Q(\theta) = \int_0^d \lambda \, dx \;\; \exp\left(-\frac{L - x\cos(\theta)}{v\tau}\right) = \frac{\lambda v\tau}{\cos(\theta)} \;\; \exp\left(-\frac{L}{v\tau}\right)\left[\exp\left(\frac{d\cos(\theta)}{v\tau}\right) - 1\right] \qquad (5.3)$$

where λ is the linear charge density, v is the drift velocity and L is the distance between the

source and the readout. For simplicity, the linear charge density is supposed constant even if there is an increase of charge at the end of the track, as described in section 3.1.2. The projection of the track length over the vertical axis is related with the pulse risetime by the formula

$$T_{\text{rise}} = \frac{d\cos(\theta)}{v} \tag{5.4}$$

The drift velocity can be eliminated from the equation 5.3 using the expression 5.4. The total charge is then expressed as

$$Q(\theta) = Q_0 \ \exp\left(-\frac{L}{v\tau}\right) \ \frac{\tau}{T_{\text{rise}}} \ \left[\exp\left(\frac{T_{\text{rise}}}{\tau}\right) - 1\right] \tag{5.5}$$

where Q_0 is the initial track charge. If the exponential factor is approximated by the first three elements of the Taylor series, the final charge is described by

$$Q(\theta) = Q_0 \ \exp\left(-\frac{L}{v\tau}\right) \ \left[1 + \frac{T_{\text{rise}}}{2\tau}\right] \tag{5.6}$$

The analysis of pulses obtained in pure argon do not show any correlation between risetime and amplitude, as shown in figure 5.14. This means that for the same level of impurities in argon and xenon, attachment is only observed in the second gas. This fact is reasonable according to the observations of section 3.3.3.

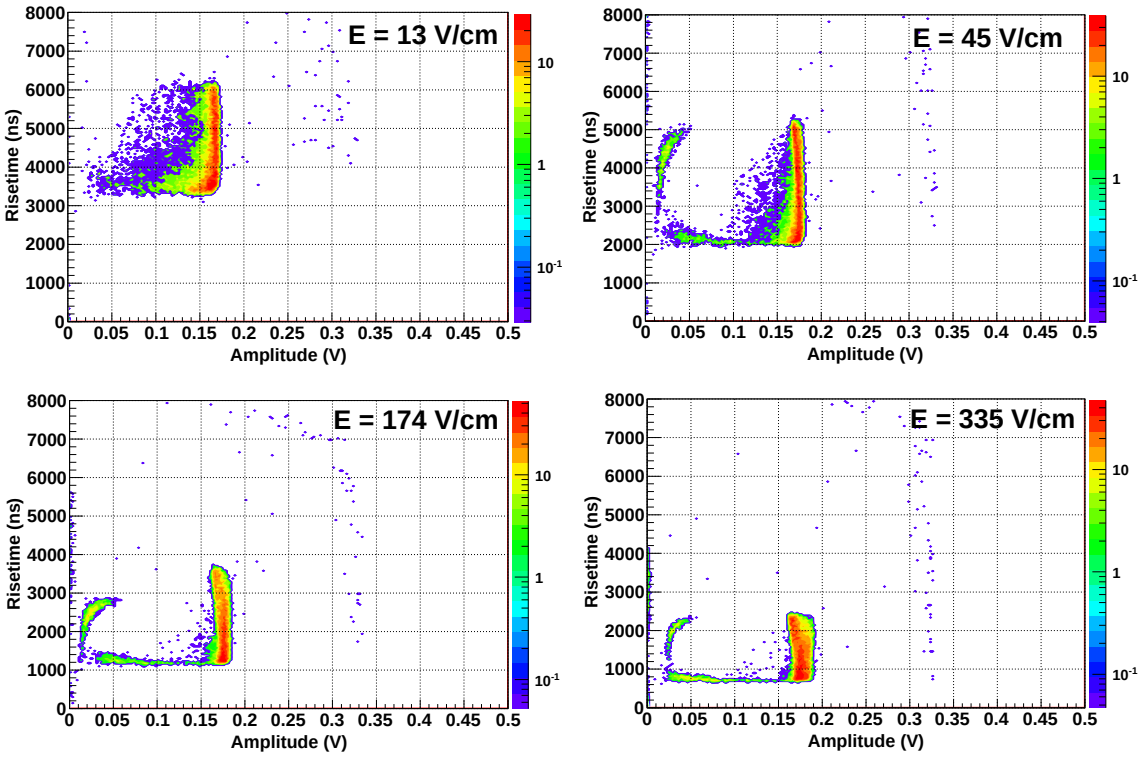

Figure 5.14: Risetime-amplitude distributions for pure argon at 4.5 bar and different drift fields. Left upper corner: E = 13 V/cm; right upper corner: E = 45 V/cm; left down corner: E = 174 V/cm; right down corner: E = 335 V/cm. The color scale indicates the number of events in logarithmic scale.

5.4.4 Gas purity

The 2D distributions calculated in the former subsection can be used to estimate the gas purity of the system. Each plot has been linearly fitted to the equation

$$T_{\text{rise}} = \alpha \text{ Amplitude} + \beta \tag{5.7}$$

The charge of equation 5.6 can be interpreted in terms of the pulse amplitude. With this expression and the equation 5.7, the mean electron lifetime τ can be calculated by

$$3.22\alpha = \frac{T_{\text{rise}}^{\max} - T_{\text{rise}}^{\min}}{A^{\max} - A^{\min}} = \frac{2\tau + T_{\text{rise}}^{\max}}{A^{\max}} \Rightarrow \tau = \frac{1}{2}\left(\alpha\ A^{\max} - T_{\text{rise}}^{\max}\right) \tag{5.8}$$

To study the gas purity in our system, we have considered several gas and drift field conditions as follows. On the 19th of June, pure xenon was introduced in the TPC at 3 and 4 bar, after having pumped all the system two hours and having reached a vacuum level of 10^{-2} mbar. Without having opened the TPC, the system was pumped all the night of the 23th of June and pure xenon was put in the TPC at 3 and 4 bar. A better vacuum level was reached (7.5×10^{-3} mbar). On the 28th July, a new oxisorb filter was installed. After having pumped and purged the system, pure xenon was measured at 3 bar on the 30th July. Due to sparks, the TPC was openend and reclosed, measuring again on the 1st of August at 3 bar after a one-night pumping.

The mean electron lifetime has been calculated for these conditions and differet drift fields, fitting the risetime-amplitude distributions to equation 5.7 and using the expression 3.22. The results are shown in figure 5.15 and in table 5.2. The maximum values obtained for the mean electron lifetime are 47 ± 5 μs and 4.0 ± 0.2 μs at 3 and 4 bar respectively. For comparison, we can estimate the mean lifetime required for a MMTPC in a $\beta\beta$ decay experiment. If the events drift about 1 meter and lose less than 1 % of their charge, the minimum mean lifetime must be longer than 60 ms in pure xenon and 6 ms in mixtures with a quencher. Therefore, this setup is far from the required values.

Day	19th		24th		30th	1st
Pressure (bar)	3	4	3	4	3	3
Max. electron lifetime (us)	7.9 ± 0.5	4.0 ± 0.2	6.8 ± 0.2	3.0 ± 0.1	47 ± 5	30 ± 2

Table 5.2: Mean electron lifetime for different conditions in pure xenon measured in the Saclay's setup in summer of 2008.

If the attachment is supposed to be caused only by oxygen, its concentration can be estimated applying equation 3.40 and using the value k(O_2, Xe) = 61 μs^{-1} bar^{-2}, taken from table 3.3. The calculated oxygen concentration is plotted versus the reduced drift field for several gas conditions in figure 5.16.

The oxygen concentration is not really decreasing when the drift field is increased but it is the coefficient k(O_2, Xe) which is decreasing, as it was explained in section 3.3.3. This dependence has not been measured yet. Nevertheless, an estimation of the real oxygen concentration can be made using values near the termal drift range, where the coefficient has been measured. In the case of xenon, this range corresponds to drift fields up to 20 V/cm/bar, as shown in figure 3.5. This approximation leads to a value of $\approx$ 3000 ppm in the data-taking of June and $\approx$ 1000 ppm the 30th of July. The estimation of 1000 ppm has a big incertitude as no pulse was acquired at very low field.

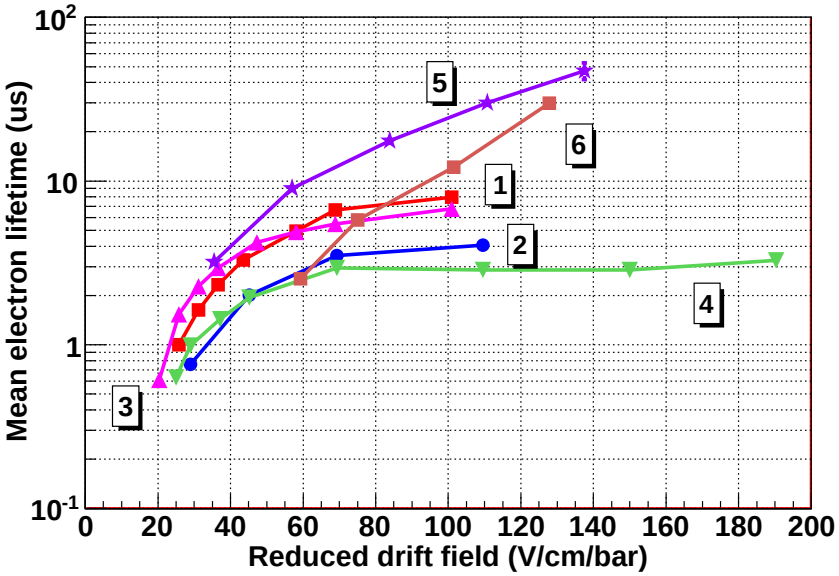

Figure 5.15: Dependence of the mean electron lifetime with the reduced drift field for different data-taking in pure xenon: on the 19th of June at 3 (1 - red squares) and 4 bar (2 - blue circles), after a one-night pumping; on the 24th of June at 3 (3 - magenta triangles) and 4 bar (4 - green inverted triangles), after a one-night pumping without opening the TPC; on the 30th July at 3 bar (5 - violet stars), after having installed a new oxisorb filter and having pumped the system during a night; and on the 1st August at 3 bar (6 - brown squares), after having opened the vessel and another night pumping.

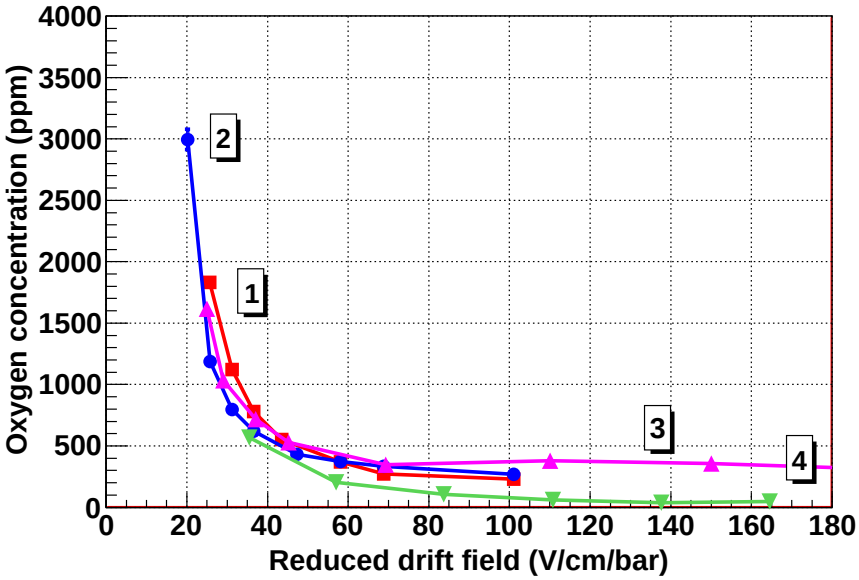

Figure 5.16: Dependence of the oxygen concentration with the reduced drift field for different data-taking in pure xenon: on the 19th of June at 3 bar (1 - red squares), on the 24th of June at 3 (2 - blue circles) and 4 bar (3 - magenta triangles); and on the 30th July at 3 bar (4 - green inverted triangles). A longer explanation of each case is made in figure 5.15.

5.4.5 Drift velocity

The same risetime-amplitude distributions calculated in subsection 5.4.3 can be used to calculate the drift velocity of electrons. According to our interpretation, the longest risetime corresponds to vertical tracks. Their length has been calculated with a Geant4 simulation (see section 7.1.2 for more details), giving respectively a value of 5.36 cm for pure argon and 2.20 cm for pure xenon at atmospheric pressure. If no diffusion effect is considered, the drift velocity can be calculated by

$$v_{\text{drift}} = \frac{L_\alpha^1}{P\, T_{\text{rise}}} \tag{5.9}$$

where L_α^1 is the length of the track at 1 bar and P is the gas pressure in bar.

The measured drift velocity for pure argon is shown in figure 5.17, where the theoretical curve generated by Magboltz has also been plotted. The clear difference between the measured and Magboltz curves can be attributed to the presence of isobutane impurities, possibly retained by the oxysorb filter. In fact, the data on the 17th July (curve 2), taken after a night-long pumping and a purge of the TPC, is nearer to theory. The combination of a pumping and a purge, not made in other cases, surely removed most part of the isobutane in the TPC.

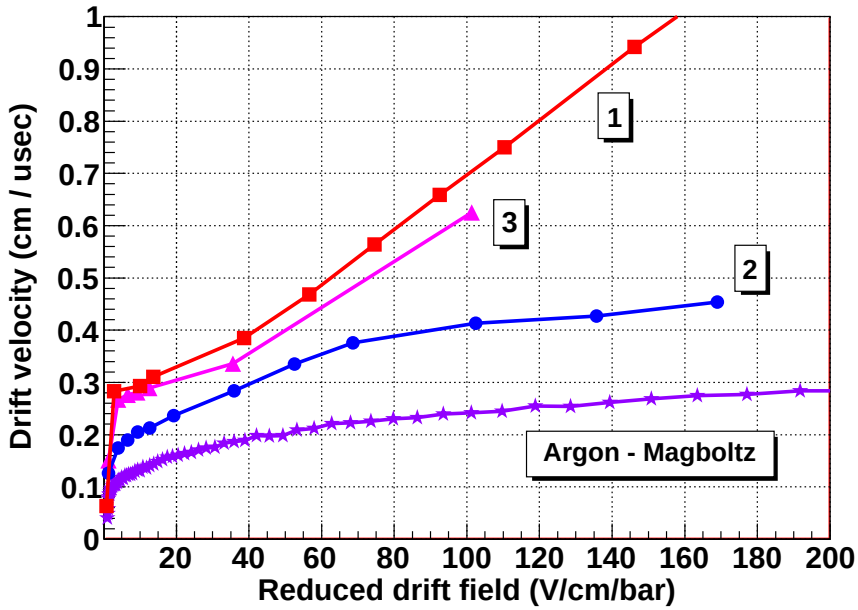

Figure 5.17: Dependence of the drift velocity with the reduced drift field for pure argon at 4.5 bar in different days of July: on the 15th, after a weekend-long recirculation through the filter (1 - red squares); on the 17th, after a night-long pumping and a purge of the TPC (2 - blue circles); and on the 18th after a pumping. As a comparison, the theoretical curve generated by Magboltz is plotted (purple stars).

A similar difference between theory and measurements is observed in pure xenon, shown in figure 5.18. The first curves like the number 1 are very far from the theory because argon-isobutane mixtures were previously used. After the installation of a brand new oxisorb in the gas system, the difference (curve 2) increased due to the presence of helium. This gas was normally used in the installation. The drift velocities (curves 3 and 4) became more closer to the theorethical ones after successive TPC pumpings.

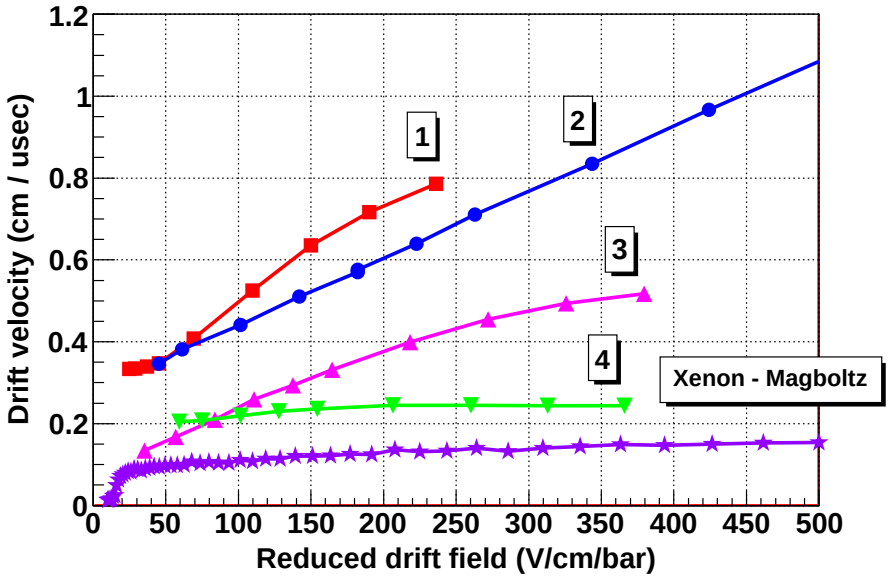

Figure 5.18: Dependence of the drift velocity with the reduced drift field for pure xenon in different conditions: at 4 bar on the 25th June after having worked with argon-isobutane mixtures (1 - red squares); at 2 bar on the 29th July (2 - blue circles) with a brand new oxisorb, previously filled with helium; at 3 bar on the 30th July (3 - magenta triangles) and on the 1st August (4 - green inverted triangles) after successive pumpings of the TPC. As a comparison, the theoretical curve generated by Magboltz is plotted (purple stars).

Attachment could also be responsible for this difference. Tracks arriving to the detector will be shorter than those initially generated because electrons of the top end will have been absorbed by impurities. Therefore, the risetime will be shorter and the drift velocity will be overestimated.

5.4.6 Energy resolution

The measured energy resolution is modest and degenerates sharply for higher pressures. The best values obtained are 3.8 % FWHM at 2 bar and 10.3 % FWHM at 4 bar. Nevertheless the pulse shape analysis described in subsection 5.4.3 also allows us to make a conservative estimation of the energy resolution in absence of attachment by keeping only events with similar risetime. These events will have minimal spread due to different attachments.

Best values for this estimation are 2.8 % FWHM at 2 bar and 4.5 % FWHM at 4 bar. They have been obtained with a risetime between 1800-2000 ns for 2 bar and 1200-1300 ns for 4 bar. We must stress that these numbers are conservative, because the subset of events kept by this selection criterium still suffer from attachment.

5.5 The determination of the absolute z-axis position

A pixelized micromegas readout with suitable electronics will be capable to determine the 3D topology of a particle interacting in the gas. However, this event could have been generated at any place along the z-axis. For the determination of the absolute coordinates of an event, it is necessary to measure the absolute time when it occurs in the TPC.

When a particle interacts in a gas, it both ionizes the medium and creates scintillation light with a wavelength between 150 and 180 nm for pure xenon [163]. In mixtures with a quencher, this light is absorbed by the quencher molecules and charges are generated. In pure gases, this light can be collected and used as the trigger of the event by:

- a plate with a photosensitive substance (like CsI) deposited on it, installed at the top part of the TPC. In the mesh two signals will be induced: one generated by the event and another one induced by the electrons created by light at the plate. The temporal separation between pulses can be translated into a distance to the photocathode.
- a micromegas detector with the photosensitive substance deposited on the mesh. In this case, the scintillation pulse will arrive first and the temporal separation will be translated into a distance to the mesh. This feature has been implemented in some GEM detectors to reduce the parallax error in x-ray detectors [164].
- a photosensor or photomultiplier.

The first possibility has been tested installing an aluminium plate with a CsI deposit [165] (called **photocathode** for simplicity) in the TPC, as shown in figure 5.19 (left). The photocathode has been fixed to the copper plate by two plastic screws to avoid any electric contact between both pieces. In these measurements, a turbomolecular pump has been used. This means that before entering the gas, a pressure between 10^{-5} - 10^{-4} mbar was reached.

The output pulses from the preamplifier have been analyzed as in section 5.4.3. In the risetime-amplitude distribution, we have observed a little curvature, as shown in figure 5.19. This curvature has been attributed to electrons generated by the scintillation light in the photocathode.

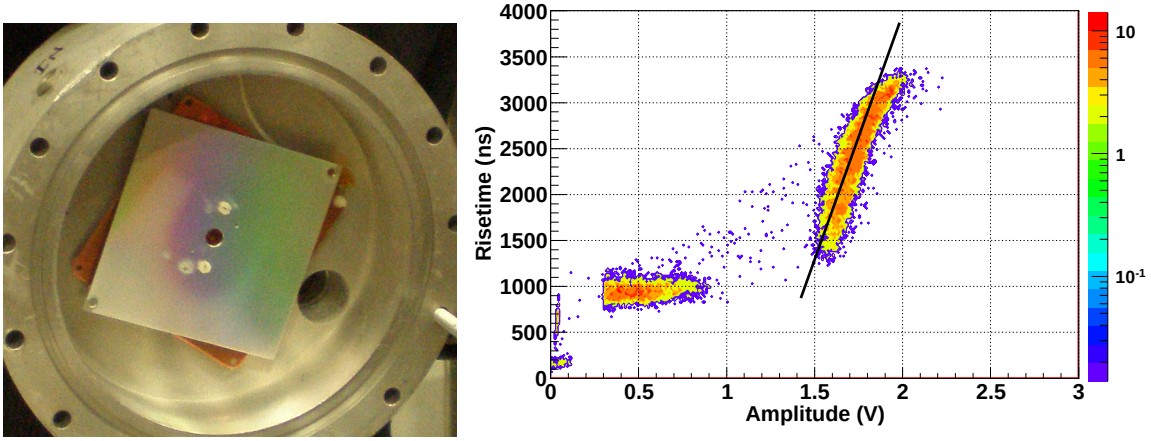

Figure 5.19: Left: A photograph of the photocathode installed in the TPC. Right: A risetime-amplitude distribution obtained with the photocathode. The color scale indicates the number of events in logarithmic scale.

At high gains, a series of secondary pulses after the main one have been observed, as shown in figure 5.20. Their origin is simple. The amplification of an event creates light. When photons arrive at the photocathode, they create electrons, which drift to the micromegas detector and are also amplificated. This process repeats several times as each new pulse has an amplitude around 13 % of the previous one. This value has been obtained comparing succesive pulses.

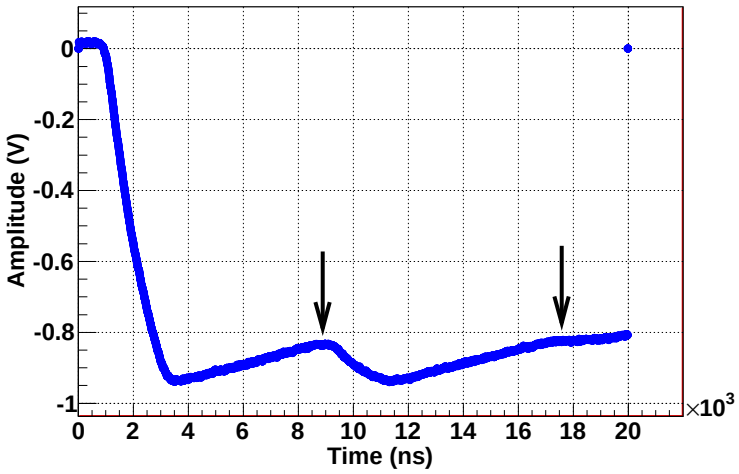

Figure 5.20: An example of a smoothed preamplifier pulse acquired in pure xenon at 2 bar with the photcathode installed in the TPC. Arrows point the position of secondary pulses.

In a second step, it is planned to test micromegas detectors with a CsI deposit on their mesh. Further details will be given in [166].

5.6 Conclusions

The former HELLAZ setup at the IRFU-CEA/Saclay has been used for testing a microbulk micromegas readout at high pressures with an alpha source. The setup consists of a high pressure TPC, a gas and a vacuum system. The energy resolution measurements of alpha particles at high pressure with this type of micromegas detectors are the first ones to be published [1].

The main result regards measurements in argon-isobutane mixtures at 4 bar. Energy resolution down to 1.8 % and 2 % FWHM at the ^{241}Am 5.5 MeV alpha line have been obtained for a wide range of drift/amplification field ratios, for percentages of isobutane of 2 % and 5 % respectively. Possible evidence for better achievable resolutions (down to 0.7 % and 0.9 % FWHM respectively) are pointed out based on the asymmetry of the measured alpha peak. Apart from that, it has been determinated that the quenching factor of alpha particles in Ar + 5 % iC_4H_{10} is almost unity, by comparing the x-rays and the alpha peak of the ^{241}Am source.

Preliminary measurements in pure xenon for pressures 2-4 bar have been presented, although the setup has been proven not to be good enough for electrons drifitng in xenon. Gains up to 200 have been reached, independently of the gas pressure. Effects of attachment in the gas have been found in the transparency curve and in the correlation between risetime and amplitude of preamplifier pulses. This dependence of pulses has been used to fix limits at the mean electron lifetime. The best values obtained are 47 ± 5 and 4.0 ± 0.2 μs at 3 and 4 bar respectively. These limits are far from the required values of 6 and 60 ms for charge losses below 1 % and drift distances above 1 meter respectively in pure xenon and xenon mixtures with a quencher.

In addition, the mean electron lifetime values have been interpreted in terms of attachment to oxygen and its concentration has been estimated. In the first data-taking, the concentration was approximately 3000 ppm. After the installation of a new oxisorb filter, this value decreased down to 1000 ppm.

The pulse shape analysis has also allowed the application of selection criteria on the risetime

for estimating the energy resolution in absence of attachment. Values of 2.8 % FWHM and 4.5 % FWHM have been respectively found at 2 and 4 bar. These values are positive and already approach the requirements of a double beta decay experiment. As it is described in next chapter, a completely new setup has been built to repeat these measurements, reducing the level of outgassing and the level of vacuum reached and obtaining better results.

Similar measurements have been done in [155] for Xe - CF_4 gas mixtures, although with considerable worse values for the energy resolution. The reason seems to be the type of readout used (woven-mesh) of significantly less precision in the dimensions of the amplification structure.

Finally, a layer with a CsI deposit has been tested in the TPC. Signals due to primary scintillation light have been observed, which points out the possibility of detecting the absolute time (and the position along the z-axis) in future TPCs. Micromegas detectors with a CsI layer on the mesh will be tested soon.

Chapter 6

Tests with a Microbulk detector in a specifically built TPC

During almost two years, a TPC at the IRFU-CEA/Saclay was used for testing micromegas detectors in gases at high pressures. As explained in the last chapter, the analysis of data showed that the gas purity in the TPC was good enough for working in pure argon and argon-based mixtures but not in xenon. The attachment limited the results and pointed out the necessity of working in a better setup.

The experience acquired in the TPC and the gas system has served in the design and builiding of a complete new setup: a high pressure TPC, a gas system and a vacuum system. This setup is described in the first section, showing a better performance than the one at Saclay. In the second section, the tests of a micromegas detector at high pressure in argon-based mixtures using an x-ray source are presented. In the last section, the tests in pure argon and xenon using an alpha source are described. These last tests have showed a better gas quality and an improvement in the energy resolution in pure xenon, giving a new estimation of the energy resolution in absence of attachment.

6.1 Setup description

The setup is divided in three parts: the gas system, the vacuum system and the TPC. The first one consists of all the elements that introduce the gas and remove it from the vessel. The second one includes the elements used to make vacuum in the vessel (and usually all the gas system) to decrease the outgassing rate from the inner walls. Finally, the TPC consists of the vessel, the drift structure and the micromegas readout.

6.1.1 The micromegas readouts

Three different micromegas readouts have been used in the measurements. All of them have been built with the *microbulk* technique described in 4.5.2 and have a gap of 50 microns. For gamma and alpha tests, two circular readouts with a diameter of 35 mm and a continuous anode have been tested, one of them is shown in figure 6.4 (right). Both of them have a copper mesh but in one of them (the Golden Micromegas number 9, GM9) a gold deposition on the mesh was made. This deposition was absent in the second one (the Copper Micromegas number 2, CM2). The first detector was tested with x-ray sources and the second in alpha measurements.

The third readout used is a pixelized micromegas shown in figure 6.1. Its anode is divided in 12×12 squared pixels of a side-length of 10 mm. The signal of all pixels is taken out by vias to

four connectors. The main goal of this detector has been the acquisition of 3D events. Results are presented in [166].

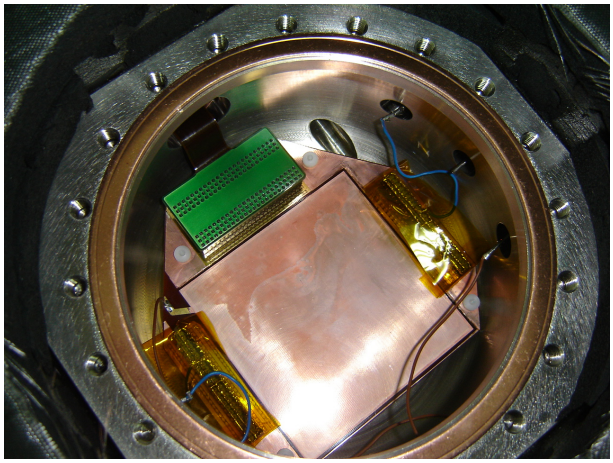

Figure 6.1: The pixelized micromegas readout installed inside the TPC.

Before their use, the three detectors were calibrated with an iron source in Ar + 5 % iC_4H_{10} to measure their absolute gain, the electron transmission curve and the energy resolution. As shown in figure 6.2, their absolute gain is similar and maximum values of 5×10^3 can be obtained before the spark limit. Their gain is about a factor 5 lower than the readout used in Saclay's measurements. Apart from that, all of them have an energy resolution of 11% FWHM at moderate amplification field and a transparency curve as the one shown in figure 4.8 (red squared line).

6.1.2 The High Pressure TPC

The high pressure TPC was built by the company Telstar according to a conceptual design based on Saclay's experience. It is a vessel made of stainless steel whose inner walls have received a special treatment (passivation and electropolish) for a lower outgassing level. It also includes ten outlets (1 CF160, 4 CF40 and 5 CF16) closed with copper joints, which assure an ultrahigh vacuum according to standards when pumping. The big CF160 outlet is used for opening and closing the TPC if any change in its inside has to be made.

One CF40 outlet is used by the vacuum system. An all-metal pressure valve is there installed, with better specifications than the Saclay one. It is able to keep the vessel tight up to gas pressures of 12 bar and vacuum levels below 10^{-6} mbar. Two of the other CF40 outlets have been reserved for signal feed-throughs of a pixelized micromegas readout, described in section 6.1.1. The last CF40 outlet has been reserved for three signal (BNC) feed-throughs. From the five CF16 outlets, three are used for high voltage (SHV) feed-throughs and the other remaining two for the gas entrance and exit. The vessel design and the outlets distribution are shown in figure 6.3.

The inner design of the TPC consists of a drift structure and a readout support, only used for little circular readouts. Both pieces are shown in figure 6.4. The first piece is composed of three peek-plastic columns, which support a circular copper plate and six copper rings. Its main goal is to keep the drift field uniform inside the vessel. For this reason, the plate works as a cathode and is successively linked to each ring by resistors of 33 MΩ. The plate has also a machined reduction with a hole for radioactive sources.

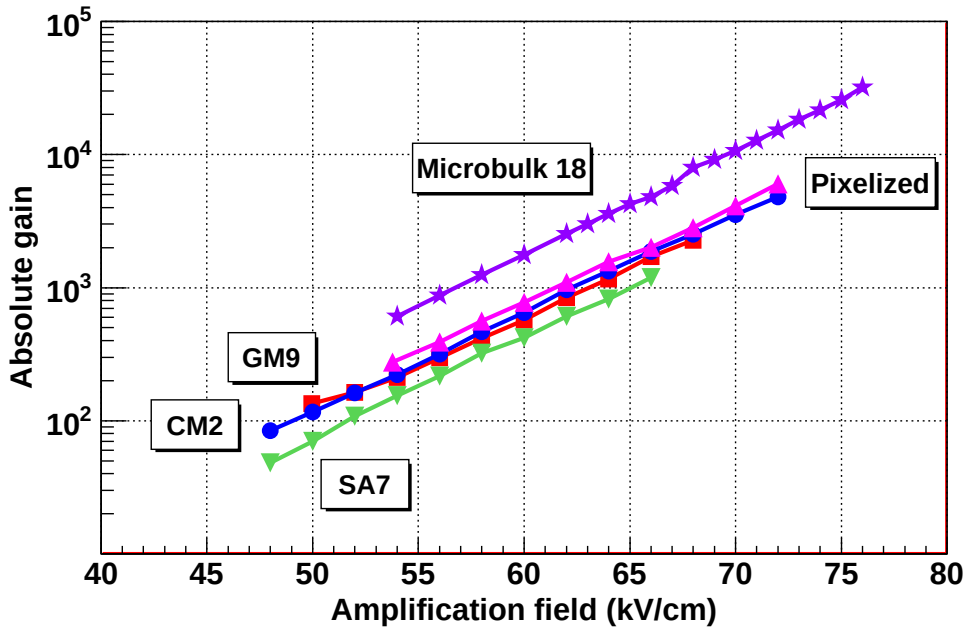

Figure 6.2: Absolute gain of the micromegas readout used in Zaragoza tests in Ar + 5 % iC_4H_{10} versus the amplification field: GM9 (red squares), CM2 (blue circles) and pixelized (magenta triangles). As a comparison, the gain of the SA7 (inverted green triangles), whose mesh is shown in figure 4.9 (right), and the readout used in Saclay (violet stars) are also plotted. The highest values of the pixelized and the CM2 are reached just before the spark limit.

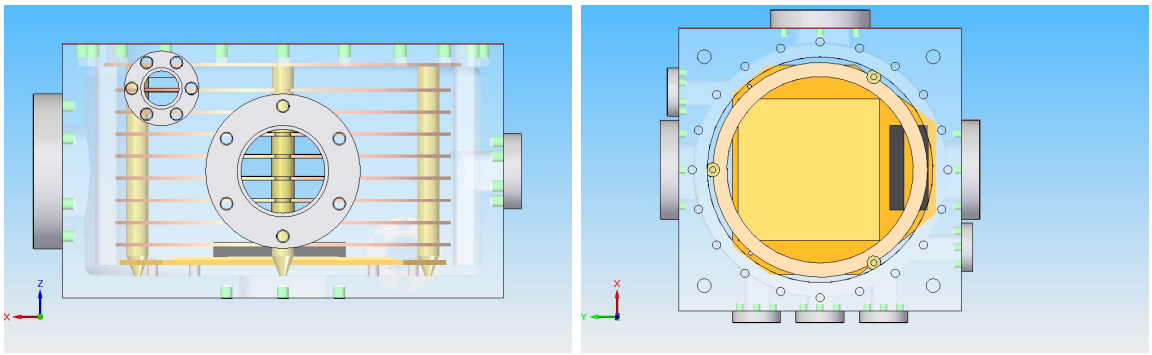

Figure 6.3: Lateral (left) and top (right) schematic views of the high pressure TPC of Zaragoza. Inside the vessel the drift structure and the pixelized micromegas readout have been included.

If the pixelized readout is used, only five rings of the structure are kept and the voltage of the last one is linked to a feedthrough which is connected to a variable resistor, serving to maintain the field uniform between the cathode and the mesh.

For the circular micromegas readouts, a support composed of a delrin-plastic base is used to which are fixed by a ring of the same material. This piece also fixes to the base a circular-corone copper plate, whose inner circle is big enough to contain the readout. This copper piece is electrically connected to the last ring of the drift structure.

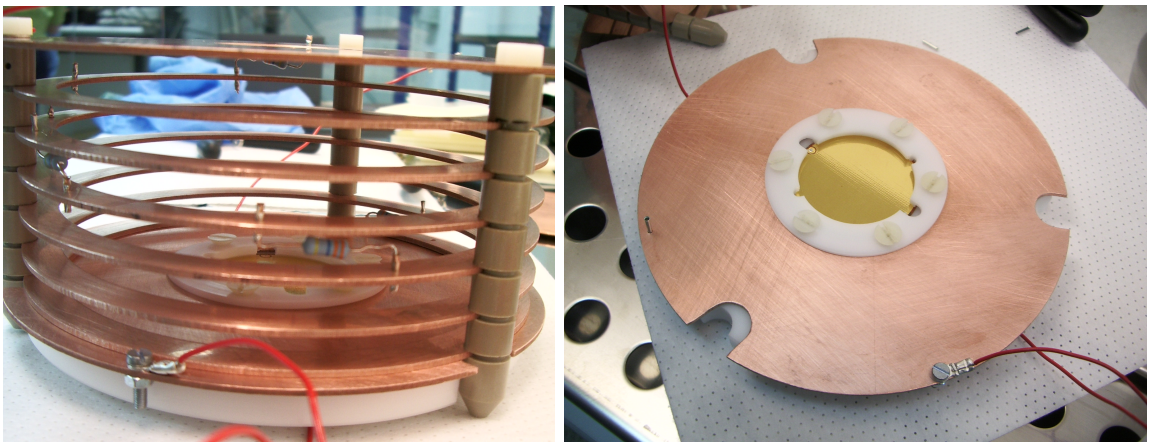

Figure 6.4: Elements inside the high pressure TPC. On the left: the drift structure, with its three pillars of pic keeping six drift plate and six copper rings, electrically linked by resistors. On the right: the detector support.

6.1.3 The gas system

The gas system has been designed to make mixtures of up to three components. For this purpouse, gas bottles have been installed outside the laboratory with three gas entrances. One entrance is for the main (or base) gas, normally argon or xenon, and the other two for quenchers, which are added in low quantities. All of them are connected to a nitrogen gas line to purge the remaining air when a new bottle is installed. The three lines are connected to a gas mixer, built by the company Iberfluid. The base gas is previously purified by an oxisorb cartridge, installed between the bottle and the mixer.

Inside the mixer, each gas line is controlled by a Bronkhorst mass flow controller and all lines end in a little mixing volume, specifically designed for a good gas mixing. Each controller has a different gas flow range: a maximum of 10 l/h for the base gas and 0.67 l/h for the two secondary. Flows are controlled by a PC software, which communicates with Bronkhorst modules by a COM network.

The final mixture can be purified by another oxysorb cartridge or a SAES filter [167], or directly enter the vessel. The gas that flows out the TPC can be thrown away to the atmosphere by a pipe with a non-return valve. This valve stops air from entering inside the gas system. The gas can also flow inside the TPC through an oil free membrane pump (KNF type PM23592-286.13), which works in gas pressures between 1 and 12 bar and has a maximum guaranteed leak of 6×10^{-6} mbar l / s.

Gas bottles are supplied by the company Praxair, which guarantees a purity 6.0 (99.9999 %) or better. Pure argon and xenon have been used as base gas and isobutane as a quencher.

6.1.4 The vacuum system

A sketch of the vacuum system is shown in figure 6.5. At one of the CF40 outlets of the vessel, a high-pressure-vacuum valve (SV) has been installed. Then there is a CF-standard T with a vacuum gauge (G) at one end and a vacuum valve (VV) at the other one. This last valve is connected to a turbomolecular pump (TURBO) by a flexible 1-meter tube. All the joints used are metallic: copper for the CF-standard and aluminium for the isoKF-standard.

Before any data-taking, the TPC is pumped for reducing the outgassing rate of the inner

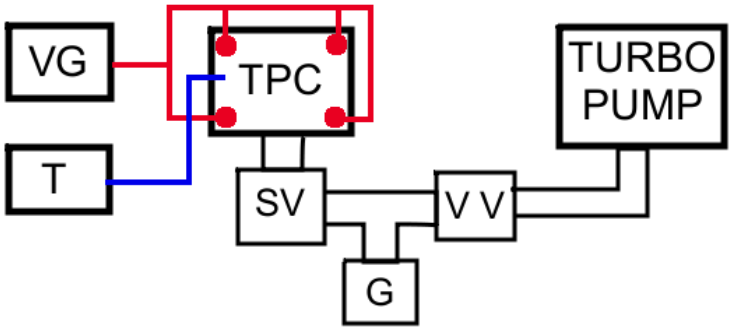

Figure 6.5: Schema of the vacuum system, described in the text.

components, as described in section 3.3.3. As this rate reduces more drastically if the vessel is baked-out, four thermal resistors have been installed at the four corners of the TPC, connected to a variable voltage generator (VVG). The vessel is heated until a temperature of 110 °C is reached, measured by a temperature sensor (T) at the outer surface. The bake-out is later repeated if the temperature is lower than 80 °C. Note that the TPC is kept at the temperature by an insulating material that completely covers it, which serves also for safety purposes.

The vacuum level inside the vessel is measured by the gauge (G). For the outgassing, the VV valve is closed and the pressure increase after few minutes is noted. The outgassing rate is then obtained by

$$\text{Outgassing rate} = \frac{\Delta P\ V}{t} \tag{6.1}$$

where t is the time and V is the volume: 2.3 l for the TPC and 2.7 l if the gas system is also pumped.

The vacuum level and outgassing rate has been measured for different pumping and bake-out times and inner materials. As shown in table 6.1, a pressure of 3 10^{-7} mbar is reached and there is practically no outgassing if no element is introduced inside the TPC. If the drift structure and the readout support are introduced, the vacuum level is not better than 10^{-5} mbar and the outgassing rate is about 10^{-5} mbar l / s. A bake-out does not reduce this value due to the poor thermal contact between the inner surface and the plastic elements, which are not effectively baked-out. These materials (peek and delrin) have the highest outgassing rate from the inner components.

6.1.5 Working procedure

The general proceduce starts with a day-long pumping of the TPC and the gas system. As it is shown in table 6.1, a vacuum level of 10^{-5} mbar and an outgassing rate of 10^{-5} mbar l / s are reached. The desired gas is then introduced in the gas system and the TPC. In the case of argon-isobutane mixtures, the mixer is used for pressures up to 3 bar, limited by the isobutane line, whose pressure is 3.1 bar. For pressures above 3 bar, each component is successively added and the gas is mixed with the recirculation pump during two hours. Finally, the in/out gas vessel valves are closed.

If one of the two circular readouts is used, the drift cathode is powered by a CANBERRA M3106D module and the micromegas anode by a CAEN N471A. Meanwhile, the mesh and the copper circular corone are both connected to ground. A positive signal is induced in the anode and read out by a CANBERRA 2004 preamplifier for gamma tests and an ORTEC 142C one

Conditons	Pumping hours	Bake-out Times	Pressure mbar	Outgassing mbar l / s
Inside empty	96	3	$3.1\ 10^{-7}$	$< 10^{-12}$
Gas in/out tubes installed	96	1	$2.1\ 10^{-7}$	$1.5\ 10^{-9}$
TPC + gas system	90	2	$5.1\ 10^{-7}$	$1.2\ 10^{-9}$
Inside components added	18	1	$7.1\ 10^{-6}$	$2.0\ 10^{-5}$
	168	1	$5.4\ 10^{-6}$	$1.0\ 10^{-5}$
Delrin base only	42	1	$1.2\ 10^{-5}$	$1.7\ 10^{-5}$
Drift structure only	48	2	$3.3\ 10^{-6}$	$2.7\ 10^{-6}$
Copper rings only	2.3	0	$7.8\ 10^{-6}$	$1.6\ 10^{-6}$

Table 6.1: Pressure and outgassing levels for different conditions at the HPTPC in Zaragoza.

for alpha ones. The preamplifier output is fed into an ORTEC VT120 amplifier/shaper and subsequently into a multichannel analyzer AMPTEK MCA-8000A for spectra building. The output of the preamplifier can be alternatively digitized directly by a Tektronix TDS5054B oscilloscope and saved into disk for further offline inspection.

If the pixelized micromegas readout is used, the anode pixels are connected to ground and the mesh is powered by the CAEN module. The last ring of the drift structure is connected via a variable resistor to ground, which serves to make uniform the field until the mesh. In this case, the negative signals induced in the mesh are those read out by the preamplifier.

6.2 X-ray measurements

The first goal of the TPC was the measurement of the energy resolution of a micromegas readout with a gamma source in argon-isobutane mixtures (0.5 %, 1 % and 2%) and pressures up to 10 bars. In this way, the whole setup was checked and a dependence of the energy resolution of x-rays with the pressure, similar to the one shown in figure 4.11 (right), has been observed. A radioactive gamma source ^{57}Co has been used, whose most intense emissions are detailed in table 6.2. As the readout has a diameter of only 35 mm, only x-rays are fully contained in the readout. A typical spectrum obtained in these conditions is shown in figure 6.6.

Type	x-ray			γ			β
Energy (keV)	6.391	6.404	7.058	14.41	122.1	136.5	699.6
Intensity (%)	16.4	32.6	5.87	9.16	85.6	10.7	99.8

Table 6.2: The most intense emissions of the radioactive source ^{57}Co.

The data-taking has followed the same procedure described in section 5.2.3. The results for transparency, gain and energy resolution are described in the following subsections.

6.2.1 Transparency

The electron transmission curves are systematically limited to low drift fields because the SHV feed-through for drift voltage is limited to low voltages. In this piece, the distance between the

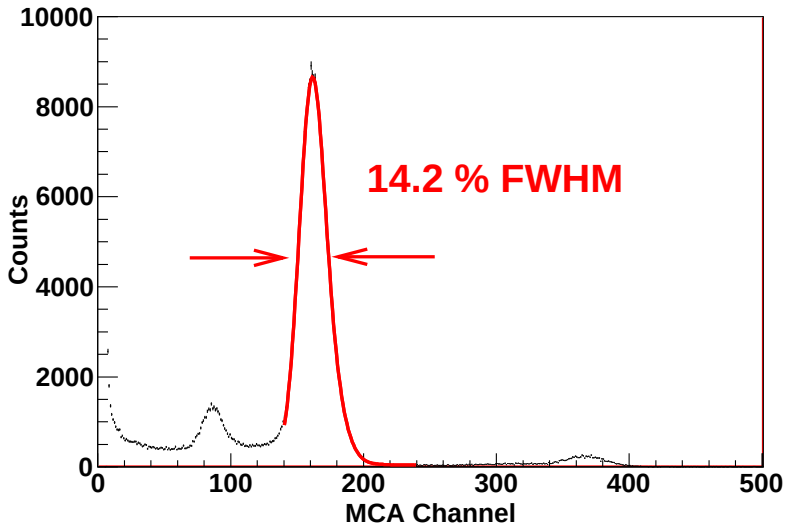

Figure 6.6: Energy spectrum obtained by the GM9 in Ar + 1 % iC_4H_{10} at 1 bar. The most intense peak is generated by the 6.4 keV x-ray. The one on the left is the argon-escape peak and the one on the right has been generated by the 14.4 keV gammas, whose electrons are not completely collected by the readout.

high voltage and the ground is very small and argon-isobutane mixture does not isolate enough for voltages higher than 2000 V. In pure gases, this problem disappears.

All transparency curves have a plateau, as the ones shown in figure 6.7, which points out that attachment effects are low. The plateau's range of drift fields has increased after the installation of the oxisorb filter for the base gas (magenta triangles) and the purification of the mixture by the SAES filter (orange stars). It seems that spectra cannot be obtained for drift fields below 20 V/cm/bar possibly due to the **ballistic effect** (pulse risetimes are longer than the preamplification decay-time) or diffusion effect.

We finally note that the proportion of isobutane is affected by the SAES filter. This is why only the base-gas oxisorb filter has been used in later measurements.

6.2.2 Absolute gain

The absolute gain versus the amplification field for Ar + 1 % iC_4H_{10} and pressures between 1 and 10 bar is shown in figure 6.8. Similar curves have been obtained for 0.5% and 2% mixtures. In almost all cases, gains greater than 3000 are reached before the spark limit. However, the detector GM9 has a maximum amplification field of 115 kV/cm, which limits the gain at high pressure.

In section 4.5.1, the theoretical gain of micromegas readouts has been described. The fit of all gain curves to the equation 4.3 permits to obtain the dependence of the electron mean free path (λ) and the ionization energy threshold (I_e) with pressure and the gas. The resulting plots are shown in figure 6.9.

The values obtained for I_e are not far from the theoretical one for pure argon (15.8 eV), detailed in table 3.1. However, its dependence with pressure was not expected and may point out a stronger effect of argon than isobutane ($I_e = 10.8$ eV) at high pressure. In fact, values for

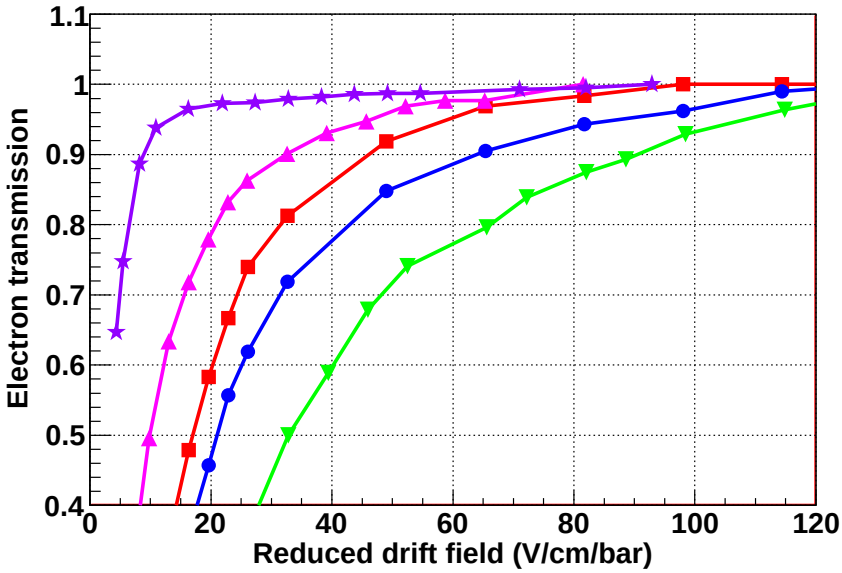

Figure 6.7: The electron transmission versus the reduced drift field in several situations: mixture without any purification (red squares) and after 3 hours of recirculation by the by-pass (blue circles); mixture with the base gas purified (magenta triangles) and after a weekend recirculation by the by-pass (green inverted triangles); and mixture purified by the SAES filter (violet stars). Note that there is no filter at the by-pass.

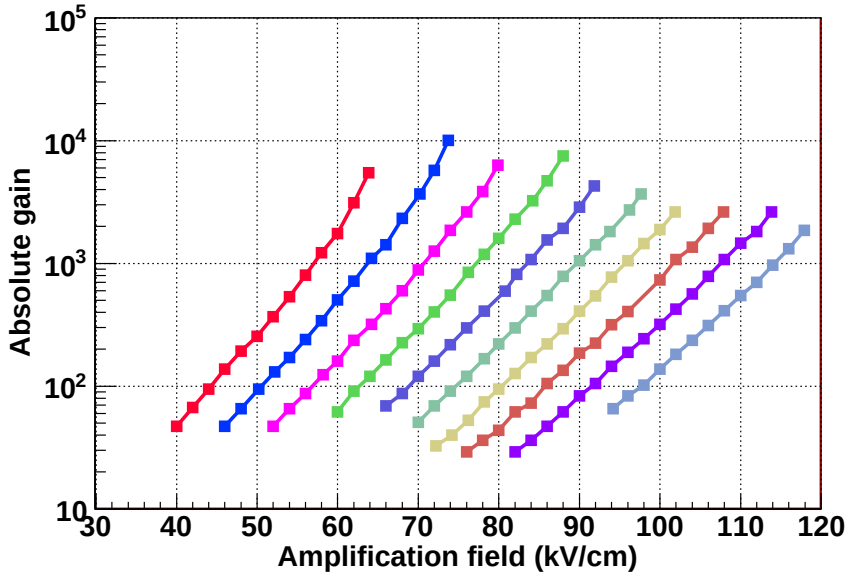

Figure 6.8: Dependence of the abbsolute gain with the amplification field in Ar + 1 % iC_4H_{10} for pressures between 1 (left side) and 10 bar (right side), in steps of 1 bar. The highest values are reached just before the spark limit.

the three mixtures are similar at low pressure but the differences increase with pressure. At 10 bar, the highest I_e values are those of Ar + 0.5 % iC_4H_{10}.

In contrast to I_e, the electron mean free path λ decreases with pressure because the gas

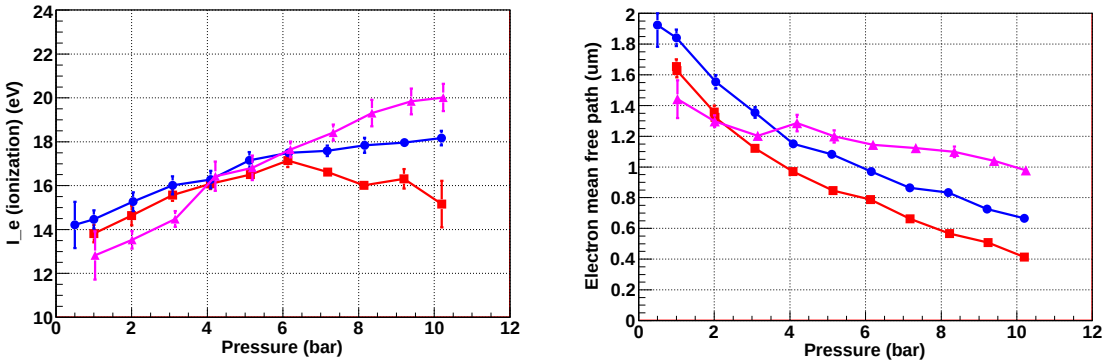

Figure 6.9: Dependence of the energy threshold for ionization (left) and the mean free electron path (right) with pressure for Argon-Isobutane mixtures of 0.5 (red squares), 1 (blue triangles) and 2 % (green circles).

density increases. However, differences between mixtures also increase with pressure and the highest values at 10 bar are obtained for Ar + 0.5 % iC_4H_{10}.

6.2.3 Energy resolution

The energy resolution previously measured in Ar + 5 % iC_4H_{10} in another setup has been confirmed. The value of 12.5 ± 0.2 % FWHM obtained is not far from the 11 % FWHM. Therefore, effects on energy resolution due to the drift structure are small. Apart from that, a fast degradation in energy resolution with pressure until a limit is reached has been systematically observed for the three mixtures considered. The best values for the 1 % mixture are shown in table 6.3. This experimental fact needs a further study.

Pressure (bar)	1.00	2.00	3.10	4.09	5.11
Res (% FWHM)	12.9 ± 0.3	13.8 ± 0.2	16.1 ± 0.4	17.1 ± 0.4	16.8 ± 0.6
Pressure (bar)	6.15	7.17	8.20	9.20	10.20
Res (% FWHM)	17.1 ± 0.4	17.3 ± 0.5	17.9 ± 0.6	17.1 ± 0.3	17.2 ± 0.4

Table 6.3: Best values for energy resolution for Ar + 1 % iC_4H_{10} at different pressures.

6.3 Alpha measurements

The final goal of these measurements is the quantification of the micromegas energy resolution at $Q_{\beta\beta}$ as in Saclay. For a better comparison, also an ^{241}Am source has been used. It consists of a circular plate (11 mm of diameter and 1 mm of thickness), which is placed at the source hole of the cathode. The plate thickness near the hole has been machined down to 0.4 mm for allowing alphas to reach the drift volume. The source activity is rather high (11.4 kBq) and causes a permanent current between the mesh and the anode (up to 26 nA at 10 bar in an argon-isobutane mixture and an amplification field of 88 kV/cm), pile-up and other effects later described.

Another change with respect to the gamma measurements is the replacement of the CANBERRA preamplifier by an ORTEC 142C one. According to Geant4 simulations, an alpha of 5.5 MeV has a length of 5.26 and 2.20 cm in pure argon and xenon respectively. As electron drift velocity in those gases is less than 0.4 cm/μs (as figures 3.5 and 3.6 show), vertical tracks can reach 10 μs at 2 bar. These tracks cannot be measured with a preamplifier with a short decaytime, like the CANBERRA one (30 μs). For this reason, it has been replaced by an ORTEC 142C preamplifier, with a decaytime longer than 100 μs.

Three types of gases have been studied: a variable argon-isobutane mixture, pure argon and pure xenon. The first one was not planned and was obtained flowing pure argon by the SAES filter. This cartridge retained the isobutane used in the gamma measurements and still freed it after a two-day continuous flow. For this reason, an oxisorb filter has been used instead for purification.

The TPC contained the variable argon-isobutane mixture from the 22nd to the 27th of July. After a night-long pumping, pure argon was introduced in the TPC by the oxisorb. This gas was used at different pressures until the 3rd of August, when the gas was changed to pure xenon. Data taking in this gas lasted two weeks, when a degradation in the gas purity was observed.

In the next subsections, the main results for the three gases are described.

6.3.1 Transparency

The electron transmission curves for the variable argon-isobutane mixture are shown in figure 6.10. As it can be observed, the plateau of the curve is very small for low pressures and its right edge moves to higher ratio of fields as the preassure is increased. In all cases, the plateau finishes before $E_{drift}/E_{amp} = 0.01$, the expected value for this type of micromegas as shown in figure 4.8 (red squared line).

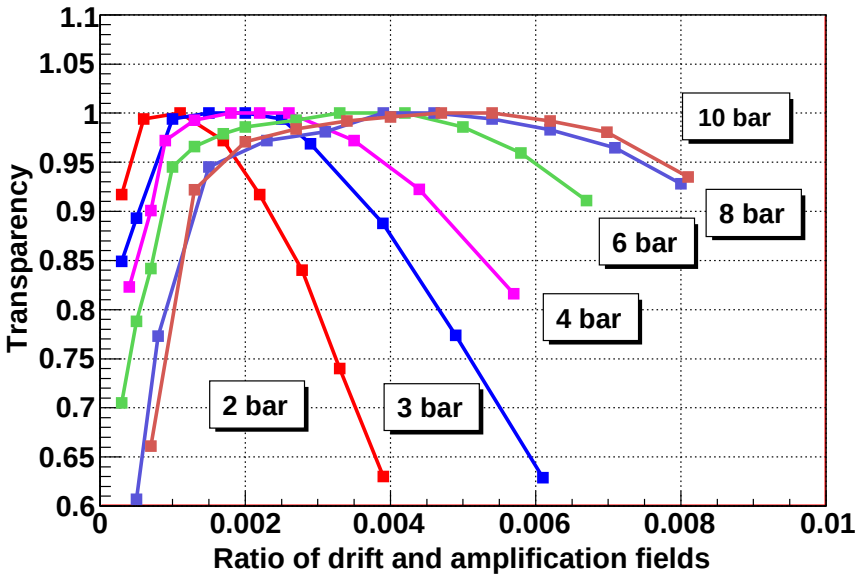

Figure 6.10: Dependence of the electron transmission with the ratio of drift and amplification fields for a variable argon-isobutane mixture at different pressures. Values are normalized to the maximum of each series.

This behaviour is attributed to the intensity of the alpha source. The big amount of electrons

drifting to the readout can modify the drift fields, causing a transparency loss. The same characteristics were observed in pure xenon and argon, which rules out any dependence on the type of gas; and in another setup with the same source, which discards any setup effect.

6.3.2 Absolute gain

The absolute gain also shows a strange behaviour, clearly affected by the high source intensity. As an example, the measured gains in pure xenon are compared to Saclay's curves in figure 6.11. The gain is not greater than 100 in any condition and for many amplification fields, it is lower than 1, i.e., the signal detected is lower than the one generated by the primary ionization. In addition to, the dependence of the gain with the amplification field is not exponential. This effect has been observed at the three studied gases and it was checked that the ratio of fields was always in the range of maximum transparency.

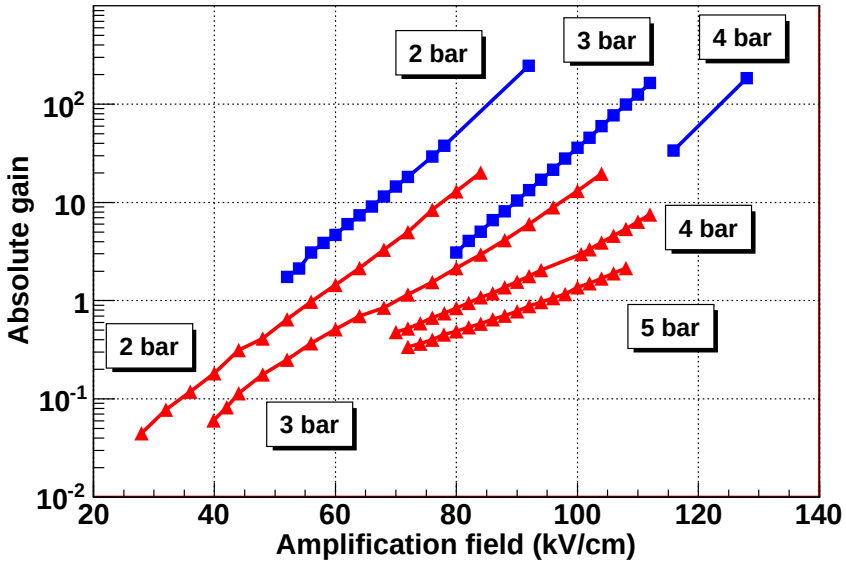

Figure 6.11: Dependence of the gain with the amplification field for pure xenon at different pressures measured in Zaragoza (red triangles) and Saclay (blue squares).

In order to avoid sparks, the amplification field applied in all pressures was not very high. At 4 and 5 bar, the intensity of the current between the mesh and the anode caused inestabilities at high amplification fields, which limited the maximum gain reached.

6.3.3 Drift velocity

In these measurements, the drift velocity has served to control the gas composisition. In the first days, pure argon was introduced in the TPC by the SAES filter. As shown in figure 6.12, the drift velocity curves at different pressures had a maximum, which only appears in argon-isobutane mixtures, as figure 3.6 indicates. This presence of isobutane in the TPC was explained by the contamination of the SAES filter, which was previously used in gamma measurements. As a consequence, this filter was replaced by a completely new oxisorb filter.

As shown in figure 6.13, pure argon velocity curves of the next days are nearer to the theoretical ones in comparison with those obtained in Saclay. Differences can be attributed to diffusion, not considered in the calculation, and impurities of isobutane still retained in the inner

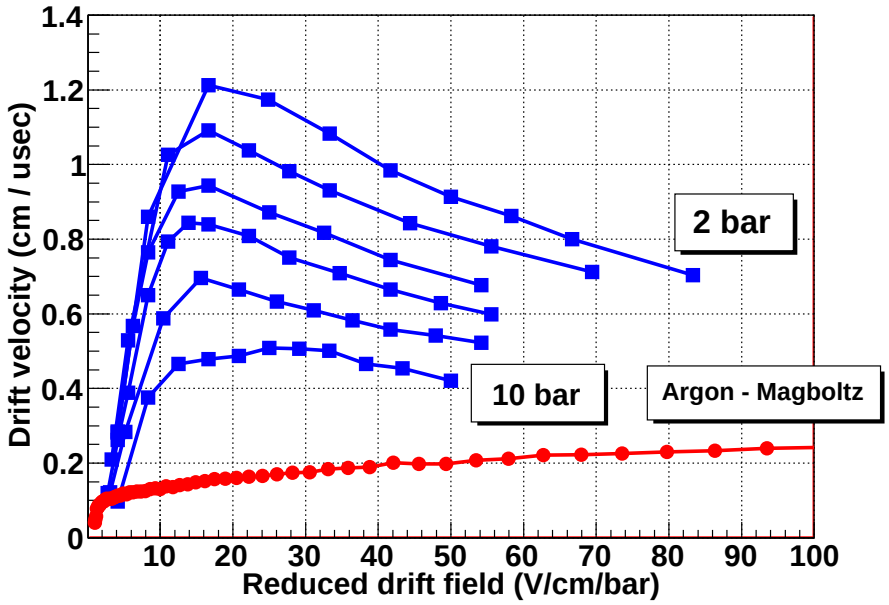

Figure 6.12: Dependence of the drift velocity with the reduced drift field for an argon-isobutane mixture at 2, 3, 4, 6, 8 and 10 bar (blue squares). As a comparison, drift velocity in pure argon (red circles) generated by the programme Magboltz is plotted.

component of the TPC and the gas system. On the 28th of July, when argon was introduced in the vessel without passing through the SAES filter, there was a difference of almost a factor 2 (curves 1 and 2). Successive pumpings and new gas have made the velocity curve get closer to that generated with Magboltz (curves 3 and 4).

In pure xenon, the drift velocity increased fastly with the drift field the first days (curves 1, 2 and 3 of figure 6.14). This increase disappeared after successive openings and pumpings of the TPC and a good match between the measured (4) and the theoretical curves was obtained.

6.3.4 Attachment

A visual comparison between the risetime-amplitude distributions at Saclay and Zaragoza allows us to conclude that the new setup has a lower level of attachment. In figures 6.15 and 6.16 these distributions are respectively plotted for the argon-isobutane mixture at 7 bar and pure xenon at 4 bar. Those figures can be respectively compared to figures 5.14 and 5.12.

We note that in the argon-isobutane mixture, pulses have been observed for fields of only 3 V/cm/bar due to the longer preamplifier decay time and the lower attachment effects. For those fields, the risetime and the amplitude have a negative linear dependence because the base line of each pulse suffers big variations due to pile-up. As the drift field is increased, this effect is replaced by attachment, which creates a positive linear dependence. For values higher than 30 V/cm/bar, attachment also disappears and there is only a little effect for events with a short risetime. Moreover, the width of the distribution does not increase as in Saclay because there is no distortion of the drift field.

In pure xenon, attachment effects are clearly lower than Saclay. This is based on the apparent independence of amplitude from risetime at pressures between 2 and 4 bar at high drift fields, as shown in figure 6.16 for 4 bar. Only the events with the shortest risetime have a lower amplitude,

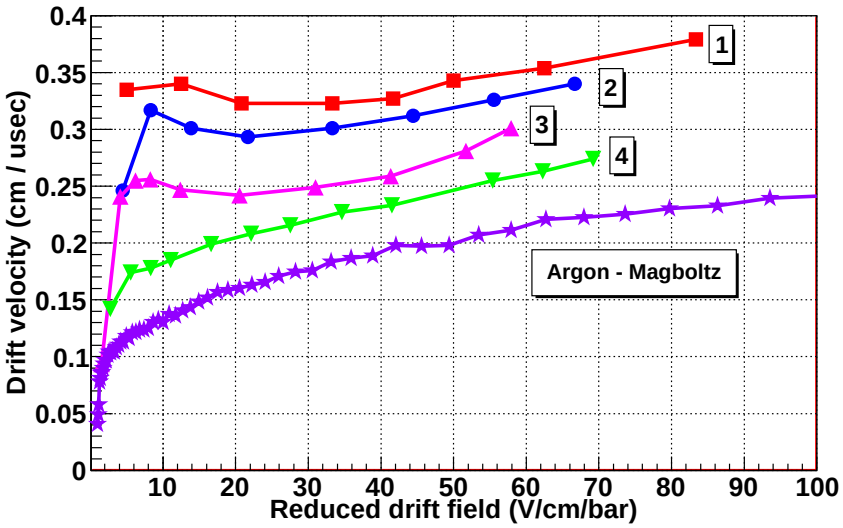

Figure 6.13: Dependence of the drift velocity with the reduced drift field for different data-taking in pure argon. Curves correspond to the 28th of July at 2 (1 - red squares) and 3 bar (2 - magenta triangles), to the 30th of July at 4 bar (3 - green inverted triangles) and to the 31st of July at 6 bar (4 - brown stars). As a comparison, the drift velocity in pure argon (violet stars) generated by the programme Magboltz is plotted.

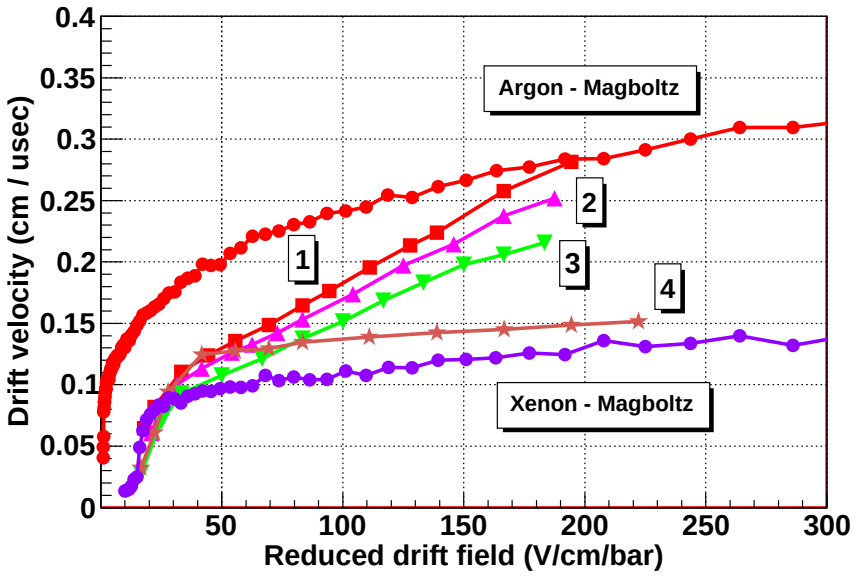

Figure 6.14: Dependence of the drift velocity with the reduced drift field for different data-taking in pure xenon. Curves correspond to the 3th of August at 3 (1 - red squares), 4 (2 - magenta triangles) and 5 bar (3 - green inverted triangles); and to the 11th of August at 3 bar (4 - brown stars). As a comparison, the drift velocity in pure argon (red circles) and pure xenon (blue circles) generated by the programme Magboltz is plotted.

which can be explained by a loss of charge at the source hole of the cathode. However, the positive linear dependence between amplitude and risetime does not disappear for any drift field

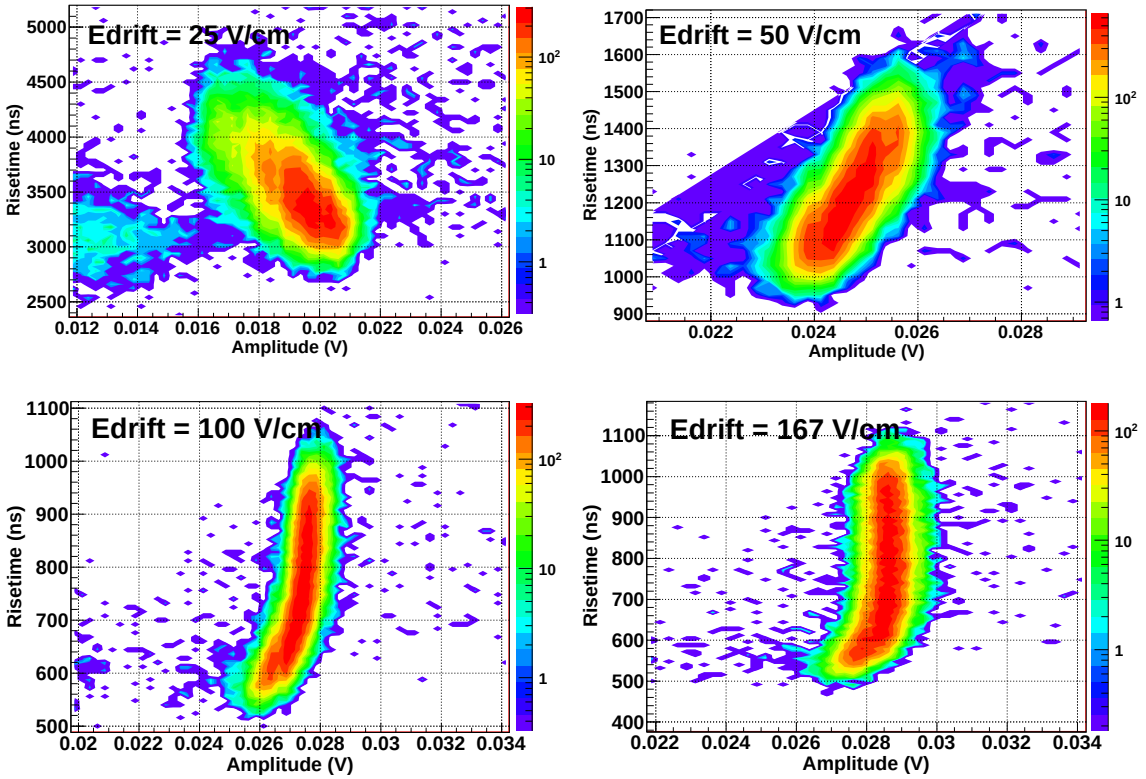

Figure 6.15: Risetime-amplitude distributions for a variable argon-isobutane mixture at 7 bar and different drift fields. Left upper corner: E = 25 V/cm; right upper corner: E = 50 V/cm; left down corner: E = 100 V/cm; right down corner: E = 166 V/cm. The gradation of color indicates the number of events in logarithmic scale.

at 5 bar, which means that some attachment cannot be avoided. This fact and the low gain are the reason why no data at higher pressure has been acquired.

In order to study the gas purity in our system, we have considered several gas and drift field conditions as follows. On the 3rd of August, pure xenon was introduced for the first time in the TPC, after having pumped the gas system and the vessel during all the weekend. A vacuum of 2.4×10^{-5} mbar and an outgassing level of 10^{-5} mbar l / s were reached. The night of the 3rd the gas was recirculated through the oxisorb filter for purification and data was taken at the same pressure. Due to sparks, the TPC was opened and pumped again during a whole day until a similar vacuum and outgassing level than previous day were reached. The pressures operated were 2 and 4 bar. The TPC was again opened and a new data was taken on the 10th August after a weekend-long pumping.

The mean electron lifetime has been calculated for these conditions and different drift fields, fitting the risetime-amplitude distributions like in section 5.4.4. The results are shown in figure 6.17 and in table 6.4. A lower limit of 0.6ms has been stablished for 3 and 4 bar. The exactitude of this bound is limited by the fit error, which is big if the amplitude is almost independent of the risetime. The values obtained are better than those of Saclay and very close to the required ones for drifting distances above 1 meter in pure xenon (60 ms) and mixtures of xenon and a quencher (6 ms).

We have observed at 5 bar that the maximum mean electron lifetime increased from 30.1 ± 0.6 to 38 ± 1 μs after a one-night recirculation through the oxisorb. This small improvement in the

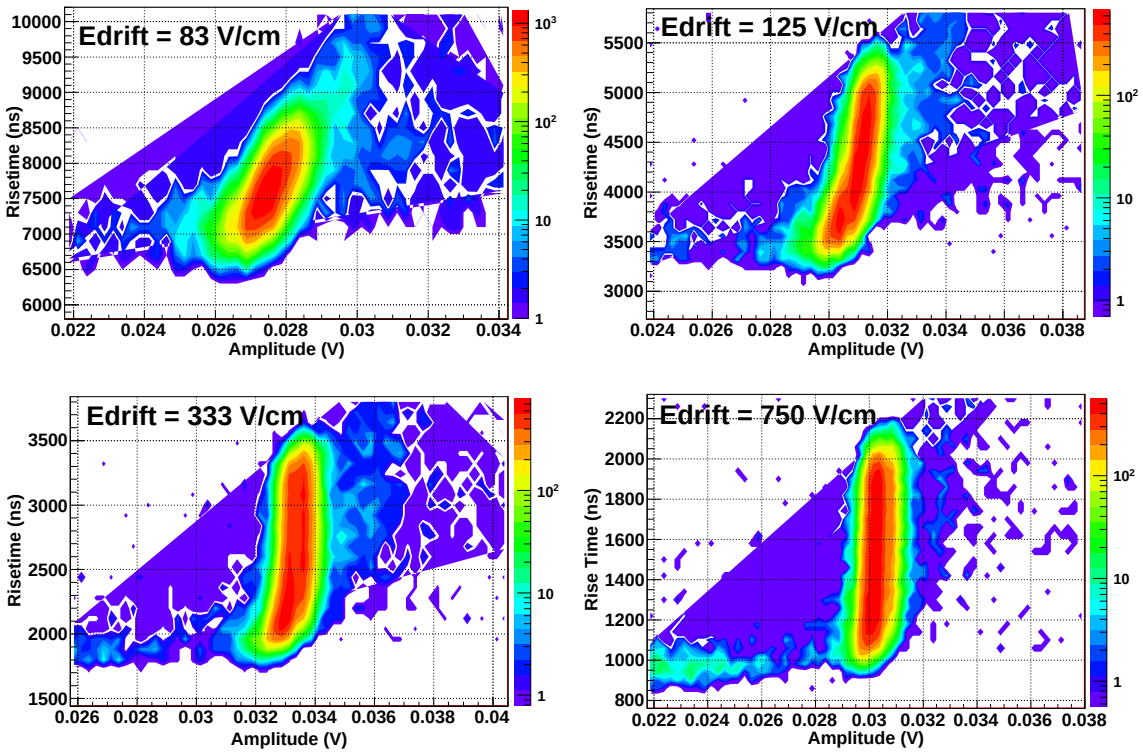

Figure 6.16: Risetime-amplitude distributions for for pure xenon at 4 bar and different drift fields. Left upper corner: E = 83 V/cm; right upper corner: E = 125 V/cm; left down corner: E = 333 V/cm; right down corner: E = 750 V/cm. The gradation of color indicates the number of events in logarithmic scale.

gas purity is positive as points out that longer lifetimes are feasible by the use of the SAES filter and a longer time of gas recirculation by the filters. In fact, the latest purification systems in liquid argon have reached a mean lifetime of 10 ms [168].

Day	Pressure bar	Max. electron lifetime μs	$[O_2]$ ppm
3rd	3	> 600	47 ± 1
	4	> 150	86 ± 1
	5	30.1 ± 0.6	72 ± 1
4th	5	38 ± 1	62 ± 1
6th	4	> 600	81 ± 1
10th	3	60 ± 2	194 ± 4

Table 6.4: Mean electron lifetime and oxygen concentration for different conditions in pure xenon measured in the Zaragoza's setup in August 2009.

If we suppose that the attachment is mainly due to an oxygen contamination of the gas, its concentration can be estimated using the equation 3.40 and the value of 61 ± 4 $\mu s^{-1} bar^{-2}$ for the $k(O_2, Xe)$. As shown in figure 6.18, the oxygen concentration reduces as the drift field is increased but as described in section 3.3.3, it is not oxygen that is reduced but the coefficient

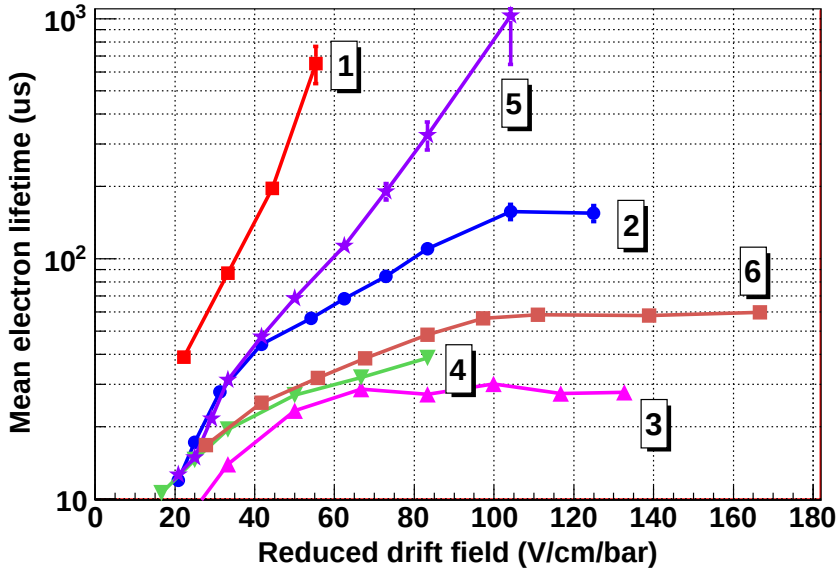

Figure 6.17: Dependence of the mean electron lifetime with the reduced drift field for different data-taking in pure xenon. On the 3rd of August we got data at 3 (1 - red squares), 4 (2 - blue circles) and 5 bar (3 - magenta triangles). After a one-night gas-recirculation through the oxysorb filter, we repeated the preassure of 5 bar (4 - inverted green triangles). Two days later we got data at 4 bar (5 - violet stars) and, on the 10th of August, at 3 bar (6 - brown squares).

$k(O_2, Xe)$. For estimating the concentration, we have to use drift fields near the thermal range, which is approximately 20 V/cm in pure xenon. These estimations are shown in table 6.4.

According to these results, a night-long gas recirculation through the oxisorb filter reduced the attachment from 80 to 60 ppm oxygen equivalent. This fact points out that longer recirculations times can further improve the gas purity. In addition, all values calculated clearly improve those obtained in Saclay setup, which were higher than 1000 ppm.

6.3.5 Energy resolution

Even if the source rate clearly affected the measurements, the values for the energy resolution were similar for the variable argon-isobutane mixture and better for pure gases than those obtained in Saclay. As an example, an energy spectrum obtained in this setup in pure xenon at 4 bar is shown in figure 6.19. In the next subsections, the measured and estimated values are discussed.

Measured energy resolution

The dependence of the energy resolution with the reduced drift field has been studied for the three gases at different pressures. For the variable argon-isobutane mixture and pure xenon, they are respectively shown in figures 6.20 and 6.21. From those plots, we can conclude:

- at low drift fields, values are worse due to attachment and pile-up effects. As the field is increased, a plateau is reached until the micromegas stops being transparent to electrons, which causes a degradation of energy resolution.

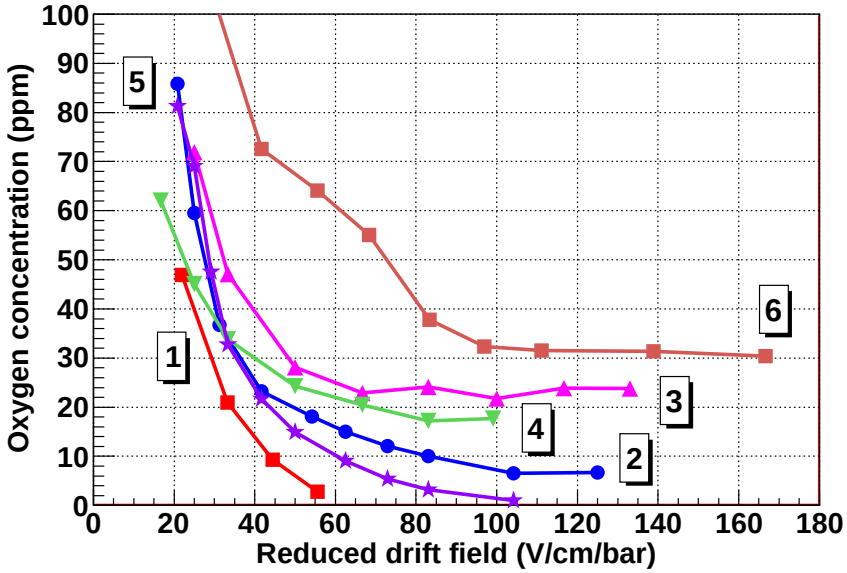

Figure 6.18: Dependence of the oxygen concentration with the reduced drift field for different data-taking in pure xenon. On the 3rd of August we got data at 3 (1 - red squares), 4 (2 - blue circles) and 5 bar (3 - magenta triangles). After a one-night gas-recirculation through the oxysorb filter, we repeated the preassure of 5 bar (4 - inverted green triangles). Two days later we got data at 4 bar (5 - orange stars) and, on the 10th of August, at 3 bar (6 - brown squares).

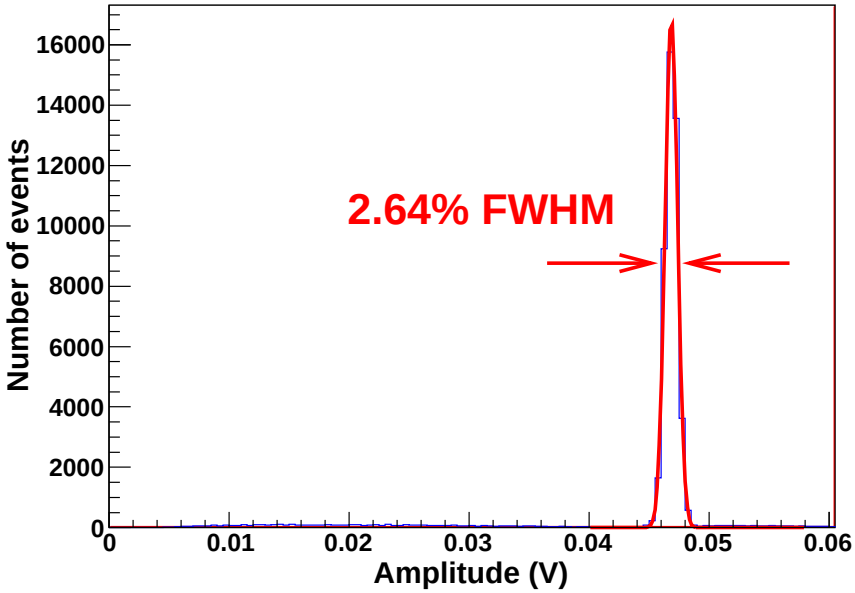

Figure 6.19: Example of an alpha peak measured at the Zaragoza's setup. The red line and the value for the energy resolution are the result of the fit to a Gaussian function.

- for low pressures, the length of the alpha tracks is greater than the readout radius. Inclinated alpha tracks are not well collected by the micromegas detector, which degrades the energy resolution. As the pressure is increased, a limit value is reached, which can only

be attributed to the intrinsic micromegas resolution, the source rate and the gas conditions (type of gas and level of attachment). For high pressures, values get worse due to attachment effects.

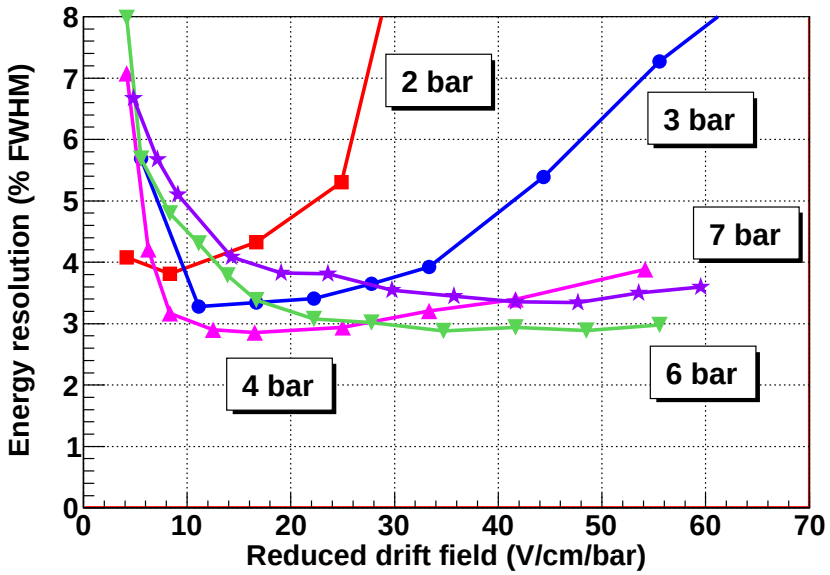

Figure 6.20: Dependence of the measured energy resolution (% FWHM) with the reduced drift field for the variable argon-isobutane mixture at 2 bar (red squares), 3 bar (blue circles), 4 bar (magenta triangles), 6 bar (inverted green triangles) and 7 bar (violet stars).

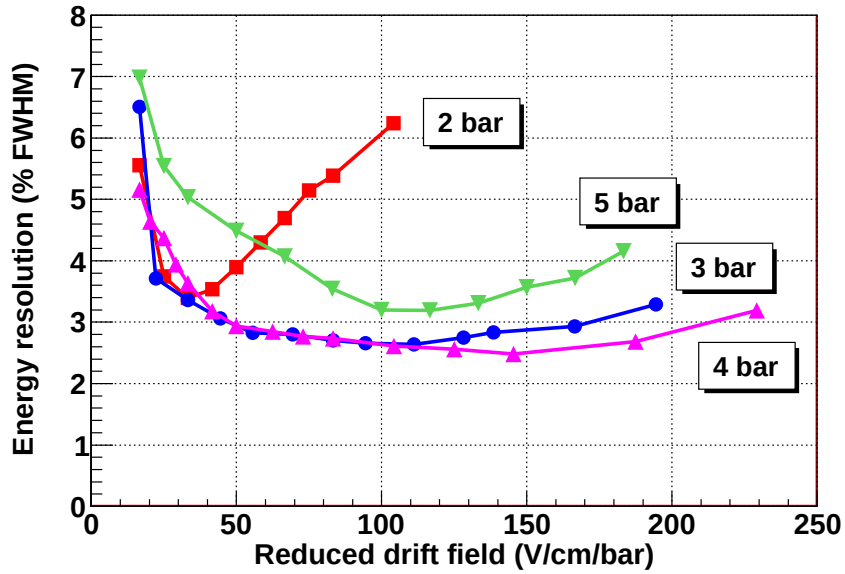

Figure 6.21: Dependence of the measured energy resolution (% FWHM) with the reduced drift field for pure xenon at 2 bar (red squares), 3 bar (blue circles), 4 bar (magenta triangles) and 5 bar (inverted green triangles).

Estimation in ideal conditions

In order to estimate the energy resolution in absence of attachment, diffusion and other effects, different selection of risetimes have been made to reduce the spread due to these effects. The length of this selection depends on the sampling bin of the Tektronix oscilloscope, whose possible values are 8, 20, 40 and 80 ns. The length chosen has been 25 for the two first cases, 40 for the third one and 80 for the last one.

The energy resolution depends on the risetime selection, as shown in figure 6.22. Events with a short risetime drift longer distances and, in consequence, suffer more the effects of attachment. This is why their energy spectrum has a worse energy resolution than a selection of events with a longer risetime. Note also that attachment still exists at high fields even if no clear effect is observed in the risetime-amplitude distribution because the correlation is covered by the width of the distribution.

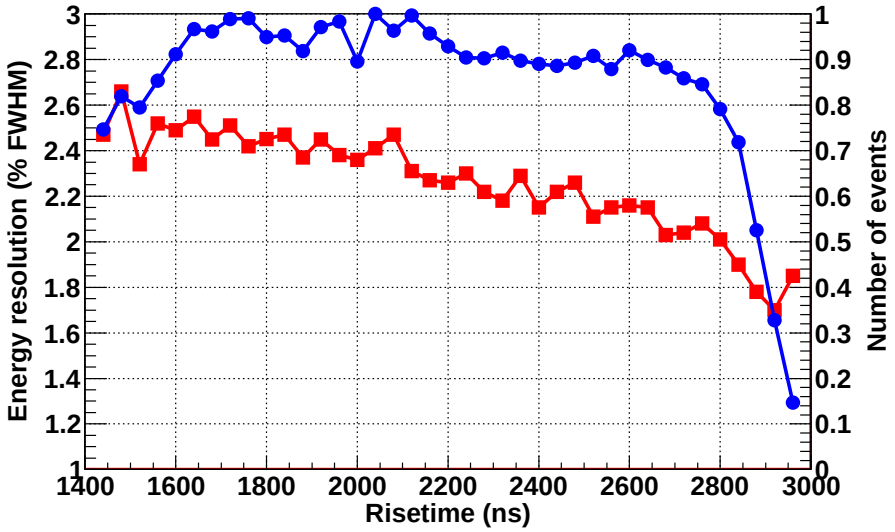

Figure 6.22: Dependence of the energy resolution (% FWHM) (red squares) and the number of events (blue circles) with the position of the selected risetimes for pure xenon at 4 bar and a drift field of 583 V/cm. The number of events has been normalized to the maximum (1454).

However, there is a sharp reduction in the number of points at the two ends of the event, which makes the results of the fit more uncertain. This is why before fitting each spectrum, a minimum number of 500 points was required to avoid errors due to low statistics. For each gas, pressure and drift field, the best value has been taken to get an estimation of the energy resolution in ideal conditions. The dependence of this estimation with the reduced drift field at different pressues for the variable argon-isobutane mixture and pure xenon is respectively shown in figures 6.23 and 6.24.

Summary

In table 6.5, the best values for the measured and estimated energy resolution are summarized.

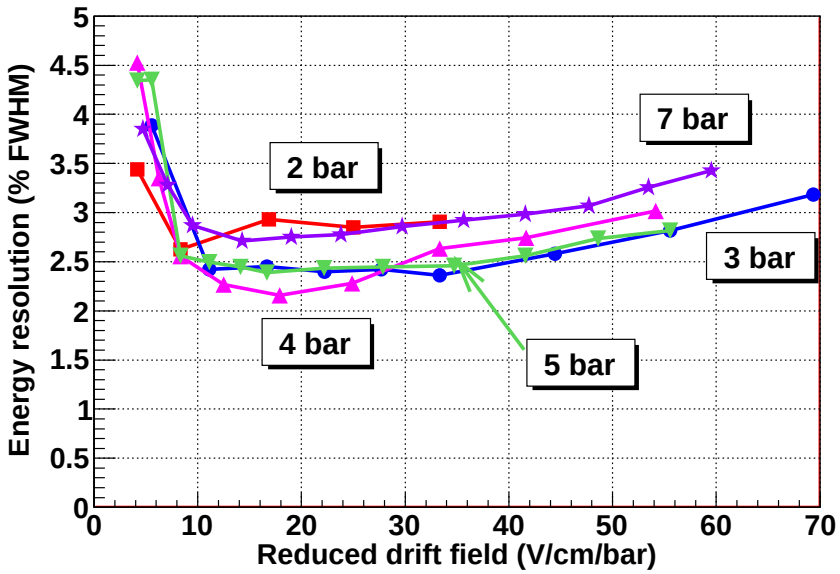

Figure 6.23: Dependence of the estimated energy resolution (% FWHM) with the reduced drift field for the variable argon-isobutane mixture at 2 bar (red squares), 3 bar (blue circles), 4 bar (magenta triangles), 6 bar (inverted green triangles) and 7 bar (violet stars).

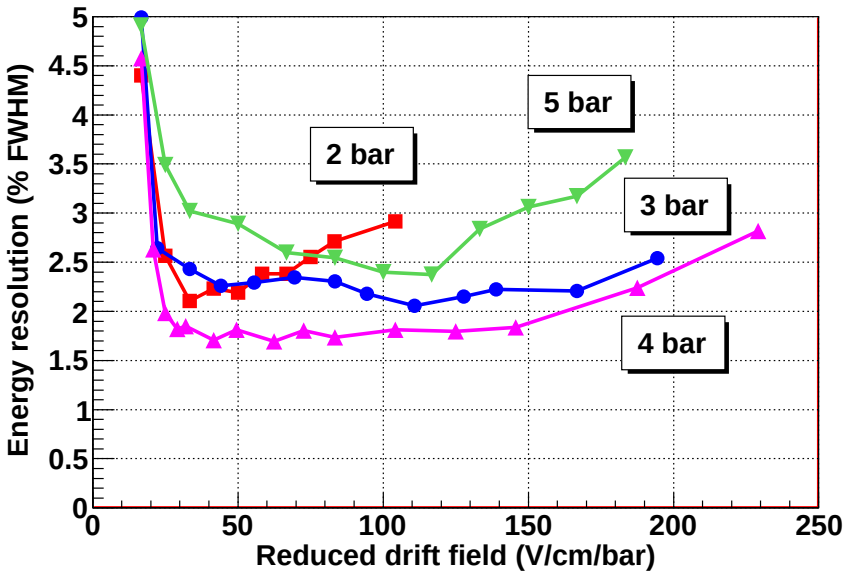

Figure 6.24: Dependence of the estimated energy resolution (% FWHM) with the reduced drift field for pure xenon at 2 bar (red squares), 3 bar (blue circles), 4 bar (magenta triangles) and 5 bar (inverted green triangles).

6.4 Conclusions

A new setup has been designed and built for testing micromegas readout for different gases and pressures up to 10 bar. The optimized design of the gas and vacuum system and a bake-out circuit has reduced the inside outgassing rate. The new drift structure and the detector support

Gas		Pressure (bar) 2	3	4	5	6	7
Argon+Iso	Measured	3.8	3.4	2.9	2.8	2.9	3.4
	Estimated	2.6	2.4	2.3	2.2	2.5	2.7
Argon	Measured	–	3.5	3.0	–	3.0	–
	Estimated	–	2.5	2.3	–	2.3	–
Xenon	Measured	3.4	2.7	2.5	3.2	–	–
	Estimated	2.2	2.2	1.8	2.4	–	–

Table 6.5: Measured and estimated energy resolution (% FWHM) in the argon-isobutane mixture, pure argon and pure xenon for different pressures.

makes the drift field more uniform and allows a better operation.

Some micromegas detectors have been tested with a gamma source in argon-isobutane mixtures (0.5 %, 1 % and 2 %) and pressures up to 10 bar. The transparency has pointed out a low level of attachment, later confirmed. The gain curves have been compared with theory, deducing two dependencies of the mean free electron path and the ionization threshold with pressure. Finally, a degradation of the energy resolution with pressure has been observed.

Alpha measurements made in Saclay have been repeated in the new setup. The source used has a high rate, which has clearly affected the gain and the electron transmission and possibly disturbed the energy resolution. Even so, the drift velocity in pure argon and xenon has been measured, in better agreement with theory than previous measurements. Energy resolution values for argon-based mixtures are similar to Saclay's values and are better for pure gases. Its dependence with drift field and pressure has also been observed.

The best value obtained in pure xenon is **2.5 %** FWHM at 4 bar. At the same pressure, a value of **1.8 %** FWHM has been estimated using a selection of risetimes. If we suppose that this value is also valid at 10 bar and the quenching factor is near 1, we deduce a value of **2.7 %** FWHM at 2480 keV. This is equivalent to an energy resolution of 1.1 % σ , i.e., 28.3 keV at $Q_{\beta\beta}$. The estimated value is a factor 2 better than the energy resolution of the Gothard experiment, which was 6.6 % FHWM.

Moreover, if the quenching factor of 6.5 given by the Gothard collaboration is instead supposed valid for pure xenon at 10 bar, the energy resolution reduces to **1.05 %** FWHM at 2480 keV. This value is equivalent to a 0.45 % σ, i.e., 11.1 keV at $Q_{\beta\beta}$. In any of these cases, we can conclude that the latest micromegas readouts are a competitive technology for the search of the double beta decay of ^{136}Xe.

In pure xenon, attachment effects are clearly lower than Saclay, as the amplitude is almost independent of risetime at pressures between 2 and 4 bar at high enough drift fields. This does not happen at 5 bar, which means that some attachment cannot be avoided. This observation has been quantified by the the mean electron lifetime. A lower limit for this variable of 0.6 ms has been stablished for 3 and 4 bar, limited by the estimation method. This bound is near the required value of 6 ms for a charge reduction of less than the 1 % in xenon-based mixtures and drift distances of about 1 meter. Therefore, the gas purity at 3 and 4 bar is almost the ideal one. At 5 bar, a maximum value of 38 ± 1 μs has been calculated.

In terms of the oxygen contamination, values around 80 ppm have been estimated for the first days and 60 ppm after one-night gas recirculation through the oxisorb filter. In addition, all

values calculated clearly improve those obtained in Saclay setup, which were higher than 1000 ppm.

The outgassing of plastic components is the main setup limitation, which causes a minimum outgassing rate of 10^{-5} mbar l / s. A reduction of the plastic components inside the TPC, a better bake-out system and the systematic recirculation of the gas by filters can further reduce the level of oxygen in the gas and increase the electron mean lifetime to values greater than 1 ms [168]. With this purity level and an alpha source with a lower rate, results will certainly be better.

Chapter 7

The design of a 100 kg TPC detector with Micromegas

A TPC with micromegas enriched in ^{136}Xe may detect the neutrinoless double beta decay ($\beta\beta0\nu$), which would imply new physics beyond the Standard Model. Even if only the standard mechanism ($\beta\beta2\nu$) were observed, information on the nuclear structure will be revealed. For those goals, apart from a good energy resolution, it is necessary to evaluate for the TPC the efficiency to signals, the level of background in the range of interest and the discrimination capabilities to reduce this level. With these three parameters and the energy resolution, the sensitivity of the detector can be evaluated.

In this chapter, the first two parameters (efficiency and background level) are evaluated in several conceptual designs of a Xenon TPC, in order to get conclusions on the possible geometry of the experiment. Two simulation codes have been created for this purpouse: a Geant4 programme, which simulates the physical interactions of particles in a geometry; and RESTSoft, a collection of c++ routines to simulate the charge creation, diffussion and pixelization in gas detectors; and to analyse these pixelized events.

The events generated have been used to evaluate the detector efficiency and the background level of the studied geometries in the ranges of interest of $\beta\beta2\nu$ and $\beta\beta0\nu$. The level of impurities of each material measured by different collaborations has been taken into account to scale the contaminations. The background rejection power of a Micromegas TPC detector will be discussed in the following chapter.

7.1 Simulation codes

The simulation chain is divided in three components: Decay0, Geant4 and RESTSoft. Each code covers a specific topic: generation of vertex, physical interactions, simulation of diffusion and pixelization, and analysis.

7.1.1 Initial particles: Decay0

The Decay0[169] is a FORTRAN code created in the 90s to generate events from the double beta decay and the decay of radioactive nuclides of all known unstable isotopes. It is divided in two parts, called:

- INIT, which reads all the parameters of the nucleus and its decays needed for the simulation. Data are taken from the libraries Evaluated Nuclear Structure Data File (ENSDF)

and Evaluated Atomic Data Library (EADL). ENSDF includes information on aproximately 2500 isotopes of the radioactive decays: decay modes, radiation type, parameters of nuclear levels and parameter of nuclear transitions. EADL contains data on atomic properties of isotopes: electron binding energies, electron capture subshell ratios, X rays and Auger electrons intensities.

- GENDEC is a Monte Carlo generator which creates an ASCII file with the emitted particles (energy, time of emission, direction and polarization). Each collection of particles of a specific decay is called an **event**.

For each background source, a Decay0 output file with 10^6 events is generated. As explained in section 7.2.2, a specific programme for signals has been created with a Decay0-format output. In the Geant4 programme, an interface to read Decay0-files has been created, so as the particles of each event could be used as the initial ones.

7.1.2 Physical simulation: Geant4

Geant4 (GEneration ANd Transport) [170, 171] is a programme for simulating the interactions of particles through matter in complex geometries. Althought it was initially conceived for high energy experiments, the most recent versions cover a wider range of fields like medicine, biology, aeronautic and radioprotection. This development has included the simulation of particles at low energy range, where double beta decay is included.

Geant4 includes a complete set of simulation tools: geometry description, definition of materials, interactions and transport of particles, detector response, events management and visualization. Physical libraries allow the study of matter-radiation interactions in a wide range of energies. Geant4 offers a wide library based on data publised by Particle Data Group (PDG), where particles and their main characteristics are defined. The code has also a modular design, which allows to use just the needed tools, optimizing the simulation.

As Geant4 has a modular design, a specific code has been developped. Its structure of classes is shown in figure 7.1. Each class has a specific task:

- *G4RunManager* is the control class. It is responsible for initializing some of them (geometry and physical processes) and execute the others (vertex definition, initial particles definition and processes simulation).
- *Manager* reads a configuration file where the geometry, the type of events and some output options are defined.
- *DetectorConstruction* defines the geometrical volumes and assigns them materials. It inherits from the predefined class G4VDetectorConstruction.
- *PhysicsList* defines the physical interactions of each particle and material and its accuracy. This last property is controlled by the step length of each interaction. It inherits from the predefined class G4VDetectorConstruction.
- *Hits* is a container class used to record information of the initial vertex, simulated particles and the hits. A hit is any deposition of energy in the gas, which excludes interactions at other possible volumes (vessel, shielding).
- *Generator* produces the initial particles (type, energy and direction) and the vertex from where they are emitted. A complete set of routines was created for generating a vertex at the different volumes of the geometry and for using events from a Decay0 output file. It inherits from the predefined class G4UserPrimaryGeneratorAction.

- *EventAction* initializes some variables before the simulation of an event. It inherits from the predefined class G4UserEventAction.
- *SteppingAction* adds to the class Hits the interactions in the gas that have deposited energy. It inherits from the predefined class G4UserSteppingAction.
- *DataOut* records in a binary file a simulated event, which was previously contained in the class Hits. It is possible to record only events which have deposited an energy in a specific range, keeping always the total number of simulated (and possibly not recorded) events.

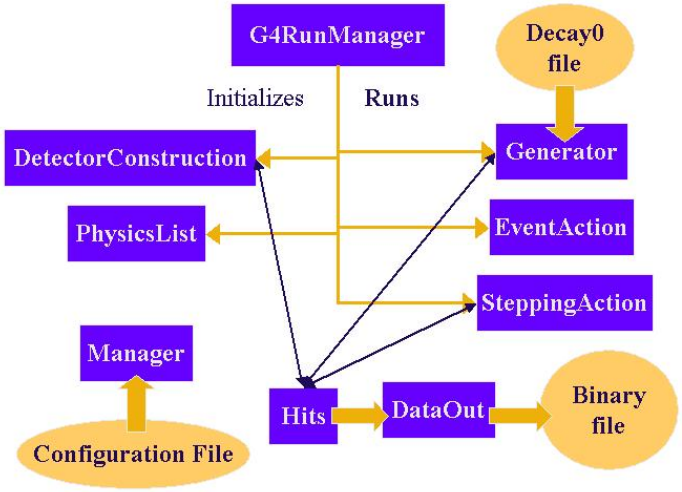

Figure 7.1: General sketch of the Geant4 simulation programme. The control class *G4RunManager* initializes the geometry (*DetectorConstruction*) and the physics (*PhysicsList*) and runs the vertex generator (*Generator*), the initialization of some variables before each simulation (*EventAction*) and records the physical interactions (*SteppingAction*). The class *Hits* contains all the information of the event and is recorded in a binary file by the class *DataOut*. The simulation is controlled by a configuration file, read by the class *Manager*.

One of the key points of any simulation is the selection of physical processes for each particle. A detailed description of this aspect is given in reference [172]. The processes chosen are

- for photons, photoelectric effect, Rayleigh effect, Compton dispersion and pair creation. Specific Geant4 routines for low energies (250 eV - 100 GeV) have been used.
- for electrons and positrons, multiple scattering, ionization, bremsstralung and positron anihilation. As for photons, low energy routines have been used.
- for ions, the multiple scattering, the ionization and the possible decays.

7.1.3 TPC simulation and analysis: RESTSoft

The output of the Geant4 simulation includes for each event a collection of energy depositions called hits. However, these are not what a TPC detects but charges, which would have previously drifted to the readout as explained in chapter 3. In order to simulate these specific features of a TPC detector and analyzing them, a library called RESTSoft has been developped in

collaboration with Alfredo Tomás Alquézar. The name stands for Software for Rare Event Searches with TPCs and was initially conceived by Igor G. Irastorza to deal with Dark Matter experiments in 2005. Later it was extended to the double beta case. The application of this programme to the dark matter case is explained in [5].

RESTSoft is written in C++ and is based on classes. It uses the library ROOT [173] for recording data in an optimized way and for making plots. RESTSoft has a modular design, i.e., it is composed of different methods to simulate each component of the TPC and to analyze the final events. Other features of this code are:

- the simulation of detector features like the diffusion of the electron clouds and the readout (pixelization).
- an interface with relevant tools like Srim [174], Geant4 or Magboltz [111].
- a common data format.

The general sketch for the double beta case is shown in figure 7.2. Four methods are used:

1. *ConversionPhys* takes each event from a Geant4 output file and records it in an object called TRestG4Event. This object contains the information of the initial particles and the list of hits. Each object is recorded in a branch of a tree, which is just a folder in ROOT language. An object called TRestSetup is also created, containing general information of the simulation like the dimensions of the detector or the gas name.

2. *ConversionDaq* converts a physical event coming from a Geant4 simulation to a pixelized event, as it would be seen by a micromegas detector. It is based on three auxiliar methods that create charge from energy depositions (TRestCharge), simulate gas diffusion effects (TRestDrift) and the pixelization according to the readout features (TRestPixel). Each converted event is recorded in an object called TRestDaqBB, which like physical objects is saved in a tree ROOT.

3. *Analysis* contains the algorithms for rejecting background events, which will be described in next chapter. The method defines a list of variables called observables. The analysis over each event gives a value for each observable recorded in *leaves* of a branch. Those objects are in ROOT language subfolders which keep a relation, i.e., it is possible to get for each analyzed event the values of all its observables.

4. *PlotAnalysis* loads a file with analysis observables and plots them in histograms. It is also possible to select events whose observables fulfil a condition. For instance, events which have deposited energy in a specific range.

Firstly, we will focus on the simulation of the TPC features. The charge created by an energy deposition is calculated as

$$Q(E_{dep}) = E_{dep}/W_{gas} \tag{7.1}$$

where E_{dep} is the energy of the deposition and W_{gas} is the mean energy necessary to create an ion-electron pair in the simulated gas. Values for W_{gas} have been taken from the table 3.1. For simplicity, charge fluctuations have not been taken into account, even if they are in most cases the main contribution to the energy resolution of a TPC. The validity of this approximation is discussed in section 7.2.2.

The second feature of a TPC to be simulated is diffusion. As explained in section 3.3.2, the width of an electron cloud is increased as it drifts to the readout. The width in the longitudinal

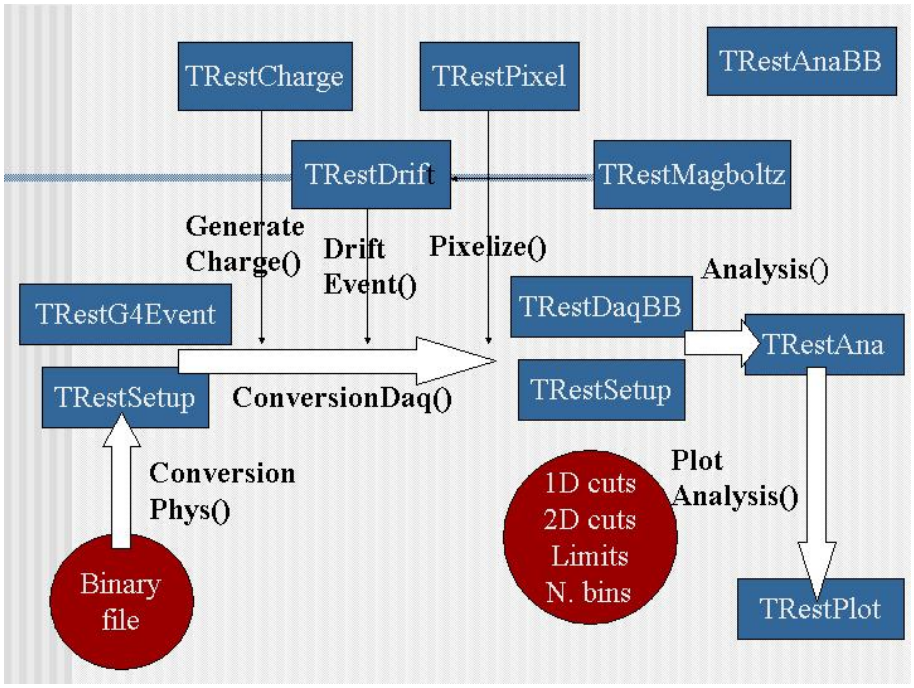

Figure 7.2: General sketch of the RESTSoft library for the double beta decay case. The binary files created by the Geant4 simulation are converted in a ROOT-format file by the method *ConversionPhys()*. The specific features of a TPC (charge generation, diffusion and pixelization) are simulated by *ConversionDaq*, which respectively uses the classes TRestCharge, TRestDrift and TRestPixel. The final events are analyzed by *Analysis()* and the results recorded in TRestAna. They are plotted by *PlotAnalysis()*, using the class TRestPlot.

(σ_L) and transversal directions (σ_T) can be calculated using the equation 3.30 and the diffusion coefficients previously generated by Magboltz. The coordinates of each charge due to diffusion follow a gaussian distribution, centered in the initial simulated point and with a sigmas the width previously calculated. The final coordinates of each charge are described by

$$\begin{aligned} x &= x_0 + \delta_T \ \cos(\alpha) \\ y &= y_0 + \delta_T \ \sin(\alpha) \\ z &= z_0 + \delta_L \end{aligned} \tag{7.2}$$

where (x_0, y_0, z_0) is the initial simulated position, α is an arbitrary angle in $[0, 2\pi]$ and δ_T and δ_L are two values generated by two gaussian distributions centered in 0 and whose sigmas are respectively σ_T and σ_L.

The granularity of the readout is simulated in the final step. Charges are grouped in pixels, boxes whose lengths are defined by the user according to the gas and the readout device features. In this step, charge is conserved.

7.2 Simulated events

A TPC detector investigating $\beta\beta$ decay will detect events of two types: signal and background. In the ^{136}Xe case, neither the two-neutrino nor the neutrinoless mode have been yet observed. The simulation of both modes is necessary to assess the detector efficiency and the background level. The description of both types is the main objective of this section.

7.2.1 Double beta decay in ^{136}Xe

The two modes of double beta decay have already been described in section 1.3.

- Two-neutrino mode:
$$^{136}_{54}\mathrm{Xe} \rightarrow ^{136}_{56}\mathrm{Ba} + \mathrm{e}^- + \mathrm{e}^- + \bar{\nu_e} + \bar{\nu_e} \tag{7.3}$$
- Neutrinoless mode:
$$^{136}_{54}\mathrm{Xe} \rightarrow ^{136}_{56}\mathrm{Ba} + \mathrm{e}^- + \mathrm{e}^- \tag{7.4}$$

The program Decay0 was planned to be used for the simulation of both modes, as it matches their angular distribution. For a comparison in the ^{76}Ge case, the reader is referred to [76]. However, the programme uses a different $Q_{\beta\beta}$ value for ^{136}Xe: 2458 keV instead of 2480 keV. Due to this fact and only for this case, a generator following the expressions 1.11 for the $\beta\beta2\nu$ and 1.19 for the $\beta\beta0\nu$ with the right value has been created and integrated in a programme which generates decay0-output-format files.

For a comparison with theory, 10^8 events of each mode have been generated and two cross-check plots have been made. One of them is the energy distribution of $\beta\beta2\nu$, shown in figure 7.3, which has its maximum at a third of $Q_{\beta\beta}$, as expected. The 3D histogram of the angle between the emitted electrons and the energy of one of the electrons is also plotted in figure 7.4. It matches the expected distribution, shown for example in [65]. These two comparisons show that events generated by this user-programme follow the theoretical expressions and can be used in a Geant4 simulation.

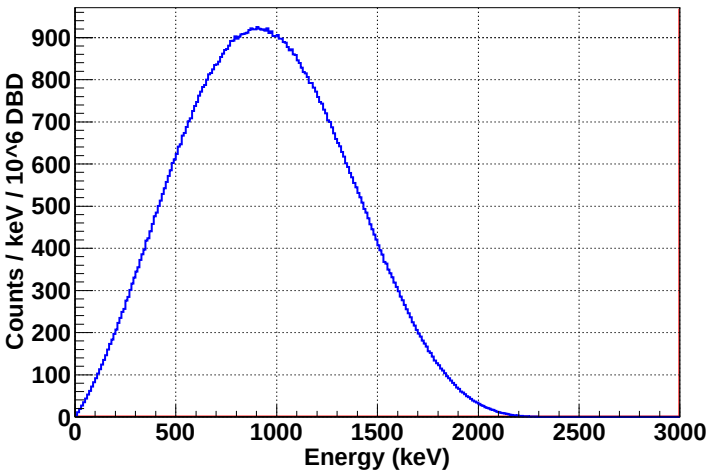

Figure 7.3: Energy distribution of the two electrons emitted in the $\beta\beta2\nu$ decay of ^{136}Xe generated by a user programme.

7.2.2 Backgrounds

As described in section 2.1, there are many components to take into account in the simulation of a detector background level. A first-look analysis can reduce them so as to obtain a reliable value with a time-limited simulation. In this study we must consider the nature of the contaminations and their origin (internal and external) and the range of interest of the deposited energy (RoI), which depends on the decay mode.

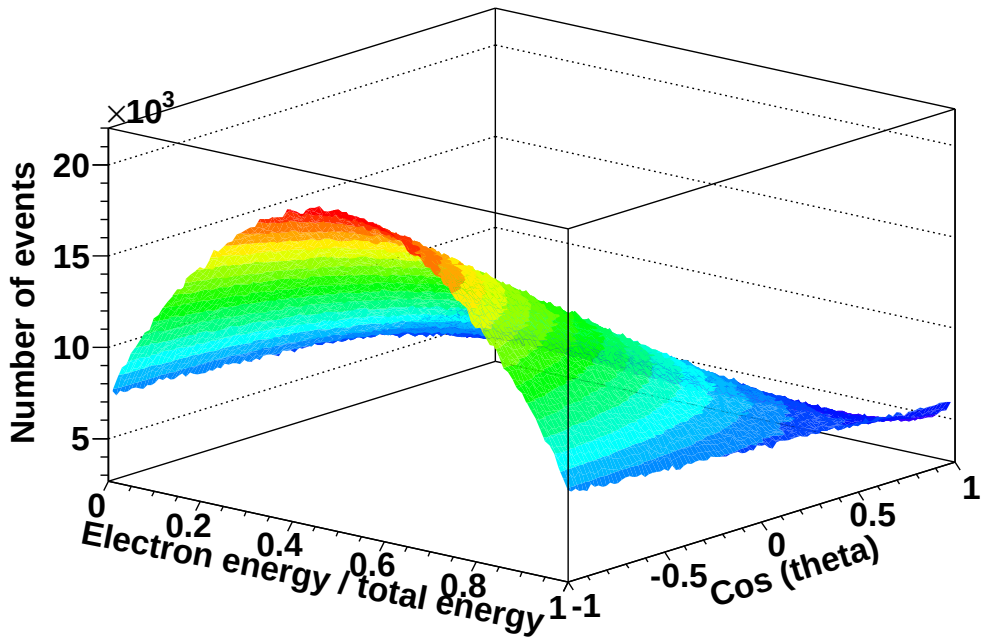

Figure 7.4: Distribution of the energy of one of the emitted electrons to the total energy and the angle between the emitted electrons in the $\beta\beta0\nu$ of ^{136}Xe generated by a user programme.

As shown in figure 7.3, the $\beta\beta2\nu$ spectrum has a range from 0 to 2480 keV, with a maximum around 820 keV. A RoI between 1 and 4 MeV has been chosen to get rid of the high background level at low energies in order to simplify simulations. For $\beta\beta0\nu$, an energy range between 2400 to 2560 keV has been defined. Two facts have been used in this decision:

- The range corresponds to a maximum energy resolution of 3 % FWHM at $Q_{\beta\beta}$. This value seems reasonable for pure xenon and xenon-based mixtures at pressures up to 10 bar, according to the results of chapters 5 and 6. Nevertheless, the objective is to reach a resolution of 1 % FWHM.
- A wide RoI is usefull for the understanding of all backgrounds near $Q_{\beta\beta}$ and to avoid any possible omission.

After the definition of the RoIs for both signals, the different background components are studied. They are classified in internal and external contaminations.

Internal contaminations

They consist in impurities in the detector itself or the materials used in the detector setup and shielding. If we consider the detector volume, the gas can be purified by recirculating through a filter. However, xenon can also be cosmogenically activated to ^{137}Xe by a neutron capture. This element decays a 67% as a beta of 4173 keV and a 30% as a beta of 3717.5 keV and a gamma of 455 keV. If xenon is activated during at least 100 days, there will be an activity of ^{137}Xe of 0.6 kg^{-1} yr^{-1} [175]. As its decay half-time is very short (3.8 minutes), this activity will be fastly reduced. In consequence, it can be neglected in this study.

There is an intrinsic contribution of the $\beta\beta2\nu$ to the RoI of the $\beta\beta0\nu$, which is mainly determinated by the halftime of the first mode and the energy resolution at $Q_{\beta\beta}$. In a detector with

an energy resolution of 3 % FWHM, the fraction of $\beta\beta2\nu$ events in the RoI of the neutrinoless mode is 3×10^{-8}, according to equation 2.2. This fraction corresponds to a level of background of 6×10^{-7} counts keV^{-1} kg^{-1} yr^{-1}, for a half-time $T^{0\nu}_{1/2} = 10^{22}$ yr, which is the lowest expected value for ^{136}Xe. Therefore, it can be neglected.

The materials for the detector setup and shielding contain impurities of radioactive elements. Natural decay chains of ^{232}Th and ^{238}U and others like ^{40}K, ^{137}Cs and ^{60}Co, are the most important ones. The ^{40}K decay consists of a gamma emission of 1460 keV and is only relevant for the $\beta\beta2\nu$ case. ^{137}Cs decay has a Q-value of 1175 keV, near the lower bound of the $\beta\beta2\nu$ RoI. For simplicity, it is not considered but it will be later taken into account in the discussion. ^{60}Co decay consists of a beta emission of 318 keV and two gammas of 1173 keV and 1332 keV. A wide range of physical processes can make these three particles deposit a total energy in the RoIs of $\beta\beta2\nu$ and $\beta\beta0\nu$.

^{232}Th decay chain

Beta decays of the ^{232}Th decay chain are shown at table 7.1. Alpha decays are omitted because they can be easily discriminated due to their short track and their deposition of energy near the container walls. Only ^{208}Tl, ^{212}Bi ^{228}Ac have a Q-value greater than 1 MeV. As shown in figure 7.5, ^{208}Tl decay has a probability of a 99 % to emit a gamma of 2614.5 keV, which can deposit an energy in the RoI of $\beta\beta0\nu$ by different processes, which will be later explained in section 8.1. The two other decays should be only considered in the two-neutrino case.

Decay	Energy (keV)	Intensity (%)
$^{208}Tl \rightarrow {}^{208}Pb$	5001.2	36.0
$^{212}Bi \rightarrow {}^{212}Po$	2254.0	64.0
$^{228}Ac \rightarrow {}^{228}Th$	2127.3	100.0
$^{212}Pb \rightarrow {}^{212}Bi$	573.8	100.0
$^{228}Ra \rightarrow {}^{228}Ac$	45.9	100.0

Table 7.1: Beta emissions of the ^{232}Th natural decay chain.

^{238}U decay chain

Beta decays of the ^{238}U decay chain are shown at table 7.2. For the same reason as in the ^{232}Th case, alpha decays are omitted. Note that only four elements have a Q-value greater than 1 MeV and a branching ratio greater than 1%. ^{210}Bi and ^{214}Pb have a Q-value near 1 MeV and can be omitted for simplicity. ^{234m}Pa has no gamma emissions greater than 1 MeV with a probability greater than 0.01 % [176]. As it will be shown later, this emission from the outer parts of the setup has a neglilible effect.

For the ^{214}Bi decay, the schema of levels is shown in figure 7.6. There is a beta emission with an energy of 3272 keV and a gamma emission of 2447 keV combined with a beta emission of 824 keV. In consequence, many initial particles can produce events in the two studied RoI.

In summary, contaminations due to ^{208}Tl, ^{214}Bi and ^{60}Co have to be considered to calculate the level of background in the RoI of $\beta\beta0\nu$. Apart from these three impurities, the isotopes ^{40}K, ^{212}Bi, ^{228}Ac and ^{234m}Pa should be also added in the two-neutrino case for energies higher than 1200 keV.

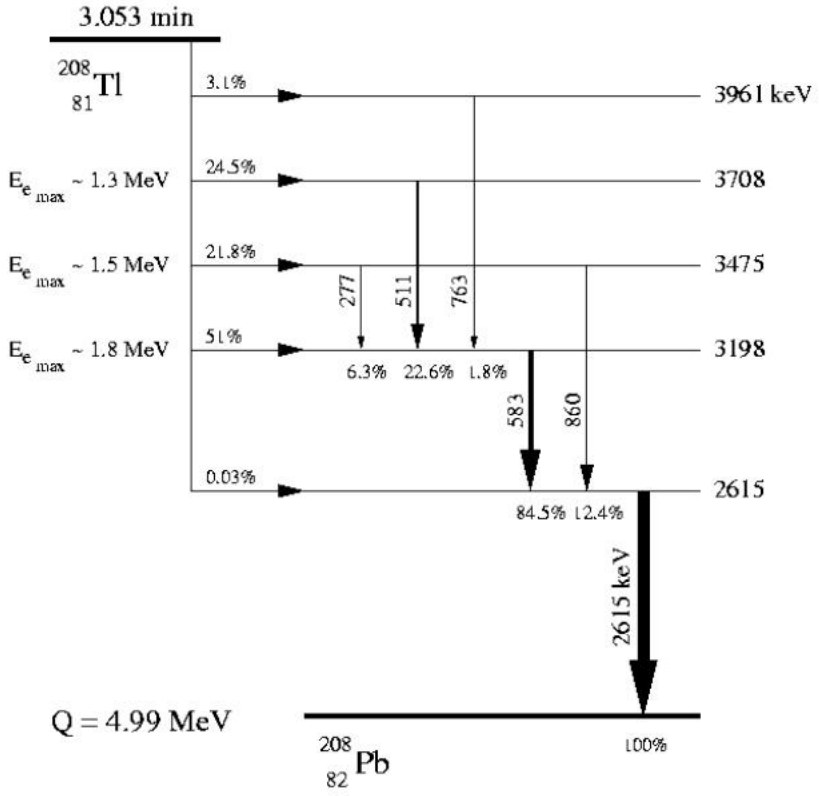

Figure 7.5: Decay scheme of ^{208}Tl. The horizontal arrows are β^- decays and the vertical arrows are γ decays. The percentages indicate the decay probability.

Decay	Energy (keV)	Intensity (%)
$^{214}Bi \rightarrow {}^{214}Po$	3272.0	99.08
$^{234m}Pa \rightarrow {}^{234}U$	2195.0	99.9
$^{210}Bi \rightarrow {}^{210}Po$	1162.1	$\approx$ 100.0
$^{214}Pb \rightarrow {}^{214}Bi$	1024.0	99.98
$^{234}Th \rightarrow {}^{234m}Pa$	273.0	100.0
$^{210}Pb \rightarrow {}^{210}Bi$	63.5	100.0
$^{210}Tl \rightarrow {}^{210}Pb$	5489.0	0.02
$^{206}Tl \rightarrow {}^{206}Pb$	1533.5	0.00013
$^{218}Po \rightarrow {}^{218}Ac$	265.0	0.02

Table 7.2: Beta emissions of the ^{238}U natural decay chain.

External contaminations

From the external contaminations, those generated by cosmic radiation (like muons) can be neglected if the detector is supposed to be placed in an underground laboratory [75]. Even without this component, the walls of this facility contain the natural chains presented in the setup materials. As they are generated outside the setup, only gammas are able to deposit energy in the detector. However, its contribution can be even higher than the internal one.

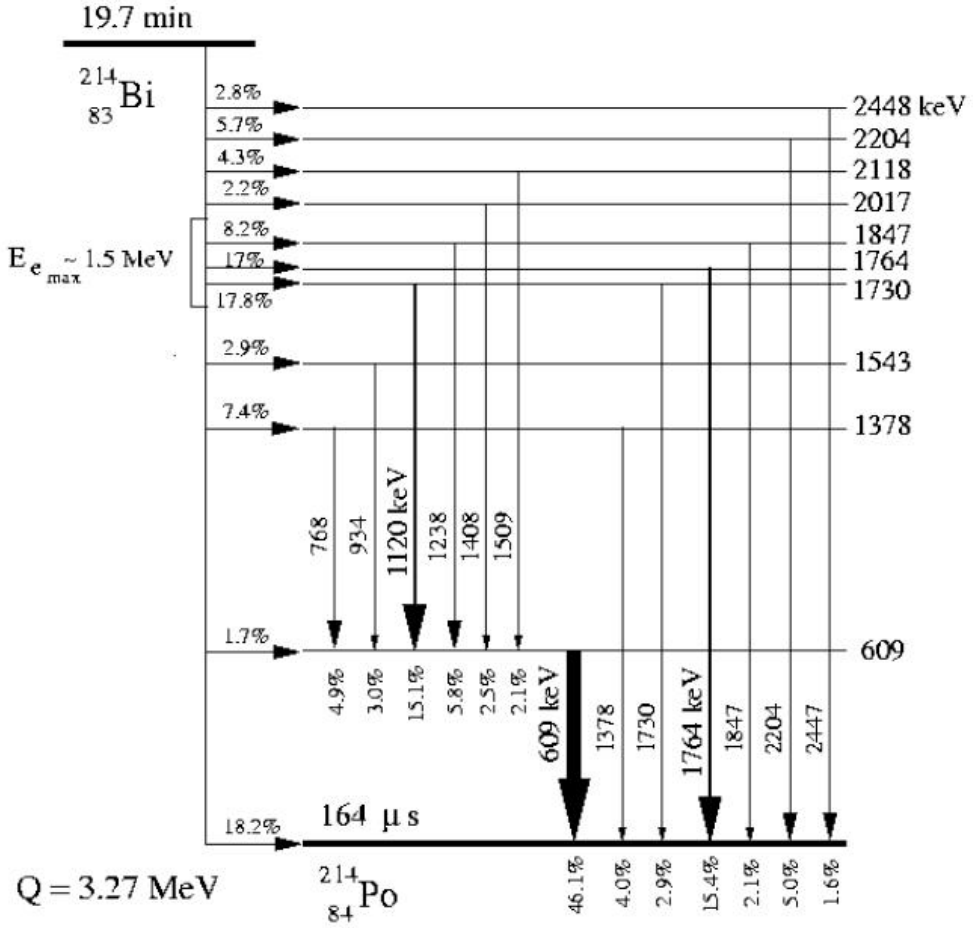

Figure 7.6: Decay scheme of ^{214}Bi. The horizontal arrows are β^- decays and the vertical arrows are γ decays. The percentages indicate the decay probability.

If we consider the flow of 2614.5 keV γs generated by ^{208}Tl measured in the Canfranc Underground Laboratory (0.17 γ cm^{-2} [74]), the level of background is 8.4×10^3 counts keV^{-1} kg^{-1} yr^{-1} in absence of shielding. This value is three orders of magnitude higher than the total internal contribution, as shown in section 7.4.3. However, it reduces to 2.8×10^2 (2.5×10) with a lead shielding of 5 (10) cm and a thicker shielding would surely reduce this contribution to negligible levels.

7.3 Geometry design

Gas detectors do not have a common design like germanium detectors, where a coaxial configuration is preferred. As a first approach, we have considered a cylindrical TPC with its inner diameter equal to its inner height. In this way, the ratio of the inner area and volume is minimized and the probability that a double beta event is fully contained in detector is maximized. This means an increase of the intrinsic detector efficiency. The gas pressure has been fixed to 10 bar and the diameter to 140 cm. Those values imply a volume of 2.155×10^3 liters, i.e., a total detector mass of 118.48 kg at 20°C.

In this study, the gas has been supposed to be a xenon-based mixture with a quencher, in order to increase the drift velocity and to reduce the diffusion coefficients to less than 100

cm/μs at 10 bar, as shown for 1 % of CH_4 in figure 3.8. This value has been used for the longitudinal and transversal diffusion coefficients in the simulation. In addition, the granularity of the micromegas has been fixed to a realistic pixel size of 5×5 mm^2 and a resolution time equivalent to a 5-mm length.

The second element to be defined is the vessel. Many materials can be used to contain gas like aluminium, stainless steel, copper ... Aluminium is a porous material and increases the time necessary to reduce the outgassing rate of the inner walls. The second one (stainless steel) has better characteristics to reach ultra-low vacuum and outgassing rates and is mechanically adequate due to its rigidity. According to [177], a cylindrical vessel with a wall thickness of only 1 cm can be leak-tight at pressures up to 15 bar. In reality, the two caps should be made spherical for avoiding tension peaks but as a first approximation, we can consider them plain.

The only drawback of stainless steel is its level of impurities. As shown in table 7.3, ^{208}Tl and ^{214}Bi contamination levels are about 1 mBq/kg and ^{60}Co level is higher than 5.5 mBq/kg. If we compare stainless steel with copper, shown in table 7.4, we note that there is an order of magnitude between the achievable level of impurities for each materal. Typical contaminations in stainless steel are about 1 mBq/kg, in contrast to the maximum levels of 0.1 mBq/kg for copper (reached in Oxygen-Free High Conductivity Copper, briefly called OFHC). The best values obtained for copper are those published by the EXO collaboration, with values of the order of μBq/kg.

Experiment	^{40}K	^{60}Co	^{208}Tl	^{228}Ac	^{214}Bi	^{234m}Pa	Ref.
Edelweiss	< 9	16 ± 10	< 2	< 2	< 3	–	[178]
Gerda	< 0.93	14 ± 0.1	< 0.04	< 0.11	< 12	< 12	[179]
	< 0.81	18.3 ± 0.7	0.54 ± 0.07	1.5 ± 0.2	54 ± 16	54 ± 16	
Rosebud	< 20	30 ± 2	10 ± 2	10 ± 2	< 10	–	[178]
Xenon	< 9	5.5 ± 0.6	< 0.69	< 1.9	< 1.7	< 1.7	[180]

Table 7.3: Levels of impurities in mBq/kg for stainless steel measured by different collaborations. Gerda and Xenon values have been calculated supossing a balance in ^{238}U and ^{232}Th decay chains.

Experiment	^{40}K	^{60}Co	^{208}Tl	^{228}Ac	^{214}Bi	^{234m}Pa	Ref.
Edelweiss	< 6	11 ± 0.5	< 0.5	–	< 1	–	[178]
	< 7	1.0 ± 0.4	< 0.85	–	< 1.3	–	
EXO	< 1	–	< 0.003	–	< 0.014	–	[22]
Rosebud	< 4	< 0.2	< 0.5	–	< 2	–	[178]
Xenon	< 0.06	< 0.0045	< 0.011	< 0.03	< 0.07	< 0.07	[180]

Table 7.4: Levels of impurities in mBq/kg for copper measured by different collaborations. Xenon values have been estimated considering a balance in ^{238}U and ^{232}Th decay chains.

For this reason, copper is normally chosen in ultra-low background experiments. For example, the Gothard collaboration used a 5 cm-thick copper vessel, tested for pressures up to 15 bar [13]. However, the construction of a vessel with walls of less thickness requires a mechanical simulation of each design considering the real yield strength of each material [177]. For OFHC copper,

values vary between 69 and 353 MPa. Several designs have been mechanically simulated with gas pressures up to 15 bar. Plain caps have been totally discarded due to the big deformation that will suffer, as shown in figure 7.7 for a 2 cm-thick copper vessel.

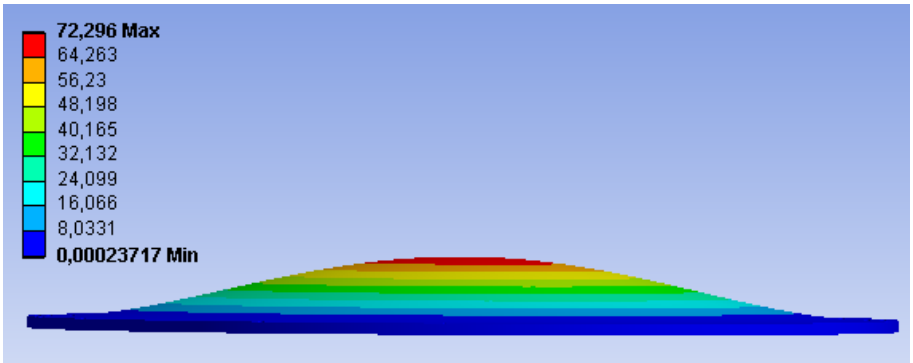

Figure 7.7: The deformation caused by pressurized gas at 15 bar in one plain cap of a cylindrical copper vessel of 20 mm of thickness [177]. The maximum deformation is 75 mm, situated at the center of the cap.

A spherical design for the caps seems more feasible. In a 2 cm-thick cylindrical vessel with two spherical caps jointed with copper screws, the maximum tensions have been observed in the screws, with values up to 55 MPa. Meanwhile, the caps and the cylindrical piece have uniform tensions of 30 MPa. If a copper with a yield strength higher than 110 MPa is used, this design will be feasible. As this question requires a more detailed study, we have simulated a stainless steel vessel of 1 cm thickness. Nevetheless, the background of a 1 cm-thick copper vessel has been estimated according to simulations results.

Another element to be defined is the shielding. Because stainless steel is not ultrapure, we have studied the effect of a copper layer between the gas and the vessel. This part is supposed to have no mechanical function, only to reduce the background generated by stainless steel. In addition to, an archeological lead cover of at least 20 cm outside the vessel is defined in order to reduce the external background to levels lower than internal ones. As shown at table 7.5, roman lead has a very low level of impurities. In many cases, only upper limits have been set.

Experiment	^{40}K	^{60}Co	^{208}Tl	^{228}Ac	^{214}Bi	^{234m}Pa	Ref.
Edelweiss	–	–	< 0.0008	–	< 0.003	–	[178]
HDM	0.44 ± 0.14	0.18 ± 0.02	< 0.008	< 0.022	< 0.0029	< 0.029	[181]
Xenon	< 28	< 0.19	< 1.5	< 3.9	< 6.8	< 6.8	[180]

Table 7.5: Levels of impurities in mBq/kg for lead measured by different collaborations.

For computational reasons, only the first 5 cm of the lead shielding have been simulated. This approximation is reasonable as the main part of the events which deposit energy in the detector are generated in this volume. This is due to the self-shielding effect of materials.

With these considerations, three geometries have been simulated depending on the thickness of the inner copper layer: no copper, 1 cm and 6 cm. Another geometry, which consists of a 1 cm-thick copper vessel and 5 cm-thick lead shielding has been estimated with the results of the

copper shielding of the second geometry and the lead shielding of the first geometry. This value should be exactly calculated in a simulation.

A summary of the three geometries is shown in table 7.6 and a view of a geometry with a copper cover is shown in figure 7.8. For each material, the background activities in table 7.7 are used to scale the importance of each component. Those values have been chosen taking into account tables 7.3, 7.4 and 7.5.

	Cover (copper)		Vessel (stainless steel)		Shielding (lead)	
Geometry	Thick(mm)	Mass(kg)	Thick(mm)	Mass(kg)	Thick(mm)	Mass(kg)
1	–	–	10.0	736	50.0	5776
2	10.0	840	10.0	756	50.0	5934
3	60.0	5404	10.0	866	50.0	6757

Table 7.6: Summary of the thicknesses and masses of each volume of the three geometries simulated in this work.

Material	^{60}Co	^{40}K	^{208}Tl	^{212}Bi	^{228}Ac	^{214}Bi	^{234m}Pa
Stainless steel	1.0	1.0	1.0	1.0	1.0	1.0	1.0
Copper	0.1	0.1	0.1	0.1	0.1	0.1	0.1
Lead	0.1	0.1	0.01	0.01	0.01	0.01	0.01

Table 7.7: Activities in mBq/kg of each impurity and material used for scaling the different background contributions.

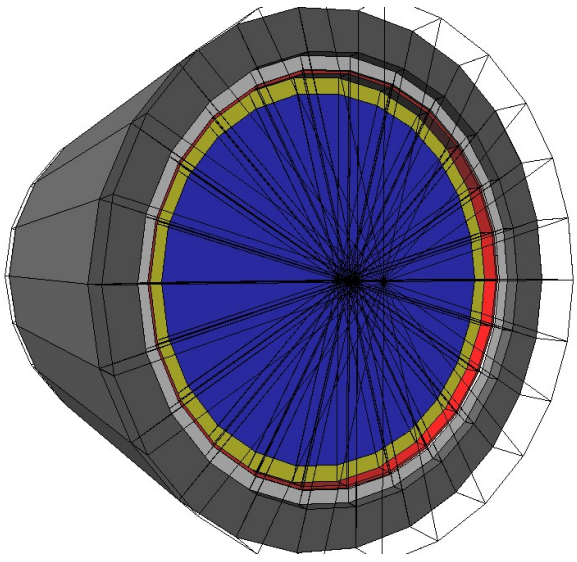

Figure 7.8: The simulated geometry with a 6 cm-thick cover. Top volumes are tranparent in this view. From the inside to the outside: the gas (blue volume), the copper cover (yellow volume), the stainless steel vessel (red volume), the 5 cm-thick lead shielding (white volume) and a 15 cm-thick lead shielding (dark grey volume).

7.4 Simulation results

After the definition of the geometry, the signals and the contaminations, a preliminary study of the sensitivity that could reach a MMTPC (Micromegas TPC) to double beta decay signals has been carried out. It takes into account the efficiency to $\beta\beta2\nu$ and $\beta\beta0\nu$ signals and the level of background in each geometry. As later explained, values are not so good. This fact shows the necessity of studying the topology of events in order to create discriminations methods.

7.4.1 Detector efficiency

The (geometrical) efficiency of the detector can be calculated simulating double beta events. The two energy spectra generated by $\beta\beta2\nu$ and $\beta\beta0\nu$ are shown in figure 7.9. The quantification of the efficiency to the two-neutrino mode is a difficult question as a continuous spectrum from 0 to 2480 keV is generated and the efficiency depends strongly on the range of energy. If it is defined between 100 and 4000 keV, the efficiency is 99.4 %. For the neutrinoless mode, the RoI is used and an efficiency of 72.4 % is obtained. These values are the same for the three geometry considered.

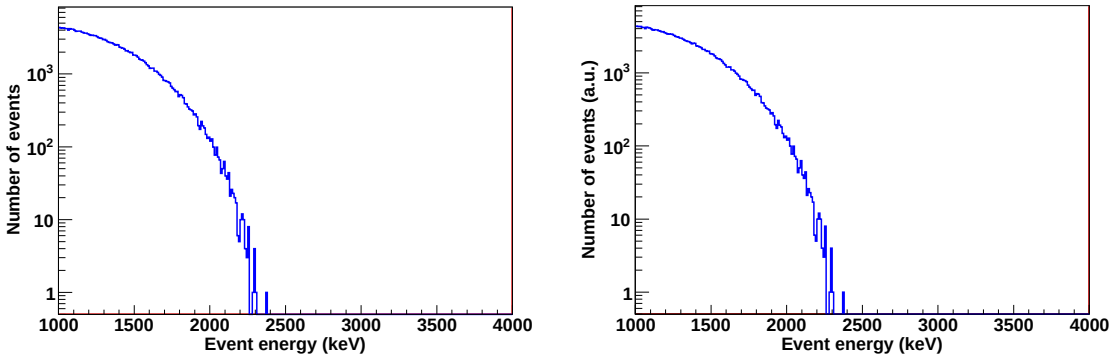

Figure 7.9: Energy spectra generated in the detector by the $\beta\beta2\nu$ and $\beta\beta0\nu$ signals respectively.

7.4.2 Background of the two-neutrino mode

The different contamination sources defined in section 7.2.2 have been simulated in each component of the three geometries defined. The spectra obtained between 1 and 4 MeV are shown in figure 7.10 for these geometries and the estimation for the copper vessel. As a comparison, we have calculated the expected signal for NEXT if the xenon were enriched an 80 % in ^{136}Xe and the $\beta\beta2\nu$ decay had respectively a half-time of 3.6×10^{20} yr (Gothard limit) or 1.6×10^{22} yr (DAMA limit).

The levels of background of the stainless steel designs are not far from the limit established by Gothard and the design with the copper vessel will improve this result. However, there is more than an order of magnitude in comparison with DAMA. The necessary background reduction to make comparable both signals has been calculated using the range of energy between 1200 and 1300 keV. The upper value has been chosen because it is not very far from the maximum of the $\beta\beta2\nu$ spectrum (at 827 keV) and from the highest Q-values of the discarded contaminations: 1175 keV for ^{137}Cs and 1162 keV for ^{210}Bi.

The limits set by Gothard and DAMA in this range of energy are 4.58 ± 0.02 and 0.103 ± 0.001 counts keV^{-1} kg^{-1} yr^{-1} respectively. In contrast, the lowest background level of the stainless

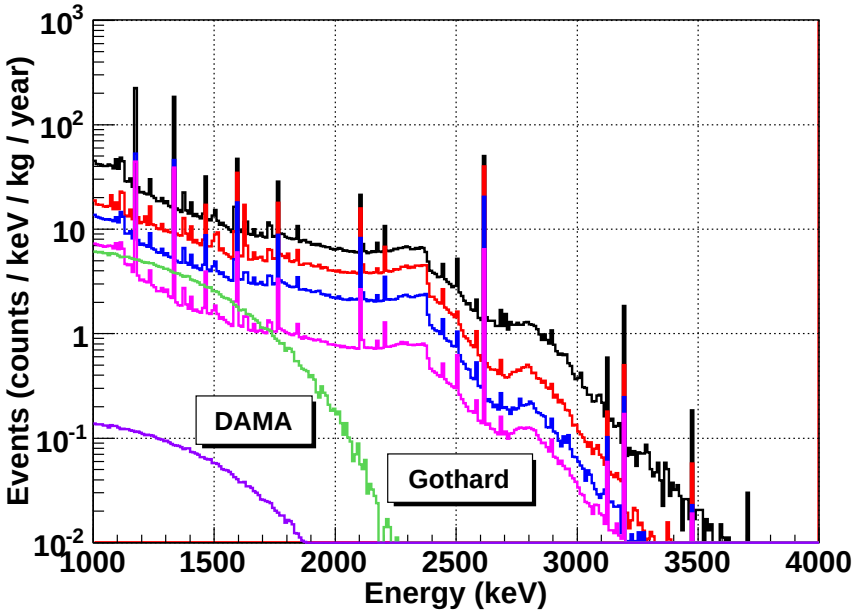

Figure 7.10: Internal background spectrum between 1 and 4 MeV for each simulated geometry: without copper (black line, top), with a 1 cm-thick copper cover (red line, middle-top) and with a 6 cm-thick one (blue line, middle-bottom). It is also plotted the estimated spectrum of a 1 cm-thick copper vessel with a 5 cm-thick lead shielding (magenta line, bottom). As a comparison, the $\beta\beta2\nu$ signal expected in NEXT enriched an 80 % in ^{136}Xe and the best limits set on $T^{2\nu}_{1/2}$ by Gothard (green line) and DAMA (violet line).

steel designs is 6.76 ± 0.01 counts keV^{-1} kg^{-1} yr^{-1} for the geometry with the 6 cm-thick copper cover, as shown in table 7.8. In consequence, a minimum reduction factor of 60 is necessary to make the level of background comparable to DAMA. In the case of the copper vessel, we obtain a value of 3.08 ± 0.01 counts keV^{-1} kg^{-1} yr^{-1}, a factor 2 better than that of the 6 cm-thick copper cover but still far from the DAMA limit.

	1 cm stainless steel vessel			
Geometry	No Cu	1 cm Cu	6 cm Cu	Cu vessel
Cover	–	2.132 ± 0.004	5.28 ± 0.01	–
Vessel	20.21 ± 0.05	12.64 ± 0.03	1.402 ± 0.004	2.132 ± 0.004
Shielding	0.946 ± 0.007	0.592 ± 0.006	$(7.37 \pm 0.09) \times 10^{-2}$	0.946 ± 0.007
Total	21.16 ± 0.05	15.37 ± 0.03	6.76 ± 0.01	3.078 ± 0.008

Table 7.8: Total background levels and contributions of each volume in the range of energy between 1200 and 1300 keV. Values are expressed in counts keV^{-1} kg^{-1} yr^{-1}.

A 1 cm-thick copper cover reduces the total background of a stainless steel vessel a 27 %. This values is almost a 69 % if its thickness is 6 cm, which is equivalent to a reduction factor of 3. In this case, the main contribution is not due to the stainless steel vessel but to the copper cover. This fact advises against a further increase of the cover thickness to reduce the background. We note also that the lead shielding generates less than the 5 % of the background events.

In figure 7.11, the contributions of each contamination to the background for the geometry without copper are shown. It is clear that the most important ones are ^{208}Tl, ^{214}Bi and ^{60}Co. According to table 7.9, they represent about the 90 % of the events. The background levels of these three contaminations are similar except for the geometry with a 6 cm-thick copper cover, where ^{208}Tl becomes the most important one, since they are the most energetic photons.

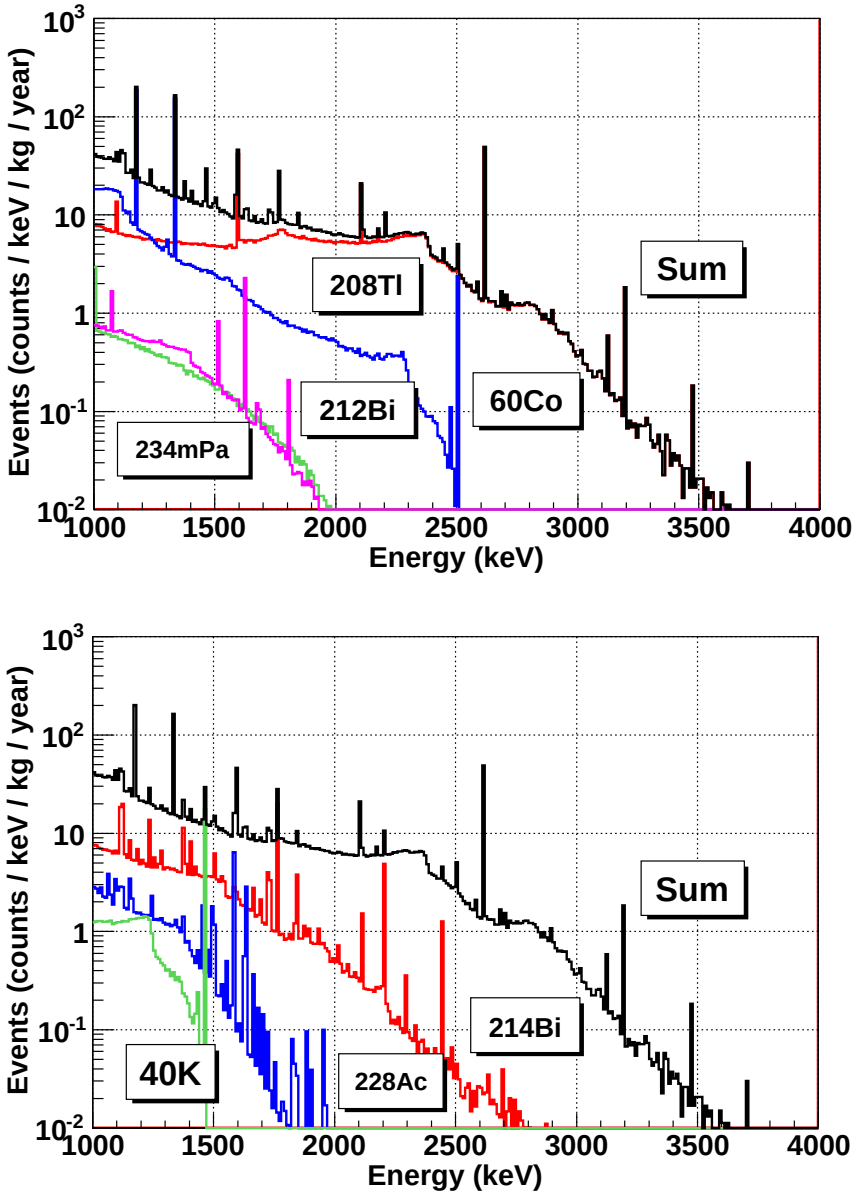

Figure 7.11: Background contributions of the different vessel contaminations for the geometry without copper cover. Top view: ^{208}Tl (red line), ^{60}Co (blue line), ^{234m}Pa (green line), ^{212}Bi (magenta line) and the total sum of all impurities simulated (black line). Bottom: ^{214}Bi (red line), ^{40}K (blue line), ^{228}Ac (green line) and the total sum of all impurities simulated (black line).

Geometry	Element	^{40}K	^{60}Co	^{208}Tl	^{212}Bi
No Cu	Vessel	0.915 ± 0.007	5.45 ± 0.02	5.57 ± 0.03	0.511 ± 0.004
	Shielding	0.130 ± 0.001	0.608 ± 0.006	0.1102 ± 0.005	$(3.3 \pm 0.1) \times 10^{-3}$
1 cm Cu	Cover	0.1029 ± 0.0004	0.616 ± 0.003	0.579 ± 0.002	$(5.6 \pm 0.1) \times 10^{-2}$
	Vessel	0.505 ± 0.004	5.03 ± 0.02	3.47 ± 0.01	0.128 ± 0.001
	Shielding	0.0799 ± 0.0004	0.368 ± 0.006	0.0823 ± 0.0004	$(2.1 \pm 0.1) \times 10^{-3}$
6 cm Cu	Cover	0.233 ± 0.002	1.310 ± 0.005	1.82 ± 0.01	$(9.1 \pm 0.1) \times 10^{-2}$
	Vessel	0.0457 ± 0.0004	0.220 ± 0.002	0.752 ± 0.003	$(1.2 \pm 0.1) \times 10^{-2}$
	Shielding	0.0081 ± 0.0002	0.040 ± 0.001	0.0180 ± 0.0001	$(2.4 \pm 0.1) \times 10^{-4}$

Geometry	Element	^{228}Ac	^{214}Bi	^{234m}Pa
No Cu	Vessel	1.472 ± 0.009	5.91 ± 0.02	0.392 ± 0.003
	Shielding	0.0174 ± 0.0001	0.0771 ± 0.0003	$< 10^{-6}$
1 cm Cu	Cover	0.162 ± 0.001	0.575 ± 0.002	0.0412 ± 0.0003
	Vessel	0.697 ± 0.004	2.822 ± 0.008	$< 2 \times 10^{-6}$
	Shielding	0.0107 ± 0.0001	0.0489 ± 0.0002	$< 10^{-6}$
6 cm Cu	Cover	0.341 ± 0.002	1.440 ± 0.005	0.0413 ± 0.0004
	Vessel	0.0616 ± 0.0007	0.310 ± 0.001	$< 2 \times 10^{-6}$
	Shielding	0.0012 ± 0.0001	0.0060 ± 0.0001	$< 10^{-6}$

Table 7.9: Contributions of the different impurities and volumes to the background level of a stainless steel vessel with different inner copper covers in the range of energy between 1200 and 1300 keV. Values are expressed in counts keV^{-1} kg^{-1} yr^{-1}.

7.4.3 Background of the neutrinoless mode

Only three isotopes (^{208}Tl, ^{214}Bi and ^{60}Co) have been considered in the neutrinoless case, as explained in section 7.2.2. In figure 7.12, the background spectra for the three geometries with the stainless steel vessel and the copper vessel are shown. For the first type of vessel, the lowest background level is 0.856 ± 0.001 counts keV^{-1} kg^{-1} yr^{-1}, obtained for the geometry with the 6 cm-thick copper cover as the table 7.10 indicates. This value reduces to 0.377 ± 0.001 counts keV^{-1} kg^{-1} yr^{-1} in the case of a copper vessel.

These levels are respectively eight and four times higher than the value published by IGEX and two orders of magnitude higher than Gothard's level. This comparison points out that a reduction using discrimination methods is possible. In fact, if we calculate the expected signals for the limits set by Gothard and DAMA experiments, we respectively obtain a value of $(2.53 \pm 0.01) \times 10^{-2}$ and $(9.26 \pm 0.02) \times 10^{-3}$ counts keV^{-1} kg^{-1} yr^{-1}.

A 1 cm-thick copper cover reduces a 40 % the total background of a stainless steel vessel and a 72 % if the thickness is 6 cm. Apart from that, the 92 % of the events are generated by ^{208}Tl emissions, as shown in figure 7.13 and in table 7.11. The second contribution is due to ^{60}Co impurities, except for the uncovered geometry, where it is comparable to that of ^{214}Bi.

7.5 Conclusions

Two simulations codes have be developped for simulating signals and backgrounds in a TPC equipped with a pixelized micromegas readout. The first one, a Geant4 code, simulates the

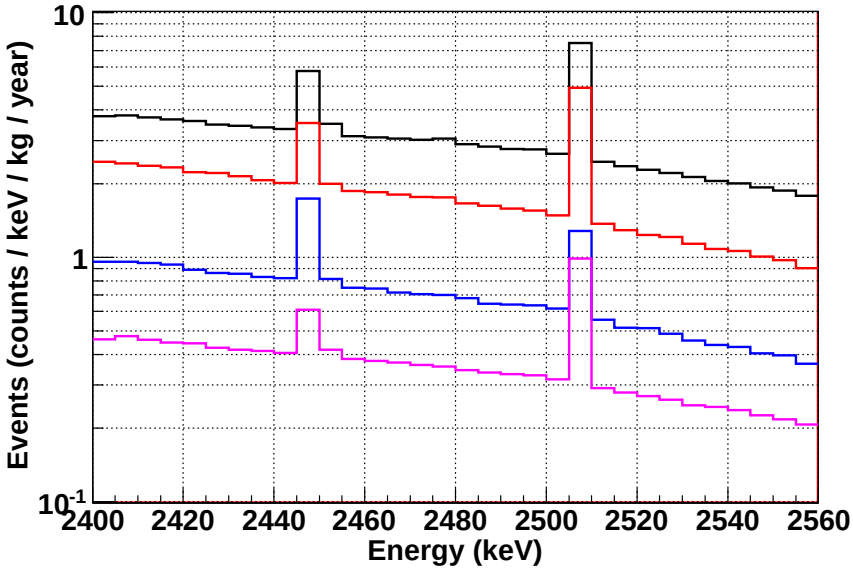

Figure 7.12: Internal background spectrum in the RoI of $\beta\beta0\nu$ for a stainless steel vessel and an inner copper shielding: 0 cm (black line, top), 1 cm (red line, middle-top) and 6 cm (blue line, middle-bottom). It is also plotted the estimated spectrum of a 1 cm-thick copper vessel (magenta line, bottom). As a comparison, the expected signal in NEXT for a ^{136}Xe enrichment of 80 % will be respectively $(2.53 \pm 0.01) \times 10^{-2}$ for Gothard and $(9.26 \pm 0.02) \times 10^{-3}$ counts keV^{-1} kg^{-1} yr^{-1} for DAMA.

	1 cm stainless steel vessel			
Geometry	No Cu	1 cm Cu	6 cm Cu	Cu vessel
Cover	–	0.338 ± 0.001	0.698 ± 0.001	–
Vessel	3.067 ± 0.004	1.526 ± 0.003	0.155 ± 0.001	0.338 ± 0.001
Shielding	0.039 ± 0.001	0.022 ± 0.001	$(2.91 \pm 0.03) \times 10^{-3}$	0.039 ± 0.001
Total	3.106 ± 0.004	1.855 ± 0.003	0.855 ± 0.001	0.377 ± 0.001

Table 7.10: Total background levels and contributions of each volume in the RoI of $\beta\beta0\nu$. Values are expressed in counts keV^{-1} kg^{-1} yr^{-1}.

physical interactions in the TPC and gives as a result a serie of energy depositions. The second one, called RESTSoft, transforms this energy in pixels, simulating the specific features of a TPC: charge generation, diffusion and pixelization. It also analizes the resulting events.

Before the simulation, the main contributions to the background of a TPC have been evaluated. Two ranges of interest have been defined, one for each $\beta\beta$ signal. In the neutrinoless mode, emissions by ^{208}Tl, ^{214}Bi and ^{60}Co have been identified as the most important ones. Apart from these three impurities, the isotopes ^{40}K, ^{212}Bi, ^{228}Ac and ^{234m}Pa must be also added in the two-neutrino mode for energies higher than 1200 keV.

Three geometries have been simulated. They consist of a 1 cm-thick stainless steel vessel, a 5 cm-thick lead shielding and an internal copper shielding with three different thickness: 0, 1 and 6 cm. A 1 cm-thick copper vessel has not been simulated but a rough estimation has been made using the results of the three former geometries.

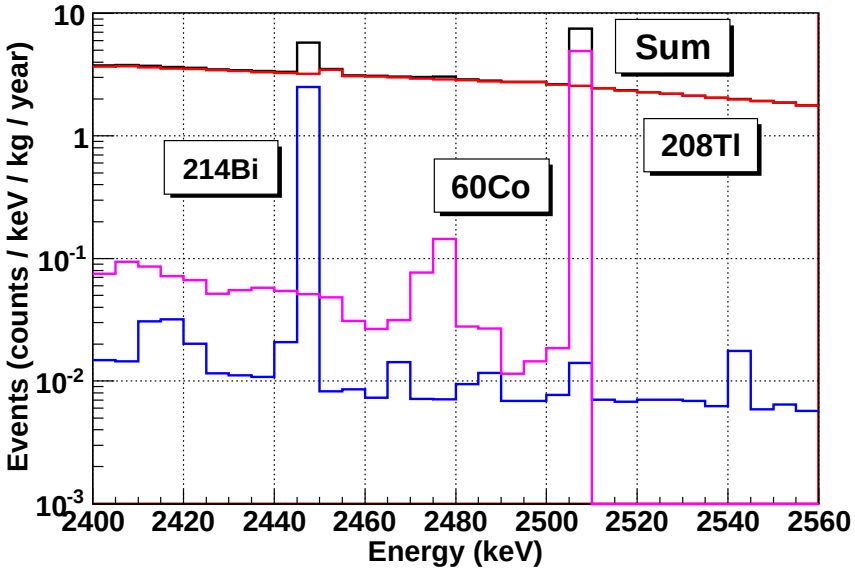

Figure 7.13: Background contributions of the different vessel contaminations for the geometry without copper cover in the RoI of $\beta\beta0\nu$ signal: ^{208}Tl (red line), ^{214}Bi (blue one) and ^{60}Co (pink one). The total background level is marked by the black line.

Geometry	Background	^{208}Tl	^{214}Bi	^{60}Co
No Cu	Vessel	2.796 ± 0.003	$(8.81 \pm 0.02) \times 10^{-2}$	0.182 ± 0.003
	Shielding	$(3.08 \pm 0.02)\ 10^{-2}$	$(1.41 \pm 0.01) \times 10^{-3}$	$(6.9 \pm 0.5) \times 10^{-3}$
1 cm Cu	Cover	0.3094 ± 0.0004	$(9.17 \pm 0.02) \times 10^{-3}$	$(1.94 \pm 0.04) \times 10^{-2}$
	Vessel	1.324 ± 0.002	$(4.90 \pm 0.01) \times 10^{-2}$	0.153 ± 0.003
	Shielding	$(1.90 \pm 0.01) \times 10^{-2}$	$(8.91 \pm 0.03) \times 10^{-4}$	$(1.6 \pm 0.3) \times 10^{-3}$
6 cm Cu	Cover	0.648 ± 0.001	$(2.37 \pm 0.01) \times 10^{-2}$	$(2.64 \pm 0.05) \times 10^{-2}$
	Vessel	0.1487 ± 0.0004	$(5.66 \pm 0.04) \times 10^{-3}$	$(1.6 \pm 0.3) \times 10^{-4}$
	Shielding	$(2.77 \pm 0.02)\ 10^{-3}$	$(1.13 \pm 0.01) \times 10^{-4}$	$(2 \pm 1) \times 10^{-5}$

Table 7.11: Contributions of the different impurities and volumes to the background level of a stainless steel vessel with different inner copper covers in the RoI of $\beta\beta0\nu$. Values are expressed in counts keV^{-1} kg^{-1} yr^{-1}.

The values for copper, stainless steel and lead materials measured by different collaborations have been taken into account for fixing the expected contamination of each volume. The level of impurities is respectively 1, 0.1 and 0.01 mBq/kg in stainless steel, copper and lead for all isotopes except for ^{60}Co and ^{40}K. For those isotopes, the contamination considered is 1 mBq/kg for stainless steel and 0.1 mBq/kg in copper and lead.

The intrinsic efficiency to signals has been estimated in a 99.4 % for $\beta\beta2\nu$ and 72.4 % for $\beta\beta0\nu$. For the two-neutrino mode, the levels of background of the stainless steel designs are not far from the limit established by Gothard, if we consider NEXT with a ^{136}Xe enrichment of 80 %. The geometry with the copper vessel improves this bound. However, there is almost two orders of magnitude between these levels and the limit set by DAMA.

We have calculated this difference using the range of energy between 1200 and 1300 keV.

The lowest level of background for the stainless steel geometries is 6.76 ± 0.01 counts keV^{-1} kg^{-1} yr^{-1}, reached for the 6 cm-thick copper cover. This value reduces to 3.08 ± 0.01 counts keV^{-1} kg^{-1} yr^{-1} for a copper vessel. In contrast, the expected value for the DAMA limit is 0.103 ± 0.001 counts keV^{-1} kg^{-1} yr^{-1}. A minimum reduction factor of 60 (30) is required to improve the DAMA result in the case of the stainless steel (copper) vessel.

For the neutrinoless mode, the lowest level of background for the stainless steel geometries is also reached for the 6 cm-thick copper cover. A value of 0.856 ± 0.001 counts keV^{-1} kg^{-1} yr^{-1} is obtained. This level reduces to 0.377 ± 0.001 counts keV^{-1} kg^{-1} yr^{-1} in the case of a copper vessel. There is respectively a factor 8 and 4 times higher between these values and that published by IGEX and two orders of magnitude comparing to Gothard. To reduce this big difference, cleaner materials and discrimination methods are necessary.

A copper shielding reduces the total background of a stainless steel vessel a 27 % (72 %) for a thickness of 1 cm and a 69 % (92 %) for 6 cm in the RoI of $\beta\beta2\nu$ ($\beta\beta0\nu$). As these values are not higher than 90 %, it seems more practical to design a radiopure copper vessel, even if the walls were thicker than 1 cm.

The main contributions to background in the RoI of $\beta\beta2\nu$ are ^{208}Tl, ^{214}Bi and ^{60}Co. They represent about the 90 % of the events. The background levels of these three impurities are similar except for the geometry with a 6 cm-thick copper cover, where ^{208}Tl becomes the most important one. In the neutrinoless case, about the 92 % of the events are only generated by ^{208}Tl. We must note that these proportions depend on the initial contamination of the materials considered for each isotope.

In next chapter, the topological features of the signals and backgrounds, recorded by a TPC, are used to define three discrimination methods. As it will be shown, the application of these methods reduce the level of background.

Chapter 8

Discrimination techniques

TPCs and micromegas detectors in particular are capable to see the geometry of an event. This geometry (normally called **topology**) is an important property to identify events of a specific type. Many examples can be given: muons crossing a gas detector leave a straight track from one side to the other; alphas have short tracks in pressurized detectors with a concentrated deposition of energy; electrons have long twisted trajectories, which end in an accumulation of charge.

The study of this topology can give key features to distinguish signals from backgrounds. Special features can be used to define a criterium to reject background events, keeping the maximum number of signals. In our case, this seems possible as high background levels have been obtained in the simulations of the last chapter.

In the first section, the topological study of signals and backgrounds motivates the introduction of three discrimination methods. They are successively studied, making a detailed description of their implementation and results. In the last section, the final spectra after the application of the discrimination methods are presented.

8.1 The topology of the events

As defined in the last chapter, an event is a set of energy deposition generated in gas interactions of particles coming from a $\beta\beta$ decay or from background. After the charge generation, drift and pixelization, these energy depositions produce a set of 3D pixels in the readout. Depending on the initial particles and the physical processes which they go through, the set of pixels will have some features that will make them unique.

In this section, the nature and the physical interactions are used to describe the topology of signal and background events. For simplicity, the $\beta\beta0\nu$ and contaminations that can generate an event in the RoI are only considered. Each type is separately treated.

8.1.1 Signal events

As explained in section 7.2.1, $\beta\beta0\nu$ consists in the emission of two electrons from the same point, sharing a total energy of 2480 keV. As shown in figure 7.4, electrons have in most cases a similar energy. Their interaction with the gas produce a continuous staggered track with two high energy depositions at both ends, as described in section 3.1.2. An example of one $\beta\beta0\nu$ event is shown in figure 8.1.

In brief, signal events have two main characteristics in a micromegas readout:

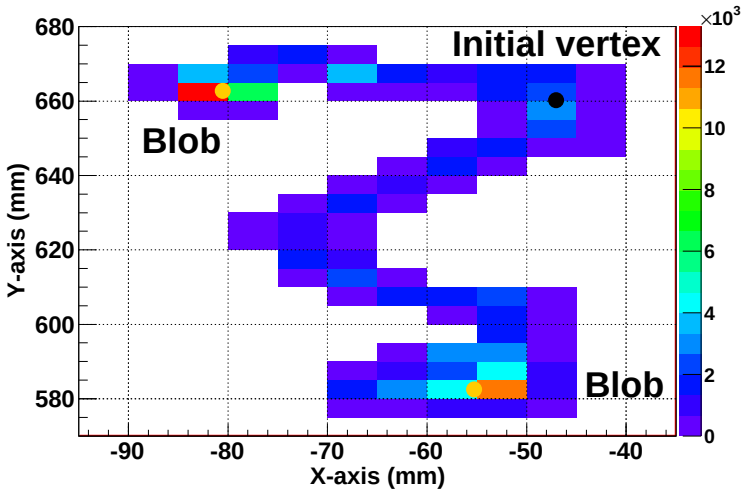

Figure 8.1: Example of a simulated $\beta\beta0\nu$ event in a TPC with a micromegas readout of 5×5 mm^2 and a mixture of xenon with a quencher at 10 bar. Electrons respectively have an initial energy of 1.509 MeV and 0.971 MeV. The gradation of color indicates the pixel charge in linear scale.

1. The continuous electron track produces a collection of continuous pixels. This fact mathematically means that there is only one **connection**, i.e., only one group of pixels linked among them by a relation of proximity.

2. At both ends of the track, we will find two high depositions of charge, called **blobs**.

About the first feature, we must note that electrons can generate photons by bremsstrahlung and therefore increase the number of connections. For electron energies between 0 and $Q_{\beta\beta}$, the probability of emission, the mean energy and the mean free path of the resulting photons has been calculated. Data is shown in table 8.1. As the emitted electrons in the $\beta\beta0\nu$ mode share equally the total energy in most cases, there is a probability of 8-9 % for each electron to emit a photon. This photon can be absorbed far from the main track as its mean free path will be of some centimeters. In some cases it will escape from the vessel, reducing the detector efficiency. As an example, one of these events is shown in figure 8.3 (left).

Energy MeV	Probability %	Mean energy keV	Mean free path cm
0.50	4	12	0.14
1.00	7	39	1.2
1.24	8	58	1.6
1.50	9	80	3.4
2.00	11	133	11
2.48	14	198	33

Table 8.1: The probability of radiating a photon, the mean energy and the mean free path for electrons with energies between 0 a 2.48 MeV.

The second fact has been checked simulating electrons of 2480 keV and comparing them with $\beta\beta0\nu$ signals. For each event, the two ends of the track have been found first using the

information given by the Geant4 simulation. The charge of each end has then been calculated using a sphere centered at both points. In each case, ends with the big and the small charge have been separated and their distributions are shown in figure 8.2.

Electrons of 2480 keV have clearly very little charge in one end in comparison with the other. In contrast, there are two similar charge depositions in the neutrinoless case. For some signals, the charge of the little blob is comparable to single-electrons events because one of the initially emitted electrons has almost all the total energy.

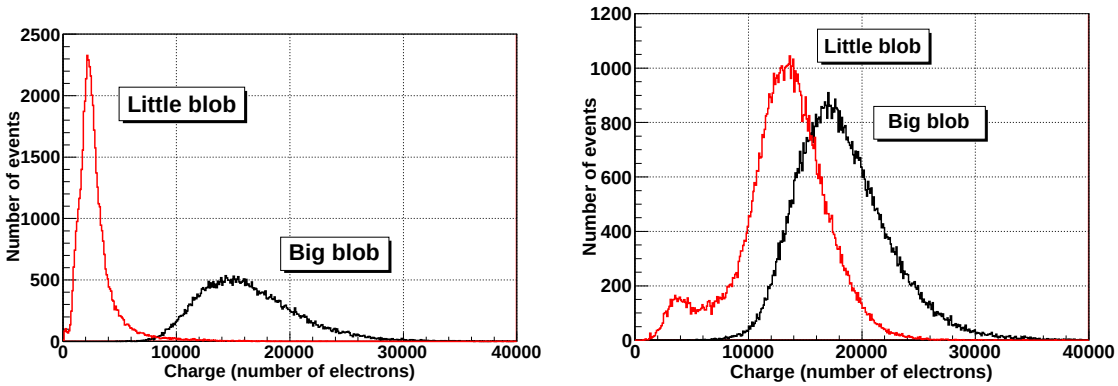

Figure 8.2: Charge distributions of the small and big blobs at both ends of the track for electrons of 2480 keV (left) and $\beta\beta0\nu$ events of ^{136}Xe (right) with a single connection.

8.1.2 Background events

Background events are generated by contaminations of materials surrounding the detector and leaving all or part of their energy in the detector. Not only the initial particles but also the physical processes they suffer have a great importance in the final topology of the event. For simplicity, only events that may deposit energy in the RoI of the neutrinoless double beta decay are studied. This fact limits the study to ^{208}Tl, ^{214}Bi and ^{60}Co isotopes.

^{208}Tl events

^{208}Tl is the most important contribution to the background level, as shown in section 7.4.3. It consists in the emission of a gamma of 2614.9 keV, normally with other gammas and electrons of lower energy as shown in figure 7.5. If these lower particles are not considered, we note that the simple physical processes by the 2614.5 keV gamma will not leave a quantity of energy in the RoI.

In the case of photoelectric absorption, an electron of the same energy is produced, outside the RoI. In the case of a Compton scattering, electrons with an energy of up to 2381 keV are generated, also outside the RoI. Finally, if the gamma suffers a pair creation, an electron and a positron are created. The second particle will annihilate with gas electrons and two photons will be created. Even if they escape or not from the TPC, the deposited energy will be outside the RoI.

This means that gamma interactions producing events in the RoI are more complicated. Some of them could be:

1. A Compton interaction in one of the external volumes (cover, vessel or shielding) creates a photon of lower energy which interacts in the detector via a photoelectric absorption or Compton scattering in the gas.

2. A multi-Compton interaction in the detector where part of the energy is lost in form of low energy gammas. They could be generated in secondary Compton interaction or bremsstrahlung radiation of energetic electrons.

3. A photoelectric absortion in the detector without other previous interactions and the emission of bremstrahlung photons which escapes from the TPC.

In the two first cases, there are two depositions of energy spatially separated. In this way, the event in the readout will have two groups of pixels, i.e., two connections. An example of this kind is shown in figure 8.3 (right). In contrast, $\beta\beta0\nu$ signals deposit in almost all cases their energy in just one connection. Therefore, this idea can be usefull to discriminate both types of events. Meanwhile, ^{208}Tl events of the third case will create just one connection and it will be more difficult to reject them.

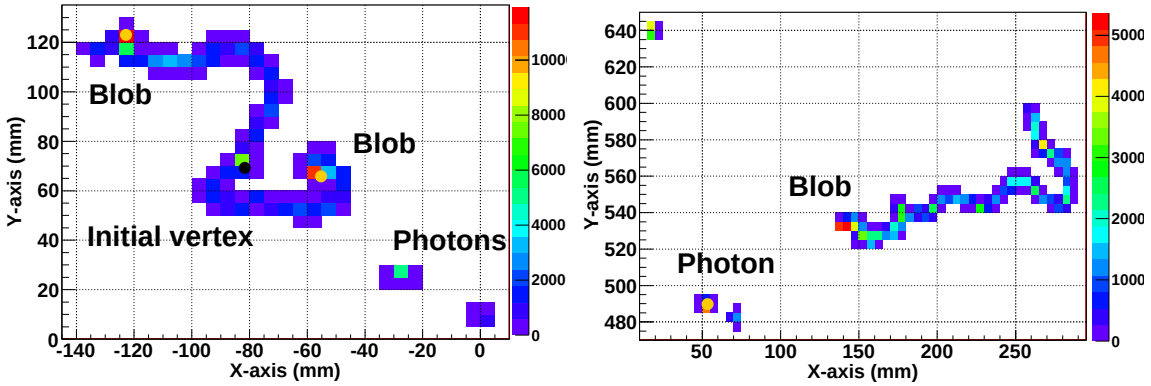

Figure 8.3: A signal (left) and a ^{208}Tl event (right) with more than one connection. At the signal event, a bremsstrahlung photon has been emitted and deposited far from the main track. Meanwhile, the background signal has been generated by a combination of physical processes. The gradation of color indicates the pixel charge in linear scale.

If photons and electrons emitted with the gamma of 2614.5 keV are also considered, the topology becomes more complicated.

- In the case of electrons, emissions near the surface of the volume in contact with the detector can have an electron energy desposit in the detection volume. This energy summed with the one generated by the Compton scattering of the 2614.5 keV photon can give a total value in the RoI. In this case, there will be two depositions of energy and can be easily discriminated. In addition, the electron deposition will be situated near the walls. If the TPC has a walls veto, it can also reject this kind of events.

- In the case of photons, an event in the RoI will have two energy depositions, caused by the Compton scattering of two or more photons, one of them of 2614.5 keV.

^{214}Bi events

The decay schema of ^{214}Bi is more complicated than the ^{208}Tl one. It is shown in figure 7.6. If electrons are not considered, only gammas with an energy greater than 2400 keV can generate an

event in the RoI. A summary of the most intense lines is made in table 8.2. The most important one is the 2447.9 keV photon because it has a big intensity and its initial energy is in the RoI. This means that it can deposit all its energy in the detector by a photoelectric absorption and if no secondary photons are emitted, the resulted event will have only one connection. In consequence, it will be difficult to reject it. Other gammas have a higher intensity and can leave their energy in the RoI by Compton scattering or a complicated process like the ^{208}Tl gamma.

Energy (keV)	2447.9	2694.7	2769.9	2921.9	2978.9	3053.9
Intensity (%)	1.570	0.031	0.025	0.014	0.014	0.021

Table 8.2: Summary of the main gamma emissions (energy and inensity) of the ^{214}Bi with an energy greater than 2 MeV. Data has been taken from [176].

In the case of electrons, only emissions near the inner surface of the volume in contact with the detector can be detected in the RoI. There are two main cases:

1. Electrons with a continuous spectrum with a maximum at 3272 keV. This case has an intensity of 18.2 %. For producing an event in the RoI, they have to lose part of their energy in the external volume. In all cases, they will deposit energy near the walls and can be discriminated by a fiducial veto.

2. Electrons with a continuous beta spectrum with a maximum at 2663 keV and the emission of a photon of 824 keV. Several cases can generate an event in the RoI. In all of them, either using a walls veto or taking into account the number of connections, they can be easily vetoed.

^{60}Co events

The ^{60}Co case is more simple. Isotopes emit two photons of respectively 1173 and 1332 keV and an electron with a continuous beta spectrum of $Q = 318.3$ keV. If the electron is absorbed in the vessel or other material, the total absorption of both photons generate an event in the RoI. Otherwise, the deposited energy is out of the RoI. This means that an event in the RoI will have two connections. The electron complicates the topology but does not change the feasibility of rejection.

Summary

Three different features of signal events, not present in background ones, have been identified in order to implement selection criteria. Their implementation and results are described in detail in the following subsections.

1. The definition of a veto volume in the xenon gas next to the walls.

2. The number of grouped pixels or connections.

3. The charge of the event ends, considered the event as continuous track.

8.1.3 The figure of merit for background reduction

The study of a selection criterium is based on two variables: the **selection efficiency** (ϵ) and the **rejection factor** (F). The first variable is defined as the ratio of signal events after and before the application of a criterium. It quantifies the acceptance of signal events. The second variable is the ratio of background events before and after the application of the selection and quantifies the background discrimination power.

An ideal selection criterium should have an efficiency near 100 % and a very high rejection factor. As this is not normally the case, a figure of merit is defined as

$$f.o.m. = \epsilon \sqrt{F} \tag{8.1}$$

This variable is based on the potential of discovery of the $\beta\beta0\nu$ expressed in equation 2.7. As it will be later shown, the rejection factor varies with energy. This is due to the different physical processes that particles have suffered before depositing an specific energy. In order to evaluate this dependency, three ranges have been defined for ^{208}Tl and ^{214}Bi contaminations, shown in table 8.3. The first one is the RoI for $\beta\beta0\nu$. The other two ranges represent a set of events mainly generated by a Compton interaction and by a photoelectric absorption respectively.

Contamination	Process	$E_{ini}(keV)$	$E_{fin}(keV)$
^{208}Tl	RoI	2400	2560
	Compton	2200	2300
	Photoelectric	2600	2630
^{214}Bi	RoI	2400	2560
	Compton	2460	2560
	Photoelectric	2445	2450

Table 8.3: Energy ranges considered in the analysis of the rejection factor for each selection criterium.

Finally, we must note that the efficiency and rejection power of each criterium are evaluated for events that were not rejected by the previous criteria.

8.2 A veto volume next to walls

8.2.1 Definition

A veto volume of 1 cm around the walls has been defined in the simulation. The length value has been chosen taking into account the pixel length. If an event has a charge deposition in this volume, it will be rejected. This definition has two mechanical implications:

1. An active area near the walls must be built. Charges arriving to this area should induce a veto signal.

2. The micromegas readout must be capable of fixing the absolute position in the z-axis. This implies the determination of the absolute time of the event as described in section 5.5.

8.2.2 Results

The application of this veto has a clear effect in events generated by isotopes with electron emissions. These include ^{234m}Pa (left figure of 8.4) and ^{212}Bi. The effect is small for the rest of the considered isotopes, as shown for ^{208}Tl at the right figure of 8.4.

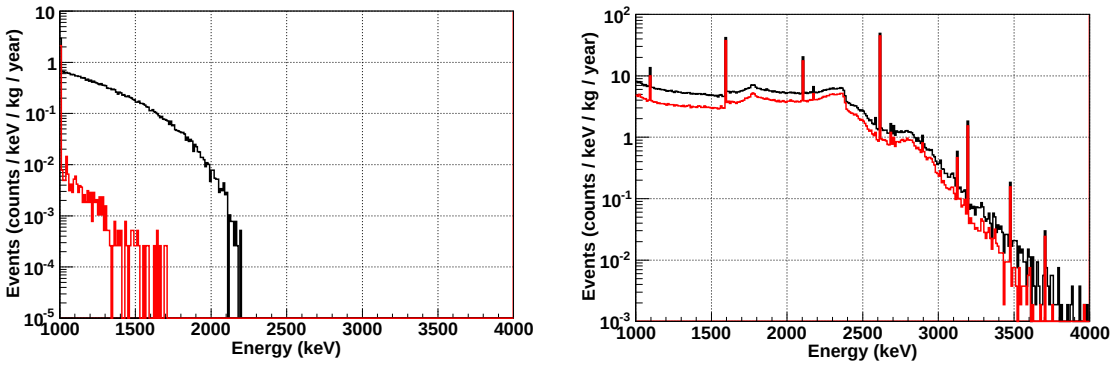

Figure 8.4: Background levels before (black line) and after (red line) the application of the walls veto for events generated by ^{234m}Pa (left) and ^{208}Tl (right) contaminations from the vessel of the geometry without copper.

The wall veto is more effective for surface contaminations as it also rejects alphas. This feature has been confirmed by the simulation of ^{208}Tl and ^{214}Bi emitted from the surface in contact with the gas, as shown in figure 8.5. In the RoI of $\beta\beta0\nu$, it has a rejection power of 8.8 ± 0.1 and 74 ± 5 for impurities of ^{208}Tl and ^{214}Bi respectively.

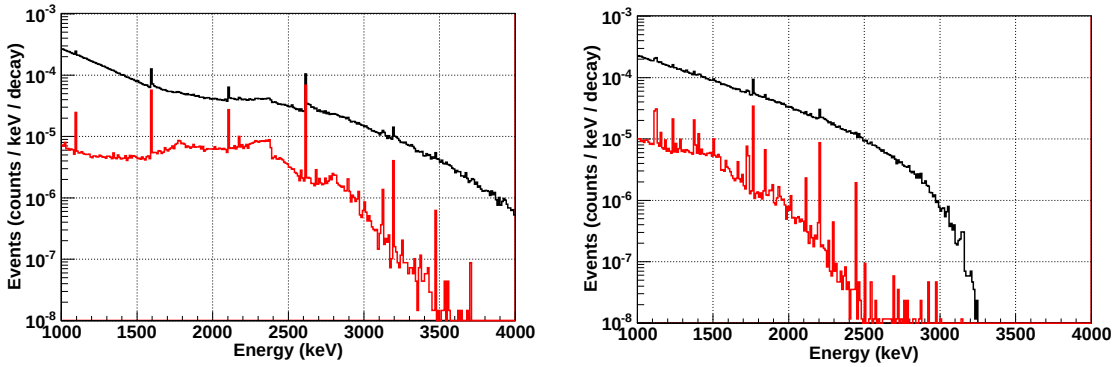

Figure 8.5: Background levels before (black line) and after (red line) the application of the walls veto for events generated by surface contaminations of ^{208}Tl (left) and ^{214}Bi (right).

Signal acceptance

The acceptance of $\beta\beta0\nu$ signals with this veto is 83.7 ± 0.3 %. In the range between 1200 and 1300 keV, the acceptance of $\beta\beta2\nu$ signals is 93.3 ± 0.2 %.

Rejection factor

The rejection factors of this selection criterium are shown in table 8.4. Values are higher for the inner layers because almost all emissions near the surface in contact with the gas are vetoed.

In addition, events produced by a Compton interaction have a higher probability of rejection than those generated by a photoelectric absorption. Best values are obtained in the RoI of ^{208}Tl as events that deposit energy suffer more complicated processes. This is not the case of ^{214}Bi, where events in the RoI have been generated in simple Compton interaction or photoelectric absorptions.

		^{208}Tl			^{214}Bi		
Geom	Layer	RoI	Compton	Photo	RoI	Compton	Photo
No copper	Vessel	1.40	1.27	1.11	1.11	1.19	1.09
	Shield	1.25	1.16	1.08	1.09	1.16	1.07
1 cm Cu	Cover	1.39	1.25	1.11	1.11	1.19	1.09
	Vessel	1.29	1.18	1.09	1.10	1.17	1.08
	Shield	1.25	1.15	1.08	1.09	1.15	1.07
6 cm Cu	Cover	1.32	1.20	1.09	1.10	1.17	1.08
	Vessel	1.22	1.14	1.07	1.08	1.14	1.06
	Shield	1.19	1.13	1.07	1.08	1.12	1.06

Table 8.4: Rejection factors of the walls veto for ^{208}Tl and ^{214}Bi impurities in different energy regions. Errors are less than 0.01

Figure of merit

As an example, the figure of merit for the stainless steel vessel has been calculated using former values in the geometry only shielded by lead. A value of 1.10 has been obtained.

8.3 A single connection

A connection is a set of pixels linked by a relation of proximity, as defined in section 8.1. The way to define this relation is the key point of the method. The simplest one is to link adjacent pixels. An example of this case is shown in figure 8.6 for an ideal 2D event. The red segments define the relations between adjacent pixels. It is clear that the event has two connections.

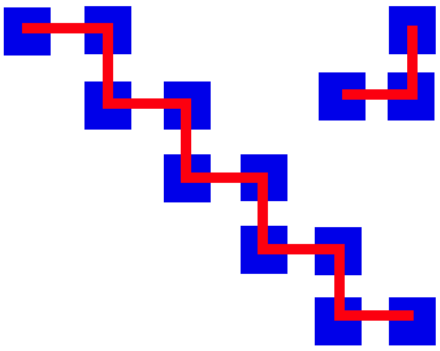

Figure 8.6: An example of a 2D event with two connection. Blue pixels are linked by a red segment only if they are adjacent.

A more general relation of proximity is the use of the distance between pixels. In our method, we called it **proximity**. Adjacent pixels are only-linked if the distance is 5 mm (the pixel path). This distance can be increased in order to avoid possible gaps in the event track and to add charge depositions due to bremsstrahlung photons. The dependence of the number of connections with this variable is studied later on.

As a selection criterium, the number of connections is fixed to 1. If an event has more than one connection, it will be rejected.

8.3.1 A method for grouping pixels

The idea of grouping pixels in connections is intuitive but its implementation in a formal method seems more complicated. In our case, the classical method of Graph's theory described in [182] has been used. It consists in identifying the pixels of the event with the vertices of a graph and their links with the segments of the graph. From an intial point, segments are used to "visit" all possible vertices. These vertices are in the same connection. In a second step, a point which is not in the connection is taken and the "visit" is repeated. The method ends when all points are grouped.

The formal method is defined in the following steps:

1. All pixels are the vertices of a graph. Two pixels are linked by a segment if the distance between pixels is less than *proximity*.
2. A variable is associated to each vertex, representing the number of its connection. The initial value is 0 (ungrouped).
3. A variable is associated to each segment, which expresses if it has been already been used (1) or not (0) by the method. The initial value is 0 (unused).
4. An empty list is initialized. In this list, the visited vertices will be written down.
5. A variable X is initialized to 1. It represents the actual connection, whose pixels are being grouped.
6. A vertex whose number is 0 is choosen. If there is none, go to step 10. Otherwise, add it to the list and set its number to X.
7. Find a segment that links the last pixel of the list to another one. If so, go to step 8. Otherwise, go to step 9.
8. Add the second vertex of the segment to the list and set its number to X. Set the segment number to 1. Return to step 7.
9. Remove the last vertex from the list. If there is none, increase X a unity and go to step 6.
10. All pixels are grouped in connections. The number of connections is X-1.

8.3.2 Results

As an example, the distribution of the number of connections has been generated for $\beta\beta0\nu$ and some contaminations from the vessel of the geometry without copper. It is shown in figure 8.7. In this case, a value of 7.2 mm has been given to *proximity*. About 56 % of the events generated by $\beta\beta0\nu$ has only one connection. In contrast, this only happens in about 1 % of those generated by ^{208}Tl. For ^{60}Co, this percentage reduces to zero, within the simulation precission. These

results prove that the selection of events with only one connection is a good selection criterium to reduce the level of background, keeping an acceptable number of signal events.

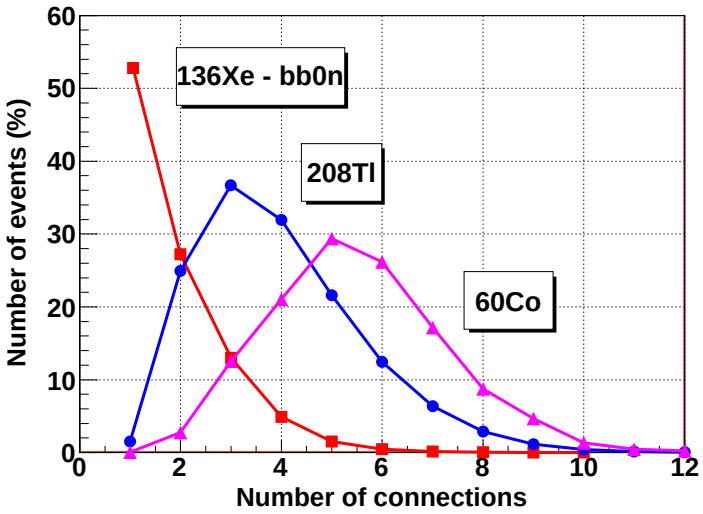

Figure 8.7: Distribution of the number of connections for events generated by $\beta\beta0\nu$ (red squares), ^{208}Tl (blue circles) and ^{60}Co (magenta triangles). Contaminations have been emitted from the 1 cm-thick stainless steel vessel of the geometry without copper cover..

Before fixing the value of the variable *proximity*, the efficiency and the rejection power of this criterium were evaluated in a wide range of values. For this purpose, events generated by ^{208}Tl contamination in the 1 cm-thick cover of the second geometry and those generated by $\beta\beta0\nu$ signals have been used. Events passing the criterium of walls have been selected and different values for *proximity* have been tested. Results are shown in table 8.5.

Prox (mm)	5.2	7.2	8.8	10.2	14.3	17.5	20.2
ϵ (%)	52.8	55.9	56.9	58.8	63.2	66.6	68.7
F	90.7	79.1	75.8	70.8	59.00	50.6	46.4
$f.o.m.$	5.03	4.98	4.95	4.95	4.86	4.74	4.68

Table 8.5: The efficiency (ϵ), the rejection factor (F) and the figure of merit ($f.o.m.$) for the one-connection criterium for different values of the variable *proximity*, comparing events produced by ^{208}Tl impurities in the 1 cm-thick copper cover of the second geometry and $\beta\beta0\nu$ signals.

As the variable *proximity* is increased, less events of each type are rejected, i.e., there is a higher efficiency for signals and a lower background rejection factor. The efficiency increases because energy depositions produced by bremsstrahlung photons near the track are added to the main connection, as explained in section 8.1. Similarly, the rejection factor decreases. As the figure of merit decreases when the variable *proximity* is increased, a low value has been selected for the analysis: 7.2 mm.

Signal acceptance

The selection efficiency of $\beta\beta2\nu$ signals is 76.7 ± 0.5 %. In the range between 1200 and 1300 keV, the acceptance of $\beta\beta0\nu$ signals is 56.1 ± 0.2 %.

Rejection factor

The rejection factors show big differences depending on the energy. In figure 8.8 the spectra of some contaminations of the 1 cm-thick cover before and after the selection criterium are shown. It is clear that the rejection factor in the Compton region is lower than in the photoelectric one. All compton events include only the energy of the electron because the gamma has escaped. There will be only one connection unless this particle generates secondary photons. Meanwhile, the rejection factor for the RoI of ^{208}Tl contamination is even higher than the others. This fact was expected from the discussion in section 8.1.

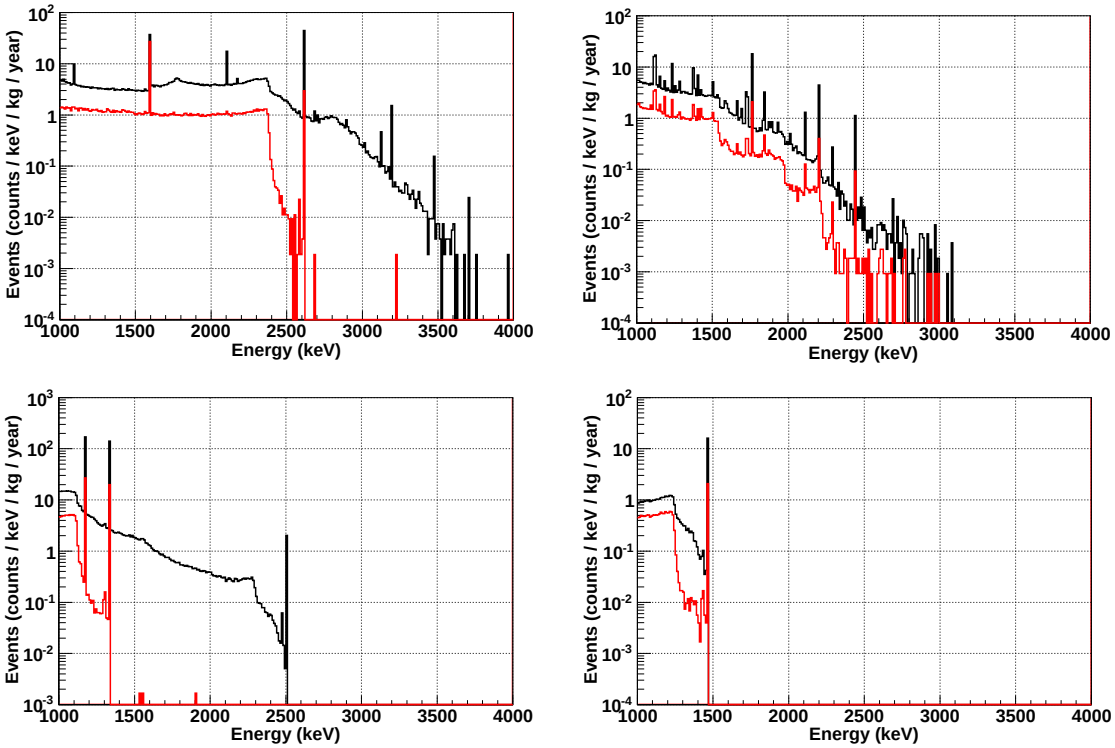

Figure 8.8: Background level before (black line) and after (red line) the application of the one-connection criterium for ^{208}Tl (left upper corner), ^{214}Bi (right upper corner), ^{60}Co (left down corner) and ^{40}K (right down corner) contaminations of the vessel in the geometry without copper cover.

The rejection power of the selection criterium in the studied regions is shown in table 8.4. In this case, events generated by a photoelectric absortion are better discriminated than those produced in a Compton interaction. The factor of difference varies between 3 and 4. For both processes, there is a little dependence with the origin of the emission.

In the RoI, the background reduction is higher for ^{208}Tl than for ^{214}Bi but the difference reduces as the origin of the contamination is more external. About the first isotope, note that the best values are obtained for the inner 1 cm-thick (copper or stainless steel) volumes.

This fact can be explained by the events generated by the 2614.5 keV photons, which suffer a Compton scattering in the vessel and the resulting photon is totally absorbed in the gas. This process, always rejected by the one-connection criterium, becomes rare for external layers and in consequence, the rejection power decreases.

		^{208}Tl			^{214}Bi		
Geom	Layer	RoI	Compton	Photo	RoI	Compton	Photo
No copper	Vessel	90.7 ± 0.9	4.02 ± 0.06	15.8 ± 0.4	9.2 ± 0.1	4.2 ± 0.1	10.6 ± 0.1
	Shield	40 ± 2	3.02 ± 0.03	11.7 ± 0.2	9.5 ± 0.1	4.4 ± 0.1	11.0 ± 0.1
1 cm Cu	Cover	85 ± 1	3.84 ± 0.04	14.8 ± 0.3	13.2 ± 0.1	4.6 ± 0.1	13.0 ± 0.1
	Vessel	53.4 ± 0.6	3.22 ± 0.03	12.3 ± 0.2	10.9 ± 0.1	4.4 ± 0.1	10.9 ± 0.1
	Shield	32 ± 1	3.22 ± 0.04	15.6 ± 0.4	11.1 ± 0.1	4.7 ± 0.1	13.2 ± 0.2
6 cm Cu	Cover	59.1 ± 0.8	3.32 ± 0.04	12.6 ± 0.3	11.1 ± 0.2	4.7 ± 0.2	13.4 ± 0.2
	Vessel	27.5 ± 0.4	3.07 ± 0.03	12.6 ± 0.2	11.2 ± 0.3	4.9 ± 0.3	13.5 ± 0.4
	Shield	22 ± 1	3.18 ± 0.04	12.1 ± 0.3	10.9 ± 0.3	5.0 ± 0.4	13.2 ± 0.4

Table 8.6: Rejection factors of the one-connection criterium for ^{208}Tl and ^{214}Bi impurities in different energy regions.

Figure of merit

As in the previous method, we have calculated the f.o.m. for the stainless steel vessel in the geometry only shielded by lead. A value of 5.34 has been obtained.

8.4 The search of two blobs

As explained in section 8.1, the presence of two blobs at the ends of the event is a distintive signature of a double beta signal. In order to find the two blobs, a blind method has been created, drawing a track between them for each event. The charge of both ends has then been calculated following the Gothard procedure and using a sphere centered at each end. On top of that, events which are almost covered by their track have been selected. The description of the blind method and the three variables used as selection criteria are described in the next subsections. Finally, their application to signal and background events is treated in the final subsection.

8.4.1 A method to find two blobs

The Gothard experiment found blobs by eye [183] but this procedure is not feasible in the presence of a huge amount of simulated events. This is why a blind method has been developped, based on two main ideas:

1. At both ends of a track a blob must be found.

2. A continuous track must be traced between one end and another, covering all the event.

It can happen that the longest track in a $\beta\beta0\nu$ event has not one blob at one end because one electron has almost all the shared energy. Apart from that, the presence of two charge accumulations does not imply that they are at the ends of the event. Initial electrons produce

during their gas interaction delta rays which deposit their charge in the track, creating a fake blob. As a possible solution to those problems, the method identifies possible blob pixels and finds the longest track that links them (first idea). Then it generates the longest track that links a blob pixel and another pixel (second idea). Finally, it chooses one of them according to a parameter.

The implementation of this method follows in essence the same philosophy as the method to find connections. The pixels of an event are identified with the vertices of a graph, which are linked by a relation of proximity. These links are the segments of the graph. In addition, pixels with little charge are removed to avoid twists, which can fake the longest track.

After the graph creation, the charge in a sphere centered in them is associated to each pixel. Those pixels with the greatest charge are marked as possible blob candidates. Finally, the two tracks described before are generated and one is chosen. As an example of this procedure, a 2D event is shown in figure 8.9.

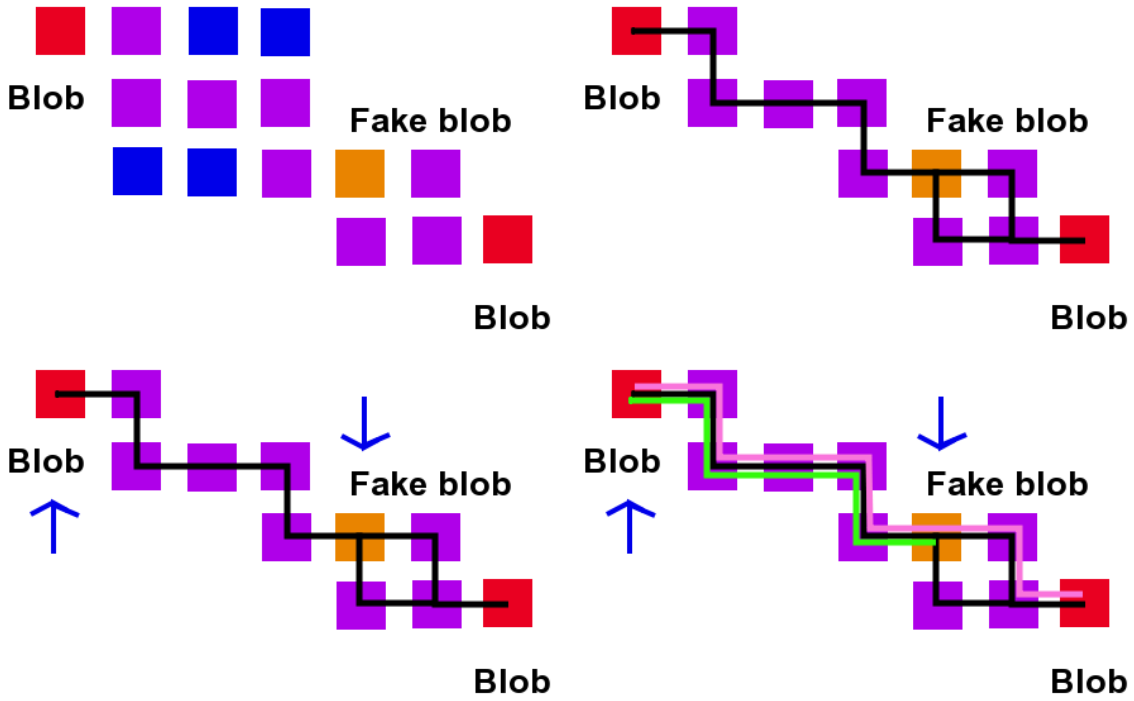

Figure 8.9: The method to find two blobs applied to a 2D event. Upper left: A 2D-event with two real blobs (red squares), a fake one (orange square), normal pixels (blue squares) and pixels with little charge (magenta squares). Upper right: When creating a graph, pixels with little charge are removed. Adjacent pixels are then linked by a (black) segment. Down left: Pixels with the greatest charge are considered blob candidates. The two candidates of this example are marked by arrows. Down right: The longest track between two blob candidates (green line, $l_1 = 6$) and the longest one between one candidate and another pixel (pink line, $l_2 = 9$) are found. If the ratio l_2/l_1 is greater than ξ, the second track is chosen. Otherwise, the first one.

The formal method consists of the following steps:

1. A graph is created. A pixel of the event is a vertex if its charge is greater than Q_{th}. Two vertices are linked by a segment if the distance between them is less than d_{seg}.

2. Pixels are sorted according to their charge. The best ones (N_{cand} pixels) are considered blob candidates and their vertices are marked.

3. The longest track between two marked vertices (l_1) is first found. Then, the longest track between a marked vertex and a normal one (l_2) is generated. If l_2/l_1 is greater than a parameter ξ, the second track is chosen. Otherwise, the first is taken.

The method does not always succeed. Two $\beta\beta0\nu$ examples are shown in figure 8.10. In the first case, the method has identified the real blobs with a good approximation. In the second one, no track between real blobs has been found. Two reasons arise for explaining these failures: a charge discontinuity or a fake blob in the middle of the event (green pixel).

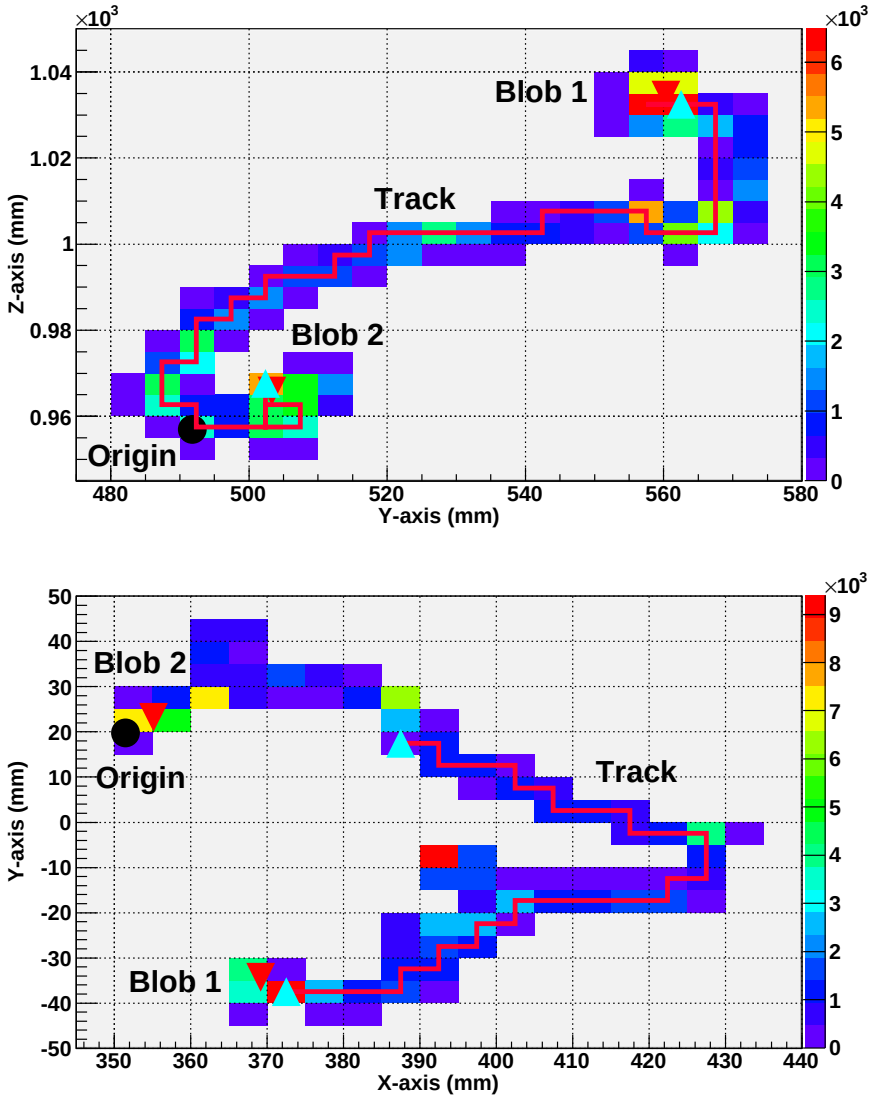

Figure 8.10: $\beta\beta0\nu$ events were the method has found the real blobs (top) and not (bottom). The main points are marked: origin (black circle), real blobs (inverted red triangles) and found blobs (light blue triangles). The gradation of color indicates the pixel charge in linear scale.

The success of this method has been evaluated calculating the distance between the real and found blobs. Different values for parameters Q_{th}, d_{seg}, N_{cand} and ξ have been tested. The

distribution with the mean distance closest to zero is shown in figure 8.11 and corresponds to parameters values of table 8.7. Note that only segments between adjacent pixels have been traced and that the second type of tracks must be a 30 % longer than the first one to be accepted.

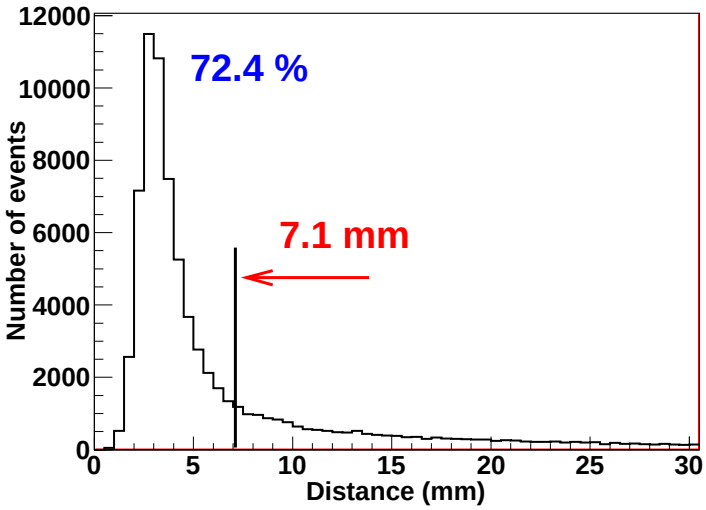

Figure 8.11: Distribution of the distance between the real and the calculated position of the two blobs of $\beta\beta0\nu$ events.

Parameter	$Q_{th}(e^-)$	$d_{seg}(mm)$	N_{cand}	ξ
Value	40	5.0	4	1.3

Table 8.7: Best values found for minimizing the distance between the real and the calculated blobs.

8.4.2 The sphere and Gothard charge

From figure 8.11, we note that the distribution of the distance has a maximum at 3.5 mm and that in about 72.8 % of the cases, the distance between the real and the generated blobs is less than 7.1 mm. For those events, a sphere centered in a generated end and a radius of 7.1 mm will contain the charge of the blob. This sphere has been used for calculating the charge of each end for ^{208}Tl contaminations and $\beta\beta0\nu$ signals, as shown in figure 8.12. Comparing the left figures of 8.2 and 8.12, there are many events where the charge of the little blob is comparable to a big one. The found blobs are big charge accumulations, produced by secondary photons or δ-rays.

In the Gothard experiment [183], the charge of each end was calculated in a different way. Events generated by different gamma sources (^{137}C, ^{22}Na, ^{88}Y and ^{232}Th) were analyzed. Single track events were selected and ends were manually identified. Two squares of area $\Delta X \times \Delta Z$ and $\Delta Y \times \Delta Z$ centered in the located points were respectively defined in each projection (XZ and YZ) and quantities Q_X and Q_Y were respectively calculated by

$$Q_u = t_u \left[1 + \left(\frac{t_u}{T}\right)\right] + \omega b_u, \text{ u = X or Y} \tag{8.2}$$

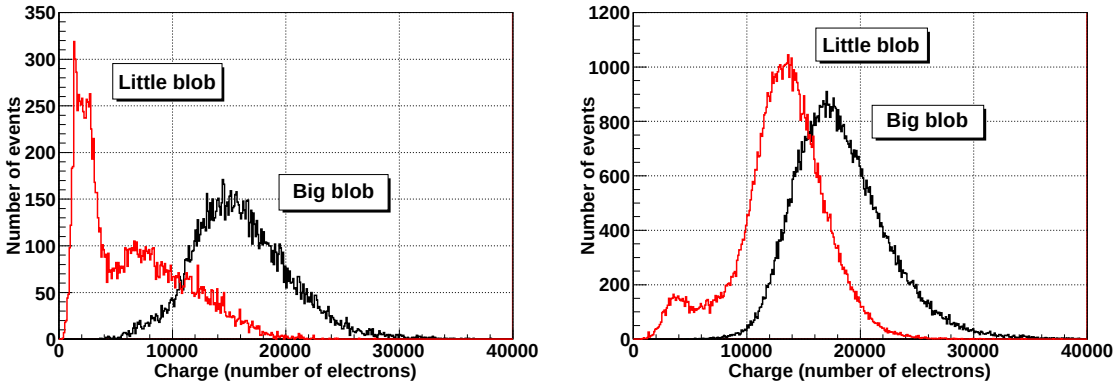

Figure 8.12: Sphere charge of the big (black line) and little blob (red line) for events generated by ^{208}Tl contaminations (left) from the vessel in the uncovered geometry and $\beta\beta0\nu$ signals (right).

where t_u is the number of pixels with charge, b_u is the number of pixels which form the blob, T is the total number of pixels in the box and α and ω are two parameters to weight the importance of blob and filled pixels. A total charge Q was then associated to each end with the geometrical mean of the two projection values

$$Q = \sqrt{Q_X \; Q_Y} \tag{8.3}$$

The distribution of Q for the beginning and the end of each track for some specific parameter values (shown in figure 8.13) is similar to the one generated for electrons of 2480 keV (left plot of figure 8.2). The variable Q is a more complicated way of calculating the end charge.

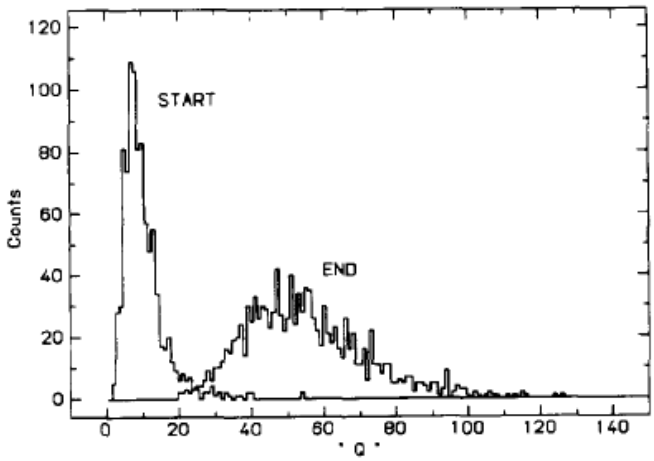

Figure 8.13: Distribution of the total charge Q, as defined in Gothard experiment, for the beginning and end of each electron track taken from [183].

This procedure has also been used to associate another charge to each end. Instead of using two square projections, a box of 7-pixels length centered in each point has been defined. The number of pixels with charge (t_u) has been first calculated and then those forming a blob (b_u), using a charge threshold of 1000 electrons. With these values and the parameters $\alpha = 1.5$ and $\omega = 8$, the Gothard charge has been calculated using the expression 8.2. The distribution for both ends and background and signal events is shown in figure 8.14. As it happens with the sphere charge, many background events can fake signals because the Gothard charge of their

little blob is very big.

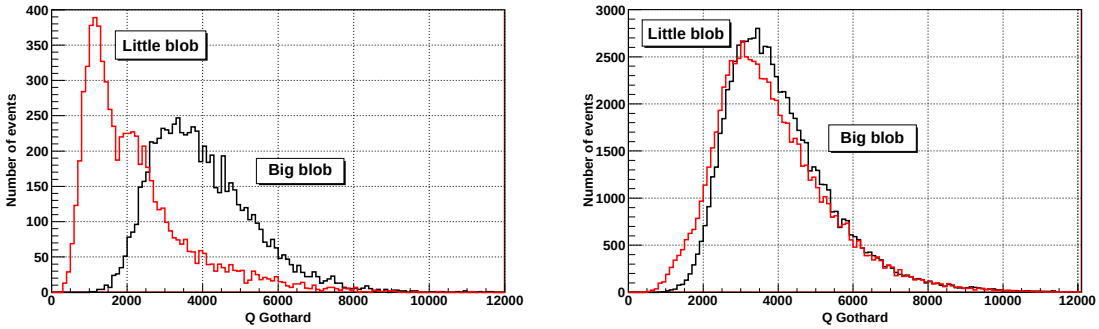

Figure 8.14: Gothard charge of the big (black line) and little blob (red line) for ^{208}Tl contaminations (left) in vessel of the uncovered geometry and $\beta\beta0\nu$ signals (right).

We have observed that the two "charges" of the little blob can be used for discriminating background and signals. Their rejection power can be increased if they are combined in a 2D criterium. The 2D histogram of both variables in figure 8.15 shows clearly that signals (left figure) and background events (right figure) are more separated. The red line marks the region of parameters for which events are accepted. Even with this improvement, the rejection power is not so high. For ^{208}Tl contaminations of the vessel in the uncovered geometry, the rejection factor is 3.34 and the $\beta\beta0\nu$ acceptance is a 88.8 %, giving a f.o.m. of only 1.63.

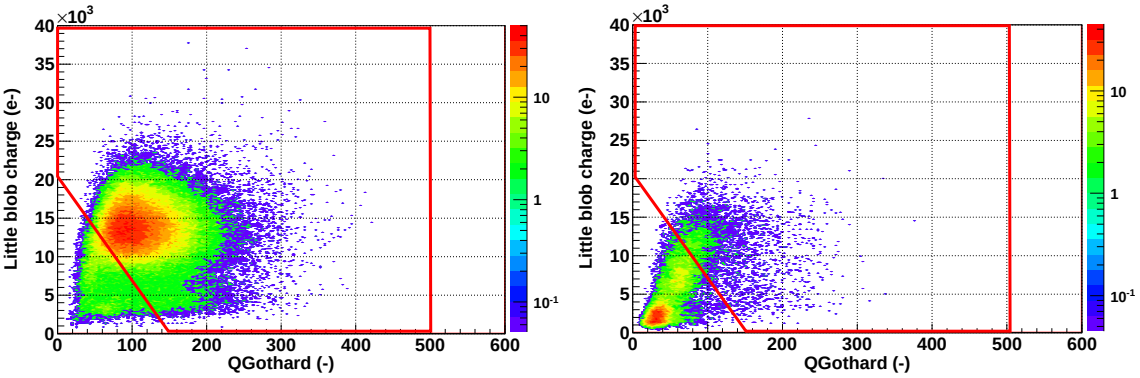

Figure 8.15: 2D histogramme of the Gothard and normal charge of the little blob for $\beta\beta0\nu$ events (left) and ^{208}Tl (right) generated in the vessel of the uncovered geometry. The selection region applied is limited by the red thick line. The gradation of color indicates the number of events in each 2D-bin of the histogramme in logarithmic scale.

8.4.3 The covering of the track

The two parameters defined before are not enough to discriminate signal and background events. The success or failure of the blob method have motivated a new one. The bottom example of figure 8.10 shows a method failure because the track does not link the two ends of the event. If the charge "around the track" is summed, it will be less that the total one. This ratio of covered and total charge has been called **covering**. Pixels "around the track" are those whose distance to track pixels is less than a chosen value. After several tests, this value has been fixed

to 15.2 mm. The distribution of the covering parameter is shown in figure 8.16 for $\beta\beta$ signals and background events generated by a ^{208}Tl contamination in the vessel of the uncovered geometry.

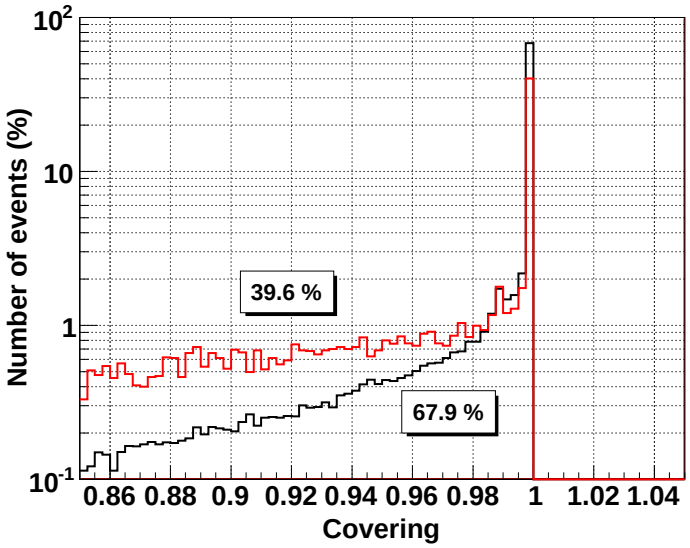

Figure 8.16: The covering for events with just one connection generated by $\beta\beta0\nu$ signals (black line) and ^{208}Tl contaminations (red line) from the vessel in the uncovered geometry.

A 67.9 % of the signal events have a track that covers all the charge. This only happens a 39.6 % of the background cases. With the aim to increase a bit the signal acceptance and avoiding rounded errors, a threshold of 0.98 has been fixed for the covering. This means that events whose parameter is less than 0.98 will be rejected. The combination of the 2D parameters region, generated by the two charges of the little blob, and this parameter allowed us to increase the rejection factor to values greater than 10, leaving a high signal acceptance.

8.4.4 Results

Signal acceptance

The acceptance of $\beta\beta0\nu$ signals is 71.2 ± 0.1 %. In the range between 1200 and 1300 keV, the acceptance of $\beta\beta2\nu$ signals is 71.8 ± 0.3 %.

Rejection factor

In table 8.8 the values of the rejection factor in the different energy regions considered are shown. We note that values in the RoI are not so high as in the other regions, possibly due to the previous high values of the one-connection criterium. There is neither a clear dependence on the origin of the contamination nor a difference between Compton and photoelectric regions.

Figure of merit

As in the other cases, we have calculated the figure of merit for the stainless steel vessel in the geometry only shielded by lead. We have obtained a value of 2.55.

		^{208}Tl			^{214}Bi		
Geom	Layer	RoI	Compton	Photo	RoI	Compton	Photo
No Cu	Vessel	12.6 ± 0.5	16.2 ± 0.8	15 ± 2	14.7 ± 0.3	19 ± 1	14.8 ± 0.4
	Shield	10 ± 1	15.8 ± 0.6	12.9 ± 0.8	12.6 ± 0.5	15 ± 2	11.8 ± 0.5
1 cm Cu	Cover	12.7 ± 0.6	17.1 ± 0.7	15 ± 1	14.5 ± 0.5	18 ± 2	13.8 ± 0.5
	Vessel	12.6 ± 0.6	15.7 ± 0.5	14.0 ± 0.8	13.6 ± 0.5	16 ± 2	12.9 ± 0.5
	Shield	13 ± 2	16.8 ± 0.8	12 ± 1	14.7 ± 0.6	18 ± 2	13.8 ± 0.6
6 cm Cu	Cover	11.0 ± 0.5	16.2 ± 0.8	15.5 ± 0.9	24 ± 5	15 ± 1	15 ± 1
	Vessel	13.0 ± 0.7	15.9 ± 0.6	13 ± 1	13 ± 1	18 ± 5	12 ± 1
	Shield	12 ± 2	17.0 ± 0.8	14 ± 1	13 ± 1	13 ± 3	13 ± 2

Table 8.8: Rejection factors of the three criteria of the blob method for ^{208}Tl and ^{214}Bi contaminations in different energy regions.

8.5 The spectra after the application of selection criteria

8.5.1 The two-neutrino mode

The application of the three selection criteria defined in former subsections has reduced a factor ≈ 13 the difference between the expected signal and the background level, as shown in figure 8.17. For the geometry with the 6 cm-thick copper cover and the range of energy between 1200 and 1300 keV, the background level has dropped from 6.76 ± 0.01 to 0.277 ± 0.003 counts keV^{-1} kg^{-1} yr^{-1}, as shown in table 8.9. In the case of the copper vessel, it reduces down to 0.077 ± 0.001 counts keV^{-1} kg^{-1} yr^{-1}.

However, the expected signal in a xenon TPC also reduces. If we consider NEXT and an enrichment of 80 % in ^{136}Xe, the expected signal using respectively the limits of Gothard and DAMA is 2.42 ± 0.01 and 0.0543 ± 0.0002 counts keV^{-1} kg^{-1} yr^{-1}. All the geometries with the levels of impurities considered are sensitive to signals with a half-time near Gothard value. In the copper vessel configuration, the expected background would be comparable to the DAMA signal.

	1 cm stainless steel vessel			
Geometry	No Cu	1 cm Cu	6 cm Cu	Cu vessel
Cover	–	0.055 ± 0.001	0.197 ± 0.003	–
Vessel	0.507 ± 0.008	0.393 ± 0.004	0.077 ± 0.001	0.055 ± 0.001
Shielding	0.022 ± 0.001	$(0.015 \pm 0.001$	0.0026 ± 0.0001	0.022 ± 0.001
Total	0.529 ± 0.008	0.464 ± 0.004	0.277 ± 0.003	0.077 ± 0.001

Table 8.9: Total background levels and contributions of each volume in the range of energy between 1200 and 1300 keV after the application of the three selection criteria. Values are expressed in counts keV^{-1} kg^{-1} yr^{-1}.

A copper cover of 1 cm thickness reduces the total background a 12 %, in contrast to the 27 % obtained before the application of the selection criteria. For the thicker cover, this reduction is a 48 %, also less than the previous 69 %. This loss of efficiency by the copper shielding is due to the lower power rejection of the one-connection criterium for external contaminations.

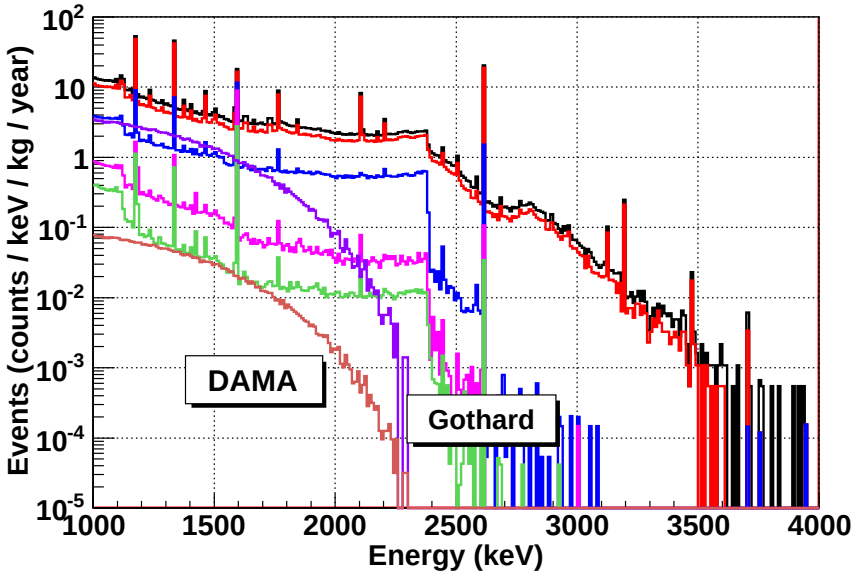

Figure 8.17: Background spectrum between 1 and 4 MeV after the succesive application of the topological selection criteria for the geometry with a 6 cm-thick copper cover. From top to bottom: initial background (black line), after the walls veto (red line), after the one-connection criterium (blue line) and after the blob criteria (magenta line). It is also plotted the estimated spectrum after the selection criteria of a 1 cm-thick copper vessel with a 5 cm-thick lead shielding (green line, bottom). As a comparison, the $\beta\beta2\nu$ signal expected in NEXT enriched an 80 % in ^{136}Xe after the selection criteria and the best limits set on $T^{0\nu}_{1/2}$ by Gothard (violet line) and DAMA (brown line).

In table 8.10, the contribution of each contamination generated in the different geometry elements is shown. ^{208}Tl and ^{214}Bi generate about 80 % of the TPC events. The little remaining percentage is shared between the other components, except for the negligible ^{234m}Pa.

8.5.2 The neutrinoless mode

As the table 8.11 shows, the lowest background level is reached for the 6 cm-thick copper geometry. Its value is $(1.27 \pm 0.04) \times 10^{-3}$ counts keV^{-1} kg^{-1} yr^{-1}, two orders of magnitude better than the value published by the IGEX collaboration and one order in comparison with Gothard and DAMA. This value improves down to $(3.3 \pm 0.2) \times 10^{-4}$ counts keV^{-1} kg^{-1} yr^{-1} for a 1 cm-thick copper vessel. However, the signal acceptance is low: only 37.6 ± 0.2 %, which leads to a selection efficiency to $\beta\beta0\nu$ events of only 28.4 ± 0.1 %.

If the stainless steel vessel is shielded by a 6 cm-thick copper cover, there is a reduction factor less than 2, lower than the factor 3.5 calculated in former chapter. This is due to the lowest rejection power of the one-connection criterium for backgrounds coming from outer volumes. Therefore, the use of a clean copper vessel seems more effective and practical in order to get ultra-low background levels.

In figure 8.18, the spectrum of the 6-cm thick copper geometry after the application of successive selection criterium is shown. We note that the one-connection criterium has the greatest rejection power. In table 8.12 the contribution of each background component and layer is detailed. From this table, we conclude that events generated by ^{60}Co are completely

Geometry	Element	^{40}K	^{60}Co	^{208}Tl	^{212}Bi
No Cu	Vessel	41 ± 2	13 ± 1	194 ± 6	11.9 ± 0.6
	Shielding	5.2 ± 0.2	4.7 ± 0.6	7.5 ± 0.1	0.18 ± 0.01
1 cm Cu	Cover	4.7 ± 0.2	1.1 ± 0.1	22 ± 5	1.31 ± 0.07
	Vessel	22.4 ± 0.8	14 ± 1	190 ± 30	6.8 ± 0.2
	Shielding	3.1 ± 0.1	4.1 ± 0.6	5.3 ± 0.1	0.107 ± 0.007
6 cm Cu	Cover	10.3 ± 0.5	8.2 ± 0.5	101 ± 2	3.2 ± 0.1
	Vessel	16.4 ± 0.8	3.6 ± 0.2	54.0 ± 0.8	0.56 ± 0.03
	Shielding	0.26 ± 0.03	0.6 ± 0.1	1.30 ± 0.02	0.009 ± 0.001

Geometry	Element	^{228}Ac	^{214}Bi	^{234m}Pa
No Cu	Vessel	58 ± 2	188 ± 4	0.05 ± 0.04
	Shielding	0.83 ± 0.03	3.60 ± 0.06	< 0.001
1 cm Cu	Cover	6.3 ± 0.2	19.6 ± 0.3	0.008 ± 0.004
	Vessel	32.3 ± 0.9	124 ± 2	< 0.002
	Shielding	0.55 ± 0.02	2.06 ± 0.05	< 0.001
6 cm Cu	Cover	15.2 ± 0.5	59 ± 1	< 0.003
	Vessel	2.8 ± 0.2	14.7 ± 0.3	< 0.002
	Shielding	0.054 ± 0.006	0.307 ± 0.007	< 0.001

Table 8.10: Contributions of the different impurities and volumes to the background level of the three simulated geometries in the range of energy between 1200 and 1300 keV after the application of the selection criteria. Values are expressed in counts keV^{-1} kg^{-1} yr^{-1}.

	1 cm stainless steel vessel			
Geometry	No Cu	1 cm Cu	6 cm Cu	Cu vessel
Cover	–	0.26 ± 0.01	0.88 ± 0.04	–
Vessel	2.31 ± 0.05	1.87 ± 0.06	0.38 ± 0.02	0.26 ± 0.01
Shielding	0.072 ± 0.008	0.041 ± 0.004	0.009 ± 0.001	0.072 ± 0.008
Total	2.39 ± 0.05	2.17 ± 0.07	1.27 ± 0.04	0.33 ± 0.01

Table 8.11: Total background levels and contributions of each volume in the RoI of $\beta\beta0\nu$ after the application of the three selection criteria. Values are expressed in 10^{-3} counts keV^{-1} kg^{-1} yr^{-1}.

vetoed. The importance of the ^{208}Tl increases with the geometry: 75 % in the case without cover, 81 % for 1 cm of copper and 88 % for 6 cm.

8.6 Conclusions

The topology of the $\beta\beta0\nu$ signal has been compared to that of background events. In this way, three discrimination methods have been developped based on three features: the distance to the walls, the existence of only one connection and the charge of the two ends of the event. These methods have been also applied in the $\beta\beta2\nu$ case. The rejection power of each selection criterium has been evaluated in the RoI of the neutrinoless mode and two other energy regions

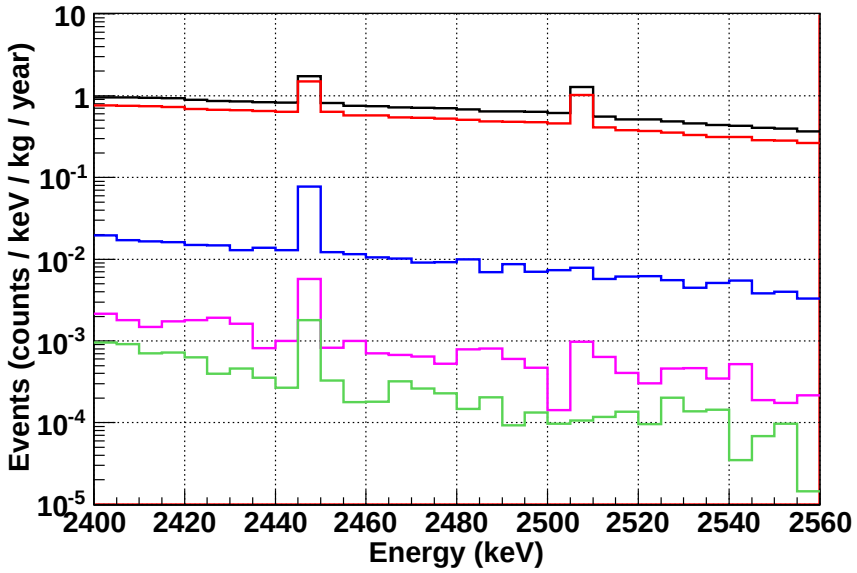

Figure 8.18: Background spectrum in the RoI of $\beta\beta0\nu$ after the succesive application of the selection criteria for the geometry with a 6 cm-thick copper cover. From top to bottom: initial background (black line), after the walls veto (red line), after the one-connection criterium (blue line) and after the blob criteria (magenta line). It is also plotted the estimated spectrum after the selection criteria of a 1 cm-thick copper vessel with a 5 cm-thick lead shielding (green line, bottom).

Geometry	Background	^{208}Tl	^{214}Bi	^{60}Co
No copper	Vessel	1.74 ± 0.06	0.58 ± 0.01	< 0.06
	Shielding	0.062 ± 0.008	0.0107 ± 0.0004	< 0.04
1 cm Cu	Cover	0.21 ± 0.01	0.052 ± 0.002	< 0.03
	Vessel	1.52 ± 0.06	0.35 ± 0.01	< 0.05
	Shielding	0.036 ± 0.004	0.0051 ± 0.0002	< 0.07
6 cm Cu	Cover	0.76 ± 0.03	0.126 ± 0.007	< 0.01
	Vessel	0.34 ± 0.02	0.036 ± 0.003	< 0.007
	Shielding	0.008 ± 0.001	0.00072 ± 0.00007	< 0.02

Table 8.12: Contributions of the different impurities and volumes to the background level of the simulated geometries in the RoI of $\beta\beta0\nu$. Values are expressed in 10^{-3} counts keV^{-1} kg^{-1} yr^{-1}.

for ^{208}Tl and ^{214}Bi contaminations. In these last ranges, events are respectively produced by photoelectric and compton interactions.

The rejection power of each method is not the same in the RoI of the $\beta\beta0\nu$. The walls veto has only a big effect for surface contaminations. The one-connection method has the best factor of merit. The blobs method is not so powerfull (≈ 12) but a further improvement seems feasible, using other features mentioned by the Gothard collaboration [183]. One of them is the existence of sharp turns or *tips* near blobs. These characteristics, different from the one-connection selection, gave a rejection power around 30 with a similar efficiency.

The application of the three selection criteria defined in former subsections has reduced

a factor $\approx$ 13 the difference between the expected signal and the background of level. The lowest values have been obtained for the geometries with the 6 cm-thick copper cover and the copper vessel. In the range of energy between 1200 and 1300 keV, values are 0.277 ± 0.003 and 0.077 ± 0.001 counts keV^{-1} kg^{-1} yr^{-1} respectively. These levels are lower that the expected signal for the Gothard limit (2.42 ± 0.01) and comparable for the geometry with the copper vessel with the DAMA limit (0.0543 ± 0.0002 counts keV^{-1} kg^{-1} yr^{-1}).

The 80 % of the background events is generated by ^{208}Tl and ^{214}Bi contaminations. The reduction of the background by the copper cover is less effective after the application of the selection criteria because the one-connection method has a lower rejection power for the external volumes. Therefore, the use of a clean copper vessel seems more effective and practical in order to get ultra-low background levels. A similar conclusion can be obtained from the neutrinoless mode.

In the neutrinoless mode, the lowest levels of background have been reached by the geometry with the 6 cm-thick copper cover and the copper vessel. The value obtained are respectively $(1.27 \pm 0.04) \times 10^{-3}$ and $(3.3 \pm 0.2) \times 10^{-4}$ counts keV^{-1} kg^{-1} yr^{-1}. These levels are more than two orders of magnitude better than IGEX and one order in comparison with Gothard. However, the selection efficiency is low: only 37.6 ± 0.2 %, which leads to a total efficiency to $\beta\beta0\nu$ signals of only 28.4 ± 0.1 %.

Events generated by ^{60}Co are completely vetoed. Most of the events in the RoI are generated by ^{208}Tl. This contribution is most important as the cover thickness is increased, reaching a value of 88 % for the 6 cm-thick cover. We note that this conclusion depends on the impurities levels defined for each volume, which in our case are the same for ^{208}Tl and ^{214}Bi in all the materials.

In this study, surface contaminations of the micromegas readout have not been simulated. The background level of this readout has been estimated in about 10^{-4} counts keV^{-1} kg^{-1} yr^{-1} after the application of the discrimination techniques [184], comparable to the expected value of the geometry with a copper vessel. We note that the level of contamination of the micromegas has been obtained without a selection of materials in the fabrication, which would surely reduce this level to negligible values.

Chapter 9

The NEXT project: description and sensitivity

The results obtained for the energy resolution, the signal efficiency and the background level are used in this chapter to calculate the sensitivity of the NEXT experiment to $\beta\beta0\nu$. A description of this project is made in the first section. The main results of this work are then summarized and a little discussion of the possible scenarios is made. In the last two sections, the sensitivity of NEXT is expressed in terms of the figure of merit defined in equation 2.7. In the case of the $\beta\beta0\nu$, it is also described calculating the expected number of events in the RoI and limits set in the effective neutrino mass.

9.1 The NEXT project: Current status

The potential of the good energy resolution of new micropattern detectors and the discrimination features of a TPC have motivated the birth of the NEXT project (Neutrino Xenon TPC) [19]. It consists in the design and construction in 5 years of a TPC filled with 100 kg of high pressure xenon enriched in ^{136}Xe. This project has already been funded by a 5-years CONSOLIDER project and approved by the Scientific Committee of the LSC. In absence of a signal, the design should be adequate to scale the mass to 1 tonne.

In an initial phase of 3 years, a 10 kg detector working with natural xenon will be built, where all the technological issues and the radioactive backgrounds will be tested. In a second phase, the definitive detector will be built, which would have the physical potential of detecting the two $\beta\beta$decay modes of ^{136}Xe. The detector should be scalable to larger masses, in the case that $\beta\beta0\nu$ were not discovered.

As a novelty, the energy, the topology and the initial time of an event will be separately measured to optimize the technology to each task. As later discussed, a particle interacting in the TPC produces light and charge. The primary scintillation photons will be immediately detected at the cathode, which will determine the initial time of the event. Then, the charge will drift to the anode, where it will be amplified and the topology reconstructed. The energy will be measured at one or both sides. A design of NEXT1-MM, shown in figure 9.1, serves to describe the future NEXT-100 setup.

As a first option for measuring the energy, not necessary the final chosen technology, the electroluminescence light (EL) is considered. It consists in the generation of light by an intense electric field between two thin metallic grids and detected by an array of photosensors, like photomultipliers (PMT), Silicon photomultipliers (SiPMT) or avalanche photodetectors (APD).

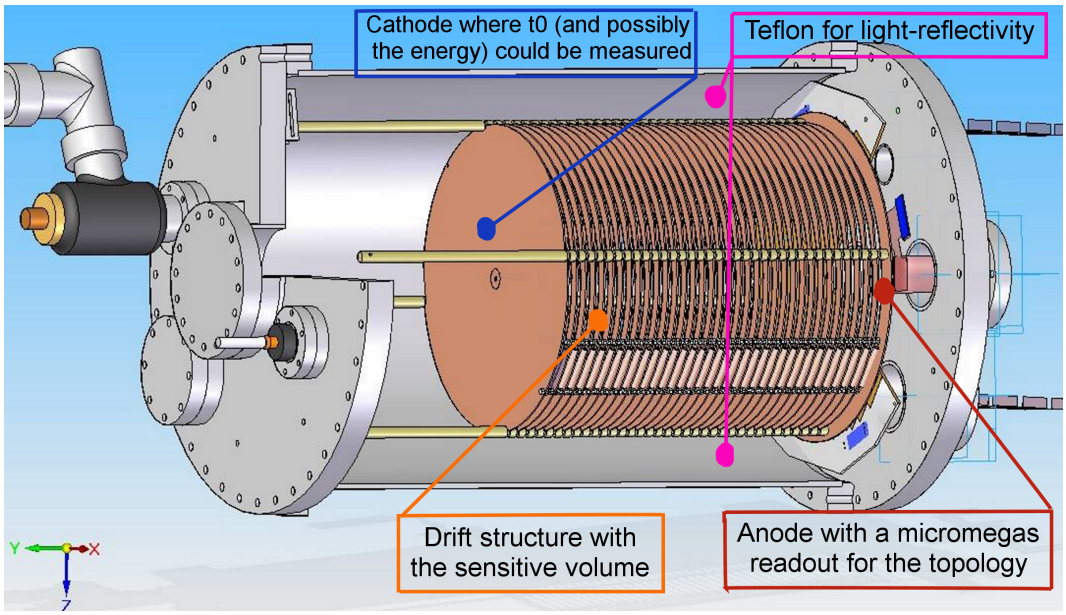

Figure 9.1: A design of NEXT1-MM [20], which serves to describe the future NEXT-100 setup. The High Pressure TPC will be equiped with two readouts: one situated at the cathode, for measuring t_0; and another at the anode, which will get the topology of the event. The energy will be measured at one or both sides. Possible technologies for both readouts are Micromegas and Electroluminiscence (EL), this one detected by PMTs, SiPMTs or APDs.

In theory, the energy resolution of this option is only limited by the variation of the primary ionization in pure xenon (described in section 3.2.2) because the detector contribution is small. This limit is 0.27 % FWHM at $Q_{\beta\beta}$.

However, this hypothesis has not been confirmed at energies above MeV and xenon at high pressure. A good approach was made in [185] in a TPC filled with pure xenon at 5.5 bar, with a drift distance of 3.8 cm and equiped with an array of 19 PMTs. A value of 2.7 % FWHM was measured at 122 keV with a gamma source of ^{57}Co. A better resolution of 2.2 % FWHM was achieved selecting events in coincidence with primary scintillation light. This result leads to an estimation of 0.49 % FWHM at $Q_{\beta\beta}$.

As a possible photosensor, the R8520-06SEL PMT from Hamamatsu Photonics is being characterized. It has a quantum efficiency of about 30 % around 175 nm, the light range of the xenon scintillation light. In addition, each PMT has a radioactivity of 0.5 mBq for the Uranium and Thorium chain. However, they cannot work in gas pressures greater than 5 bar. The actual goal of the experiment is to work at pressures around 10 bar.

The main drawback of the EL option is that the distance between the two thin grids which produce the light must be uniform. To reduce the bends of the grids, they should be strongly tighten to their frame, which is a mechanical challenge for big readouts. In contrast, a micromegas detector (described in section 4.5) is built by photolithography techniques, making uniform the gap where charge is amplified even with high surfaces like in T2K (9 m^2) or COMPASS (1.5 m^2). In addition, the gap can be tuned (as described in section 4.5.1) in order to compensate the fluctuations due to defects of flatness between the mesh and the anode plane.

As already described, micromegas readouts have many other competitive features: they are not limited by pressure, can reach a gain of 100 in pure xenon and are ultraclean in terms of radiopurity. However, this technology must demostrate in pure xenon at high pressure an

energy resolution better than 1 % FWHM at 2480 keV and its capacity for detecting the primary scintillation light. These two features among others are part of a continuous work of research made in a collaboration between the groups of Zaragoza and IRFU/CEA-Saclay.

9.2 Possible scenarios of NEXT

We first summarize the results of chapters 6 and 8. Three possible values have been estimated for the energy resolution, based on different suppositions. Energy resolutions are expressed in % FHWM as this window will be used for the following calculations. The three cases are the following ones:

- An energy resolution of 1.8 % FWHM at 5.5 MeV has been estimated for pure xenon at 4 bar using a selection of pulses with similar risetimes. If this value is supposed also valid at 10 atm and the quenching factor is supposed approximately 1, an energy resolution of 2.8 % FWHM, i.e., 69.4 keV at $Q_{\beta\beta}$ is obtained. This is the most conservative scenario.

- If the quenching factor of 6.5 at 5 atm measured by the Gothard collaboration is supposed instead at 10 atm, the value reduces to 1.1 % FWHM, i.e., 27.3 keV at $Q_{\beta\beta}$. A better gas system and an alpha source with a lower rate or an electron source can give soon this result. This is an optimistic but probable scenario.

- If a value of 11.0 % FWHM is supposed for the energy resolution at 5.9 keV in pure xenon at 10 bar, a final value of 0.54 % FWHM, i.e., 13.3 keV at $Q_{\beta\beta}$ is obtained. This is the most optimistic (and probably unrealistic) estimation.

In the case of the background level, we can consider three scenarios:

- A vessel made of stainless steel is the most realistic option for the geometry. We can supposse a 1 cm-thick vessel, shielded by a 6 cm-thick copper layer and by an external archeological lead shielding. The values respectively obtained for the $\beta\beta2\nu$ and $\beta\beta0\nu$ signals are 0.277 ± 0.003 and $(1.27 \pm 0.04) \times 10^{-3}$ counts keV^{-1} kg^{-1} yr^{-1}. This is the most conservative scenario.

- If a 1 cm-thick copper vessel can be built, the values obtained before are reduced to 0.077 ± 0.001 and $(3.3 \pm 0.2) \times 10^{-4}$ counts keV^{-1} kg^{-1} yr^{-1} for the two-neutrino and the neutrinoless mode respectively. This is an optimistic but probable option.

- In the most optimistic (and probably unrealistic) scenario, we can suppose a 1 cm-thick copper vessel built with the copper measured by the EXO collaboration (< 3 μBq/kg for ^{208}Tl and < 14 μBq/kg for ^{214}Bi). If we neglect the possible contribution of the readout, we obtain the values of $(4.85 \pm 0.05) \times 10^{-3}$ and $(2.1 \pm 0.1) \times 10^{-5}$ counts keV^{-1} kg^{-1} yr^{-1} in the RoIs of $\beta\beta2\nu$ and $\beta\beta0\nu$.

The combinations one to one of the three cases for the energy resolution and those of the background level give three scenarios, which can classified as conservative, optimistic and aggressive. The sensitivity of NEXT in these cases will be studied for four possible mass-time exposures (Mt): 100, 500, 1000 and 5000 kg yr. They correspond to a one year and five years running of a TPC with 100 kg or 1 tonne of xenon. In the case of one tonne, we suppose that the results for the energy resolution and background are conserved, even if the final dimensions of the detector are increased. In all cases, we will supposse an enrichment of 80 % in ^{136}Xe.

9.3 The two-neutrino mode

In this mode, the figure of merit F_D has been calculated using the range of energy between 1200 and 1300 keV for the three scenarios studied and considering a confidence level of 90 %. The results are shown in table 9.1. We note that the best limit of 1.6×10^{22} yr can be improved for all cases. Values higher than 10^{24} yr can only be set by a mass-time exposure higher than 5000 kg yr for the optimistic scenario and by 500 kg yr for the aggreassive one.

	Mt (kg yr)			
Scenario	100	500	1000	5000
Steel + 3 %	8.1×10^{22}	1.8×10^{23}	2.6×10^{23}	5.8×10^{23}
Copper + 1 %	1.5×10^{23}	3.4×10^{23}	4.9×10^{23}	1.1×10^{24}
EXO Copper + 0.5 %	6.1×10^{23}	1.4×10^{24}	1.9×10^{24}	4.3×10^{24}

Table 9.1: The lower limits set in the half-time of the two-neutrino mode (expressed in years) with a confidence level of 90 %. Values have been calculated using the range of energy between 1200 and 1300 keV.

9.4 The neutrinoless mode

Before calculating the lower limits of the half-time of the neutrinoless mode, we can estimate the expected number of events in the RoI of the $\beta\beta0\nu$. These values will express quantitatively if the level of background in the experiment is too elevated in order to be competitive. They are shown in table 9.2 for the four exposition masses considered.

	Mt (kg yr)			
Scenario	100	500	1000	5000
Steel + 3 %	8.8 ± 0.3	44 ± 2	88 ± 3	440 ± 15
Copper + 1 %	0.90 ± 0.05	4.5 ± 0.3	9.0 ± 0.5	45 ± 3
EXO Copper + 0.5 %	0.030 ± 0.001	0.14 ± 0.01	0.28 ± 0.01	1.4 ± 0.1

Table 9.2: Mean number of background events in the RoI of the $\beta\beta0\nu$ signal for each scenario and the different exposure masses.

From this table, we can conclude that the optimistic scenario is the most adequate for a detector mass around 100 kg as only few events will be detected after an exposure time of 5 years. For a detector mass of 1 tonne, the aggreassive scenario seems the best option for a competitive experiment.

The lower limits of $T^{0\nu}_{1/2}$ are shown in table 9.3 for the three scenarios considered and a confidence level of 90 %. In the conservative scenario, a limit of 1.1×10^{25} yr will be reached, improving an order of magnitude the previous limit set by DAMA. Values greater than 10^{26} yr can be easily obtained for a mass-time exposure higher than 1000 kg yr in the optimistic scenario. Values greater than 10^{27} yr can be only obtained in the aggreassive case, with a detector of 1 tonne and 5 years of data-taking.

	Mt (kg yr)			
Scenario	100	500	1000	5000
Steel + 3 %	1.1×10^{25}	2.4×10^{25}	3.5×10^{25}	7.8×10^{25}
Copper + 1 %	3.4×10^{25}	7.7×10^{25}	1.0×10^{26}	2.4×10^{26}
EXO Copper + 0.5 %	1.9×10^{26}	4.3×10^{26}	6.2×10^{26}	1.4×10^{27}

Table 9.3: The lower limits for the half-time of the neutrinoless mode (expressed in years) with a confidence level of 90 % fixed in the six scenarios studied.

The former values serve for estimating the range of neutrino effective masses that will be explored by a TPC, using the equation 1.16 and the nuclear figure of merits calculated in table 1.7. The ranges obtained are respectively shown in tables 9.4 and 9.5 for the QRPA and the NSM models.

The wide F_N ranges of the QRPA case make it difficult to discard mass hierarchies. The known neutrinoless claim can be confirmed or totally discarded for a detector of 100 kg only in the most optimistic scenarios. In the conservative case, an exposure time of 5000 kg yr will be necessary. The quasi-degenerate mass hierarchies can only be totally explored in the aggreassive scenario with a one-tonne-mass experiment and five years of data-taking. The exploration of the inverted hierarchy requires a further reduction of the level of background.

	Mt (kg yr)			
Geometry	100	500	1000	5000
Steel + 3 %	$193 - 535$	$129 - 358$	$109 - 301$	$73 - 201$
Copper + 1 %	$109 - 303$	$73 - 202$	$62 - 170$	$41 - 114$
EXO Copper + 0.5 %	$46 - 127$	$31 - 85$	$26 - 71$	$17 - 48$

Table 9.4: The ranges of the effective neutrino masses (in meV) explored with a confidence level of 90 % in the different scenarios considered and the matrix elements calculated by the QRPA model.

The NSM method gives narrower ranges of F_N values in comparison with the QRPA model. The claim of Klapdor will be confirmed or totally discarded in only 1 year of data-taking in the two most optimistic scenarios. Meanwhile, the quasi-degenerate mass models can only be explored for a mass-time exposure higher than 500 kg yr in the aggreassive option. Effective neutrino masses below 20 meV will be only reached if the background level is further reduced or the efficiency of the detector is improved.

The dependence of the effective neutrino masses explored by NEXT with the exposure time is shown in figure 9.2. We have used the lower value of F_N for the NSM model (1.83×10^{-13} yr).

This study is a first approach to the sensitivity of NEXT-100 and should be completed with a more detailed simulation of the geometry, a precise measurements of the level of impurities of each material, a further development of detectors and better discrimination methods. Nevetheless, we can conclude that the NEXT project has a big potential and will be a competitive experiment in the search of the double beta decay of ^{136}Xe.

	Mt (kg yr)			
Geometry	100	500	1000	5000
Steel + 3 %	270 – 356	181 – 238	152 – 200	102 – 134
Copper + 1 %	153 – 201	102 – 135	86 – 113	57 – 76
EXO Copper + 0.5 %	64 – 84	43 – 56	36 – 48	24 – 32

Table 9.5: The ranges of the effective neutrino masses (in meV) explored with a confidence level of 90 % in the different scenarios considered and the matrix elements calculated by the NSM model.

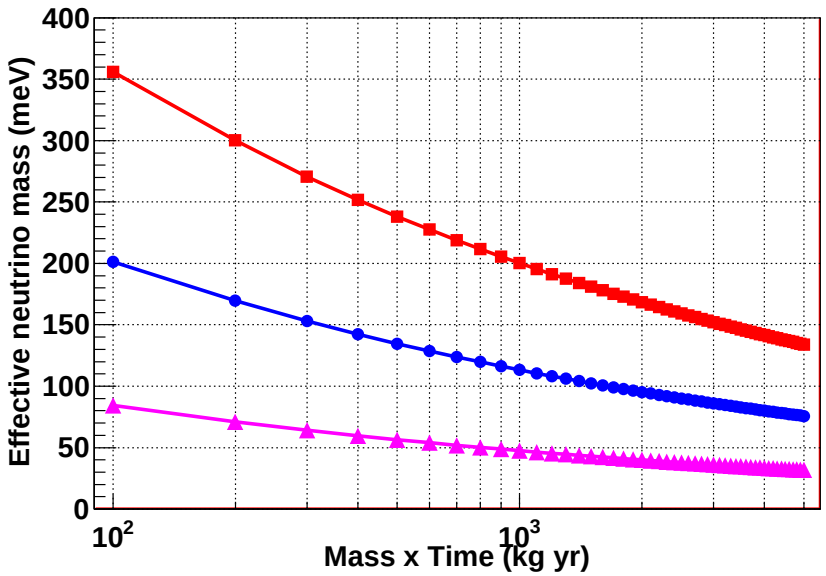

Figure 9.2: Depedence of the sensitivity of NEXT in terms of the effective neutrino mass with the time of exposure for the three scenarios studied: conservative (stainless steel vessel + 3 % FWHM - red squares), optimistic (copper vessel + 1 % FWHM + blue circles) and aggressive (EXO copper vessel + 0.5 % FWHM + magenta triangles).

Chapter 10

Summary and conclusions

This thesis has studied the viability of a TPC equipped with a micromegas readout and filled with 100 kg of xenon enriched in ^{136}Xe for an experiment of double beta decay. From this process, neither the allowed two-neutrino mode nor the neutrinoless case has been observed, which makes it more attractive. Apart from that, the xenon has the advantage that its nuclear factor of merit is greater than that of other isotopes like ^{76}Ge and ^{130}Te, which makes it more sensitive to the $\beta\beta0\nu$ signal.

Three parameters have been studied: the energy resolution at $Q_{\beta\beta}$, the background level in the RoI of the two expected signals ($\beta\beta2\nu$ and $\beta\beta0\nu$) and the detector efficiency. Other important parameters like the gain stability, the tracking capability and the surface contamination have been omitted as they have been described in other works.

The energy resolution at $Q_{\beta\beta}$

In order to estimate the energy resolution, the newest micromegas readouts (type microbulk) have been characterized with a ^{241}Am source which emits an alpha of 5.486 MeV. Two different setups have been used: one previously used by the HELLAZ experiment and a completely new one, where the experience learnt in the former setup has been applied.

The tests in the first setup have shown an energy resolution down to 1.8 % and 2 % FWHM for argon-isobutane mixtures at 4 bar and percentages of isobutane of 2 % and 5 % respectively. A possible evidence for better achievable resolutions (down to 0.7 % and 0.9 % FWHM respectively) has been pointed out based on the asymmetry of the alpha peak. Moreover, the quenching factor of alpha particles for the 5 % mixture has been measured by comparing the x-ray and the alpha peaks. A value around unity has been obtained.

The preliminary measurements in pure xenon for pressures 2-4 bar have shown clear effects of attachment in the electron transmision curve and in the correlation between the risetime and the amplitude of the preamplifier pulses. A simple model of attachment has explained this correlation and has been used to fix upper limits at the mean electron lifetime: 47 ± 5 and 4.0 ± 0.2 μs at 3 and 4 bar respectively. Supposing oxygen as the main cause of attachment, its concentration has been estimated in 1000 ppm, just after the installation of a new oxisorb filter.

As an estimation of the energy resolution in better gas conditions, events with similar risetime have been selected to minimize the spread due to attachment. Values of 2.8 % and 4.5 % FWHM have been respectively found at 2 and 4 bar.

The new setup has been designed and built for testing micromegas readouts in different gases and pressures up to 10 bar. The optimized design of the gas and vacuum system and the

bake-out circuit have reduced the inside outgassing rate to 10^{-5} mbar l / s. In pure xenon, attachment effects are clearly lower than Saclay, as the amplitude is almost independent of risetime at pressures between 2 and 4 bar at high enough drift fields. This does not happen at 5 bar, which means that some attachment cannot be avoided. This observation has been quantified by the mean electron lifetime.

A lower limit for this variable of 0.6 ms has been stablished for 3 and 4 bar, limited by the estimation method. This bound is near the required value of 6 ms for a charge reduction of less than the 1 % in xenon-based mixtures and drift distances of about 1 meter. Therefore, the gas purity at 3 and 4 bar is almost the ideal one. At 5 bar, a maximum value of 38 ± 1 μs has been calculated. In terms of the oxygen contamination, values around 80 ppm have been estimated for the first days of data-taking and 60 ppm after one-night gas recirculation through the oxisorb filter. These values clearly improve those obtained in the Saclay setup, which were higher than 1000 ppm.

The alpha measurements in this setup seem to have been affected by the high rate of the source. Some of them are the variation of the transparency plateau with pressure and the low gain values, sometimes lower than the unity. The energy resolution could have also been affected. Even so, the drift velocity in pure argon and xenon has been measured, in better agreement with theory than previous measurements. The energy resolution values for argon-based mixtures are similar to Saclay's values and are better for pure argon and xenon. Its dependence with drift field and pressure has also been observed.

The best value obtained in pure xenon is 2.5 % FWHM at 4 bar. At the same pressure, a value of 1.8 % FWHM has been estimated using a selection of risetimes. If we suppose that this value is also valid at 10 bar and the quenching factor is near 1, we deduce a value of 2.7 % FWHM at 2480 keV (28.3 keV σ). If the quenching factor of 6.5 reported by the Gothard collaboration at 5 bar is used instead, the energy resolution at $Q_{\beta\beta}$ reduces to 1.05 % FWHM (11.1 keV σ). These estimations are positive and can be easily improved with a reduction of the plastic components inside the TPC, a better bake-out system, the systematic recirculation of the gas by filters; and an alpha source with a lower rate.

The efficiency and the background level

Two simulation codes have been developped for simulating signals and backgrounds in a TPC equipped with a pixelized micromegas readout. The first one, a Geant4 code, simulates the physical interactions in the TPC and gives as a result a serie of energy depositions. The second one, called RESTSoft, transforms these depositions in pixels, simulating the specific features of a TPC: charge generation, diffusion and pixelization. It allows also to analize the events.

Before the simulation, the main contributions to the background of a TPC have been evaluated. Two ranges of interest have been defined, one for each $\beta\beta$ decay mode. In the neutrinoless case, emissions by ^{208}Tl, ^{214}Bi and ^{60}Co have been identified as the most important ones. Apart from these three impurities, the isotopes ^{40}K, ^{212}Bi, ^{228}Ac and ^{234m}Pa must also be considered in the two-neutrino case for energies higher than 1200 keV.

Three geometries have been simulated. They consist of a 1 cm-thick stainless steel vessel, a 5 cm-thick lead shielding and an internal copper shielding with three possible thickness: 0, 1 and 6 cm. A vessel completely made out of copper is an attractive option due to the radiopurity of copper but its construction is a mechanical challenge. This is why stainless steel has been chosen as the material of the vessel in the simulations. Nevertheless, a rough estimation of the background of a 1 cm-thick copper vessel has been made with the results of the three former geometries. The values measured by different collaborations to fix the expected contamination

of each material. Values around 1, 0.1 and 0.01 mBq/kg have been respectively assigned to stainless steel, copper and lead, except for ^{60}Co and ^{40}K.

The detector efficiency has been estimated in 99.4 % for $\beta\beta2\nu$ and 72.4 % for $\beta\beta0\nu$. The lowest background levels have been obtained for the geometry with a 6 cm-thick copper cover and that with the copper vessel. For the two-neutrino mode, these levels (6.76 ± 0.01 and 3.08 ± 0.01 counts keV^{-1} kg^{-1} yr^{-1} in the range between 1200 and 1300 keV) are close to Gothard limit (2.42 ± 0.01) but far from that of DAMA (0.103 ± 0.001). For the neutrinoless mode, the lowest levels are respectively 0.856 ± 0.001 and 0.377 ± 0.001 counts keV^{-1} kg^{-1} yr^{-1}. There is a difference greater than 4 between these values and that published by IGEX and two orders of magnitude comparing to Gothard. This fact points out that a reduction by discrimination methods is possible.

The topology of the $\beta\beta0\nu$ signal has been compared to that of background events in the RoI. In this way, three discrimination methods have been developped based on three features: the distance to the walls, the existence of only one connection and the charge at the two ends of the event. These methods have also been applied in the $\beta\beta2\nu$ case. The rejection power of each selection criterium has been evaluated in the RoI of the neutrinoless mode and two other energy regions for ^{208}Tl and ^{214}Bi contaminations, where most of the events are respectively produced by photoelectric and Compton interactions.

The one-connection criterium has the best rejection power of the three cuts, with values around 90 for the most internal volumes. The blobs method is not so powerful (values around 12) but an improvement seems feasible as the Gothard collaboration reached a value around 30 with a similar efficiency. The walls veto has only a big effect for surface contaminations.

The application of the three selection criteria defined in former subsections has reduced a factor ≈ 13 the difference between the expected signal and the background of level. The lowest values have been obtained for the geometries with the 6 cm-thick copper cover and the copper vessel. For the two-neutrino mode and the range of energy between 1200 and 1300 keV, values of background are 0.277 ± 0.003 and 0.077 ± 0.001 counts keV^{-1} kg^{-1} yr^{-1} respectively. These levels are better that the expected signal for the Gothard limit (2.42 ± 0.01) and comparable with the DAMA limit (0.0543 ± 0.0002 counts keV^{-1} kg^{-1} yr^{-1}) for the geometry with the copper vessel.

In the neutrinoless mode, the lowest levels of background have been reached by the geometry with the 6 cm-thick copper cover and the copper vessel. The values obtained are respectively $(1.27 \pm 0.04) \times 10^{-3}$ and $(3.3 \pm 0.2) \times 10^{-4}$ counts keV^{-1} kg^{-1} yr^{-1}. These levels are more than two orders of magnitude better than IGEX and one order in comparison with Gothard. However, the selection efficiency is low: only 37.6 ± 0.2 %, which leads to a total efficiency to $\beta\beta0\nu$ signals of only 28.4 ± 0.1 %. In the two-neutrino mode, the 80 % of the background events are generated by ^{208}Tl and ^{214}Bi contaminations. The most important contribution in the RoI of $\beta\beta0\nu$ is due to ^{208}Tl.

The NEXT experiment: description and sensitivity

The results presented in this work have motivated the project NEXT, which proposes the construction of a Xenon TPC of 100 kg enriched in ^{136}Xe for a double beta decay experiment in 5 years. As a novelty, the energy, the topology and the initial time of an event will be separately measured for optimizing the technology to each task. The primary scintillation photons produced by a particle will be immediately detected at the cathode, which will determine the initial time of the event. Then, the generated charge will drift to the anode, where it will be amplified and the topology reconstructed. The energy will be measured at one or both sides.

As a first option for measuring the energy, not necessary the final chosen technology, the electroluminescence light (EL) is considered. It consists in the generation of light by an intense electric field between two thin metallic grids and detected by an array of photosensors. In theory, the energy resolution is only limited by the variation of the primary ionization in pure xenon, which is 0.27 % FWHM at $Q_{\beta\beta}$. However, this hypothesis has not been confirmed at energies above MeV and xenon at high pressure.

The main drawback of the EL option is that the distance between the two thin grids which produce the light must be uniform. For reducing the bends of the grids, they should be strongly tighten to their frame, which is a mechanical challenge for big readouts. By contrast, a micromegas detector is built by photolithography techniques, making uniform the gap where charge is amplified. In addition, the gap can be tuned in order to compensate the fluctuations due to defects of flatness between the mesh and the anode plane.

The results obtained for the energy resolution, the efficiency and the background level have been combined to estimate the sensitivity of NEXT in a $\beta\beta$ decay experiment. This experiment is suppossed equipped with a Micromegas readout and filled with pure xenon enriched an 80 % in ^{136}Xe. We have considered three scenarios: conservative (geometry with a stainless steel vessel and an energy resolution of 2.8 % FWHM), optimistic (a copper vessel and a 1.1 % FWHM) and aggressive (an EXO copper vessel and a 0.54 % FWHM). The sensitivity has been studied in a range of mass-time exposures between 100 and 5000 kg yr, equivalent to detector masses of 100 kg and 1 tonne and times between 1 and 5 years.

For the two-neutrino case, NEXT will set a limit better than DAMA (1.6×10^{22} yr) in all cases in absence of signal. Values higher than 10^{24} yr can be only set by a mass-time exposure higher than 5000 kg yr for the optimistic scenario and by 500 kg yr for the aggreassive case.

For the neutrinoless mode and the conservative scenario, a limit of 1.1×10^{25} yr will be reached for the half-time, improving an order of magnitude the previous limit set by DAMA. Values greater than 10^{26} yr can be easily obtained for a mass-time exposure higher than 1000 kg yr in the optimistic scenario. Values higher than 10^{27} yr can be only obtained in the aggreassive case, with a detector of 1 tonne and 5 years of data-taking.

The calculated values for the half-time and the nuclear factor of merit define the range of neutrino effective masses that will be explored by NEXT. In the case of the QRPA model, mass ranges are too wide to explore the different hierarchies. The known neutrinoless claim can be confirmed or totally discarded for a detector of 100 kg only in the most optimistic scenarios. In the conservative case, an exposure time of 5000 kg yr will be necessary. The quasi-degenerated mass hierarchies can only be totally explored in the aggreassive scenario with a one-tonne-mass experiment and five years of data-taking. The exploration of the inverted hierarchy requires a further reduction of the level of background.

The NSM method gives narrower ranges of F_N values in comparison with the QRPA model. The claim of Klapdor will be confirmed or totally discarded in only 1 year of data-taking in the two most optimistic scenarios. Meanwhile, the quasi-degenerated mass models can only be explored for a mass-time exposure higher than 500 kg yr in the aggreassive option. Effective neutrino masses below 20 meV will be only reached if the background level is further reduced or the efficiency of the detector is improved.

This study is a first approach to the sensitivity of NEXT-100 and should be completed with a more detailed simulation of the geometry, a precise measurements of the level of impurities of each material, a further development of detectors and better discrimination methods. Nevetheless, we can conclude that the NEXT project has a big potential and will be a competitive experiment in the search of the double beta decay of ^{136}Xe.

Bibliography

[1] T. Dafni *et al.*, Energy resolution of alpha particles in a Micromegas detector at high pressure, *Nucl. Instrum. Meth. A* **608** (2009) 259.

[2] T. Dafni *et al.*, New Micromegas detectors for rare event searches: axions and $\beta\beta$ decay, *Preprint*: PoS(idm 2008)106. Proceedings of the 7th International Workshop on The Identification of Dark Matter.

[3] T. Dafni *et al.*, MICROMEGAS for Rare Event Searches, Proceedings of the IEEE 2008, Dresden.

[4] F. J. Iguaz *et al.*, Energy resolution of alpha particles in a Micromegas detector at high pressure, Proceedings of the 4th Symposium on Large TPCs for Low Energy Rare event Detection, *J. Phys. Conf. Ser.* **179** (2009) 012007.

[5] A. Tomás *et al.*, Development of Micromegas towards Double Beta Neutrinoless Decay Searches, *JINST* **4** (2009), P11016, Proceedings of the 1st International Conference on Micro Pattern Gaseous Detectors (MPGD2009), Crete.

[6] F. Reines and C. L. Cowan, Free Antineutrino Absorption Cross Section. I. Measurement of the Free Antineutrino Absorption Cross Section by Protons, *Phys. Rev.* **113** (1959) 273.

[7] N. Fatemi-Ghomi, Measurement of the Double Beta Decay Half-life of ^{150}Nd and Search for Neutrinoless Decay Modes with the NEMO3 Detector, PhD Thesis, University of Manchester, 2009.

[8] S. R. Elliot and J. Engel, Double Beta Decay, *Preprint* arXiv:hep-ph/0202264.

[9] F. Simkovic *et al*, The $0\nu\beta\beta$-decay nuclear matrix elements with self-consistent short range correlations, *Phys. Rev. C* **79** (2009) 055501, *Preprint* arXiv:nucl-th/09020331.

[10] J. Menéndez and A. Poves, Disassembling the Nuclear Matrix Elements of the Neutrinoless $\beta\beta$ Decay, *Nucl. Phys. A* **818** (2009) 139, *Preprint* arXiv:nucl-th/08013760.

[11] H. Klapdor-Kleingrothaus *et al.*, First Evidence for Lepton Number Violation and of the Majorana Character of Neutrinos, *Modern Physics Letters A* **16** (2001) 2409.

[12] C. E. Aalseth *et al.*, IGEX ^{76}Ge neutrinoless double-beta decay experiment: Prospects for next generation experiments, *Phys. Rev. D* **65** (2002) 092007.

[13] R. Luescher *et al.*, Search for $\beta\beta$ decay in ^{136}Xe: new results from the Gotthard experiment, *Phys. Lett. B* **434** (1998) 407.

[14] Y. Giomataris, P. Rebourgeard, J. P. Robert and G. Charpak, MICROMEGAS: A high - granularity position - sensitive gaseous detector for high particle - flux environments, *Nucl. Instrum. Meth. A* **376** (1996) 29.

[15] P. Colas, I. Giomataris and V. Lepeltier, Ion backflow in the Micromegas TPC for the future linear collider, *Nucl. Instrum. Meth. A* **535** (2004) 226.

[16] T. Papaevangelou *et al.*, Development and performance of Microbulk Micromegas detectors, Proceedings of the 1st International Conference on Micro-Pattern Gaseous Detectors (MPDG 2009), to be published.

[17] J. Dolbeau, I. Giomataris, P. Gorodetzky, T. Patzak, P. Salin and A. Sarat, The solar neutrino HELLAZ project, *Nucl. Phys. Proc. Suppl.* **138** (2005) 94.

[18] J. F. O'Hanlon, A User's Guide to Vacuum Technology, 3rd Edition (2003), John Wiley and Sons, Inc.

[19] M. Ball *et al.* NEXT: A Neutrinoless Double Beta Decay Experiment, IEEE Transactions On Nuclear Science 2009.

[20] design made by J. Castell, reproduced with permission.

[21] R. Bernabei *et al.*, Investigation of $\beta\beta$ decay modes in ^{134}Xe and ^{136}Xe, *Phys. Lett. B* **546** (2002) 23.

[22] N. Ackerman *et al*, Status of EXO-200, Proceedings of the DPF-2009 Conference, Detroit, MI, July 27-31, 2009 1.

[23] A. Morales, Review on Double Beta Decay Experiments & Comparison with Theory, *Nucl. Phys. (Proc. Suppl.)* **77** (1999), 335-345.

[24] S. R. Elliot and J. Engel, Double Beta Decay, *J. Phys G* **30** (2004), R183.

[25] F. T. Avignone, G. S. King and Yu. G. Zdesenko, Next generation double beta decay experiments: Metrics for their evaluation, *New J. Phys.* **7** (2005) 6.

[26] D. O. Caldwell (Editor), Current Aspects of Neutrino Physics, Springer, Berlin, 2001.

[27] M. Goeppert-Mayer, Double Beta-Disintegration, *Phys. Rev.* **48** (1935) 512.

[28] E. Majorana, Teoría simmetrica dell'electrone e del positrone, *Nuovo Cimento* **14** (1937) 171.

[29] F. Reines *et al.*, Evidence for High-Energy Cosmic-Ray Neutrino Interactions, *Phys. Rev. Lett.* **15** (1965) 429.

[30] R. Davis, D. S. Harmer and K. C. Hoffman, Search for Neutrinos from the Sun, *Phys. Rev. Lett.* **20** (1968) 1205.

[31] G. Danby *et al.*, Observation of High-Energy Neutrino Reactions and the Existence of Two Kinds of Neutrinos, *Phys. Rev. Lett.* **9** (1962) 36.

[32] G. S. Abrams *et al.*, Measurements of Z-boson resonance parameters in e^+e^- annihilation, *Phys. Rev. Lett.* **63** (1989) 2173.

[33] D. Decamp *et al.*, A precise determination of the number of families with light neutrinos and of the Z boson partial widths, *Phys. Lett. B* **235** (1990) 399.

[34] K. Kodama *et al.*, Observation of tau neutrino interactions, *Phys. Lett. B* **504** (2001) 218.

[35] K. S. Hirata *et al.*, Observation of 8B solar neutrinos in the Kamiokande-II detector, *Phys. Rev. Lett.* **63** (1989) 16.

[36] Q. R. Ahmed *et al.*, Measurement of the Rate of $\nu_e + \mathrm{d} \rightarrow \mathrm{p} + \mathrm{p} + e^-$ Interactions Produced by ^{8}B Solar Neutrinos at the Sudbury Neutrino Observatory, *Phys. Rev. Lett.* **87** (2001) 071301.

[37] B. Pontecorvo, Mesonium and Antimesonium, *J. Exptl. Theoret. Phys.* **33** (1957) 549.

[38] Z. Maki, M. Nakagawa, and S. Sakata, Remarks on the unified model of elementary particles, *Prog. Theor. Phys.* **28** (1962) 870.

[39] R. Becker-Szendy *et al.*, Electron- and muon-neutrino content of the atmospheric flux *Phys. Rev. D.* **46** (1992) 3720.

[40] Y. Fukuda *et al.*, Atmospheric ν_μ/ν_e ratio in the multi-GeV energy range, *Phys. Lett. B* **335** (1994) 237.

[41] Y. Fukuda *et al.*, Evidence for Oscillation of Atmospheric Neutrinos, *Phys. Rev. Lett.* **81** (1998) 1562.

[42] K. Eguchi *et al.*, First Results from KamLAND: Evidence for Reactor Antineutrino Disappearance, *Phys. Rev. Lett.* **90** (2003) 021802.

[43] Ling-Lie Chau and Wai-Yee Keung, Comments on the Parametrization of the Kobayashi-Maskawa Matrix, *Phys. Rev. Lett.* **53** (1984) 1802.

[44] B. Aharmin *et al.*, Electron energy spectra, fluxes, and day-night asymmetries of ^{8}B solar neutrinos from measurements with NaCl dissolved in the heavy-water detector at the Sudbury Neutrino Observatory, *Phys. Rev. C* **72** (2005) 055502.

[45] Y. Ashie *et al.*, Evidence for an Oscillatory Signature in Atmospheric Neutrino Oscillations, *Phys. Rev. Lett.* **93** (2004) 101801.

[46] M. Apollonio *et al.*, Limits on neutrino oscillations from the CHOOZ experiment, *Phys. Lett. B* **466** (1999) 415.

[47] C. Kraus *et al.*, Final Results from phase II of the Mainz Neutrino Mass Search in Tritium β Decay, *Eur. Phys. J. C* **40** (2005) 447.

[48] V. M. Lobashev *et al.*, Direct search for mass of neutrino and anomaly in the tritium beta-spectrum, *Phys. Lett.* **460** (1999) 227.

[49] H. Klapdor-Kleingrothaus *et al.*, Latest results from the HEIDELBERG-MOSCOW double beta decay experiment, *Eur. Phys. J.* **12** (2001) 147.

[50] O. Elgaroy and O. Lahov, *J. Cosmol. Astropart. Phys* **04** (2003) 004.

[51] S. King, Measurement of the Double Beta Decay Half-Life of ^{100}Mo to the 0_1^+ Excited State, and ^{48}Ca to the Ground State in the NEMO 3 Experiment, PhD Thesis, University College London, 2008.

[52] A. Gouvea, On Determining the Neutrino Mass, FNAL Theory Seminar, March 30, 2006.

[53] S. C. Curran, J. Angus, and A. L. Cockcroft, The Beta-Spectrum of Tritium, *Phys. Rev.* **76** (1949) 853.

[54] V. M. Lobashev, The search for the neutrino mass by direct method in the tritium beta-decay and perspectives of study it in the project KATRIN, *Nucl. Phys. A* **719** (2003) 153.

[55] A. Osipowicz *et al.*, KATRIN: A next generation tritium beta decay experiment with sub-eV sensitivity for the electron neutrino mass, *Preprint* arXiv:hep-ex/0109033.

[56] M. Doi, T. Kotani, E. Takasurgi, Approximations for double-beta-decay formulas, *Phys. Rev. C* **37** (1988) 2104.

[57] K. Zuber, Neutrino Physics, *Institute of Physics*, 2004.

[58] F. Simkovic *et al.*, Additional nucleon current contribution to neutrinoless double β decay, *Phys. Rev. C* **60** (1999) 055502.

[59] I. Ogawa *et al.*, Search for neutrino-less double beta decay of ^{48}Ca by CaF_2 scintillator, *Nucl. Phys. A* **730** (2004) 215.

[60] A. S. Barabash *et al.*, NEMO-3 double beta decay experiment: lastest results, *Preprint* arXiv:hep-ex/0610025.

[61] F. A. Danevich *et al.*, Search for 2β decay of cadmium and tungsten isotopes: Final results of the Solotvina experiment, *Phys. Rev. C* **68** (2003) 035501.

[62] T. Bernatowicz *et al.*, Precise determination of relative and absolute $\beta\beta$-decay rates of ^{128}Te and ^{130}Te, *Phys. Rev. C* **47** (1993) 806.

[63] C. Arniboldi *et al.*, Nuclear Quantum Optics with X-Ray Laser Pulses, *Phys. Rev. Lett.* **96** (2005) 142501.

[64] A. S. Barabash *et al.*, Investigation of double-beta-decay processes at the NEMO-3 tracking detector, *Phys. At. Nucl.* **68** (2005) 414.

[65] H. V. Klapdor-Kleingrothaus, I. V. Krivosheina, I. V. Titkova, Particle and nuclear physics parameters-how do they affect the tracks of double beta events in a germanium detector, and their separation from gamma events, *Physics Letters B* **632** (2006) 623.

[66] J. Menéndez, Double Beta Decay with Shell Model, ILIAS 6th Annual meeting, Dresden, 16-19 February 2009.

[67] E. Caurier, J. Menéndez, F. Nowacki and A. Poves, Influence of Pairing on the Nuclear Matrix Elements of the Neutrinoless $\beta\beta$ Decays, *Phys. Rev. Lett.* **100** (2008) 052503.

[68] F. Simkovic, A. Faessler, V. Rodin, P. Vogel and J. Engel, Anatomy of the $0\nu\beta\beta$ nuclear matrix elements, *Phys. Rev. C* **77** (2008) 045503, *Preprint* arXiv:nucl-th/07102055.

[69] J. P. Schieffer *et al*, Nuclear Structure Relevant to Neutrinoless Double Decay: ^{76}Ge and ^{76}Se, *Phys. Rev. Lett.* **100** (2008), 112501.

[70] B. P. Kay *et al*, Nuclear structure relevant to neutrinoless double decay: The valence protons in ^{76}Ge and ^{76}Se, *Phys. Rev. C* **79** (2009), 021301 (R).

[71] J. Suhonen and O. Civitarese, Effects of orbital occupancies on the neutrinoless $\beta\beta$ matrix element of ^{76}Ge, *Phys. Lett. B* **668** (2008) 277.

[72] S. R. Elliot and P. Vogel, *Ann. Rev. Nucl. Part. Sci.* **52** (2003) 115.

[73] F. T. Avignone, S. Elliott and J. Engel, Double beta decay, Majorana neutrinos and neutrino mass, *Rev. Modern. Phys.* **80** (2008) 481.

[74] G. Luzón *et al*, Characterization of the Canfranc Underground Laboratory: Status and future plans, Proceedings of the 6th International Workshop on The Identification of Dark Matter, World Scientific, pp. 514-519.

[75] L. Pandola *et al.*, Monte Carlo evaluation of the muon-induced background in the GERDA double beta decay experiment, *Nucl. Instrum. Meth. A* **570** (2007) 149.

[76] H. Gómez, Estudio de la sensibilidad de un experimento de desintegración doble beta con detectores de Ge de nueva generación, PhD thesis, University of Zaragoza, 2009.

[77] C. E. Aalseth *et al.*, Neutrinoless double beta decay of ^{76}Ge: first results from the International Germanium EXperiment (IGEX) with six isotopically enriched detectors, *Phys. Rev. C* **59** (1999) 2108.

[78] D. González *et al.*, Pulse-shape discrimination in the IGEX experiment, *Nucl. Instrum. Meth.* **515** (2003) 634.

[79] M. Gunther *et al.*, Heidelberg-Moscow $\beta\beta$ experiment with ^{76}Ge: full setup with five detectors, *Phys. Rev. D* **55** (1997) 54.

[80] H. Klapdor-Kleingrothaus *et al.*, Reply to a Comment of article "Evidence for Neutrinoless Double Beta Decay" *Preprint* arXiv:hep-ph/0205228.

[81] H. Klapdor-Kleingrothaus *et al.*, Background analysis around $Q_{\beta\beta}$ for ^{76}Ge double beta decay experiments, and statistics at low count rates, *Nucl. Instrum. Meth. A* **510** (2003) 281.

[82] H. Klapdor-Kleingrothaus *et al.*, Measurement of the ^{214}Bi spectrum in the energy region around the Q-value of ^{76}Ge neutrinoless double-beta decay, *Nucl. Instrum. Meth. A* **511** (2003) 335.

[83] H. Klapdor-Kleingrothaus *et al.*, Support of evidence for neutrinoless double beta decay, *Phys. Lett. B* **578** (2004) 54.

[84] Y. Zdesenko *et al.*, Has neutrinoless double β decay of ^{76}Ge been really observed?, *Phys. Lett. B* **546** (2002) 206.

[85] F. Feruglio *et al.*, Neutrino oscillations and signals in β and $0\nu2\beta$ experiments, *Nucl. Phys. B* **637** (2002) 345.

[86] A. Giuliani *et al.*, Current double beta decay experiments, *Nucl. Phys. B (Proc. Suppl.)* **138** (2005) 267.

[87] C. Arniboldi *et al.*, A calorimetric search on double beta decay of ^{130}Te, *Phys. Lett. B* **557** (2003) 167.

[88] C. Arniboldi *et al.*, Results from a search for the $0\nu\beta\beta$-decay of ^{130}Te, *Phys. Rev. C.* **78** (2008) 035502.

[89] R. Arnold *et al.*, Technical design and performance of the NEMO3 detector, *Nucl. Instrum. Meth. A* **536** (2005) 79.

[90] A. S. Barabash *et al*, Double beta decay: present status, *Preprint* arXiv:hep-ex/08072948.

[91] R. Arnold *et al.*, Study of 2β-decay of Mo-100 and Se-82 using the NEMO3 detector, *JETP Lett.* **80** (2004) 429.

[92] A. S. Barabash *et al.*, NEMO3 and SuperNEMO double beta decay experiments, *J. Phys. Conf. Ser.* **39** (2006) 347.

[93] J.C. Vuilleumier *et al.*, Search for neutrinoless double-β decay in ^{136}Xe with a time projection chamber, *Phys. Rev. D* **48** (1993) 1009.

[94] The Majorana Collaboration, White Paper on the Majorana Zero- Neutrino Double-Beta Decay Experiment, *Preprint* arXiv:nucl-ex/0311013.

[95] S. Elliot *et al.*, The Majorana project, *J. Phys. Conf. Ser.* **39** (2006) 341.

[96] I. Abt *et al.*, GERDA Letter of Intent, A new ^{76}Ge Double Beta Decay Experiment at LNGS, *Preprint* arXiv:hep-ex/0404039.

[97] B. Majorovits, The GERDA neutrinoless-double-beta decay experiment, *Proceedings of Science, IDM 2008* (2008) 69.

[98] C. Arnaboldi *et al.*, CUORE: a cryogenic underground observatory for rare events, *Nucl. Instrum. Meth. A* **518** (2004) 775.

[99] M. Danilov *et al.*, Detection of very small neutrino masses in double-beta decay using laser tagging *Phys. Lett. B* **480** (2000) 12.

[100] W. R. Leo, Techniques for Nuclear and Particle Physics Experiments, Springer-Verlag Berlin Heidelberg, 1994.

[101] W. Blum and L. Rolandi, Particle Detection with Drift Chambers, Springer-Verlag Berlin Heidelberg, 1993.

[102] M. J. Berger *et al.*, XCOM: Photon Cross Sections Database, National Institute of Standarts and Technology (NIST).

[103] D. E. Groom, N.V. Mokhov and S.I. Striganov, Muon stopping power and range tables 10 MeV - 100 TeV.

[104] Wikipedia encyclopedy, Helmut Paul (own work), 9th May 2006.

[105] L. G. Christophorou, Atomic and Molecular Radiation Physics, Wiley, London 1971.

[106] M. Chefdeville, Development of Micromegas-like gaseous detectors using a pixel readout chip as collecting anode, PhD Thesis, University of Amsterdam, 2009.

[107] S. F. Biagi, Accurate solution of the Boltzmann transport equation, *Nucl. Instrum. Meth. A* **273** (1988) 533.

[108] B. Stacey, Relation of Electron Scattering Cross-Sections to Drift Measurements in Noble Gases, Bachelor thesis, MIT, June 2005.

[109] C. Ramsauer, Uber den Wirkungsquerschnitt der Gasmolekule gegenuber langsame Elektronen, *Ann. Phys.* **66** (1921) 546.

[110] L. G. Christophorou, D. V. Maxey, D. L. McCorkle and J. G. Carter, Xe-containing fast mixtures for gas-filled detectors, *Nucl. Instrum. Meth.* **171** (1980) 491.

[111] S. F. Biagi, Montecarlo simulation of electron drift and diffusion in counting gases under the influence of electric and magnetic fields, *Nucl. Instrum. Meth.* **421** (1999) 234 Programme and cross sections available in http://www.cern.ch/magboltz.

[112] A. Peisert and F. Sauli, Drift and Diffusion of electrons in gases: A compilation, CERN 84-08, Experimental Physics Division, 1984.

[113] B. Jean-Marie, V. Lepeltier and D. L'Hote, Systematic measurement of electron drift velocity and study of some properties of four gas mixtures: A-CH_4, A-C_2H_4, A-C_2H_6, A-C_3H_8, *Nucl. Instrum. Meth.* **152** (1979) 541.

[114] A. Andronic et al., Drift velocity and gain in argon- and xenon-based mixtures, *Nucl. Instrum. Meth. A* **523** (2004) 302.

[115] Th. Berghofer, J. Blumer, J. R. Horandel, A measurement of drift velocities of electrons in xenon-methane mixtures, *Nucl. Instrum. Meth. A* **525** (2004) 544.

[116] D. L. McCorkle, L. G. Christophorou and S. R. Hunter, Electron attachment rate constants and cross-sections for halocarbons, Proc. Second International Swarm Seminar, Oak Ridge, USA, 1981, Pergamon, New York, 1981.

[117] H. Shimamori and H. Hotta, Mechanism of thermal electron attachment to O_2: Isotope effect studies with $^{18}O_2$ in rare gases and some hydrocarbons, *J. Chem. Phys.* **81** (1984) 1271.

[118] M. Huk, P. Igo-kemenes and A. Wagner, Electron attachment to oxygen, water and methanol in various drift chamber gas mixtures, *Nucl. Instrum. Meth. A* **267** (1988) 107.

[119] S. R. Hunter, J. G. Carter and L. G. Christophorou, Low energy electron attachment to SF_6 in N_2, Ar and Xe buffer gases, *J. Chem. Phys.* **90** (1989) 4879.

[120] A. Andronic *et al.*, Pulse height measurements and electron attachment in drift chambers operated with Xe,CO_2 mixtures, *Preprint* arXiv:physics/0303059v1.

[121] E. Kuffel, Condensation Nuclei produced by the Ultra-violet Irradiation of Humid Air or Humid Argon, *Proc. Phys. Soc.* **74** (1959) 297.

[122] M. E. Rose and S. A. Korff, An Investigation of the Properties of Proportional Counters. I, *Phys. Rev.* **59** (1941) 850.

[123] F. Sauli, Gas detectors: Recent developments and future perspectives, *Nucl. Instrum. Meth. A* **419** (1988) 189.

[124] F. Sauli and A. Sharma, Micropattern Gaseous Detectors, *Annu. Rev. Nucl. Part. Sci* **49** (1999) 341.

[125] H. Geiger, E. Rutherford, An Electrical Method of Counting the Number of α-Particles from Radio-Active Substances, *Proc. Royal Soc. A* **81** (1908) 141.

[126] H. Geiger, W. Muller, *Phys. Zeits.* **29** (1928) 839.

[127] G. Charpak *et al.*, The use of multiwire proportional counters to select and localize charged particles, *Nucl. Instrum. Meth.* **62** (1968) 262.

[128] D. R. Nygren and J. N. Marx, The Time Projection Chamber, *Physics Today* **31** (1978), 46.

[129] A. Oed, Position-sensitive detector with microstrip anode for electron multiplication with gases, *Nucl. Instrum. Meth. A* **263** (1988) 351.

[130] G. Charpak, Nobel Lecture, 1992.

[131] K. Kleinknecht, Detectors for particle ratidation, 2nd edition, Cambridge University Press, Cambridge (1998).

[132] R. Bouclier *et al.*, Performance of gas microstrip chambers on glass substrata with electronic conductivity, *Nucl. Instrum. Meth. A* **332** (1993) 100.

[133] F. Angelini *et al.*, Test-beam study of the performance of the microstrip gas avalanche chamber, *IEEE Trans. Nucl. Sci.* **37** (1990) 112.

[134] F. Sauli, Gas detectors: achievements and trends, *Nucl. Instrum. Meth. A* **461** (2001) 47.

[135] J. Bohm, High rate operation and lifetime studies with micro-strip gas chambers, *Nucl. Instrum. Meth. A* **360** (1995) 34.

[136] A. Barr, Construction, test and operation in a high intensity beam of a small system of micro-strip gas chambers, *Nucl. Instrum. Meth. A* **403** (1998) 31.

[137] F. Sauli, GEM: A new concept for electron amplification in gas detectors, *Nucl. Instrum. Meth. A* **386** (1997) 531.

[138] T. Zeuner, The MSGC-GEM Inner Tracker for HERA-B, *Nucl. Instrum. Meth. A* **446** (2000) 324.

[139] B. Ketzer *et al.*, Trends and highlights of VCI 2004, *Nucl. Instrum. Meth. A* **535** (2004) 79.

[140] D. Raspino *et al.*, Status of triple GEM muon chambers for the LHCb experiment, *Nucl. Instrum. Meth. A* **581** (2007) 283.

[141] G. Ruggiero, The TOTEM Detectors, *Proc. of the XIth International Conference of Elastic and Diffractive Scattering Towards the High Energy Frontiers*, Blois, France (2005).

[142] I. Tserruya, Development of a triple GEM UV-photon detector operated in pure CF4 for the PHENIX experiment, *Nucl. Instrum. Meth. A* **523** (2004) 345.

[143] B. Peyaud *et al*, KABES: a novel beam spectrometer for NA48, *Nucl. Instrum. Meth. A* **535** (2004) 247.

[144] S. Aune *et al.*, Performance of the micromegas detector in the CAST experiment, *Nucl. Instrum. Meth. A* **573** (2007) 38.

[145] E. Ferrer-Ribas *et al*, A new Micromegas line for the CAST experiment, *Nucl. Instrum. Meth. A* **581** (2007) 217.

[146] F. Kunne *et al*, The 40×40 cm^2 gaseous microstrip detector Micromegas for the high-luminosity COMPASS experiment at CERN, *Nucl. Instrum. Meth. A* **536** (2005) 61.

[147] Y. Kudenko *et al*, The near neutrino detector for the T2K experiment, *Nucl. Instrum. Meth. A* **598** (2009) 1.

[148] Y. Giomataris, Development and prospects of the new gaseous detector Micromegas, *Nucl. Instrum. Meth. A* **419** (1998) 239.

[149] G. Barouch *et al.*, Development and prospects of a fast gaseous detector Micromegas, *Nucl. Instrum. Meth. A* **423** (1999) 32.

[150] J. Va'vra *et al.*, Measurement of electron drift parameters for helium and CF_4-based gases, *Nucl. Instrum. Meth. A* **324** (1993) 113.

[151] J. Derré *et al.*, Fast signals and single electron detection with a MICROMEGAS photodetector, *Nucl. Instrum. Meth. A* **449** (2000) 314.

[152] J.P. Mols and E. Ferrer-Ribas, photographs at the microscope reproduced with permission.

[153] A. Delbart *et al.*, New developments of Micromegas detector, *Nucl. Instrum. Meth. A* **461** (2001) 84.

[154] P. Jeanneret *et al.*, Performance of a new Micromegas detector, with woven wire mesh,in CF_4, *Nucl. Instrum. Meth. A* **500** (2003) 133.

[155] L. Ounalli, J. L. Vuilleumier, D. Schenker and J. M. Vuilleumier, New gas mixtures suitable for rare event detection using a Micromegas TPC detector, *JINST* **4** (2009) P01001, *Preprint* arXiv:hep-ex/0810.0445.

[156] J. Derré *et al.*, Spatial resolution in Micromegas detector, *Nucl. Instrum. Meth. A* **459** (2001) 523.

[157] J. Derré *et al.*, First beam test results with Micromegas, a high-rate, high-resolution detector, *Nucl. Instrum. Meth. A* **412** (1998) 47.

[158] A. Delbart *et al.*, Performance of MICROMEGAS with preamplification at high intensity hadron beams, *Nucl. Instrum. Meth. A* **478** (2002) 205.

[159] I. Giomataris *et al.*, Micromegas in a bulk, *Nucl. Instrum. Meth. A* **560** (2006) 405, *Preprint* arXiv:physics/0501003.

[160] T. Papaevangelou, Talk Given at the Fourth Symposium on Large TPCs for Low Energy Rare Event Detection, Paris, December 1819, 2008 <http://www-tpc-paris.cea.fr>.

[161] Messer Industriegase GmbH, http://www.messergroup.com/.

[162] Glenn F. Knoll, Radiation Detection and Measurement. John Wiley and Sons, 3rd edition, 2000.

[163] A. Bolotnikov and B. Ramsey, Studies of light and charge produced by alpha-particles in high-pressure xenon, *Nucl. Instrum. Meth. A* **428** (1999) 391.

[164] T. Meinschad, L. Ropelewski and F. Sauli, Detection ofprimary and field-enhanced scintillation in xenon with a CsI-coated GEM detector, *Nucl. Instrum. Meth. A* **547** (2005) 342.

[165] CsI deposit made by André Braem (CERN-PH).

[166] A. T. Alquézar, PhD. Thesis in preparation, University of Zaragoza, 2010.

[167] SAES Getters S.p.A., http://www.saesgetters.com/.

[168] A. Curioni *et al*, A regenerable filter for liquid argon purification, *Nucl. Instrum. Meth. A* **605** (2009) 306.

[169] O. A. Pokratenko *et al.*, Event generator DECAY4 for simulation of double beta processes and decays of radiactive nuclei, *Phys. At. Nucl.*, **63** (2000) 1282-1287.

[170] S. Agostinelli *et al.*, GEANT4-a simulation tookit, *Nucl. Instrum. Meth. A* **506** (2003) 250-303.

[171] J. Allison *et al.*, GEANT4 developments and applications, *IEEE Transactions on Nuclear Science* **53** (2006) 270.

[172] GEANT4 Collaboration, Physics Reference Manual, http://geant4.cern.ch (2005).

[173] ROOT, a framework for data processing, http://root.cern.ch.

[174] SRIM, the Stopping and Range of Ions in Matter, http://www.srim.org.

[175] G. Luzón, private communication.

[176] Table of Isotopes Decay Data, http://nucleardata.nuclear.lu.se/nucleardata/toi.

[177] J. Castell, private communication.

[178] ILIAS database on radiopurity of materials, http://radiopurity.in2p3.fr.

[179] W. Maneschg *et al.*, Measurements of extremely low radioactivity levels in stainless steel for GERDA, *Nucl. Instrum. Meth. A* **593** (2008) 448.

[180] E. Aprile *et al.*, The search for dark matter with the XENON experiment, Talk Given at the Fourth Symposium on Large TPCs for Low Energy Rare Event Detection, Paris, December 1819, 2008 <http://www-tpc-paris.cea.fr>.

[181] G. Heusser, Low level counting from meteorites to neutrinos, *Proc. Low Radioactive Techniques* 2004 p. 29.

[182] A. G. Olaverri, Teoría de grafos y combinatoria, Subject notes, University of Zaragoza.

[183] H. T. Wong, D. A. Imel, V. Jörgens, M. Treichel and J. C. Vuilleumier, Event identification with a time projection chamber in a double beta decay experiment on ^{136}Xe, *Nucl. Instrum. Meth. A* **329** (1993) 163.

[184] H. Gomez *et al*, article in preparation.

[185] A. Bolozdynya *et al*, A high pressure xenon self-triggered scintillation drift chamber with 3D sensitivity in the range of 20-140 keV deposited energy, *Nucl. Instrum. Meth. A* **385** (1997) 225.